## ABSTRACT

COBURN, JONATHAN DAVID. Erosion Characterization of Advanced Plasma Facing Materials (PFMs) for Magnetic Fusion Reactors (Under the direction of Dr. Mohamed Bourham and Dr. John Gilligan).

Plasma-facing materials in future large-scale fusion reactors must be designed to withstand high heat fluxes from extreme off-normal events such as edge localized modes and unmitigated plasma disruptions. The erosion rates of possible tungsten-alternative materials were tested under high heat flux conditions in the DIII-D National Fusion Facility and the electrothermal (ET) plasma source facility at Oak Ridge National laboratory. The plasma-facing materials of interest are high-purity β-3C CVD silicon carbide and MAX phase ceramics $Ti_3SiC_2$ and $Ti_2AlC$. A new analysis method was developed to characterize net erosion using a combination of focused ion beam microscopy, scanning electron microscopy, and atomic force microscopy. SiC and $Ti_3SiC_2$ were exposed to both L- and H-mode plasma discharges in the DIII-D divertor using the DiMES probe. Samples survived average heat fluxes of 2 – 10 $MW/m^2$ over 16 seconds. The new micro-trench erosion measurement technique measured $Ti_3SiC_2$ and SiC erosion rates of 0-9 nm/s and 27-73 nm/s, respectively. Additionally, average ion impact angle estimates for an incident B-field angle of ~1.5° from surface parallel were made using micro-trench impact patterns. Measurements ranged from $\theta = 24^o - 34^o$ with respect to $B_t$ and $\phi = 51.5^o - 55^o$ below the surface normal. Samples of SiC, $Ti_3SiC_2$ and $Ti_2AlC$ were exposed to the ET plasma source along-side tungsten and monocrystalline silicon. Samples experienced heat fluxes of 0.9 – 1 $GW/m^2$ from single and multiple 1 ms plasma discharges. Tungsten samples exhibited pronounced melt-layer formation and deformation, with measured molten pits 2 – 10 μm in diameter and melt-layer depths of up to 7 μm deep. Surface erosion rates for $Ti_3SiC_2$ and $Ti_2AlC$ ranged from 80 – 775 μm/s and 85 – 470 μm/s, respectively. Both MAX phases exhibited extreme surface fracture and material ejection, with damage depths past 4 μm for $Ti_2AlC$ and 11 μm for $Ti_3SiC_2$. SiC displayed the best performance, in one case surviving 15 consecutive ET plasma exposures of about 0.9 $GW/m^2$ heat flux with an average erosion rate of about 26 μm/s and no surface fracturing. SiC erosion rates ranged from 23 – 128 μm/s. Comparing material performance across both experiments, high-purity CVD SiC exhibits the best overall potential for use as a plasma-facing material in large-scale fusion reactor.

Erosion Characterization of Advanced Plasma Facing Materials (PFMs) for Magnetic Fusion Reactors

by
Jonathan David Coburn

A dissertation submitted to the Graduate Faculty of
North Carolina State University
in partial fulfillment of the
requirements for the degree of
Doctor of Philosophy

Nuclear Engineering

Raleigh, North Carolina
2018

APPROVED BY:

| | |
|---|---|
| _____ | _____ |
| Dr. Mohamed Bourham<br>Committee Co-Chair | Dr. John Gilligan<br>Committee Co-Chair |
| _____ | _____ |
| Dr. Igor Bolotnov | Dr. K. Linga Murty |
| _____ | |
| Dr. Alexei Saveliev | |

## DEDICATION

This dissertation is dedicated to my amazing wife, Sara Coburn, for her constant support and encouragement over the long course of this research endeavor. I also dedicate this dissertation to my family and friends, whose love, reassurance, and abundant jokes of graduating kept me motivated to succeed.

## BIOGRAPHY

Jonathan David Coburn is a resident of Raleigh, North Carolina, and formerly from Washington, North Carolina. He received a Bachelors of Science in Nuclear Engineering in May of 2013, followed by a Masters of Nuclear Engineering in December of 2013, at North Carolina State University. Jonathan has been involved in numerous research projects throughout his academic career, starting as a nuclear physics undergraduate researcher at NC State. That research opportunity led to internships at GE Hitachi, Sandia National Laboratories, and eventually US ITER and Oak Ridge National Laboratory which inspired this dissertation work. Notable research topics from his academic experience, outside of the dissertation research, include ultra-cold neutron sources, pyrochemical reprocessing of spent fuel, fission chambers, arc-jet plasma thrusters, and disruption mitigation system modeling.

Jonathan Coburn is currently a graduate student subcontractor in the Fusion and Materials for Nuclear Systems Division at Oak Ridge National Laboratory. After completion of the PhD, he will begin work as a Monaco/ITER Post-Doctoral Fellow with the ITER Organization in Cadarache, France.

## ACKNOWLEDGMENTS

I wish to express my extreme gratitude for Dr. Mohamed A. Bourham. Dr. Bourham has been my graduate advisor throughout my time at North Carolina State University, and was invaluable in shaping my academic career path. He is a one-of-a-kind professor, inspiring, encouraging, and always willing to address any problems his students are facing. I'm particularly thankful for the encouragement he has constantly provided. Whether it was for a class research project or a dissertation experiment, if there was a desire to pursue it, Dr. Bourham would always encourage me to do so and provide guidance to make it happen. I am truly grateful for his dedication, support and inspiration through my entire experience as a Nuclear Engineering student at NC State.

There are many other researchers and scientists I wish to acknowledge for making this collaborative dissertation research possible. Firstly, I am thankful to Dr. Ezekiel Unterberg from Oak Ridge National Laboratory (ORNL) for serving as a technical consultant on my dissertation committee. Dr. Unterberg's willingness to take me on as a graduate student at ORNL, and his guidance through the many experiments that were made possible, is truly appreciated. It was an invaluable experience being able to conduct plasma exposure experiments at ORNL and the DIII-D National Fusion Facility alongside leading researchers in the fusion community. I also wish to thank Dr. Chad Parish at ORNL for his mentorship in materials science and microscopy. Dr. Parish provided countless hours of time aiding me with and training me on the microscope resources available at ORNL. Most of the post-experiment material analysis done for this dissertation was only possible thanks to his service.

I wish to acknowledge Dr. Joseph Barton for serving as the primary author for DIII-D experiment proposal 52-02. I am grateful for his willingness to lead the experiment and for his assistance in analyzing and interpreting the results. I also wish to acknowledge Dr. Trey Gebhart at ORNL for his willingness to conduct the electro-thermal exposure experiments using his ET plasma source. Dr. Gebhart's aid was invaluable in planning and executing the multiple ET campaigns required for the final exposure experiment. I am grateful to Dr. Ane Lasa for giving me permission to utilize her computational MPR scripts, as well as for taking the time to assist me in modifying them for my experiment needs. I am thankful to Dr. Dean Beauchenaur from Sandia National Laboratories, Dr. Michel Barsoum from Drexel University, and Dr. Chad Parish for

providing the material samples used in this research. Finally, I want to extend a special thanks to Dr. David Rasmussen at US ITER for providing me my first avenue for conducting fusion research at ORNL. His guidance and encouragement, along with the opportunities provided to converse with other researchers in the fusion community, laid the groundwork for what would eventually become my dissertation.

This dissertation material is based upon work supported by the U.S. Department of Energy, Office of Science, Office of Fusion Energy Sciences, using the DIII-D National Fusion Facility, a DOE Office of Science user facility, under Awards DE-FC02-04ER54698. It is also supported by the DOE via UT Batelle, LLC Subcontract 4000145506. Academic support was received through the GAANN Fellowship awarded to Jonathan Coburn (P200A150035). DIII-D data shown in this paper can be obtained in digital format by following the links at https://fusion.gat.com/global/D3D_DMP. This work was performed in part at the Analytical Instrumentation Facility (AIF) at North Carolina State University, as well as the Low Activation Materials Development and Analysis (LAMDA) laboratory at Oak Ridge National Laboratory.

## TABLE OF CONTENTS

LIST OF TABLES ..... viii
LIST OF FIGURES ..... ix

**Chapter 1 – Introduction** ..... 1
1.1 – Introduction ..... 1
1.2 – Background on Tokamak Devices ..... 2
1.3 – Current Fusion Reactor Materials ..... 7
1.4 – Purpose of Study ..... 9
References ..... 11

**Chapter 2 – Erosion Mechanisms of Plasma Facing Materials** ..... 12
2.1 – Physical Sputtering ..... 13
2.1.1 – The Plasma Sheath ..... 15
2.2 – Melting and Boiling ..... 18
2.3 – Sublimation ..... 20
2.4 – Other Erosion Mechanisms ..... 22
References ..... 24

**Chapter 3 – Abnormal Events: Disruptions and Edge Localized Modes** ..... 26
3.1 – Disruptions ..... 26
3.1.1 – Causes of Disruptions ..... 27
3.1.2 – Impact of Disruptions ..... 32
3.2 – H-mode and ELMs ..... 35
3.2.1 – Types of ELMs ..... 38
3.2.2 – Summary of ELM Control Methods ..... 39
3.3 – Behavior Expected on Future Tokamak Reactors ..... 40
References ..... 43

**Chapter 4 – Alternative Plasma Facing Materials for Next Gen Tokamak Reactors** ..... 45
4.1 – Silicon Carbides ..... 45
4.1.1 – Monocrystalline and Polycrystalline SiC ..... 46
4.1.2 – SiC/SiC Composites ..... 47
4.2 – MAX Phase Ceramics ..... 48
4.2.1 – $Ti_3SiC_2$ and $Ti_2AlC$ ..... 50
References ..... 52

**Chapter 5 – Methods of PFM Erosion Studies** ..... 53
5.1 – Focused Ion Beam Micro-Trench Technique ..... 53

5.2 – DIII-D National Fusion Facility ..... 60
5.2.1 – Background on DIII-D ..... 60
5.2.2 – DiMES Experiment on DIII-D ..... 61
5.2.2.1 – Experimental Method ..... 62
5.2.2.2 – MATLAB Modeling for Preliminary DiMES Experiment ..... 65
5.2.2.3 – Preliminary DiMES Experiment on DIII-D ..... 69
5.3 – Electrothermal Plasma Sources ..... 73
5.3.1 – Background on Electrothermal Plasmas ..... 73
5.3.2 – ET Experiment at Oak Ridge National Laboratory ..... 79
5.3.3 – ETFLOW Simulations ..... 82
References ..... 84

**Chapter 6 – Results of PFM Erosion Studies** ..... 88
6.1 – DIII-D Experiment ..... 88
6.1.1 – Experiment Details ..... 88
6.1.2 – Micro-trench Erosion Rates ..... 93
6.1.3 – Average Ion Impact Angles ..... 97
6.1.4 – Summary ..... 99
6.2 – Electrothermal Plasma Source Experiment ..... 100
6.2.1 – Experiment Details ..... 100
6.2.2 – Heat Flux Analysis ..... 105
6.2.3 – Microscopy Analysis – Silicon ..... 114
6.2.4 – Microscopy Analysis – Tungsten ..... 117
6.2.5 – Microscopy Analysis – $Ti_3SiC_2$ ..... 122
6.2.6 – Microscopy Analysis – $Ti_2AlC$ ..... 129
6.2.7 – Microscopy Analysis – Silicon Carbide ..... 134
6.2.8 – Combined Erosion Results and Discussion ..... 138
6.3 – ETFLOW Simulations ..... 143
6.3.1 – Ablation Simulations Without Vapor Shielding ..... 143
6.3.2 – Ablation Simulations With Vapor Shielding ..... 145
References ..... 149

**Chapter 7 – Discussion and Conclusion** ..... 150
7.1 – DIII-D Experiment (Physical Sputtering Regime) ..... 150
7.2 – ET Experiment (Melting/Sublimation Regime) ..... 153
7.3 – Overall PFM Performance ..... 157
7.4 – Final Remarks and Future Work Suggestions ..... 161
References ..... 164

**Appendix** ..... 165

## LIST OF TABLES


**Table 5.1** Ideal shot plan for experiment 52-02 ..... 65
**Table 6.1** Average ion impact angle estimations ..... 99
**Table 6.2** Final ET experiment shot plan ..... 105
**Table 6.3** Summary of measured sample emissivities ..... 106
**Table 6.4** Ablation constant values from ETFLOW simulations w/o vapor shielding ..... 144
**Table 6.5** Efficiency ratio results for ETFLOW simulations with vapor shielding ..... 147
**Table 7.1** Ranking of material performance during DIII-D experiment ..... 153
**Table 7.2** Ranking of material performance during ET experiment ..... 156
**Table 7.3** Overall ranking of material performance across all experiments ..... 159

## LIST OF FIGURES


**Figure 1.1** Schematic of a tokamak magnetic field configuration ..... 3
**Figure 1.2** Plasma particle motion in toroidal field configurations..... 4
**Figure 1.3** Interior of JET tokamak and cross section of diverted tokamak plasma ..... 5
**Figure 1.4** Performance comparison between tokamaks, accelerators, and transistors ..... 6
**Figure 1.5** The ITER tokamak design ..... 7
**Figure 1.6** Sample PFM erosion rate comparison ..... 10
**Figure 2.1** Physical sputtering yield for Be, C, and W by D and self-sputtered ions..... 15
**Figure 2.2** Zones of charge balance within the plasma sheath..... 16
**Figure 2.3** Zones of the plasma sheath in the presence of an oblique B field..... 17
**Figure 2.4** Computed ion trajectories with varying initial velocity distributions ..... 18
**Figure 2.5** Examples of melting and vaporization in W..... 19
**Figure 2.6** Temperature vs energy change ..... 21
**Figure 3.1** Sequence of disruption events ..... 28
**Figure 3.2** Plasma parameters during a theoretical disruption on ITER ..... 28
**Figure 3.3** Kink and tearing mode instabilities ..... 31
**Figure 3.4** Power density on JET divertor during a disruption ..... 33
**Figure 3.5** Simulation of ITER vertical instability..... 34
**Figure 3.6** Chart of different modes of confinement..... 36
**Figure 3.7** ELMs on MAST ..... 37
**Figure 3.8** Peeling/Ballooning stability limit and variation of stability boundaries ..... 38
**Figure 4.1** Crystal structure of silicon carbides..... 47
**Figure 4.2** Atomic structure of MAX phase ceramics..... 49
**Figure 5.1** Example 10 x 10 micro-trench for DIII-D experiments ..... 55
**Figure 5.2** Example 10 x 12 micro-trench for ET experiments..... 55
**Figure 5.3** Schematic of micro-trench edge ..... 56
**Figure 5.4** AFM tapping mode and probe tip..... 58
**Figure 5.5** Example AFM data for FIB tungsten sample ..... 59
**Figure 5.6** Modified AFM tips ..... 60
**Figure 5.7** DiMES probe assembly ..... 63
**Figure 5.8** DiMES surface temperature estimations ..... 64
**Figure 5.9** Example micro-trench geometries in MPR-Trench..... 67
**Figure 5.10** Ion impact angle distribution functions ..... 68
**Figure 5.11** Sample map for preliminary DiMES experiment ..... 70
**Figure 5.12a** Preliminary experiment micro-trench cluster, unexposed ..... 71
**Figure 5.12b** Preliminary experiment micro-trench cluster, exposed ..... 71
**Figure 5.13** Square micro-trench from preliminary experiment, post-exposure..... 73
**Figure 5.14** Layout of typical ET discharge system..... 74
**Figure 5.15** Assembled ORNL ET source..... 75

**Figure 5.16** Electrical system for ORNL ET source ..... 80
**Figure 5.17** ORNL ET source setup ..... 81
**Figure 5.18** Assembled ET plasma source at ORNL ..... 81
**Figure 6.1** Schematic of DiMES head and samples ..... 89
**Figure 6.2** Example 4 x 10 micro-trench before and after plasma exposure ..... 90
**Figure 6.3** Example 10 x 10 micro-trench with AFM data ..... 91
**Figure 6.4** Example temperature data from DIMES IRTV ..... 93
**Figure 6.5** SiC and $Ti_3SiC_2$ erosion rate vs heat flux ..... 94
**Figure 6.6** SiC erosion rate vs height location ..... 95
**Figure 6.7** SiC erosion rate vs heat flux, with trendlines ..... 96
**Figure 6.8** Ion impact patterns ..... 98
**Figure 6.9** ET sample dimensions ..... 101
**Figure 6.10** Example 10 x 12 FIB micro-trench in $Ti_2AlC$ ..... 103
**Figure 6.11** FIB bitmap image for depth markings ..... 103
**Figure 6.12** Diagram of ET sample target ..... 107
**Figure 6.13** Post-exposure image of ET target holder ..... 110
**Figure 6.14** Temperature and heat flux density from IR camera ..... 111
**Figure 6.15** Time-lapse of IR temperature data frames ..... 111
**Figure 6.16** Example profiles of ET current and power ..... 112
**Figure 6.17** Heat flux as a function of maximum ET source power ..... 113
**Figure 6.18** Silicon Micro-trench Example #1 ..... 115
**Figure 6.19** Silicon Micro-trench Example #2 ..... 116
**Figure 6.20** Silicon Micro-trench Overlay Image ..... 117
**Figure 6.21** Tungsten Micro-trench Example #1 ..... 118
**Figure 6.22** Tungsten Micro-trench Example #2 ..... 119
**Figure 6.23** Tungsten Micro-trench Example #3 ..... 120
**Figure 6.24** Tungsten Micro-trench Example #4 ..... 121
**Figure 6.25** Tungsten Label Image ..... 122
**Figure 6.26** $Ti_3SiC_2$ Micro-trench Example #1 ..... 123
**Figure 6.27** $Ti_3SiC_2$ Micro-trench Example #2 ..... 125
**Figure 6.28** $Ti_3SiC_2$ Micro-trench Example #3 ..... 126
**Figure 6.29** $Ti_3SiC_2$ Micro-trench Overlay Image #1 ..... 127
**Figure 6.30** $Ti_3SiC_2$ Micro-trench Example #4 ..... 128
**Figure 6.31** $Ti_3SiC_2$ Micro-trench Overlay Image #2 ..... 128
**Figure 6.32** $Ti_2AlC$ Micro-trench Example #1 ..... 129
**Figure 6.33** $Ti_2AlC$ Micro-trench Example #2 ..... 131
**Figure 6.34** $Ti_2AlC$ Micro-trench Overlay Image ..... 132
**Figure 6.35** $Ti_2AlC$ Micro-trench Example #3 ..... 133
**Figure 6.36** $Ti_2AlC$ Label Image ..... 133
**Figure 6.37** Silicon Carbide Micro-trench Example #1 ..... 135

**Figure 6.38** Silicon Carbide Micro-trench Example #2 ..... 136
**Figure 6.39** Silicon Carbide Overlay Image ..... 137
**Figure 6.40** Overlaid image for material loss measurement parameters ..... 138
**Figure 6.41** Max surface erosion rate vs heat flux, single exposures ..... 140
**Figure 6.42** Max surface erosion rate vs heat flux, multiple exposures ..... 141
**Figure 6.43** Max surface erosion rate vs heat flux, all exposures ..... 142
**Figure 6.44** ETFLOW results of total eroded mass and thickness ..... 145
**Figure 6.45** Vapor shielding efficiency ratios for $Ti_3SiC_2$ ..... 146
**Figure 6.46** Thickness losses for alternative PFM candidates for 500 μs disruptions ..... 148
**Figure 7.1** Visual comparison of overall PFM performance ..... 160
**Figure 7.2** Combined PFM erosion rate comparison as a function of heat flux ..... 162

# CHAPTER 1 – INTRODUCTION

## 1.1 – Introduction

The quality of life in various countries is often correlated with per capita energy usage [1]. As the population increases and as the developing world evolves closer to the needs and lifestyles of the developed world, global energy demand is expected to drastically increase. Some estimates predict that electricity demand alone will increase by a factor of 3 by the year 2050 [1]. Rather than rely on fossil fuels, the world is slowly but deliberately moving towards carbon-free energy sources in an effort to secure reliable energy while combating global climate change. Carbon-neutral, carbon-free, and renewable energy sources have the potential to fill some of this need and are rapidly being developed, particularly wind and solar power. However, in the best-case development scenarios, even accounting for advanced energy storage technologies, these renewable sources are hindered by both low energy density and temporal variations. A global energy solution depends on the operation of a clean, reliable source of baseload power. Nuclear fission is a viable option to meet this demand, although it is still plagued by concerns of safety, radioactive waste, and proliferation.

Fusion energy offers an attractive solution to the growing global demand for energy. If properly harnessed, engineered, and controlled at an affordable cost, electricity generation from nuclear fusion can provide nations with energy security while avoiding further environmental degradation from fossil fuels [1]. It offers the same upsides of nuclear fission without the concerns of accident scenarios or proliferation, all with minimum, short-lived radioactive waste. Harnessing nuclear fusion in a controlled, sustainable way is a research challenge that spans back over 50 years. Multiple methods of fusion energy production have been explored, including magnetic confinement, inertial confinement, electrostatic confinement, and pinch configurations [1]. Tokamak-based fusion devices, which utilize magnetic confinement methods, have demonstrated the greatest fusion energy performance thus far [2]. Global progress in tokamak fusion experiments has even motivated the construction of the International Thermonuclear Experimental Reactor (ITER), the world's first large-scale tokamak device designed to achieve net fusion energy gain. However, many physics and engineering challenges remain for ITER and beyond. Harnessing nuclear fusion in a controlled, sustainable way is a multifaceted challenge. The goal of this dissertation is to contribute to the ongoing fusion research addressing these challenges. Of the

many research topics, this dissertation delves into the investigation of suitable plasma-facing materials for advanced magnetic-confinement fusion reactors. In doing so, this research will play a small but important part in making fusion power a viable global energy solution.

### 1.2 – Background on Tokamak Devices

Magnetic confinement fusion devices take advantage of the electric charges of plasma particles and confine them in a magnetic bottle. Specially designed magnetic field configurations restrict charged particle motion across the magnetic field lines while promoting motion along them. The name "tokamak" is an acronym of the Russian words "тороидальная камера с магнитными катушками" (***to****roidal'naya* ***ka****mera s* ***ma****gnitnymi* ***k****atushkami),* which translates to "toroidal chamber with magnetic coils" [2]. In the tokamak, the plasma is formed in the shape of a torus through specifically designed toroidal and poloidal magnetic field configurations. A toroidal magnetic field $B_\phi$ is not sufficient to confine the plasma alone, as the curvature of the field lines produces opposing particle drifts for the charged ions and electrons [2]. This effect leads to a charge separation, electric field formation, and eventual loss of plasma. For a tokamak, a poloidal magnetic field $B_\theta$ is added by imposing a toroidal current within the plasma, often at a much smaller magnitude than $B_\phi$. The combined toroidal and poloidal magnetic field lines spiral around the torus structure in nested toroidal surfaces, forming what are referred to as closed magnetic flux surfaces [2]. Lastly, to counteract radial expansion forces, vertical magnetic fields are induced via vertical field coils to achieve radial equilibrium. Figure 1.1 highlights how the toroidal and poloidal field lines are developed in a tokamak device using magnetic field coils. Figure 1.2 demonstrates the physics behind particle motion in a toroidal magnetic field versus a toroidal plus poloidal field configuration.

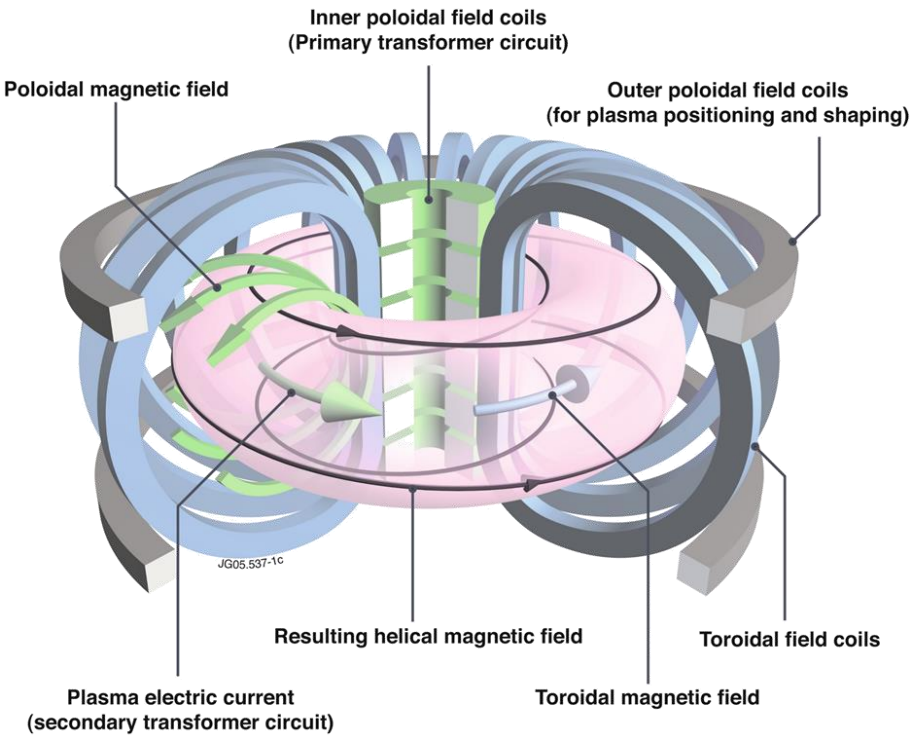


**Figure 1.1** – Schematic of a tokamak magnetic field configuration [3]

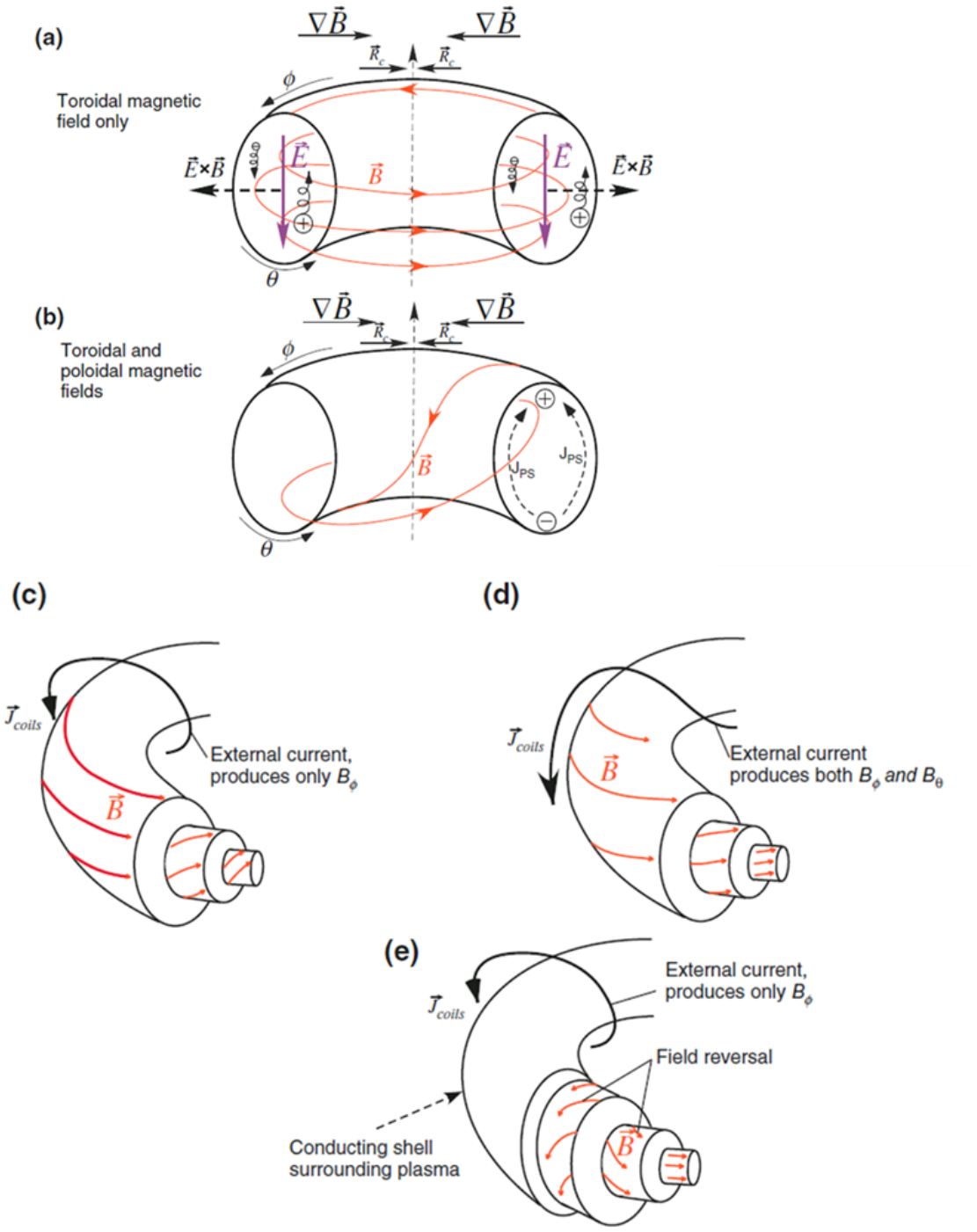


**Figure 1.2** – (a) A simple toroidal magnetic field configuration, demonstrating the particle drifts, charge separation, and E x B drift that arises. (b) A helical magnetic field from toroidal and poloidal field components, which removes charge separation. (c) Tokamak configuration. (d) Stellerator configuration. (e) Reversed field pinch configuration. [2]

Modern tokamaks operate in a diverted shape which deviates slightly from the configuration in Figure 1.2 (c). In this configuration, the last closed flux surface is opened up such that a cross point, or X-point, is formed as in Figure 1.3 (Right). The now open magnetic flux surfaces are then directed to target plates in a component called the divertor. The divertor is designed to manage the thermal loads from plasma particles that escape the separatrix, are transported through the scrape-off layer, and eventually impact the divertor plates at the strike point location [1,2]. Divertors allow for efficient exhaust of escaped plasma particles and helium ash, reducing the impact of built-up impurities on the plasma core. The tokamak plasma is usually initiated in a limited configuration, then the plasma shape is modified into a diverter configuration using the poloidal field coil currents [1]. Depending on the design, tokamaks can operate with a single diverted configuration at the top or bottom of the torus, as in Figure 1.3, or with a doubly diverted configuration.

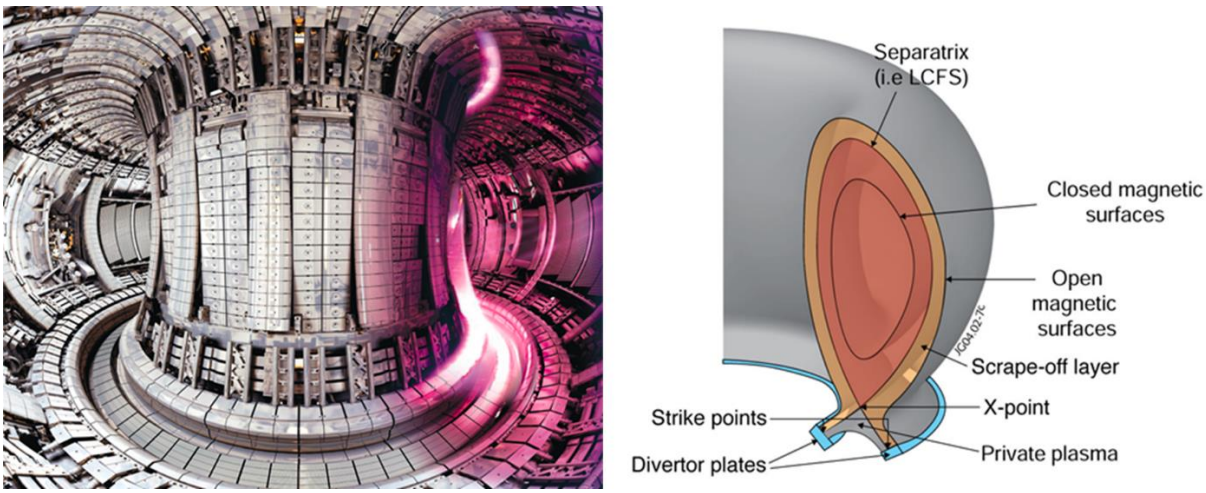


**Figure 1.3** – (Left) A composite image of the interior of the JET tokamak before and during plasma operations, highlighting the plasma impact within the lower divertor region. (Right) A cross-section outlining the regions of a diverted tokamak plasma [4]

The basic tokamak design has significantly advanced through the past few decades. There have been extensive improvements in confinement, transport properties, operating density, and plasma stability, allowing for the discovery and exploration of new, efficient confinement regimes. The fusion triple product ($nT\tau$), a combination of the plasma density, temperature, and confinement time, designates the minimum requirements to achieving a “burning fusion plasma”,

where plasma heating by products of the fusion reaction is sufficient to balance out thermal losses and maintain the desired plasma temperature. Achievements in the triple product have kept pace with other high-tech industries, increasing at a slightly higher rate than Moore's Law, at least up to the 1990's [5]. Figure 1.4 highlights this growth rate in fusion capabilities compared to processor chips and particle accelerators. Today, tokamaks are the most advanced toroidal confinement system and are the most promising candidate for the first generation of fusion reactors. By further increasing the reactor size and magnetic field strengths, energy storage and confinement are expected to finally improve to the point of generating a burning fusion plasma and surpassing energy breakeven.

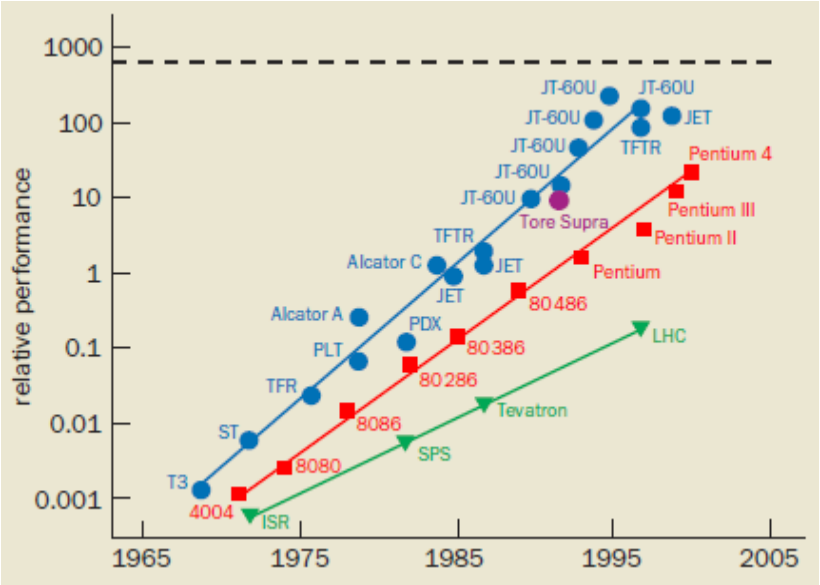


**Figure 1.4** – Performance comparison between tokamak plasma achievements (blue), the energy of particle accelerators (green), and the number of transistors on processor chips (red). The relative performance of fusion plasmas is defined by the fusion triple product. The dashed line indicates the performance expected on ITER [5]

International fusion research effort has culminated in the design and construction of the ITER device. Scientists and engineers from over 35 nations have banded together to construct the world's first tokamak device capable of producing net fusion-energy [1,2,6]. ITER is scaled to be 10 times greater than today's largest tokamak devices in order to increase the amount of plasma stored energy and potential of fusion energy production [6]. A cross-section of the ITER device is

displayed in Figure 1.5 which highlights important design features and components and their material composition. ITER is introducing plasma-facing materials (PFMs) and components (PFCs) to a largely unexplored territory. The combination of high particle fluxes, over long pulse lengths, at high power flux densities raises serious material integrity questions that must be addressed. The materials and designs for ITER's plasma-facing components have already been solidified and are currently under construction. Although ITER is planned to be the first fusion device to generate net fusion energy, it will not capture the power it produces as electricity. Next-generation fusion devices will be required that are scaled and designed based on ITER's performance. These fusion reactors will demand even greater fusion performance and will likely require advanced material solutions to counter any problems uncovered during ITER operation. Thus, any next-generation materials studies should begin by evaluating material performance under ITER-like conditions.

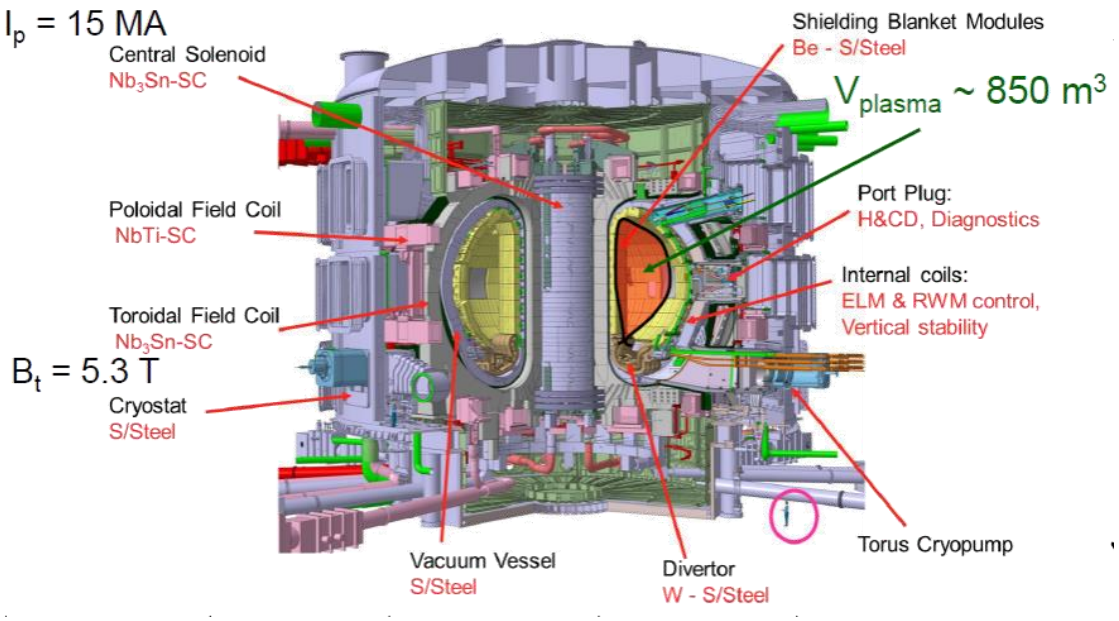


**Figure 1.5** – The ITER tokamak design [7]

### 1.3 – Current Fusion Reactor Materials

The main functions of the tokamak first wall and divertor PFCs are to capture high-energy neutrons and protect in-vessel components from radiative and conductive heat loads, all while minimizing plasma impurity concentrations. Unlike today's operating machines, ITER will be the

first to experience significant net erosion due to its high power, long pulse operations. Normal operations will see large but manageable heat loads on PFCs on the order of 0.25-10 $MW/m^2$ [8,9]. The main hazard in regard to heat flux driven erosion comes from off-normal, transient events which grow in severity with increased plasma stored energy. In particular, materials must withstand high heat fluxes from edge localized modes (ELMs), vertical displacement events (VDEs), and thermal quench phases of plasma disruptions. Erosion from these extreme events degrades PFM lifetime and disperses particulates/aerosol into the reactor's vacuum vessel, further quenching the plasma and coating the interior components. For ITER, uncontrolled type I ELMs and disruptions are capable of producing $GW/m^2$ scale heat fluxes during $Q_{DT}$ = 10 operations [2,10].

To meet these requirements and others, ITER has chosen a combination of beryllium and tungsten as plasma-facing materials, which are then supported by other structural and shielding materials like copper and steel. The entire first wall will be comprised of beryllium. Beryllium is mainly chosen for its low-Z properties that minimize the impact of impurities in the plasma core [11]. It is also non-reactive with hydrogen isotopes and a natural oxygen getter. Solid beryllium has been used in the JET tokamak for both limiter and divertor tiles and has demonstrated good plasma compatibility through multiple operations [12]. The trade-off is a high rate of physical sputtering and a low melting point if any undesired plasma impact occurs. For the divertor, ITER's original strategy was to take a multi-stage approach, starting with a carbon-fiber-composite (CFC) and W divertor for the non-nuclear phase of operation and then moving to a full W divertor for deuterium-tritium (DT) operations [10]. The major downsides to using CFC were strong tritium retention and chemical sputtering, rendering the material unusable during D-T operations. For that, tungsten is the material of choice due to its high melting point and high-Z, which strongly reduces erosion due to physical sputtering. However, tungsten's high-Z also means any W impurities will have an extreme impact on plasma performance due to radiation losses. A CFC divertor, which is low-Z and sublimates rather than melting, offered a more forgiving material that would reduce risks of material damage as ITER came online. ITER has now elected to forego CFC and start operations with a full W divertor, which is expected to survive well into the nuclear phase [8]. R&D efforts by ITER scientists have been accelerated to determine how to safely operate a W divertor in the high power, high stored energy device. The two main issues are core impurity concentration and material integrity. The most outstanding and complex issue associated with W

is the possibility of material melting under transient heat fluxes [8]. ITER is expecting to meet these demanding material challenges; the divertor and first wall designs are complete and are currently in the procurement phase. These concerns set the precedent for next-generation fusion material studies, in which materials must be designed to be superior to Be and W in reactor-relevant environments.

### 1.4 – Purpose of Study

The goal of this dissertation is to characterize the relative erosion properties of advanced plasma-facing material candidates and compare them to current fusion material choices. Studies were undertaken to analyze the erosion of selected PFMs under the high heat flux conditions expected in future tokamak reactors, for 5 – 10 $MW/m^2$ steady state conditions and ~$GW/m^2$ transient conditions due to ELMs and disruptions. A dataset of the erosion rate of these materials was developed so that materials can be easily compared to one another. This dataset was comprised of both simulated and experimental data spanning a wide range of heat flux regimes: physical sputtering, melting, and sublimation dominated erosion regimes. The plan leverages the relationship between NC State University, Oak Ridge National Laboratory, and the DIII-D National Fusion Facility to carry out collaborative research using state-of-the-art fusion facilities and simulation tools. In doing so, the desire is to collect enough data to create a chart similar to the one in Figure 1.6, comparing the erosion rates of the candidate PFMs to current fusion materials across reactor-relevant heat flux regimes.

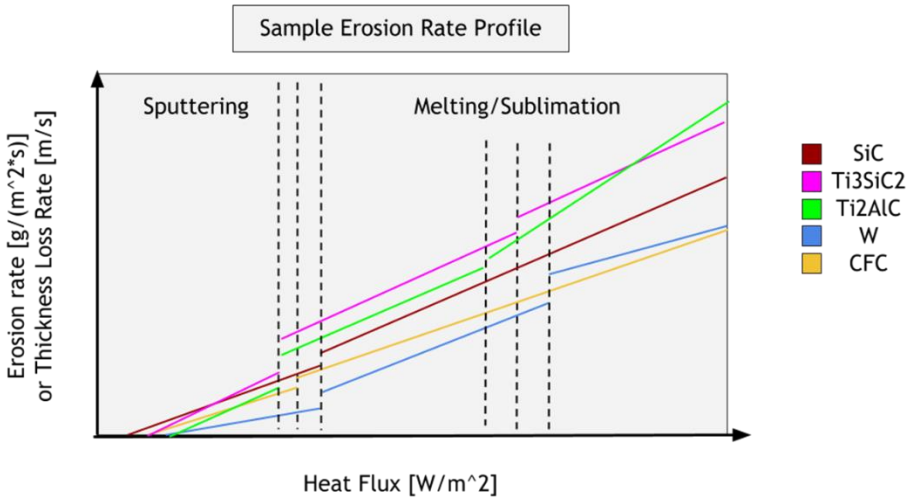


**Figure 1.6** – A sample PFM erosion rate comparison as a function of impinging heat flux, representing the final results goals of this research work.

A secondary goal of the dissertation is to utilize advanced microscopy capabilities for any experimental PFM sample analysis. It is important to physically measure any erosion thickness using a non-destructive, post-mortem technique. In collaboration with Oak Ridge National Laboratory, a new analysis method was developed for larger material samples that are more representative of plasma-facing components. Material samples were successfully characterized before and after all plasma exposure experiments using this method.

## REFERENCES


[1] M. Kikuchi et al. *Fusion Physics*. Chapter 7, 2012

[2] V. Igochine, *Active Control of Magneto-Hydrodynamic Instabilities in Hot Plasmas*. *Springer series on Atomic, Optical, and Plasma Physics*, vol. 83, 2015

[3] "Tokamak Principle." 20 Sept. 2011, www.euro-fusion.org

[4] "Plasma-Material Interactions." Dutch Institute for Fundamental Energy Research, https://www.differ.nl/research/plasma-material-interactions Accessed 24 September 2018

[5] G. T. Hoang and J. Jacquinot, "Controlled Fusion: The Next Step." *Physics World*, vol. 17, no. 1, 2004

[6] "What is ITER?" www.iter.org Accessed 15 Aug. 2018

[7] A. Loarte, "ITER and Pedestal Physics." Presentation, 2015 ITER International School, USTC, Hefei, China 2015

[8] R.A. Pitts et al. "A Full Tungsten Divertor for ITER: Physics Issues and Design Status," *Journal of Nuclear Materials*, vol. 438, 2013, S48-S56

[9] M. Merola et al. "ITER Plasma-facing Components." *Fusion Engineering and Design*, vol. 85, 2010, pp. 10-12

[10] R.A. Pitts et al. "Physics Basis and Design of the ITER Plasma-Facing Components," *Journal of Nuclear Materials*, vol. 415, 2011, S957

[11] ITER Physics Basis Editors, "ITER Physics Basis." *Nuclear Fusion*, vol. 39, no. 12, 1999

[12] L. Horton et al. "The JET ITER-like Wall Experiment: First Results and Lessons for ITER." *Fusion Engineering and Design*, vol. 88, 2013, pp. 434-439

## CHAPTER 2 – EROSION MECHANISMS OF PLASMA FACING MATERIALS

Plasma-surface interactions within the tokamak lead to erosion of the first wall components, especially during abnormal events with high heat flux exposures and high energy particle impacts. This material loss from the wall then causes an influx of impurities into the plasma, where impurities can either enter the core plasma or be redistributed along the walls due to material transport [1]. The combination of erosion, material transport, and re-deposition will result in some components undergoing net material erosion while others experience net material deposition. It is the areas where net erosion is prevalent that limit the plasma-facing component (PFC) lifetime [1]. In present-day tokamak devices, the net erosion of divertor plates has a minimal impact on PFC lifetime. Typical discharge times are on the order of seconds, with records as high as 100 s [2,3,4]. The bigger concern for these short discharges is the release of impurities into the core plasma, which dilutes the plasma composition and leads to unwanted power loss from thermal radiation [3]. However, for ITER and the large-scale reactors that will follow, higher heat and particle fluxes over hundreds of seconds of exposure time make net erosion a serious concern [1]. Plasma-facing materials must be chosen to offer low erosion losses while balancing other concerns for plasma contamination, tritium retention, neutron activation, and effects on the thermal/mechanical properties.

When discussing material erosion, it is important to distinguish between gross and net erosion. Gross erosion refers to all loss of material that occurs from the surface, ignoring where that material is transported. It is often measured in-situ in tokamaks using spectroscopic methods. Net erosion refers to the total amount of material that leaves and is deposited onto the surface, accounting for any redeposition of material that occurs at the measurement area. The redeposition process is complex in a tokamak environment. For sputtering-dominated erosion, atoms with large Larmor radii can exhibit prompt redeposition in a strong magnetic field. There can be local redeposition where sputtered ions barely interact with the plasma edge, or there can be global migration and redeposition as ions are transported through the plasma edge and core. Unless an experiment is specifically designed to prevent redeposition, what is usually measured in post-mortem analysis is inherently the net erosion from a given plasma exposure.

## 2.1 – Physical Sputtering

A material surface can begin the erosion process even before approaching it's melting temperature when the surface experiences impact from high-energy particle fluxes. This phenomenon occurs when plasma particles, either ions or neutrals, strike the surface with high enough energy to remove surface atoms via collisions. This is classically referred to as physical "sputtering", the removal of surface-level lattice atoms via particle bombardment which can drastically change the surface morphology [5]. Erosive sputtering was first observed almost 150 years ago on cathodes in electric gas discharge tubes and was consequently named "cathode sputtering" [5].

Mass loss due to sputtering is one of the many physics mechanisms that take place when high-energy particles impact a material. Today the physics of sputtering is relatively well understood. If the binding energy of lattice atoms in the target material is small (10's of eV) compared to the energy of the impacting particle, a scattering event between the two will result in the lattice atom being knocked out of its position via momentum transfer. The atom knocked away is known as the "primary knock-on atom" (PKA). Depending on the angle of impact and ejection, the PKA can either be itself sputtered or go on to collide with other lattice atoms and form "secondary knock-on atoms" (SKAs). These SKAs can themselves escape the surface as sputtered atoms. Several physical sputtering regimes can be identified depending on the energy of the incident particles, the impact angle, and collision cross sections for the projectile/target pairs [5]. The single knock-on regime refers to when PKAs receive enough energy to sputter away from the surface, without having enough energy to generate sputtering SKAs. This regime is typical for light ions and lower energy heavy ions. The linear cascade regime represents what happens when PKAs do possess enough energy to generate a cascade of SKAs that increase the sputtering yield. The spike regime applies to heavy ion impacts, where the collision density within the target lattice is so high that the majority of atoms in an entire volume are displaced.

Physical sputtering only occurs if the surface atom receives enough energy to exceed its surface binding energy [3]. The threshold energy, $E_T$, represents the incident ion energy below which sputtering cannot occur. For the most extreme case of head-on collisions, $E_T$ is given by:

$$Eq.1. \quad E_T = \frac{E_s}{\gamma(1-\gamma)}$$

Where $E_s$ is the surface binding energy, which is often taken as the energy of sublimation, and γ is in this case the maximum energy fraction that can be transferred in a two-body collision, $\gamma = 4m_1m_2/(m_1 + m_2)^2$ [2,3]. The most common sputtering event for light incident ions, i.e. D and T, involves two collisions: a projectile ion penetrates the material and collides within the lattice, reflecting the projectile back towards the surface layer. The second collision then occurs on a first-layer atom from below, ejecting that lattice atom [2]. The additional term of (1-γ) in Equation 1 accounts for this reflection process [3].

Physical sputtering is often characterized in the literature by the sputtering yield, Y, which represents the number of sputtered atoms per incident particle. Y is dependent on the projectile and target masses, the projectile energy and angle of incidence, the target material's threshold energy and energy of sublimation. Experimental results are usually summarized by plotting the sputter yield against the incident ion energy E. If Y is plotted against $E/E_T$, there is a general, semi-empirical curve that describes the sputter yield of a given projectile/target pair across a wide energy range [3]. For ions of normal incidence (θ = 0), this sputter yield curve takes the form of the Bohdansky formula [2,3]:

$$Eq.2 \quad Y(E,\theta = 0) = QS_n\left(\frac{E}{E_{TF}}\right)g\left(\frac{E}{E_T}\right)$$

where Q is the yield factor, which depends only on the surface binding energy and the ion/target masses. $S_n(E/E_{TF})$ is the nuclear stopping cross section, where $E_{TF}$ is a characteristic Thomas-Fermi energy, and $g(E/E_T)$ takes into account threshold effects, both of which have analytical forms [2,3]:

$$Eq.3 \quad S_n(\varepsilon) = \frac{3.441\sqrt{\varepsilon}\ln(\varepsilon + 2.718)}{1 + 6.355\sqrt{\varepsilon} + \varepsilon\left(6.882\sqrt{\varepsilon} - 1.708\right)}, \quad \varepsilon = \frac{E}{E_{TF}}$$

$$Eq.4 \quad g(\delta) = \left(1 - \delta^{\frac{2}{3}}\right)(1 - \delta)^2, \quad \delta = \frac{E_{th}}{E}$$

With known values for Q, $E_T$, and $E_{TF}$, Equation 3 can be used to predict sputter yields of normal incidence for any ion/target combination. Example sputter yield curves for different ion/target pairs are shown in Figure 2.1. The sputter yield decreases with increasing sublimation energy, increases with increasing incident particle energies, increases with increased projectile mass, and decreases with increased target mass. As for angular dependence, the sputter yield increases as the angle of incidence θ increases with respect to the surface normal [3,5]. To the first order, Y increases by a factor of cos(θ). Angular distribution calculations of incident ions when

they impact a divertor or first wall are difficult. There are effects of the ion Larmor radius, the acceleration in the plasma sheath, E x B drift effects, and the surface roughness [3, 6]. The effective sputtering yield for tokamak experiments is typically about twice that of code predictions for normal incidence, which is often deemed good enough by experimenters [2,3]. As for the sputtered atoms, their angular distribution is approximated well enough by a cos(θ) distribution. Strong crystalline effects have been observed in single-crystal targets.

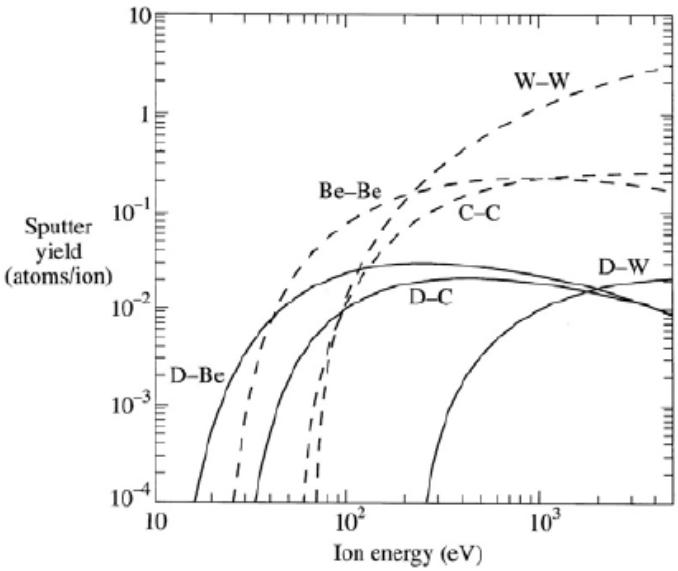


**Figure 2.1** – Energy dependence of the physical sputtering yield for Be, C, and W by D and self-sputtered ions, calculated from the TRIM Monte Carlo Code [3]

2.1.1 – The Plasma Sheath

An overview of the plasma sheath and its impact on ion parameters is essential when considering erosion due to physical sputtering. The electrostatic plasma sheath, also known as the Debye sheath, represents a relatively thin layer of plasma attached to the divertor (or limiter) target surface [3]. Since the electron thermal velocity is higher than that of ions, the more mobile electrons reach the wall earlier, building up a negative charge. This capture leads to a depletion zone for the electrons, causing an electric field to establish near the target surface which repels electrons and attracts ions [3,7]. The acceleration effect within the electric field causes both electrons and ions to reach the ion sound speed $c_s$ at the sheath edge, given by Equation 5 [3].

$$Eq.5 \quad v_i = v_e = c_s = \left[\frac{T_i + T_e}{m_i}\right]^{\frac{1}{2}}$$

The floating electric potential that forms between the target surface and the sheath edge, $V_f$, is determined by the requirement of zero net current at the surface:

$$Eq.6 \quad V_f = \frac{1}{2}\frac{T_e}{e}\ln\left[\frac{2\pi}{(1-\delta)^2}\left(\frac{m_e}{m_i}\right)\left(1+\frac{T_i}{T_e}\right)\right]$$

Where δ is the total secondary electron emission coefficient due to both ions and electrons. For a deuterium plasma, for example, with $T_e = T_i$ and $\delta = 0$, $V_f \approx -3T_e/e$ [3]. Example variations in electric potential, ion velocity, and electron and ion densities $n_e$ and $n_i$, along with distinctions between the plasma, pre-sheath, and Debye sheath, are portrayed in Figure 2.2.

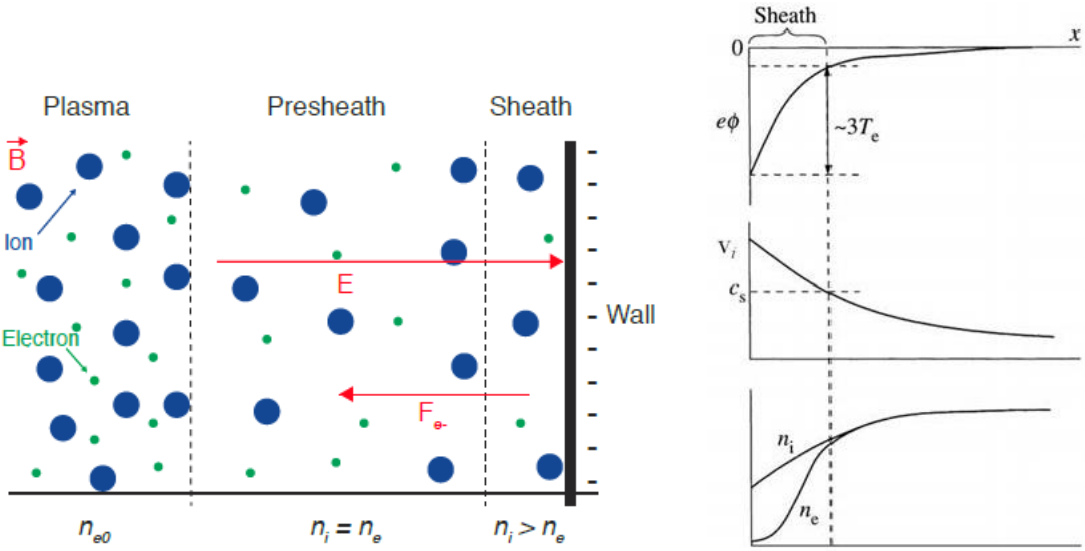


**Figure 2.2** – (Left) Various zones of charge balance within the plasma sheath that forms outside of a plasma-facing wall component [7]. (Right) Example spatial variation of the electric potential, ion velocity $v_i$, and ion and electron densities $n_i$ and $n_e$ within the electrostatic plasma sheath [3]

The typical thickness of the Debye sheath is on the order of a few Debye lengths, which is typically $10^{-5}$ – $10^{-6}$ m [2,3,7]. The presence of an electric potential within this thin sheath directly affects ion motion, accelerating them towards the plasma-facing surface. This trajectory is further complicated in the presence of a strong magnetic field. Charged electrons and ions gyrate along magnetic field lines due to the Lorentz force as they travel through the bulk plasma. Although the

core plasma is nested within closed flux surfaces, modern tokamaks operate in a diverted configuration as described in Section 1.2. These divertors are designed such that the open magnetic field lines within the scrape-off layer impact the divertor surface at shallow, oblique angles, often a few degrees from the surface parallel [2,3]. The presence of the angled magnetic field lines causes a magnetic pre-sheath to form. This sheath, also known as the Chondura sheath, is quasi-neutral and is typically a few Larmor radii in thickness, on the order of mm to cm [2,7]. Figure 2.3 highlights the different zones of the combined Chondura and Debye sheaths and their impact on electron and ion motion.

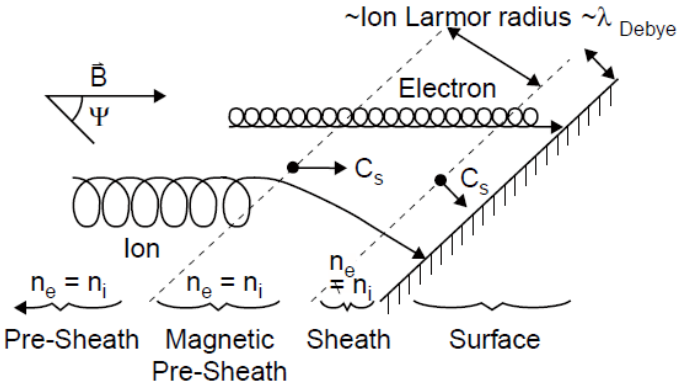


**Figure 2.3** – Zones of the plasma sheath in the presence of an oblique magnetic field [2]

The gyromotion of high-energy ions causes variance in the initial trajectory when entering the magnetic pre-sheath and Debye sheath, further altering the ion motion as it accelerates towards the plasma-facing surface. One further complication arises from the combined presence of the magnetic and electric fields within the total plasma sheath. An E x B drift force manifests, deflecting the 'guiding center motion' of the gyrating ions in a direction perpendicular to the magnetic field lines [7,8]. This drift force combined with the gyromotion drastically changes the ion impact angle in the 3D space. Figure 2.4 depicts a computational model of ion motion as they approach the divertor surface, accounting for gyromotion, acceleration in the Debye sheath, and the effects of E x B drift, highlighting their combined effect on the final ion impact angle onto the plasma-facing material surface.

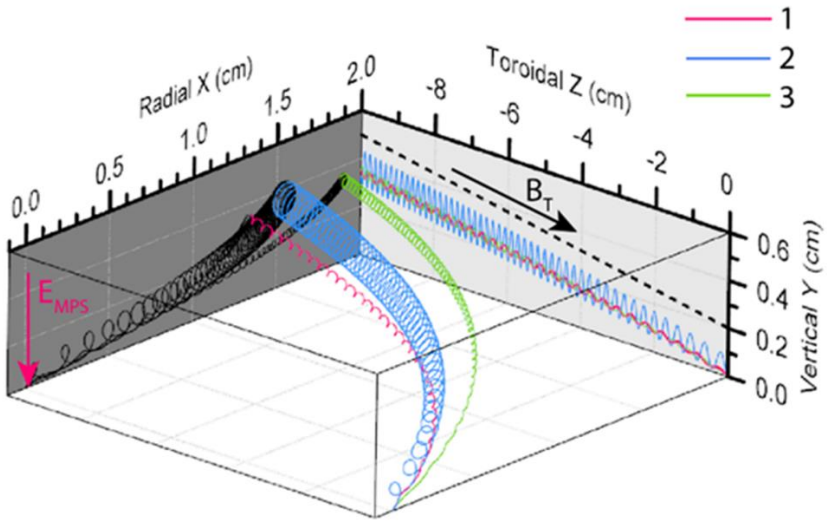


**Figure 2.4** – Computed ion trajectories for $D^+$ ions with varying initial velocity distributions, where the R-Z plane represents the material surface at Y = 0 [8].

As discussed in Section 1.2, the sputtering yield for a given ion/target pair is dependent on the incident energy and impact angle. Thus, it is important to understand that changes in the total plasma sheath, either by the tokamak operating conditions or by the surface geometry itself, will change the ion impact parameters and thereby alter the amount of erosion by physical sputtering.

## 2.2 – Melting and Boiling

The surface temperature of plasma-facing components will rise under prolonged exposure to high energy plasma fluxes. For metallic materials, the surface can begin to melt and/or boil, paving the way for macroscopic erosion mechanisms much more severe than physical sputtering. Under steady-state operation in ITER-scale devices, key PFCs like ITER's W divertor and Be first wall will be designed with adequate cooling such that normal operating temperatures will be well below material melt limits. However, during high energy transients from ELMs and disruptions, a complex combination of melting, boiling, and vaporization are predicted. For a single off-normal event, surface vaporization losses may be on the order of microns, while melt layer thicknesses could range from tens to hundreds of microns [9,10]. Such deep melt layers are what set the stage for massive material loss. Figure 2.5 provides illustration of this problem with example

calculations of temperature, melt layer thickness, and vaporization thickness in tungsten for a 10 MJ/m$^2$, 1 ms disruption [11]; Figure 2.5 also shows results from QPSA plasma gun experiments which demonstrate the melting of ITER W mono-blocks under ITER-relevant conditions [12].

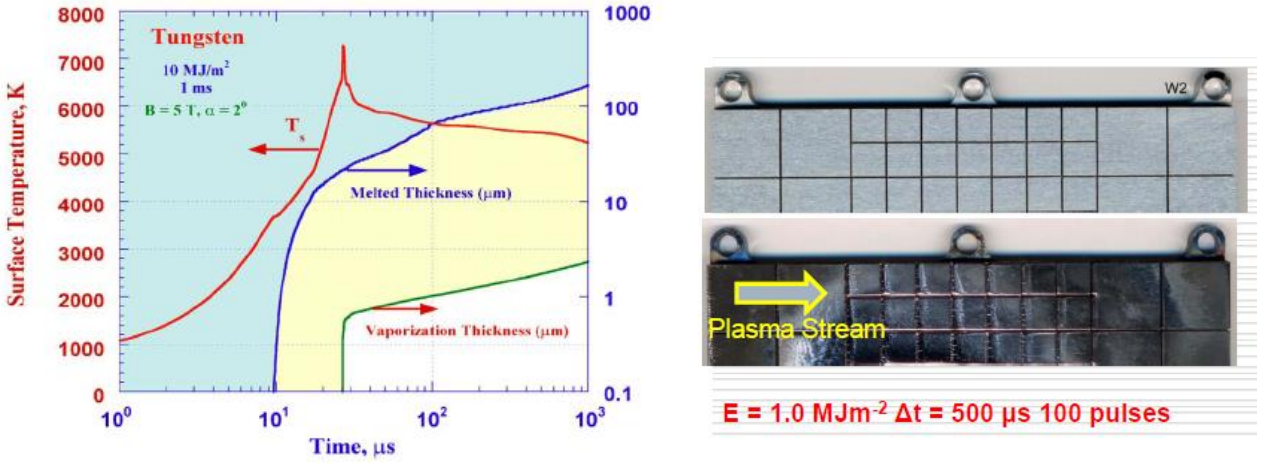


**Figure 2.5** – (Left) An example calculation of temperature, melt layer thickness, and vaporization thickness in tungsten for a 10 MJ/m$^2$, 1 ms disruption using HEIGHTS [11]. (Right) Experiment results from QPSA plasma gun demonstrating the melting of ITER W mono-blocks under ITER-relevant conditions [12].

The formation of a surface melt layer does not directly imply a loss of material, just a change of state from solid to liquid. It is the interaction of that melt layer with phenomena within the tokamak environment (plasma fluxes, Lorentz forces, pressure gradients, gravitational forces, etc.) that can lead to severe erosion through melt-layer motion and splashing [9,10,13]. Macroscopic splashing of the developed melt layer can lead to a continuous ejection of molten metals into the plasma core, risking plasma contamination and termination if the molten droplets are too large and/or frequent [9,10]. If the melt layer surface temperature exceeds the boiling threshold, the formation and bursting of surface bubbles can cause additional material loss as liquid droplets are ejected into the plasma with each burst [10].

Estimating an average erosion rate for material surfaces in the melting/boiling regime is naturally complicated. The dynamics of melt layer formation are governed by: 1) the temperature-dependent thermal conductivity and specific heat of the material, 2) the magnitude, angle, and time duration of the impinging heat flux, and 3) cooling systems, if applicable. Separately, once melt

layer dynamics are accounted for, the various causes of melt layer loss are largely dependent on the tokamak/device exposure conditions. Plasma pressure gradients and Lorentz forces have both been experimentally observed to play a major role in melt layer motion [12]. On the TEXTOR tokamak, for example, melt layers were observed to flow perpendicular to the B-field direction on W limiter samples [9,12]. This motion was attributed to the Lorentz force. In experiments on QPSA, a linear plasma accelerator, macroscopic motion of molten material at the edge of erosion craters was concluded to be caused by plasma pressure gradients [9]. In various electrothermal plasma experiments, melt layer motion on liner surfaces was observed to follow the plasma flow direction [13,14]. In addition, gravitational forces must be considered for any angled PFCs. Finally, ELMs and disruptions can lead to drastic changes in pressure gradients, magnetic and electric fields, and plasma fluxes, all of which will alter melt layer motion.

Multiple theoretical models for the melt layer have been explored in the literature, focusing on complex variables such as viscous stability, splashing wave velocity, droplet ejection rates, bubble growth, etc. [9,10,14]. Since the erosion phenomena in this region cannot be directly correlated to just the impinging heat flux, the specific mechanisms for modeling melting/boiling mass loss fall outside the scope of this dissertation and will not be studied in detail.

### 2.3 – Sublimation

Not all materials exhibit melting when exposed to high heat fluxes. Under high temperature vacuum conditions, some non-metallic materials instead undergo direct sublimation. Example materials include graphite and silicon carbide, both of which are important to this dissertation work. Sublimation directly leads to macroscopic erosion as vaporized material leaves the PFM surface and enters the core plasma. In general, the energy needed to sublime a substance depends on the material and its temperature, and must be enough to [15]:

1) Excite the solid substance to its maximum heat (energy) capacity
2) Sever all intermolecular interactions holding the solid together
3) Excite the unbonded atoms of the substance so it reaches a minimum heat (energy) capacity in the gaseous state

This amount of energy is commonly referred to as the heat of sublimation or energy of sublimation. For normal substances that transition through all 3 phases, the magnitude of the energy of sublimation can be thought of as a combination of the energies required to transition from solid to gas, as seen in Figure 2.6.

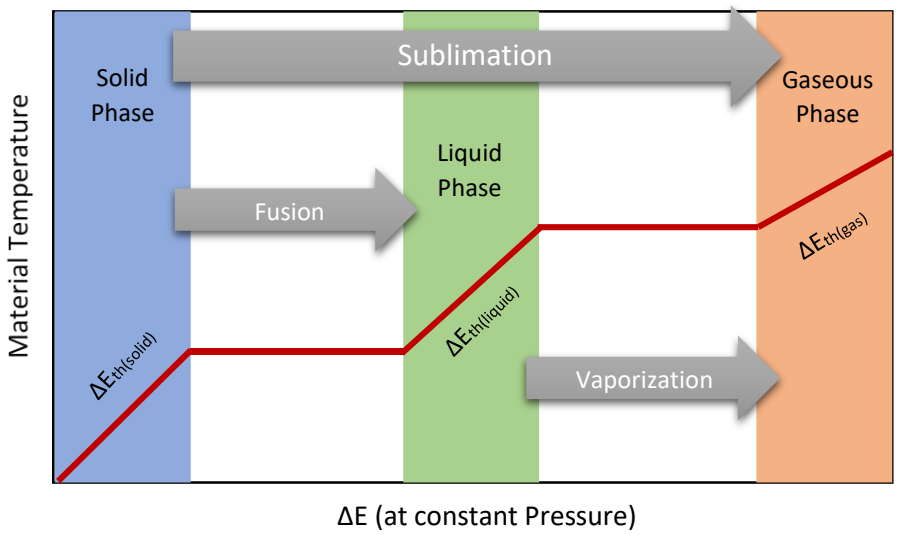


**Figure 2.6** – Sample graph of Temperature vs Energy Change for a substance, showing the relationship between the heat of sublimation, heat of fusion, and heat of vaporization. Based on [15].

If a plasma-facing material exceeds its temperature threshold and enters a sublimation dominated regime, the erosion rate of the material surface becomes directly proportional to the heat of sublimation:

$$Eq.7 \quad \dot{n}_{ablation} \propto \frac{Q''}{H_{sub}}$$

Where $\dot{n}$ is the number density of the ablated material, Q'' is the heat flux impacting the material surface, and $H_{sub}$ is the heat of sublimation [14,16]. In this regime, the erosion rate should linearly increase as the impinging heat flux increases. The delivery mechanism for the heat flux becomes irrelevant (changes in ion species/density/temperature, increased radiant heat flux, etc.), as any deposited energy above the $H_{sub}$ threshold will go on to continuously sublimate the material surface.

It is important to note that this simple relationship only applies to the heat flux that directly impacts the material surface. Phenomena such as vapor shielding modifies the equation by introducing a vapor shielding factor to account for energy absorption through the vapor shield. For high intensity, short timespan plasma exposures, the continuous evaporation of material can form a vapor cloud above the PFM surface. This vapor cloud then inadvertently absorbs a fraction of the energy from the incoming heat flux, shielding the surface and reducing its erosion rate by reducing the heat flux magnitude at the material surface [14]. Shielding effects such as vapor shielding depend on both the vapor species and the physics of the heat flux delivery mechanism. Thus, any changes in plasma flux parameters can turn PFM erosion rates into a non-linear relationship in the sublimation regime and should be accounted for.

### 2.4 – Other Erosion Mechanisms

There are a few special cases of material erosion mechanisms that are not related to the goals of this dissertation, but are worth covering for consistency. The first is often referred to as chemical sputtering. Chemical reactions between incident ions and/or neutrals with the PFM surface can lead to measurable erosion as gaseous product molecules form and leave the material surface [3]. In fusion devices, the most commonly observed example occurs between hydrogen isotopes and carbon, such as the below reaction for methane.

$$Eq.8 \quad 4H + C \rightarrow CH4$$

Carbon in particular has been extensively used as a limiter or divertor material due to its low Z, low sputtering yields, and lack of melting. However, its chemical sputtering yields can be comparable or even higher than the physical sputtering yields, depending on the plasma conditions [2,3]. The hydrocarbons that chemically form have a low binding energy with the surface, and thus can be released at relatively low temperatures. Additionally, unlike physical sputtering, there is no well-defined threshold energy below which chemical sputtering stops [2,3]. Thus, for carbon, chemical sputtering can dominate during low temperature plasma discharges and under detached divertor conditions.

Another common erosion mechanism comes from arcing on the plasma-facing material surface. In general, arcing occurs when material evaporates from a cathode surface, ionizing and allowing for the flow of current in the presence of a high electric potential. Current flows within

the cathode or anode to a localized point on the surface, where joule heating leads to electron emission via either thermionic or field emission [3]. In a plasma environment, the presence of the plasma sheath over a PFM surface can produce what's known as unipolar arcing. Electrons from the arcing point on the PFM (acting as a cathode) are accelerated through the plasma sheath away from the surface [3]. These arcs then lead to erosion at the origin points on the cathode due to extreme heating. Surface material is released in the form of ions, neutrals, and solid or molten droplets. Although electron temperatures of only 5-10 eV are needed to initiate an arc, ion ejections at energies of 50 – 100 eV have been observed [3]. The magnitude of macroscopic erosion from vapor and droplet ejection is dependent on the arc current, the material composition, and starting material temperature. One interesting feature of arcing is the well documented arc direction in tokamak devices. In the presence of strong magnetic fields, arcing is observed to occur in the direction opposite the J x B force on both limiters and walls. Although arcing is commonly seen in tokamaks, it is usually only observed during the current rise, before the plasma reaches MHD stability. As devices improve and steady state plasma discharges are elongated, the relevance of erosion rates from arcing will conceivably be minimized.

## REFERENCES


[1] ITER Physics Basis Editors, "ITER Physics Basis." *Nuclear Fusion*, vol. 39, no. 12, 1999

[2] P. Stangeby, *The Plasma Boundary of Magnetic Fusion Devices*, IOP Publishing, 2000

[3] M. Kikuchi et al. *Fusion Physics*. Chapter 7, 2012

[4] Chinese Academy of Sciences. "China's 'artificial sun' sets world record with 100 second steady-state high performance plasma." *Phys.org*, 6 July 2017, https://phys.org/news/2017-07-china-artificial-sun-world-steady-state.html Accessed 20 August 2018.

[5] R. Behrisch & W. Eckstein, *Sputtering by Particle Bombardment*, Springer, *Topics in Applied Physics*, 2007

[6] R. Khaziev and D. Curreli, "Ion energy-angle distribution functions at the plasma-material interface in oblique magnetic fields." *Physics of Plasmas*, vol. 22, no. 043503, 2015

[7] M. Hellwig, "Influences of 3D geometry and surface roughness on plasma-wall interaction processes on tungsten surfaces." Dissertation, Ruhr University Bochum, 2016

[8] C. Chrobak, "Characterizing Erosion and Redeposition of Aluminum in DIII-D Divertor Plasmas." Dissertation, UC San Diego, 2018, https://escholarship.org/uc/item/2vv5m4wh

[9] G. Miloshevesky and A. Hassanein, "Stability and erosion of melt layers developed on plasma facing components of tokamaks," *Nuclear Fusion*, vol. 64, no. 043016, 2014

[10] Y. Shi et al. "Boiling induced macroscopic erosion of plasma facing components in fusion devices." *Fusion Engineering and Design*, vol. 86, 2011, pp. 155-162

[11] A. Hassanein and J. Konkashbaev, "Lifetime evaluation of plasma-facing materials during a tokamak disruption," *Journal of Nuclear Materials*, vol. 233, 1996

[12] Y. Ueda, "Pulsed Heat Load Effects on Plasma Facing Materials", Presentation, 2015 ITER International School, USTC, Hefei, China, 2015

[13] G.E. Dale and M. A. Bourham, "Melt layer erosion and resolidification of metallic plasma facing components." Proc. 17th IEEE/NPSS Symposium on Fusion Engineering, vol. 2, 1997, pp. 892-895

[14] N. Almousa, "Modeling Electrothermal Plasma with Boundary Layer Effects", Dissertation, NC State University, Nuclear Engineering, 2016

[15] K. Nakajima, "Heat of Sublimation", 6 Feb. 2018, *Chemistry Libretexts*, https://chem.libretexts.org/Core/Physical_and_Theoretical_Chemistry/Thermodynamics/Energies_and_Potentials/Enthalpy/Heat_of_Sublimation Accessed 22 May 2018

[16] A. L. Winfrey et al. "A Study of Plasma Parameters in a Capillary Discharge with Calculations Using Ideal and Nonideal Plasma Models for Comparison with Experiment." *IEEE Transactions on Plasma Science*, vol. 40, no. 3, 2012

# CHAPTER 3 – ABNORMAL EVENTS: DISRUPTIONS AND EDGE LOCALIZED MODES

## 3.1 – Disruptions

Disruptions in a tokamak are defined as a rapid loss of the confined plasma and its intrinsic plasma current. Such disruptions result in major heat loads to plasma facing components (PFCs) and materials (PFMs) within the tokamak, as well as large electromagnetic forces on the tokamak structural components [1]. The energy stored within the tokamak plasma increases with larger device dimensions; if L = the linear dimension of the device, then the stored energy rises as $L^5$, and the energy dissipated during a disruption rises as $L^3$ [1]. If the reactor doubles in size, energy loads imparted to the tokamak wall, even if uniformly distributed, increase by an entire order of magnitude. Thus, disruptions become a major constraint when designing large tokamaks such as ITER, which is about double the size of JET. The major issues that arise from a disruption in a tokamak device are as follows:

1) Rapid heat loss from the plasma will impact the inner wall and the divertor. For a high performance ITER plasma, ~350 MJ of thermal energy will be dissipated in ~1ms, with an impact duration of 1.5-3 ms [1,2].
2) Large electromagnetic forces will act upon the conducting structure that contains the plasma. These forces are due to induced eddy and halo currents, which in ITER could be upwards of 8000 tons [1].
3) High energy runaway electrons due to rapid decay of the plasma current, which have the potential to damage the inner wall. For ITER, it is estimated that 10 MA of current can be generated by 10-20 MeV runaway electrons [1].

These key issues highlight the need for adequate disruption detection, avoidance, and mitigation when designing large tokamaks such as ITER. Without avoiding and mitigating disruptions, severe damage can occur to the device, limiting its capabilities to achieve a burning fusion plasma.

### 3.1.1 Causes of Disruptions

Plasma disruptions are bound to occur when performance stability limits are exceeded. The main controlled parameters in a tokamak are the plasma current ($I_p$), the toroidal magnetic field ($B_\phi$), the plasma density often determined by the electron density ($n_e$), the additional plasma heating, and finally the shape of the plasma [1]. Additional heating may be due to high energy neutral particles injected into the plasma or due to radio frequency (RF) waves that resonate with ion and/or electron gyro-frequencies (ICRH or ECRH). This heating controls the plasma temperature and kinetic pressure, influencing the pressure profile.

The first publication on disruptions in tokamaks was by E. P. Gorbunov and K. A. Razumova in 1963, entitled "The effect of a strong magnetic field on the magnetohydrodynamic stability of plasma and the containment of charged particles in the 'Tokamak'". The paper focuses on how plasma becomes unstable in tokamaks and stellerators for currents much less than the critical current outlined by the Kruskal-Shafranov criterion [3]. This stability criterion is for a simple model, an ideally conducting plasma column (with a circular cross-section) in a strong magnetic field surrounded by a vacuum.

$$Eq\ 1. \qquad q(a) = \frac{aB_\phi}{RB_\omega} > 1$$

Where a, R are the minor and major radii of the plasma, and $B_\phi$ and $B_\omega$ are the toroidal and poloidal magnetic fields, respectively [4]. The ratio q represents the helicity of magnetic field lines at the plasma edge, and is often referred to as the safety factor due to its close connection to disruptions [5]. Disruptions observed in the 1963 publication showed that the Kruskal-Shafranov criterion was only approximate and led to a change in theoretical requirements for stability to q(a) > 2. This change in safety limitations began a more thorough scientific investigation of disruptions in tokamak devices.

Disruptions themselves are usually caused by macroscopic changes in plasma stability. The typical sequence of events for a disruption is highlighted below in Figures 3.1 and 3.2.

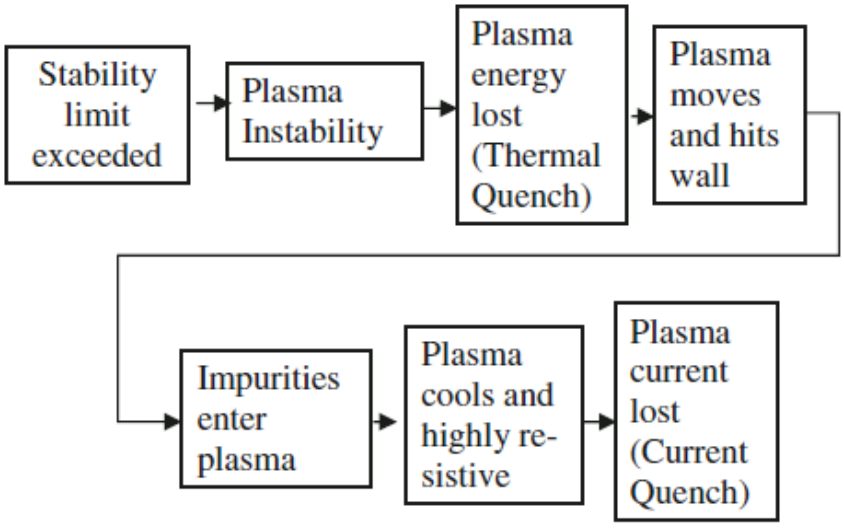


**Figure 3.1** – Sequence of events for a typical tokamak plasma disruption [1]

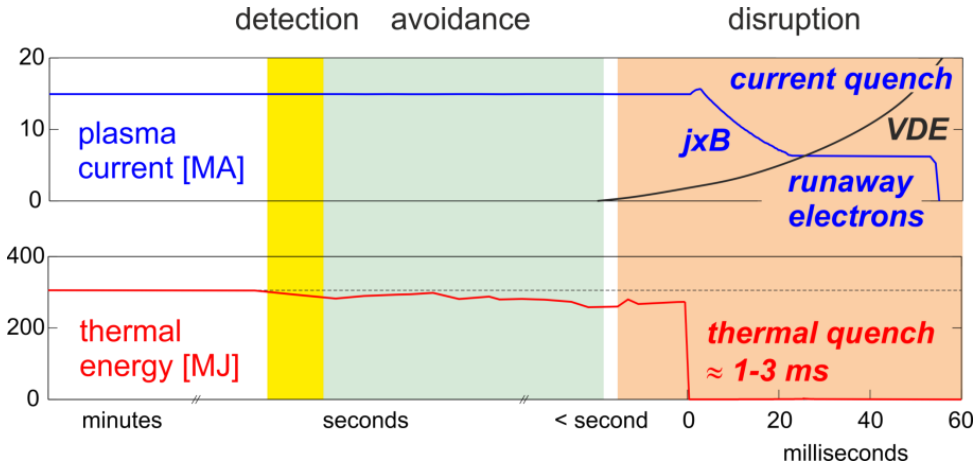


**Figure 3.2** – Plasma parameters during a theoretical disruption on ITER [2]. There is a rapid loss of plasma stored energy (red), usually seen in the electron temperature $T_e$, representing the thermal quench. What follows is a gradual decay of plasma current (blue), which is the current quench phase. Finally, the growing helical distortion in the plasma during the disruption, before the thermal quench, can result in a vertical displacement of the plasma current centroid (black).

Hard limits on tokamak operating space are imposed by various modes of instability that can arise. In diverter tokamaks the limit at 95% of the edge poloidal flux, $q_{95}$, is a good estimate for the edge-q, such that the operating limit becomes $q_{95} > 2$. For example, modes of instability referred to as ideal external kink modes, shown visually in Figure 3.3, become unstable for an

edge-q < 2. Additionally, there is an empirical limit to the plasma density known as the Greenwald limit, which is directly proportional to the average current density. This limit is due to the increased edge radiation that occurs at higher density, which can lead to radiative collapse, MHD destabilization, and a disruption [1,5].

$$Eq\ 2.\ Greenwald\ Limit: \qquad n_e(10^{20}m^{-3}) < n_g(10^{20}m^{-3}) = \frac{I_p(MA)}{\pi a^2}$$

At the hard limit of $q_{95} \sim 2$, instabilities grow extremely fast, on the Alfven timescale $\pi R_o/v_a$ (~1 μs). Throughout the disruption itself, the plasma evolves through force-balance equilibria over a range of timescales. The shortest time scale is approximately 1 millisecond, 1000x the Alfven timescale, while the longest timescale can be on the order of a second [6]. The wide variation in causes, time scales, and expressions of plasma disruptions are what make them difficult to predict, let alone avoid and mitigate.

Although this dissertation work is more focused on the impact of disruptions on plasma-facing materials, a brief overview of disruption causes and classifications will be covered here. Some sources focus solely on the MHD instabilities responsible for a disruption [1], while others focus more on the root cause of the instability rather than its characteristics [5]. Looking at the modes of MHD instabilities themselves, it's easy to classify instabilities by answering three questions [1]:

1) What drives the instability? Common drivers include plasma current, pressure, and particle/density.
2) Is it a "resistive" or "ideal" instability? Ideal instabilities refer to cases when flux surfaces within the plasma are preserved, such that the instability only changes their shape. These instabilities are often called "kink" instabilities since they tilt and kink the plasma. Zero resistivity is also implied for ideal MHD instabilities. Resistive instabilities, on the other hand, require changes in the magnetic field line topology, usually in small regions such as the X-points. Although small, these regions strongly impact the global plasma equilibrium. Resistive instability modes typically manifest as

tearing modes and neoclassical tearing modes, the names of which imply the tearing and reconnection of the magnetic field lines.

3) What is the location of the instability? Internal modes refer to instabilities inside the plasma, while external/free boundary modes refer to events at the plasma boundary.

The original disruption experiments testing the Kruskal-Shafranov criterion were concerned with external kink modes. As previously stated, these instability modes tilt and kink the plasma away from an ideal toroidal shape; for external kinks, it is the plasma boundary that is distorted rather than the core magnetic field lines. These pressure-driven external kink modes limit the operating β and ultimately limit the pressure that can be achieved in ideal plasmas [7]. Internal kink modes are also possible, as seen in Figure 3.3.

Tearing modes manifest by breaking or tearing magnetic flux surfaces, forming magnetic islands within which particle motion is confined. With a finite plasma resistivity, ideal MHD breaks down around rational surfaces when the safety factor q happens to match up with the poloidal and toroidal mode numbers: $q = n/m$. The safety factor q inherently represents the number of toroidal transits per poloidal transit a particle takes while traversing the tokamak, where m is denoted the poloidal mode number and n the toroidal mode number [7, 8]. There are classical tearing modes which are linearly unstable when $I_p$ is unstable and the tearing mode island has a lower magnetic energy than the original plasma. There are also neoclassical tearing modes (NTMs), which occur at high β even in a classically stable plasma [7]. NTMs rotate with the electron fluid component of the plasma, but in large tokamaks they tend to stop rotating as they grow towards disruption. This is referred to as mode locking, and occurs primarily due to eddy currents driven in the conducting structures around the plasma. This locking causes loss of the high confinement H mode and the continued mode/island growth can lead to a disruption [7]. The $q_{95}$ limit and the density limits often manifest themselves as m=2, n=1 NTMs. As NTMs are a high β event, they limit what β can be effectively achieved in a tokamak, which is a particular concern for ITER.

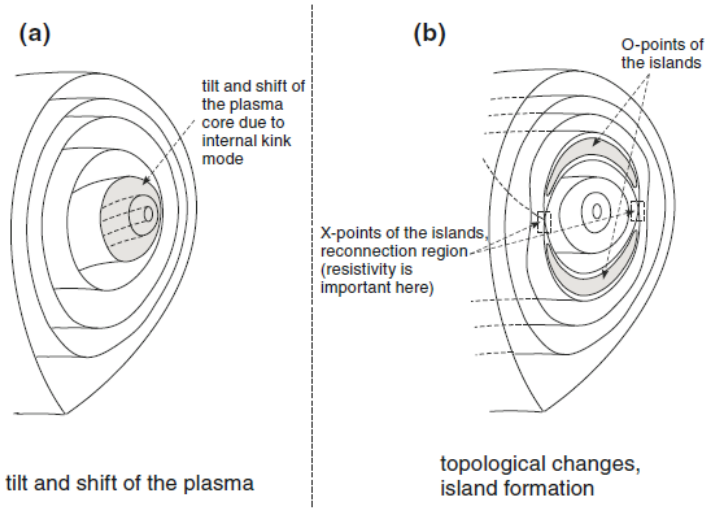


**Figure 3.3** – a) an ideal MHD internal kink instability, and b) a resistive tearing mode MHD instability [1]

Along with well-studied MHD instabilities, there are other manifestations of plasma instability. One mechanism is through radiative cooling of the edge. Plasma radiation comes from bremsstrahlung, cyclotron radiation, and line radiation from impurity ions, recombination, and/or partially ionized plasma ions [5]. Of particular importance is line radiation from impurity ions, both low-Z and high-Z. Radiation from low-Z ions, for example, are shown to increase with lower edge temperatures [5]. Any increase in radiative loss could create a positive feedback loop of lowering temperatures, resulting in an inward contraction of the temperature profile and a radiative collapse of the core plasma. These types of radiation limit disruptions are sometimes referred to as edge cooling disruptions [1]. In terms of β imposed limits, internal transport barriers may occur, which cause strong pressure profile peaks that lead to rapid disruptions. At high plasma pressure, resistive wall modes can also occur. Even rapid transitions of the plasma, such as L-H or H-L transitions, may trigger a disruption.

Finally, present day devices now have a D-shaped cross-section in order to improve plasma confinement and stability, as seen in Figure 1.3 of Chapter 1. This shape choice allowed for increased plasma current operations for a given aspect ratio and $B_t$ and leads to a natural formation of the separatrix, which then allows for easy H-mode operation [1]. However, the trade-off for vertically stretching the plasma is an inherent instability to vertical perturbations. The plasma must be held in place by a control system, and if the control system fails (due to hardware failure, rapid plasma parameter changes, programming error, etc.) the plasma will shift upwards or downwards

[1]. This unwanted motion is called a Vertical Displacement Event (VDE), and can lead to the plasma impacting the wall, triggering a disruption. The reverse can also happen: a minor disruption may occur and then rapid changes of plasma parameters can cause a vertical instability.

### 3.1.2 Impact of Disruptions

When it comes to inner wall components of the tokamak, excessive heat loads are the most significant consequence of disruptions. Heat loads manifest in both the thermal quench phase, when thermal energy is lost from the plasma, and the current quench phase, when magnetic energy is also converted to heat. The rough governing parameter for surface heating via conduction is $U/(A*\tau^{0.5})$, where U is the incident energy, A is the area, and $\tau$ is the timescale of the heat deposition [1]. The ideal heat load is therefore one which spreads the energy uniformly over a large surface area, over a long length of time. That is why radiative losses in tokamaks are more desirable than concentrated heat deposition. During the current quench, most of the magnetic energy is converted into heat energy via Ohmic heating once the plasma becomes highly resistive. That heat energy is then radiated to the walls fairly uniformly. The rest of the magnetic energy is inductively coupled into various structural components. In JET, around 80% of the magnetic energy is consumed through Ohmic heating [1]. An example illustration of the power density on the JET divertor during ELMs and disruptions is shown in Fig. 3.4.

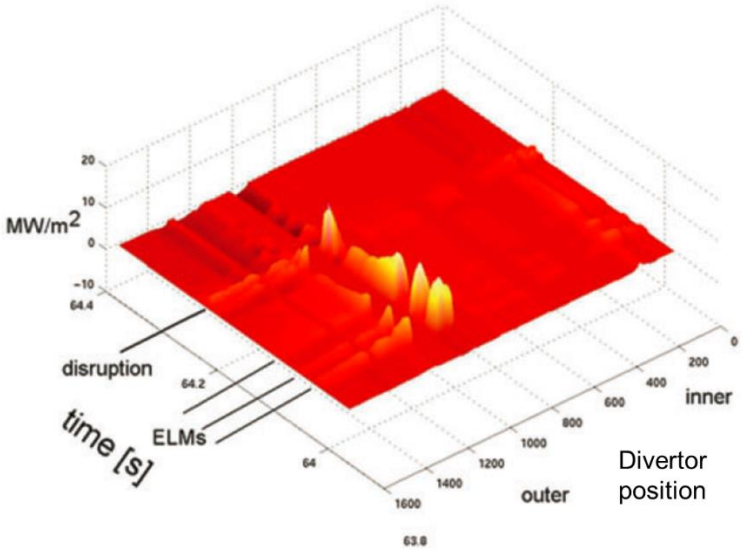


**Figure 3.4** – Power density on diverter during an H-mode density limited disruption on JET [9]

The bigger concern is concentrated heat loads from the thermal quench. In the case of a high performance ITER plasma, where ~350 MJ of energy is released over ~ 1ms during a disruption, a severe heat load placed directly on the divertor would cause significant melting, splashing and erosion, with estimated energy depositions anywhere from 10-200 MJ/m^2 [1,10]. Luckily, there are a couple of intrinsic factors that somewhat mitigate the heat load in diverted tokamaks [1]. 1) For most tokamak disruptions, the thermal energy of the plasma at the time of the thermal quench is lower than its peak value (however there are exceptions at high-β where little confinement is lost before a disruption). 2) Some thermal quench energy is lost via radiation; the amount depends on the wall materials that lead to impurities in the plasma. JET, for example, lost around 75% of its thermal energy via radiation when equipped with carbon walls, but only lost 50% with its new tungsten/beryllium wall. 3) The width of the scrape-off layer, through which the heat is transported to the divertor, is broadened during the thermal quench. The broadening, ranging from 5 – 20, significantly reduces the corresponding heat flux incident on the divertor surface. These intrinsic mitigation factors do lessen the disruption heat loads to the divertor, but further mitigation is essential to prevent significant erosion, melting, and other damage to the divertor as well as other plasma-facing components.

Although this dissertation work focuses on material erosion due to heat fluxes, it is important to understand the additional consequences of plasma disruptions. During the current

quench phase of a disruption, large electromagnetic forces act on the vessel structure. The decay of toroidal plasma current induces eddy currents in the surrounding conductors, and since those conductors are immersed in a magnetic field, they are subject to a JxB force [11]. This often takes the form of a compressive force. In addition, due to vertical instability within elongated plasmas, the plasma can experience unwanted vertical motion after large perturbations in plasma equilibrium. Vertical motion of the plasma induces a toroidal current in the vessel components and therefore a net vertical force on the vessel, on the order of the vessel weight [11]. The plasma will continue its vertical motion until it intersects with either the top or bottom divertor (in the case of tokamaks with two divertors), which begins acting as a limiter. The limited plasma continues to shrink and shift vertically until it disappears. Then what were once contained, closed flux surfaces within the plasma are now open magnetic flux surfaces flowing within the vessel structure. This plasma region is called the halo, and the halo current is defined as the poloidal component of the current flowing from the halo onto the vessel structures and back during the current quench of a disruption [11]. Figure 3.5 is an illustration of a simulation of an ITER plasma undergoing a vertical instability.

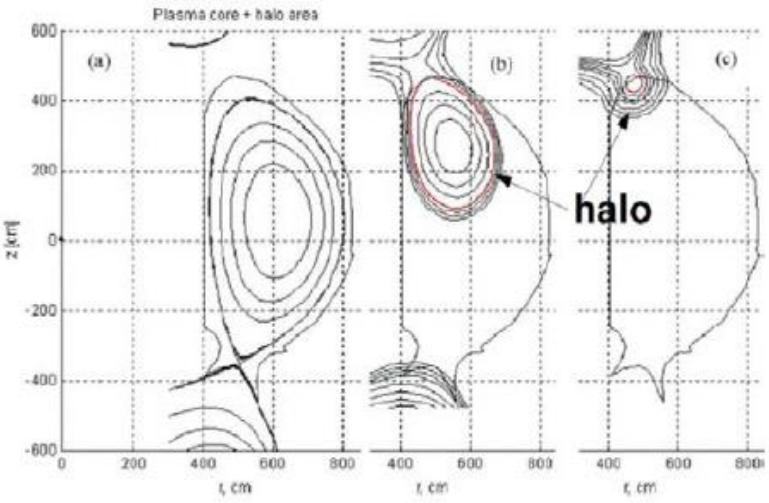


**Figure 3.5** – Simulation of an ITER plasma undergoing a vertical instability [11]

Eddy currents and halo currents can result in large vertical forces on in-vessel components. Halo current in particular contributes strongly to the vertical forces on plasma during a disruption, acting to slow down its displacement. If there are any toroidal asymmetries in the halo current, strong tilting moments and sideways forces act on the vessel, estimated at up to 0.8 MN for ITER

operations [2]. The maximum halo current can be up to 50% of the previously intact plasma current, and must be monitored in all tokamaks due to its strong potential to damage the in-vessel components it flows through.

During a disruption, plasma material interactions with the first wall lead to an influx of impurities into the plasma and an increase in its effective charge, $Z_{eff}$. Coupled with a relatively low electron temperature, $T_e$, this effect drastically raises the plasma's resistivity η [1].

$$Eq\ 3. \qquad \eta \propto \frac{Z_{eff}}{T_e^{\frac{3}{2}}}$$

$$Eq\ 4. \qquad E_D = \frac{e^3 n_e \ln(\Lambda)}{4\pi\varepsilon_o^2 T_e}$$

From Ohm's law, a large electric field is generated by E = ηJ, where J is the existing plasma current density. If this electric field becomes larger than the quantity known as the Drieicer field (Eq 4), the electrons traveling through said field can overcome the drag forces from plasma collisions, accelerating them to 'runaway energies' of 10-20 MeV [11]. Up to two-thirds of the original plasma current can be carried by runaway electrons during a disruption [1]. Even more worrisome, the formation of secondary runaway electrons via close angle scattering is likely in large tokamaks such as JET and ITER. These collisions lead to an exponential growth or avalanche of runaway electrons that then go on to damage the vessel. Significant damage from runaway electrons has been observed in large tokamaks such as Tore Supra and JET [1], where thermal energy is deposited upon striking the material surface (along with some magnetic energy converted and deposited as thermal energy). To prevent significant damage to the first wall, runaway electrons must be controlled or prevented in large tokamaks.

### 3.2 H-mode & ELMs

The High Confinement mode for tokamak plasma operation was first achieved at the ASDEX tokamak on February 4th, 1982 [12]. As neutral beam heating was supplied to the ASDEX plasma, its confinement suddenly improved and the turbulences at the plasma edge disappeared, forming a steep plasma pressure gradient along the plasma edge. In the following years, H-mode was observed in several other tokamaks, including PDX and DIII-D in the US, the Joint European Torus (JET), and Japan's JT-60. In 1993, H-mode was achieved in the German W7-AS stellarator

as well, demonstrating it was a generic feature of toroidal plasma configurations [13]. In H-mode, strong transport barriers form at the plasma edge which creates the observed steep pressure gradient referred to as the edge pedestal, as seen in Figures 3.6 and 3.7. H-mode increases plasma energy confinement time $\tau_e = W_{plasma}/P_{input}$, where $W_{plasma}$ is the plasma stored energy and P is the power, by about a factor of 2 compared to what is now known as low confinement mode, L-mode [13]. Without H-mode, ITER would need to be almost twice as large to achieve its designed energy gain of $Q = P_{Fusion}/P_{input} = 10$. $P_{fusion}$ is proportional to $W^{\alpha}_{plasma}(\,where\ \alpha{\sim}2-3)$, and for H-mode the pedestal energy $W_{ped}$ makes up a large portion of $W_{plasma}$. With $W_{ped} = 3P_{ped}V_{plasma}$, where $P_{ped}$ is now pedestal pressure and V is volume, the maximum achievable Q in ITER becomes directly determined by pedestal pressure $P_{ped}$. This relationship highlights the importance of operation in H-mode with the highest possible plasma pressure gradient [14].

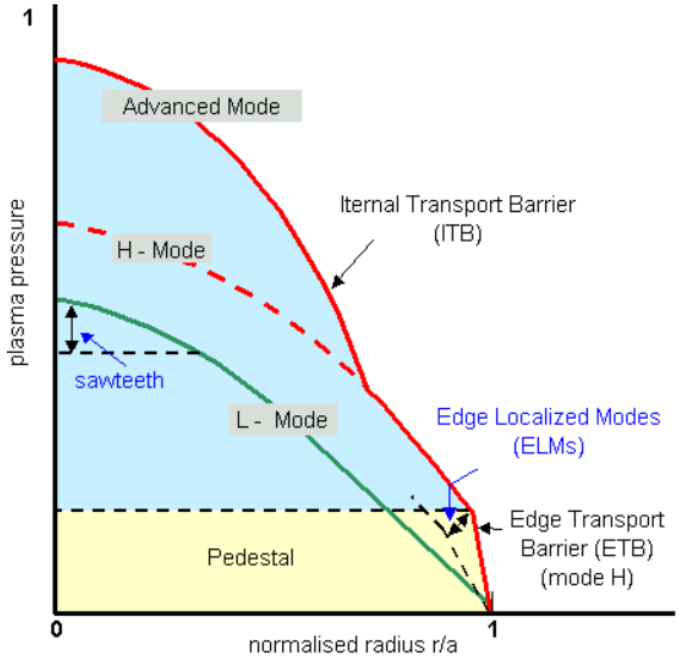


**Figure 3.6** – Chart of different modes of confinement [15]

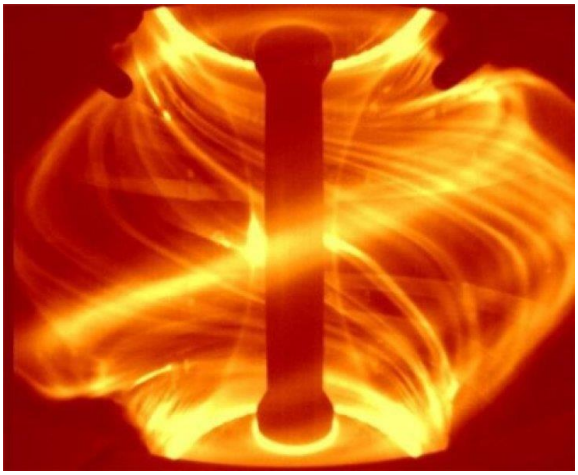

**Figure 3.7** – High-speed video image of the start of ELMs in a plasma in MAST [16]

Operating in H-mode does come with its own set of drawbacks. If the pressure gradient and/or the current density at the edge pedestal exceed a certain threshold value, magneto-hydrodynamic (MHD) instabilities known as Edge Localized Modes (ELMs) are bound to occur. ELMs manifest when plasma conditions at the edge become unstable, offering a short-term avenue for the plasma to release excess energy and particles and return to stable conditions. The edge stability is often short lived, leading to repetitive ELMs as the edge pedestal collapses towards a shallower pressure gradient, rebuilds, and collapses again. ELM energy loss from the edge collapse takes place within a few hundred microseconds depending on the machine and the plasma conditions, ejecting large amounts of heat and particles into the scrape-off layer (SOL) and onto the plasma facing components [8]. ELMs physically manifest as helical ribbons of plasma arcing off from the main torus, as previously shown in Figure 3.7. Based on experimental data and supported by modeling, three types of ideal MHD instabilities are expected at the transport barrier which can lead to ELMs [8]: 1) Kink/peeling modes, which are driven by edge plasma current density and show no toroidal dependence, 2) Ballooning modes, which are driven by edge plasma pressure gradient and exhibit the largest amplitude on the torus' outboard side, and 3) Coupled peeling-ballooning modes, which are driven by both edge pressure gradient and edge bootstrap current. Figure 3.8 shows the peeling/ballooning stability limit and the variation of stability boundaries with plasma triangularity.

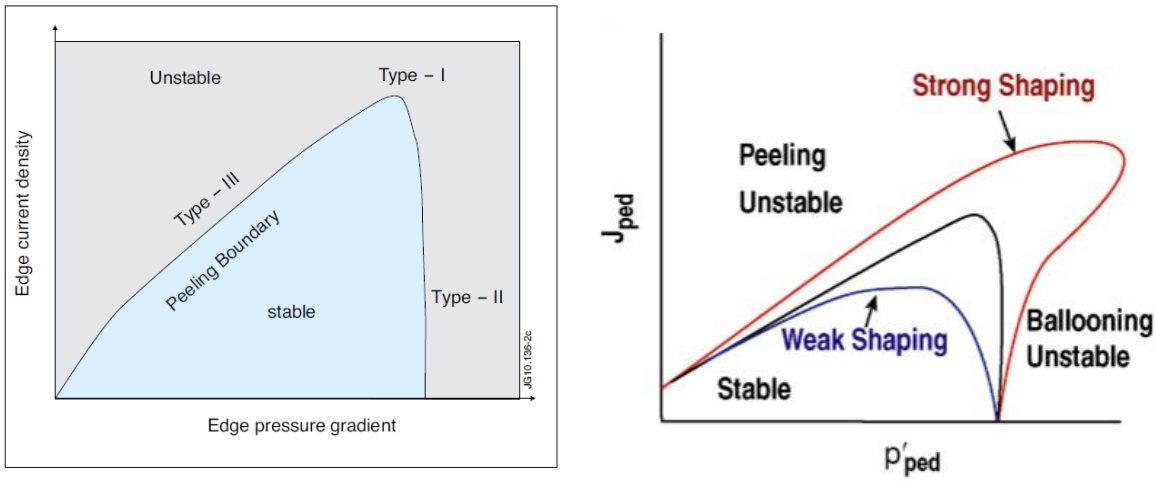


**Figure 3.8** – (Left) Peeling/Ballooning Stability Limit [8]. (Right) Variation of stability boundaries with plasma triangularity [17]

### 3.2.1 Types of ELMs

Three types of ELMs are commonly accepted in the literature. They are classified according to their size, frequency dependence on heating power, and driving mechanisms for approaching the theoretical peeling-ballooning stability limit. The three types of ELMs were first classified on the DIII-D tokamak, with the numerical sequences of the names signifying the history in which each was found [18]. The first and most ubiquitous are Type I ELMs, aka. "large" or "giant" ELMs. They are driven towards the stability limit via both plasma pressure and edge current density. As heating power increases, the ELM frequency increases. They exhibit low edge transport and no toroidal dependence. Energy losses for Type I ELMs are much larger than the other types, up to ~20% of $W_{ped}$. This amount of energy loss per ELM is unacceptably high when scaled up to ITER-size machines. Next are Type II ELMs, aka. "grassy" ELMs. They are driven towards the ballooning limit via increases in pressure gradient, and are only seen in high density, strongly shaped plasmas with high triangularity. Compared to Type I, Type II ELMs exhibit higher frequencies and lower magnitudes with almost as good plasma confinement, resulting in transient heat loads tolerable for ITER-scale machines. They are observed in a narrow operating window, so Type II ELMs might not be possible in burning plasma; on JET, they are often seen within a mixed Type I/II regime. Finally, there are Type III ELMs, aka. "small" ELMs. They are driven by current density towards the peeling stability limit, and appear when plasma resistivity is high

(which leads to low edge temperatures). Type III ELM frequency decreases with increasing heating power, the opposite of Type I. Being small in magnitude, they exhibit sufficient heat loads. However, due to their high frequency Type III ELMs also cause strong degradation of energy confinement compared to Type I/II, due to energy transport during ELM ejection. The stable region for plasma operation in terms of plasma pressure and current density is displayed in Figure 3.8, along with unstable regions for Type I, II, and III ELMs based on their driving mechanisms. Other ELM types have been observed and classified across the literature, such as compound ELMs and Type V ELMs, but they are less common and usually reported without much detail.

### 3.2.2 Summary of ELM Control Methods

Every tokamak is unique in its design, so ELM control methods naturally vary between devices. Each method exhibits varying degrees of success in terms of initiating, mitigating, and/or suppressing ELMs. Mitigation refers to controlling ELM energy magnitudes $\Delta W_{ELM}$ to remain manageable. Pacing methods, for example, achieve this control by manipulating ELM frequency $f_{ELM}$, relying on the observed inverse relationship as described in [19].

$$Eq\ 5. \quad \frac{\Delta W_{ELM} f_{ELM}}{W} * \tau_E = \frac{\Delta W_{ELM} f_{ELM}}{P} \approx 0.2 - 0.4$$

Suppression simply refers to the complete avoidance of ELMs in an otherwise ELM-ing regime, usually due to reduction in the pressure profile just below the stability limits. What follows is a brief description of current ELM control methods for mid-size tokamak devices which hold potential for use on ITER and ITER-scale devices.

The first method focuses on the use of radiative divertors. This concept is considered one of the primary techniques to decrease inter-ELM heat loads on the divertor. Also referred to as impurity gas seeding or gas puffing, the general concept is to puff an impurity gas such as argon, nitrogen, or another noble gas onto the divertor just before ELM impact. The neutral gas atoms interact with the heat and particles from the ELMs via collision, molecular dissociation, ionization, and excitation, absorbing and uniformly radiating away the excessive heat load [8]. Next there is the vertical kick method, where purposefully inducing a vertical displacement of the bulk plasma

(by a few ~cm) can trigger Type I ELMs. By applying vertical "kicks" to the plasma at a certain frequency, usually via vertical stability coils, the ELM frequency can also be controlled in order to reduce $\Delta W_{ELM}$ [8]. Similarly, there is the pellet pacing control method, where frozen fuel pellets are shot into the plasma edge at a high frequency. The impact of the pellets at the plasma edge during H-mode operation triggers an ELM due to ablation of the pellet by the hot plasma. The goal is to synchronize the ELM frequency to the pellet pacing frequency, allowing for ELM mitigation and $\Delta W_{ELM}$ control.

One method developed to suppress ELMs, rather than just mitigate their effects, uses additional edge magnetic fields. Edge resonant magnetic perturbation fields (RMP fields) are small, externally induced perturbations of the equilibrium magnetic field in the plasma edge. The perturbations are constructed to resonate at certain magnetic flux surfaces within the plasma edge which have the same helicity, which is related to the safety factor $q = \frac{aB_\phi}{RB_\omega} = \frac{n}{m}$. RMPs are designed to produce a static perturbation field with the proper resonant q value, with the goal of affecting ELM formation at the plasma edge. Various configurations on different tokamaks are found to have drastically different effects of ELM triggering, mitigation, and suppression. One relatively new ELM control method uses a supersonic molecular beam injection (SMBI) technique on the plasma edge. The molecular injections are shallow compared to pellets, and the SMBI pulses are not directly correlated with individual ELMs, but mitigation has been successfully demonstrated [20,21]. Finally, relatively new and successful techniques using lithium injections have been developed on a handful of machines. Most notable is a Li aerosol injection system, where μm-scale Li droplets are injected into the plasma SOL to evaporate. Exceptional ELM suppression has been demonstrated using this system, boasting a record 18s of ELM-free H-mode [21,22].

### 3.3 Behavior expected on Future Tokamak Reactors

The baseline scenario for ITER is to operate in inductive H-mode and achieve a positive fusion energy gain. To do so, the ITER plasma must possess a high triangularity, low electron collisionality $\nu_e \leq 0.2$, and operate near the Greenwald density limit. More importantly, the baseline regime is expected to be a Type I ELM H-mode regime; examining current research, the

ITER Organization (IO) has found no sufficient evidence to change to another regime with small/no ELMs [7].

Of the three classified types of ELMs, Type I ELMs are unfortunately the largest in magnitude, releasing a considerable fraction of the plasma stored energy content onto PFCs. Based on the scaling from present tokamaks, a ~20% release of pedestal energy from ITER will result in a worst-case scenario of 15-20 MJ energy release. Across a 0.8 $m^2$ inner divertor, Type I ELMs could produce heat loads ~17-20 $MJ/m^2$, magnitudes unacceptable for ITER PFCs in terms of lifetime and material integrity. Per IO standards, they must be mitigated to < 1 MJ per ELM to sustain acceptable energy losses and avoid major PFC erosion, or simply suppressed entirely.

Two methods designed for ELM control are being directly implemented in ITER: pellet injection and RMP field coils. The specifics for the pellet injection designs are currently under development through US ITER and ORNL. What is known is that there will be two HFS and one LFS injection points. Expected pellet conditions are between 17-33 $mm^3$, with maximum speeds of 300 m/s, injection frequencies ranging from 45-60 Hz, and expected species of D, DT, or H [14]. With testing results from DIII-D and JET, there is stronger confidence in using pellet pacing on ITER, although more tests for scalability are recommended. The RMP designs are more solidified: 27 in-vessel coils arranged in a 3x9 array, 3 coils (one upper, mid and lower plane) per vessel sector. These coils will allow for n = 3 and 4 RMP fields with the capability of phase shifts as in KSTAR, and are undergoing engineering design finalization [14]. ELM control using vertical kicks would be possible in ITER, but the required plasma displacement is high at 0.06-0.09m and could lead to severe VDEs [7]. The practicality of radiative divertors on ITER are uncertain, as their use depends strongly on other ELM control methods reducing divertor heat loads to levels already expected of ELM mitigation, now considered < 0.5 $MJ/m^2$. As for more recent ELM control/suppression techniques, namely the SMBI and Li aerosol techniques demonstrated on KSTAR and EAST, no direct plans have been made for ITER.

In terms of disruptions, ITER has set an engineering limit for the number of disruptions that can be tolerated. For plasmas operated at high current, and hence containing more stored energy, a disruption fraction of 10% has been set, only 1% of which may be VDEs [5]. VDEs lead to the highest forces on the tokamak structural components, presenting large operational consequences completely separate from first wall material integrity. There are two mitigation techniques that are being implemented on ITER. The first is a Massive Gas Injection (MGI)

system, which puffs a relatively large volume of inert gas into the tokamak vacuum chamber. The second is a Shattered Pellet Injection (SPI) system, which launches large frozen pellets down a delivery tube, then purposefully shatters the speeding pellets just before entry into the vacuum chamber. Both techniques operate on the same principle: introduce a large volume of atoms into the plasma ($10^{24}$ – $10^{25}$ particles) to absorb energy and terminate the plasma before it can impact plasma facing components [2]. The key differences are how those introduced particles penetrate the plasma. MGI gases largely interact with the plasma edge, never penetrating into the plasma core. SPI is the opposite, with the shattered pellet pieces penetrating through the edge and ablating once they hit the plasma core. In both cases, plasma operation is completely terminated.

## REFERENCES


[1] T.C. Herder, *Active Control of Magneto-hydrodynamic Instabilities in Hot Plasmas.* Chapter 7, Springer, 16 September 2014.

[2] M. Lehnen, "Disruptions in ITER and strategies for their control and mitigation," Presentation, 21st PSI Conference, Kanazawa 2014

[3] E. P. Gorbunov and K. A. Razumova. "The effect of a strong magnetic field on the magnetohydrodynamic stability of plasma and the containment of charged particles in the 'Tokamak,'" Soviet Atomic Energy, Volume 15, Issue 5, 1963, pp. 1105-1112

[4] Zakharov, et al. "Understanding Disruptions in Tokamaks." *AIP Physics of Plasmas*, vol. 19, no. 055703, 2012

[5] P.C. de Vries et al. "Survey of Disruption Causes at JET." *Nuclear Fusion*, vol. 51, no. 053018, 2011

[6] A. H. Boozer, "Theory of Tokamak Disruptions." *Physics of Plasmas*, vol. 19, no. 058101, 2012

[7] R. J. La Haye, "Neoclassical Tearing Modes and Their Control." *Physics of Plasmas*, vol. 13, no. 055501, 2006

[8] Y. Liang & JET EFDA contributors, "Overview of Edge Localized Modes Control in Tokamak Plasmas." Fusion Science and Technology, vol. 59, no. 3, 2011

[9] V. Riccardo et al. "Disruptions and disruption mitigation." *Plasma Physics and Controlled Fusion*, vol. 45, 2003

[10] A. Hassanein, G. Federici, I. Konkashbaev, A. Zhitlukhin and V. Litunovsky, "Materials Effects and Design Implications of Disruptions and off-normal events in ITER." *Fusion Engineering and Design*, vol. 39-40, 1998, pp. 201-210

[11] M. Kikuchi et al. *Fusion Physics*. Chapter 3, 2012

[12] ITER Physics Basis Editors, "ITER Physics Basis." *Nuclear Fusion*, vol. 39, no. 12, 1999

[13] R. Arnoux, "How Fritz Wagner "Discovered" the H-mode," 19 June, 2009 https://www.iter.org/newsline/86/659

[14] A. Loarte, "ITER and Pedestal Physics." Presentation, 2015 ITER International School, USTC, Hefei, China 2015

[15] "Magnetic Confinement – Modes of Confinement." 9 January, 2016 http://www-fusion-magnetique.cea.fr/gb/fusion/physique/modesconfinement.htm

[16] A. Kirk et al. “Observation of Lobes Near the X Point in Resonant Magnetic Perturbation Experiments on MAST.” *PRL*, vol. 108, issue 25, 2012

[17] P. Snyder, “Physics of the H-mode Pedestal and the EPED Model.” Presentation, 2015 ITER International School, USTC, Hefei, China 2015

[18] H. Zohm, “Edge Localized Modes (ELMs).” *Plasma Phys. Control. Fus.*, vol. 38, 1996

[19] P.T. Lang et al. “ELM Control Strategies and Tools: Status and Potential for ITER,” Nuclear Fusion, **53** (2013) 043004

[20] J. Kwak et al. “An Overview of KSTAR Results.” *Nuclear Fusion*, vol. 53, no. 104005, 2013

[21] J.S. Hu et al. “ELM mitigation by means of supersonic molecular beam and pellet injection on the EAST superconducting tokamak.” *Journal of Nuclear Materials*, vol. 463, 2015

[22] B. Wan et al. “Advances in H-mode Physics for Long-pulse Operation on EAST.” *Nuclear Fusion*, vol. 55, no. 104015, 2015

# CHAPTER 4 – ALTERNATIVE PLASMA FACING MATERIALS FOR NEXT GENERATION TOKAMAK REACTORS

Plasma-facing materials past ITER will require many, if not all, of the properties mentioned previously: erosion resistance, high melting/sublimation points, adequate mechanical properties, high thermal conductivity, plasma compatibility, low tritium retention, irradiation tolerance, and adequate cost and availability. They must be able to handle steady-state plasma conditions at elevated temperatures under constant neutron, photon, and ion bombardment, along with unexpected disruptions stronger than any tokamak can currently produce. Thus, any advanced material should be evaluated under conditions that are as relevant as possible to future reactor conditions.

## 4.1 – Silicon Carbides

The first material of interest is silicon carbide. Pure, single crystal SiC is a ceramic material with a great combination of desired properties: high sublimation point (~2700 °C), low density (3.21 g/cm^3), high mechanical strength (>600 MPA), high elastic modulus (>400 GPa), high thermal conductivity (>360 W/mK), and good material integrity under neutron irradiation [1,2,3]. Its average low-Z is appealing in terms of plasma compatibility, so long as physical sputtering rates are not too high to offset this advantage. SiC sublimates instead of melting, and it is non-magnetic, both properties ideal for handling unexpected disruptions, ELMs, and eddy/halo current forces. The mechanical properties and conductivities depend on the specific SiC crystal type, or polymorph. Of the 200+ polytypes, there are the α-4H and α-6H structures that offer higher thermal conductivities and mechanical strengths, which are used extensively in fabrication, semiconductors, and even jewelry industries under the mineral name “moissanite” [4]. Unfortunately, these α-phase polytypes have a hexagonal crystal structure which thermally expands asymmetrically. The most commonly used β SiC, β-3C, has a lower thermal conductivity than the α-phases, but it does offer a zinc-blend cubic crystal structure which thermally expands symmetrically. The only major drawback of monolithic SiC is its inherent brittleness as a ceramic, leading to a high probability of failure under excess forces if used as a structural material [3]. Thus, materials science researchers have been working since the 1970’s to construct adequate silicon carbide matrix composites with well-engineered mechanical properties for structural applications

in fusion, fission, aerospace, and other industries. Much progress has been made in the past two decades on $SiC_f/SiC$ composites to this end [1,3,5]. In this dissertation, the desire is to study the erosion rates of mono-crystalline, polycrystalline, and matrix SiC composites, as any could be used as direct plasma-facing materials.

### 4.1.1 – Monocrystalline and Polycrystalline SiC

The fundamental structure of SiC is a covalently bonded tetrahedron, either $SiC_4$ or $CSi_4$. As for the larger crystal structure, over 200 polytypes have been reported, which stem from a wide variety of stacking sequences of the Si-C planes [2,4]. Of these, the most common polytypes are 3C, 4H, 6H, and 15R. The number shows the repetition of the Si-C stacking sequence and the letter represents the crystal structure: C for cubic, H for hexagonal, and R for rhombohedral. The various polytypes are illustrated in Fig 4.1 [2]. The 3C SiC is the only polytype to exhibit the cubic crystal structure, and is referred to as β-SiC. Every other polytype is therefore classified as α-SiC. 4H and 6H α-SiC are currently the only crystal structures that can be lab-grown in bulk, leading to their popularity in the jewelry industry, semiconductor industry, and laboratory material needs [4]. SiC polytype stability is largely temperature dependent. For lower temperatures, β-SiC is the most stable; as temperature increases to around 2100 ºC, the crystal structure transforms to a hexagonal structure. Of course, the formation process of the SiC and its associated impurities/deviation from Si:C stoichiometry also affects the polytype stability [2].

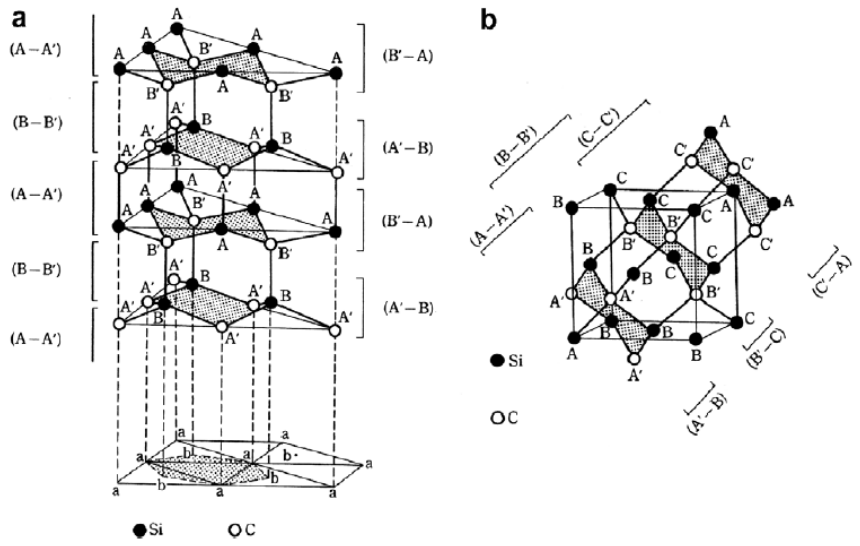


**Figure 4.1** – Crystal structures of α-SiC (a) and β-SiC (b) [2]

In terms of material properties relevant to a fusion environment, the 4H and 6H SiC exhibit the highest values of thermal conductivity (490 W/mK and 370 W/mK at RT, respectively) compared to the 3C (360 W/mK at RT) [6]. Of course, fabricating single-crystal plasma-facing components of adequate size is both mechanically and economically unfeasible, so polycrystalline material properties should be taken into consideration. Crystal structure combines with fabrication properties, such as grain size, density/porosity, and purity, to produce a polycrystalline product with a unique set of thermo-mechanical properties. In terms of thermal concerns, anisotropic thermal expansion of any α-SiC material is the biggest concern for high-temperature fusion environments. Large thermal shocks within a polycrystalline material would more easily lead to fracture and failure. Thus, the isotropic 3C structure is the best basis for a polycrystalline SiC plasma-facing component (PFC). From there, choosing a product with increased grain size and a near ideal density (no voids or micro-cracks) allows for maximized thermal properties.

### 4.1.2 – SiC/SiC Composites

Continuous SiC-based fibers were first created in the mid-1970's at Tohoku University, Japan [7]. From there, a race began to develop ceramic fiber-reinforced ceramic matrix composites (CMCs) for the nuclear industry. The importance of these fiber-reinforced materials is the ability of the fibers to minimize the probability of disastrous fracture through the bulk structure. By

controlling how the fibers are made and how they are interwoven into the matrix, engineers can tailor the material's physical and mechanical properties to meet their needs; they can create a material with increased pseudo-ductility and with more predictable fracture mechanics [5,8]. The ability to use SiC as both the fiber and matrix materials then allows engineers to take advantage of SiC's attractive elemental properties (radiation properties, plasma compatibility, etc.) while substantially improving its toughness/brittleness. The application of these SiC/SiC composites as a fusion reactor blanket material was first proposed in the late 1970's [5]. Since then, many iterations of these composites were developed through various processes, with the first radiation-tolerant SiC/SiC composite being fabricated in 1999 [5]. A key factor in its success was maintaining material purity through a chemical vapour infiltration (CVI) production process. Studies on this 3rd generation SiC/SiC composited demonstrated radiation tolerances over a wide range of irradiation temperatures and neutron fluences.

Radiation stability of the fiber/matrix structure was the initial concern for the composites while advancing their "technological readiness level". Now, with the most recent development progress reported in [9], SiC/SiC composites are now being developed as an engineering material for both fusion and fission applications. SiC based CMCs are being actively considered for use as a first-wall structural material, for helium cooled ceramic breeding blankets, liquid-metal blanket concepts, and most notably W divertor flow channel inserts [5,9]. Although SiC/SiC composites could prove a robust PFC/PFM by themselves, no mature concepts are currently being pursued. Hence the emphasis on radiation stability studies rather than erosion properties. If SiC CMCs are adopted in a future tokamak, their erosion properties should indeed be evaluated and compared to monolithic/polycrystalline SiC, in case the structural material is accidentally exposed to plasma impact during a severe disruption event.

### 4.2 – MAX Phase Ceramics

The other leading PFM candidate to be studied is a class of materials known as MAX phase ceramics, unique materials that bridge the gap between metal and ceramic properties. They are a family of layered compounds with a chemical formula $M_{n+1}AX_n$, where M is an early transition metal, A is an A group element, and X is carbon or nitrogen [10]. Near close-packed M-X layers are interwoven with purely A-group layers, resulting in layered hexagonal crystal structures. N =

1, 2, or 3 for the molecular composition, and is used to designate the various phases. Most MAX phase ceramics are 211 (n = 1), while the rest are either 312 (n = 2) or 413 (n = 3), as illustrated in Figure 4.2. They were first discovered back in the 1960's, and then were left relatively untouched until 1996, when Drs. Barsoum and Houng at Drexel University developed successful manufacturing techniques for $Ti_3SiC_2$ [10]. Since then, increased interest in MAX phase research has led to the discovery of over 60 different MAX phases.

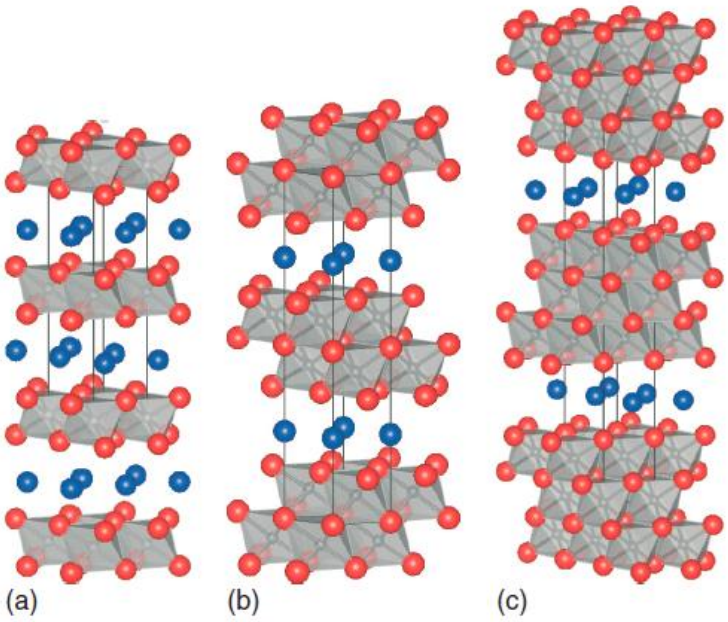


**Figure 4.2** – Atomic structures of a) 211, b) 312, and c) 413 MAX ceramics [10]. Red spheres represent M atoms, gray spheres X atoms, and blue spheres A atoms.

MAX phases exhibit high thermal and electrical conductivities for ceramics due to their respective MX layers. In terms of mechanical properties, they exhibit the exact opposite of their MX property expectations: they are easily machinable, fatigue resistant, thermal shock resistant, and relatively damage tolerant. This unexpected set of mechanical properties is largely due to the layered structure. The MX bonds exhibit metallic properties with strong bonds (covalent + ionic), while the M-A interlayer bonds are relatively weak, allowing for controlled shear slip systems [10]. MAX phases are the only polycrystalline solids that deform via both kink and shear band formation, with dislocation glides occurring exclusively in the basal planes. Additionally, MAX phases exhibit exceptional thermal stability and retention of mechanical properties at elevated

temperatures (1000+ °C), making them appealing for use in a nuclear environment under high temperatures with high thermal/mechanical shocks.

### 4.2.1 – $Ti_3SiC_2$ and $Ti_2AlC$

Despite the large amount of MAX phases discovered and researched, most studies in the literature have focused on $Ti_3SiC_2$, $Ti_3AlC_2$ and $Ti_2AlC$. MAX Phases are relatively new to research for nuclear applications, with a handful of radiation effects studies for fission applications, and with no published exposures to plasma sources. Recent works [11,12,13] analyzing the irradiation properties of a few commercially available MAX Phases point to $Ti_3SiC_2$ and $Ti_2AlC$ as the more promising candidates. It is reported that under 5.8 MeV Ni irradiation (10 – 30 dpa, 400 & 700 °C), the $Ti_3SiC_2$ appeared more damage tolerant than both $Ti_3AlC_2$ and $Ti_2AlC$ [12]. Evidence of less retained radiation damage at higher temperatures was observed for all materials, suggesting radiation defect annealing. Loss of damage tolerance properties due to grain boundary cracking was observed in the Al MAX phases, and it was suggested that these MAX phases not be used for near-400 °C operations. It was also reported that multiple MAX phases were irradiated in a 6 MW research reactor at MIT (up to ~0.1 dpa, 360 & 695 °C) [11]. Irradiation-enhanced dissociation of some MAX phases was observed, but $Ti_3SiC_2$ and $Ti_2AlC$ remained relatively stable. That study concluded that $Ti_3SiC_2$ and $Ti_2AlC$ were the most promising materials for high-temperature reactor operations. Although this research focuses on high heat flux erosion characteristics, strong radiation resistance is an equally important property of next-generation plasma-facing materials. Thus, the irradiation properties of $Ti_3SiC_2$ and $Ti_2AlC$, combined with their relative industry availability, make them the ideal first subjects for this dissertation's high heat flux plasma exposure studies.

Comparing thermal properties, $Ti_2AlC$ possesses a slightly higher thermal conductivity (46 W/mK at RT) than $Ti_3SiC_2$ (34 W/mK at RT), as well as a slightly higher specific heat (556 J/kg*K vs 520 J/kg*K) [10]. One important property of these MAX phases in relation to fusion environments is their temperature limitation. Rather than melting or sublimating, MAX phases tend to dissociate at high temperatures under high vacuum conditions. They decomposed to their respective binary carbide or nitride substance through sublimation of their A-group elements [14]. The decomposition process is relatively slow, but it limits their steady-state operating temperature

to a range between 1300 – 1800 °C. Multiple factors affect the effective temperature limit: porosity, purity, the specific A-group element, and vacuum conditions. The Al in $Ti_2AlC$, for example, has a lower vapor pressure than the Si in $Ti_3SiC_2$ [10,14]. With all of these factors affecting the MAX phase characteristics, there is an understandable discrepancy in the literature. Going by Barsoum et al, it is reported that the steady-state temperature limitations for $Ti_3SiC_2$ and $Ti_2AlC$ are about 1700 °C and 1600 °C, respectively [10].

## REFERENCES


[1] L.L. Snead et al. “Silicon Carbide Composites as Fusion Power Reactor Structural Materials.” *Journal of Nuclear Materials*, vol. 417, 2011

[2] L.L. Snead et al. “Handbook of SiC Properties for Fuel Performance Modeling.” J*ournal of Nuclear Materials*, vol. 371, 2007

[3] Ivekovic et. al. “Current status and prospects of SiCf/SiC for fusion structural applications”, *Journal of the European Ceramic Society*, vol. 33, 2013

[4] K. Nassau et al. “Synthetic Moissanite: A New Diamond Substitute.” *Gems & Geology*, 1997

[5] Y. Katoh et al. “Current Status and Recent Research Achievements in SiC/SiC Composites.” *Journal of Nuclear Materials*, vol. 455, 2014, pp. 387-397

[6] “Silicon Carbide Thermal Properties.” http://www.ioffe.rssi.ru/SVA/NSM/Semicond/SiC/thermal.html Accessed 10 May 2018

[7] S. Yajima, J. Hayashi, *Nature*, vol. 261, 1976, pp. 683-685

[8] Y. Katoh et al, “Current status and critical issues for development of SiC composites for fusion applications”, *Journal of Nuclear Materials*, vol. 367-370, 2007, pp. 659-671

[9] T. Koyanagi et al. “Recent progress in the development of SiC composites for nuclear fusion applications.” *Journal of Nuclear Materials*, vol. 511, 2018, pp. 544-565

[10] M. Barsoum, *MAX Phases: Properties of Machinable Ternary Carbides and Nitrides*, Wiley-VCH Verlag GmbH & Co, 2013

[11] D.J. Tallman et al. “Effect of Neutron Irradiation on Select MAX Phases.” *Acta Materialia*, vol. 85, 2015

[12] D.W. Clark et al. “High Temperature Ion Irradiation Effects in MAX Phase Ceramics,” *Acta Materialia*, vol. 105, 2016

[13] D. J. Tallman et al. “Effects of neutron irradiation of Ti3SiC2 and Ti3AlC2 in the 121-1805 C temperature range”, *Journal of Nuclear Materials*, vol. 484, 2017, pp. 120-134

[14] I. Low & W. Pang, “A Comparative Study of Decomposition Kinetics in MAX Phases at Elevated Temperature”, *Advanced Ceramic Coatings and Materials for Extreme Environments II*, 2013, pp. 179-185

# CHAPTER 5 – METHODS OF PFM EROSION STUDIES

A comprehensive erosion study on the selected PFMs requires an ambitious set of experiments on state-of-the-art plasma devices. Devices must be selected that can provide fusion reactor-relevant high heat fluxes from plasmas with equally relevant properties. ITER is being designed to handle 0.25 - 10 MW/m$^2$ heat fluxes to the divertor during normal operation, while ELMs and disruptions have the capability of producing several GW/m$^2$ of heat flux. In order to cover this wide range of energy conditions, two experiments were conducted using two different devices: the DIII-D tokamak operated by General Atomics and an electrothermal (ET) plasma source operated by Oak Ridge National Laboratory (ORNL). DIII-D produces heat fluxes relevant to normal ITER operating conditions, providing data in a physical sputtering-dominated erosion regime. The ET source covers the higher regime with heat fluxes and time spans close to those expected of ITER-scale ELMs and hard disruptions, capable of producing melting and sublimation across PFM samples. Additionally, computational simulation tools were developed to plan, support, and interpret the experiments for these devices. This section will cover the capabilities of and experiment plans at DIII-D and ORNL, along with details on the unique method that was used to measure erosion rates on the PFM sample surfaces.

## 5.1 – Focused Ion Beam Micro-Trench Technique

It is important to physically measure the net erosion thickness loss on each sample using a non-destructive, post-mortem technique. Most established techniques to do this require thin films or coatings of the desired material. A new analysis method was developed specifically for larger samples that are more representative of plasma-facing components. The method utilizes a combination of focused ion beam (FIB) microscopy, scanning electron microscopy (SEM), and atomic force microscopy (AFM) to both alter and characterize the modified samples before and after plasma exposure.

A focused ion beam is used to carve micrometer-scale trenches into polished sample surfaces for erosion loss measurements. The depth of each micro-trench is characterized using SEM imaging and AFM mapping data. Each micro-trench also has fiducial depth markings etched into the trench walls. In the divertor region, an angled plasma flux will impact the sample surface. As the top surface of the samples erodes during plasma exposure, certain walls of the micro-

trenches will be shadowed from any particle flux depending on their orientation. The integrated, post-exposure changes in trench geometry combined with in-situ diagnostics provide a measure of the net erosion rate for each material. The post-exposure thickness loss can be measured either by

1) Measuring the shadowed fiducial depth markings with SEM imaging, or
2) Measuring the height difference between the sample surface and trench floor with a SEM or AFM.

An example micro-trench is shown in Figure 5.1. It is 10 μm x 10 μm in length and width, and about 4 μm in depth, designed specifically for the erosion experiments on DIII-D. The dimensions of each trench, along with the specific fiducial markings used to mark the shadowed trench walls, are chosen and optimized for the specific plasma exposure experiment. The ET sample micro-trenches, for example, needed to be much deeper and required more complex erosion fiducial markings, as demonstrated in Figure 5.2. Specific details and explanations for the DIII-D and ET experiment are demonstrated in Chapter 6.

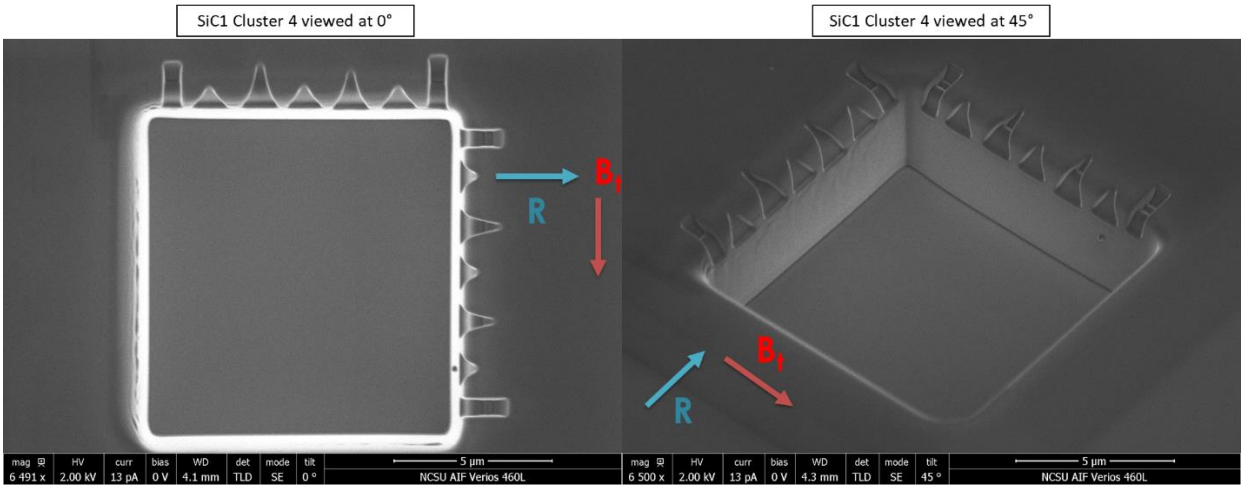


**Figure 5.1** – A square 10 µm x 10 µm micro-trench in a sample of SiC, viewed from above and from a rotated, 45° angled view.

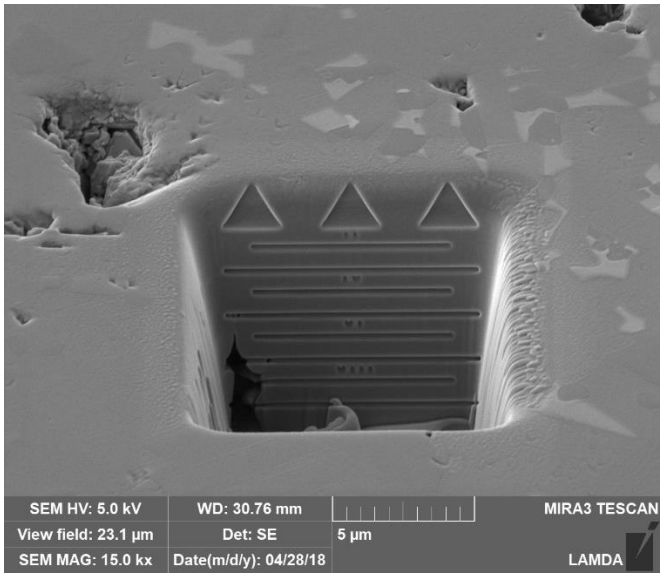


**Figure 5.2** – A 10 µm x 12 µm micro-trench, more than 10 µm deep, in a sample of $Ti_3SiC_2$. The ET source samples required fiducial markings for greater depths within the micro-trench.

***Measurement method #1 – SEM imaging***

Pre- and post-experiment measurements of the micro-trench depths are complex. Initially it was thought that only one angled SEM image was necessary to calculate each micro-trench depth. By milling the micro-trenches perpendicular to the surface normal, and then etching the fiducial markings at a known angle and specified scale, SEM images taken at that same angle

before and after exposure would directly give the thickness change via comparison. However, that method only holds true if the programmed rectangular trenches are milled to near-perfect shape, especially in regards to the trench walls. It was impossible to mill perfect geometries in an acceptable timeframe for these experiments; the tops of the micro-trench walls were often sloped and rounded, with the degree of rounding varying between materials and FIB conditions such as beam current. Due to this rounding, one angled SEM image gave inconsistent erosion depth results.

An appropriate measurement technique was therefore developed that utilized height/length measurements taken at two different angles. By measuring the same features at different views, the two unknown variables of height (depth) and slope (from edge rounding) could be separated and quantified. A cross-sectional schematic describing the sloped edges and measured variables, along with a corresponding SEM image, are shown in Figure 5.3.

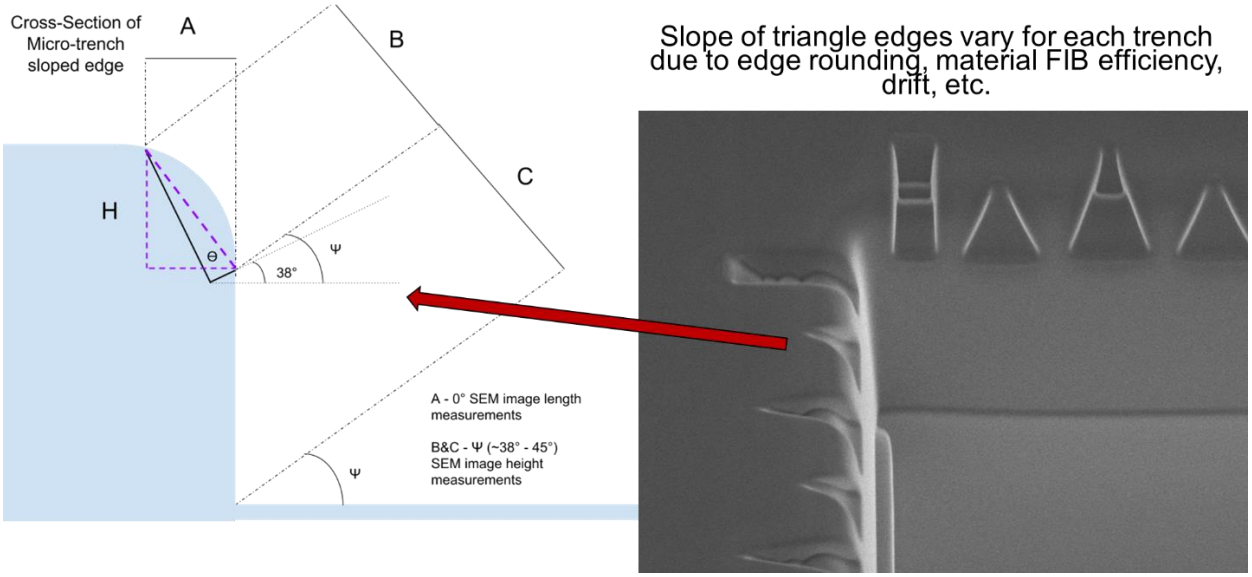


**Figure 5.3** – (Left) Schematic of sloped micro-trench edge with FIB markings, and (Right) corresponding angled SEM image depicting the FIB marking geometry on the sloped edges.

As illustrated in Fig. 5.3, the shaded blue represents a cross-section of the material, the black lines along the rounded edge represent the approximate shape of the FIB fiducial markings, and the purple lines mark the height H and sloping angle θ that are measured for each marking. The value for H is the overall goal, showing how much the top surface erodes due to plasma exposure relative to the shadowed, bottom portion of the fiducial markings. The image views

chosen were 1) a top-down image of the sample surface and 2) an angled image close-or-equal-to the FIB angle. Each fiducial marking was carved at a 38° angled to the surface parallel, the physical angle of the mounted Focused Ion Beam. Measurement A represents the marking length projected into the top-down image, and measurement B represents the length of the same marking but projected into the angled image, taken at Ψ° from the surface parallel. H and θ are then determined from A and B via the following equations:

$$Eq\ 1. \quad \theta = \tan^{-1}\left(\frac{\frac{B}{A} - \cos(\Psi)}{\sin(\Psi)}\right)$$

$$Eq\ 2. \quad H = \frac{B}{cos(\theta - \Psi)}\sin(\Psi)$$

Through trial and error of various marking geometries, the triangular fiducial markings across the sloped trench edges worked best for this measurement technique. The top triangle tips could be placed at the approximate location where sloping ends, effectively pointing to where the micro-trench geometry ends and the flat sample surface begins. The triangular markings were also ideal for plasma fluxes not properly aligned with the micro-trench walls, as seen in the DIII-D preliminary experiment with silicon in Section 5.2.2.3.

***Measurement method #2 – AFM mapping***

The other measurement method is to construct a topographic map of each micro-trench. By gathering 3D height data of the micro-trench structure, erosion depth could be easily calculated through pre- and post-exposure comparisons. In the AIF facility at NC State University, a new atomic force microscope was recently purchased that boasts the necessary capabilities: The Asylum MFP 3D Origin+ AFM. An AFM operates by using a cantilever with nanometer-scale tips to scan and map a sample surface. The cantilever can be used in a variety of modes to perform nanomechanical, nanoelectrical, and electromechanical material characterizations. For this dissertation work only the simplest of AFM capabilities is of interest: the ability to generate 3D topographic maps via a tapping mode (AC mode). In this mode, the cantilever oscillates at a set frequency and "taps" the surface as it scans across the sample, depicted visually in Figure 5.4. Feedback from the cantilever motion then gives surface height data at each tapped point, which is used to render a 3D map. The Asylum AFM has the capability to scan areas 40 μm x 40 μm or greater, with a maximum ΔZ measurement of 15 μm at a resolution of < 0.06 nm [1]. These

dimensional capabilities are perfect for the FIB micro-trench geometries, provided a suitable, high aspect-ratio AFM tip is used. An example of AIF's AFM capabilities is shown in Figure 5.5.

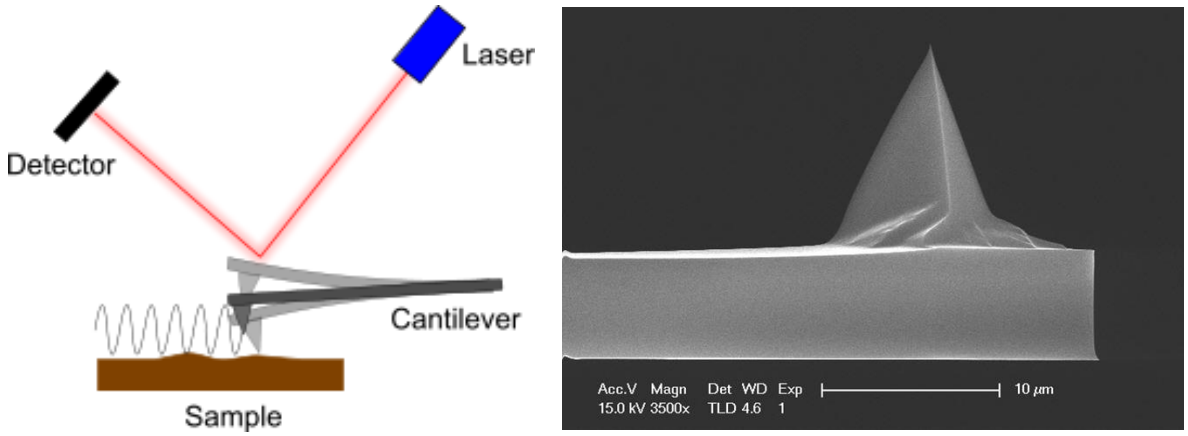


**Figure 5.4** – (Left) Depiction of the AFM tapping mode [2]. (Right) SEM image of typical AFM probe tip at the end of the cantilever [3].

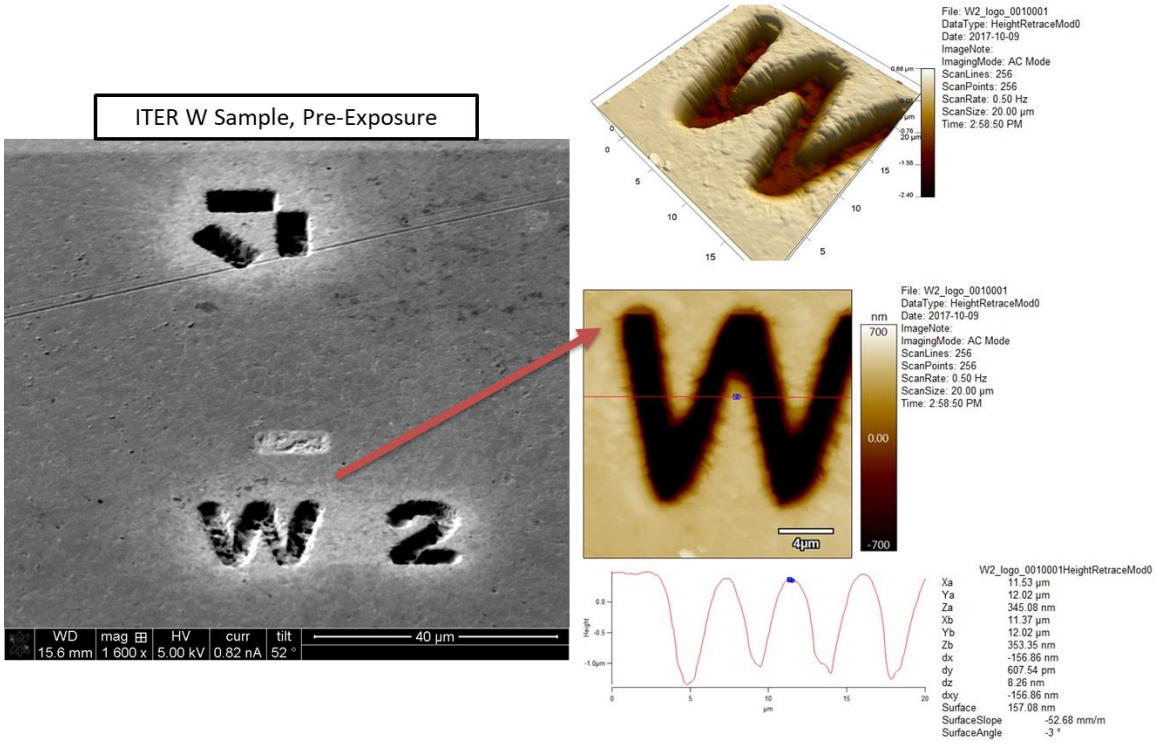


**Figure 5.5** – Example of AFM data taken on an ITER-grade W sample with FIB micro-trenches and labels. The figure shows the original SEM image (center) alongside 3D height maps, 2D height maps, and 2D line traces of height profiles from the 3D AFM data.

Although the ΔZ capability of the MFP Origin+ is listed as 15 µm, in practice the AFM is much more limited. The Z resolution decreases as the ΔZ oscillation increases, and the actual oscillatory motion of the AFM tip limits which geometries can be properly mapped. In order to map micro-trenches on the order of 4 – 5 µm deep, high aspect ratio tips are needed; the tips need to be long enough to reach the micro-trench floor, while at the same time being thin enough to fit inside the trench and map most of the floor area. The wider the AFM tip, the less area that can be mapped due to the tip sides impacting the micro-trench walls and effectively missing the edges of the floor. Working together with AIF researchers, a FIB was used to manufacture the desired high aspect-ratio tips from spare, normal aspect-ratio tips. Most of the tips were made to be about 10 µm tall and about 1-2 µm wide, perfect for fitting into the optimized micro-trench geometries for DIII-D, described later in Section 5.2.2.2. An example of a typical AFM tip alongside the self-manufactured high aspect-ratio tips is shown in Figure 5.6.

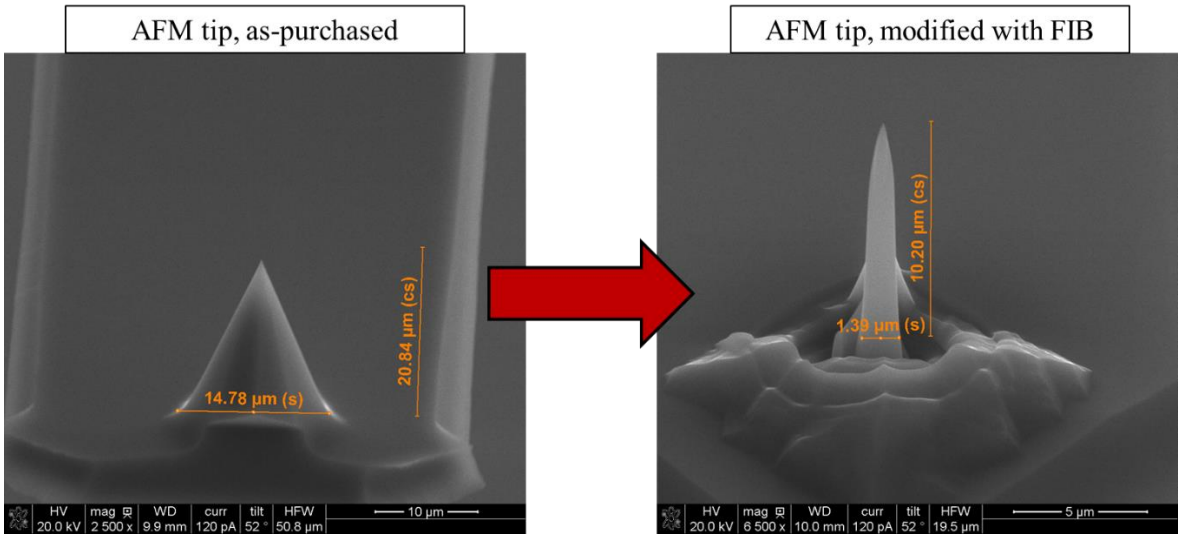


**Figure 5.6** – (Left) An example AFM tip donated by AIF with no FIB modifications. (Right) The same AFM tip after being modified with a FIB. The new tip geometry has a much higher aspect ratio, ~10.2/1.4 ≈ 7.3, in order to profile the planned micro-trench geometries.

## 5.2 – DIII-D National Fusion Facility

### 5.2.1 – Background on DIII-D

The DIII-D National Fusion Facility is a tokamak device operated by General Atomics in San Diego, California. Although considered a mid-size tokamak, DIII-D is the largest magnetic fusion experiment and the only operating tokamak in the US, with a major radius R = 1.67m and a minor radius a = 0.67m. DIII-D is a DOE Fusion Energy Sciences (FES) user facility, allowing researchers to propose and conduct experiments on DIII-D that complement FES research priorities. The main research goals of DIII-D include [4,5]: Resolving disruption problems in tokamaks, providing the basis for divertor solutions for future tokamaks, including a Fusion Nuclear Science Facility (FNSF) and a demonstration power plant (DEMO), exploring the physics of burning plasma, investigating steady state tokamak operation, and developing 3D optimization of the tokamak concept. The DIII-D facility is founded on a strong level of operational flexibility in order to explore physics and conditions relevant to future devices. DIII-D boasts an adaptive field-shaping coil system for multiple plasma shapes, diversified heating and current drive systems, internal and external error-field coils, upper and lower divertors, a comprehensive

diagnostic suite for plasma parameters, and an advanced digital control system for plasma feedback control [4,6].

### 5.2.2 – DiMES Experiment on DIII-D

A material exposure experiment on DIII-D was proposed through the Advanced Materials Validation (AMV) group of the DIII-D Boundary/PMI Center, which is responsible for studying divertor optimization and plasma-material interactions for DIII-D. Materials of interest for this dissertation are SiC and MAX phase ceramics, testing them possible tungsten-alternative PFMs. The experiment was marked #52-02, "Sputtering and Damage Properties of Alternate Materials in Reactor-Like Plasma Conditions," and examined various alternative divertor materials' performance in a realistic tokamak environment. The final experiment mini-proposal (MP) was comprised of multiple proposals put forth to the AMV group. What follows is a description of this consolidated proposal with an emphasis on the experimental details pertaining to the dissertation.

Experiment #52-02 is comprised of two main studies. The first is designed to test the damage resistance of a new tungsten (W) alloy, Ultra-Fine Grain W (UFG W) [7], and compare its performance with "ITER-grade" W under reactor-relevant divertor conditions. UFG W has already demonstrated resistance to surface damage in electron beam experiments, warranting further testing in a tokamak environment. The second study examined the erosion properties of SiC, SiC foam, and two different MAX phase ceramic materials. The test utilized the Divertor Material Evaluation System (DiMES) which holds samples flush to the lower divertor of DIII-D [8]. In this way, samples were exposed to reactor-relevant, tokamak plasma fluxes in order to compare their sputtering erosion properties. For the W samples, the experiment exploited high transient heat fluxes from H-mode ELMs in DIII-D to create surface roughening and cracking. These plasma conditions allow a direct comparison of the performance of UFG W against ITER grade W under reactor relevant divertor conditions. Before and after plasma exposure, samples were surface characterized via microscopy at Sandia Livermore. For the ceramics, the materials include: polycrystalline 3C silicon carbide, MAX phase ceramics $Ti_3SiC_2$ and $Ti_2AlC$, and silicon carbide coated graphite foam. Careful L-mode exposures of these materials determines their viability in direct comparison with ITER-grade tungsten, highlighting the importance of improved

material properties such as thermal shock resistance, thermal conductivity, and decreased sputter yields for low-Z material.

The more specific goals of these experiments include obtaining integrated and time-dependent sputtering erosion data for each material as a function of reactor-relevant heat fluxes, exposing new promising materials to DIII-D for the first time, directly comparing material erosion rates to one another, and implementing novel methods of erosion thickness loss measurements fit for bulk materials. The measurement method using focused FIB micro-trench structures has the added benefit of obtaining incident ion trajectory information. Additionally, results for two of the materials, the high-purity 3C SiC and the SiC coated graphite foam, have directly contributed to the AMV group's FY18 runtime guidance and its other SiC-focused experiments.

#### 5.2.2.1 – Experimental Method

The MP was designed to introduce surface damage and enhanced erosion to samples across two halves of the shot plan. The first part of the experiment exposed one DiMES probe to H-mode plasmas, focusing more on W samples (see Fig. 5.4). These discharges have an attached outer strike point (OSP) using a lower single null (LSN) shape in ELM H-mode and moderate line averaged density. The nominal shape and physics settings are the same as reference shot number 172368 in the DIII-D database. This discharge has a total injected power of approximately 4 MW and an ELM frequency of 10 Hz. Based on the change in temperature of the samples, the 2-second OSP dwell time given by the reference shot may be increased, with the goal of inducing as much heat flux as possible without melting the W samples.

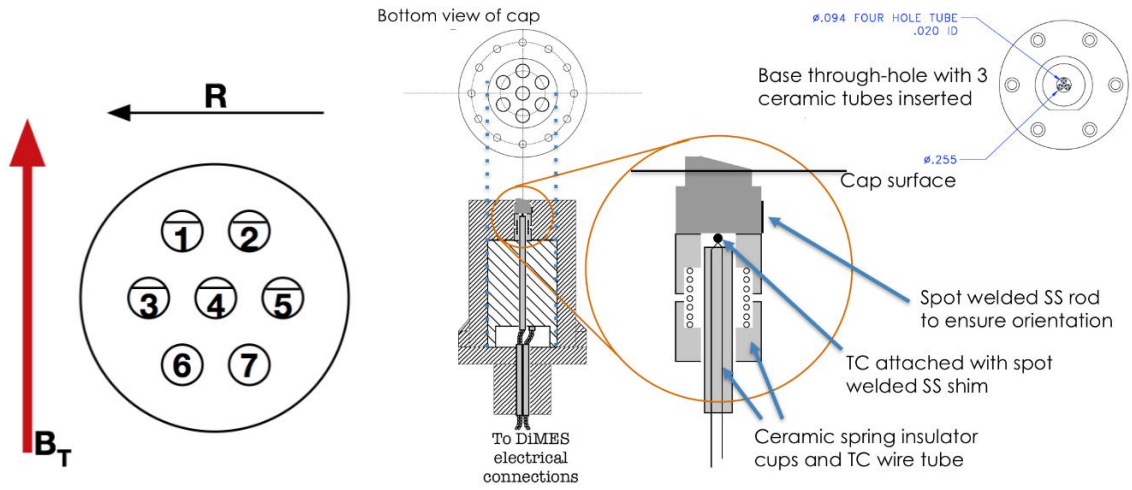


**Figure 5.7** - New DiMES probe assembly. The left image shows a conceptual layout of the 7-button holder. Samples in positions 1-5 have a 15° angle relative to the horizontal, while 6-7 are flush to the DiMES probe surface. The middle and right images show how each DiMES sample fits within the rest of the probe assembly. The samples themselves are thermally insulated with ceramic cups and springs, and there is room for thermocouples for the W sample experiments.

The second portion of the shot plan exposed another DiMES probe to L-mode plasmas and focused more on the SiC and MAX phase samples. These discharges have an attached outer strike point (OSP) using a lower single null (LSN) shape in L-mode and moderate line averaged density. The nominal shape and physics settings are the same as reference DIII-D shot number 171437, which had an average NBI heating power of 1 MW. Based on a simple thermal analysis shown in Figure 5.8, these settings would ensure survivability of the ceramic samples, with no melted or chipped material contaminating the vacuum vessel.

Heat flux values were determined by infrared (IR) imaging data. DIII-D is equipped with a 60° IR camera viewing graphite divertor tiles, as well as an IRTV that looks directly at the DiMES head. Along with careful monitoring via the IRTV, the changes in temperature can be monitored via thermocouples (TC) spot welded to the non-plasma exposed side of select W samples. The TCs provide the change in temperature at the bottom of the samples during the discharge, and this data is used to calculate the change in temperature at the surface. Additionally, between each discharge, a visible light camera ensures that the samples are not melting or shattering. Samples in the DiMES probe are three times thicker than usually designed, so that the bulk $\Delta T$ will not approach the melting temperature. The samples are pushed up from the bottom with a spring inside

a ceramic cup, and the diameter of the sample is about 0.02" smaller than the hole for the sample in the DiMES cap. Therefore, the sample is only in thermal contact with the cap at the "collar" of the sample just under the cap surface. The MAX phase ceramics are the limiting material in terms of maximum operating temperature. Reported melting/dissociation points are about 1700 °C and 1600 °C for $Ti_3SiC_2$ and $Ti_2AlC$, respectively. Therefore, during exposure it is strongly advised to keep the surface temperature of these samples well below those points, Thus, an artificial temperature threshold of 1500 °C is designated in the experiment.

To create an ITER-relevant plasma heat flux, samples are angled 15° from the horizontal that protrude up about 1.2 mm from the probe surface (see middle section of Figure 5.7). Samples in positions 1-5 (Figure 5.7) have this angle and samples 6-7 are flush with the DiMES surface. Due to the layout of the sample positions, samples at position 1 and 2 are slightly shadowed on the edges due to the raised buttons in positions 3-5. Figure 5.8 shows the predicted surface temperatures from a simple 1-D model for 2s of heat fluxes expected on the angled samples. The ~12MW/m$^2$ condition is sufficient to reach surface damage goals for the W experimenters. The surface temperatures for the MAX phase ceramics are predicted to exceed the designated 1500 °C threshold. Therefore, SiC and MAX phase samples were exposed to an L-mode plasma, based on reference shot 171437, where the heat flux is ~6 MW/m$^2$ on the angled samples.

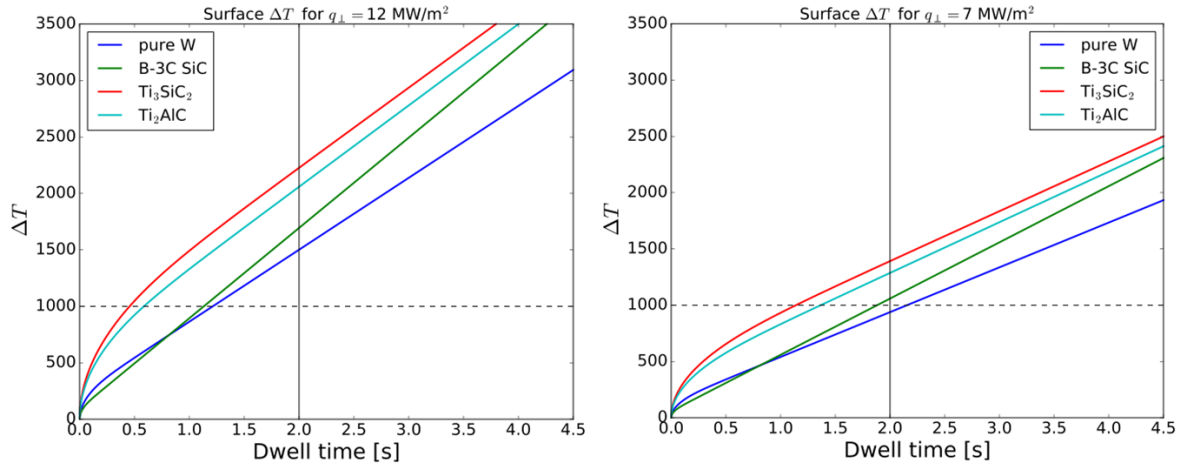


**Figure 5.8** – Surface temperature estimations of 15° angle samples, calculated with a 1-D heat equation with a heat flux of 12 MW/m$^2$ (Left) and 7 MW/m$^2$ (Right). For a 2-second strike point dwell time, the MAX phase samples exceed their designated surface temperature limits under 12 MW/m$^2$, while under 7 MW/m$^2$ all materials stay well below the designated temperature limits.

Table 5.1 lists the ideal shot plan along with the detailed diagnostic requirements on a shot-by-shot basis. Shot plan sections 1-3 pertain to the W-focused experiment, while shot plan sections 4-6 are the focus of this dissertation's experiment. The three different spectroscopic methods are a filtered DiMES TV, the MDS spectrometer, and filterscopes pointed at DiMES, have a cyclic plan for capturing sputter rate data for the various materials indicated. This cycling method heavily depends on being able to reliably reproduce the desired H-mode or L-mode discharges, so that the spectroscopy signals can be directly compared with one another.

Table 5.1 – Ideal shot plan for Experiment 52-02

| Shot plan section | Objective | Shot # | IRTV | DiMES TV | MDS | Filterscopes on DiMES |
|---|---|---|---|---|---|---|
| 1 | Establish H-mode reference shot w/ sweep, 1st DiMES head | 1 | Yes | W | Si | W |
| | | 2 | Yes | W | Si | W |
| 2 | Repeat discharge w/ fixed OSP, test exposure time on DiMES of | 3 | Yes | W | Si | W |
| 3 | Repeat desired H-mode discharges | 4 | Yes | W | Si | W |
| | | 5 | Yes | Si | C | W |
| | | 6 | Yes | C | W | W |
| | | 7 | Yes | W | Si | W |
| 4 | Establish L-mode reference shot w/ sweep, no DiMES head present | 8 | Yes | Si | Ti | Si |
| 5 | Repeat reference shot, 2nd DiMES head, test 1s dwell time | 9 | Yes | Si | Ti | Si |
| | test 2s dwell time | 10 | Yes | Si | Ti | Si |
| 6 | Repeat desired L-mode discharge | 11 | Yes | Si | Ti | Si |
| | | 12 | Yes | W | C | Si |
| | | 13 | Yes | C | Si | Si |
| | | 14 | Yes | Si | W | Si |
| | | 15 | Yes | W | Ti | Si |

5.2.2.2 – MATLAB Modeling for Preliminary DiMES Experiment

In terms of numerical results, the main experiment objective is to obtain the erosion rates for all materials as a function of the impinging heat flux. Erosion data is obtained in-situ through spectroscopic methods and then post-experiment utilizing a combination of atomic force microscopy and scanning electron microscopy as described in Section 5.1. FIB micro-trenches give an integrated erosion thickness loss of the bulk material, which is translated into an average erosion rate based on IR heat flux data. Any preferential sputtering rates would be solely determined by the relative spectroscopy signals during repeated discharges.

To ensure the success of the DiMES experiment, it was highly encouraged to develop a basic computational model to test and optimize the micro-trench geometry, as well as plan a preliminary experiment to test the micro-trench measurement technique. For the computational modeling, a set of Monte-Carlo scripts being developed at ORNL was recommended. The original script, named "MPR", was created in order to perform erosion, reflection, and migration calculations on sculpted material surfaces due to ion bombardment [9]. The script is capable of deriving local impact angle and density distributions on a specified rough surface, which is needed to derive spatially resolved erosion and re-deposition values [9]. The end goal of using the MPR script was to test whether material surfaces could be roughened/manufactured in such a way that the material's total, global sputtering rate was reduced. The original MPR script of Dr. Ane Lasa was modified to investigate erosion and re-deposition in the FIB-manufactured micro-trench geometries. The modified script predicts particle impact, erosion, and redeposition patterns within the micro-trenches, which could be used to optimize the micro-trench geometry [10]. The new set of scripts is informally referred to as "MPR-Trench."

There were three key steps to modifying MPR to suit the DIII-D experiment needs:

1) Implement realistic FIB micro-trench geometries into modeled surface
2) Introduce ion angle distribution functions relevant to tokamak divertors
3) Utilize energy and angle dependent sputter yield models for relevant materials

The material target surface in MPR is modeled by a continuous, multivariable equation in a 3D cartesian coordinate system. This continuity limitation made modeling the walls and edges of the micro-trenches somewhat challenging. Through trial and error, it was decided that a hyperbolic tangent function worked best to construct the trenches in 3D space, as described in Equation 3:

$$Eq.3 \quad z = \frac{A}{2}\left[tanh\big(S(x - bx)\big) + tanh\big(S(y - by)\big)\right]$$

where z = the surface height, A = the trench depth, bx = half of the trench length (along x), by = half of the trench width (along y), and S represents a slope shaping coefficient. In practice, Z, bx, and 'by' would be controlled during the focused ion beam process. The slope shaping coefficient S depends on how precisely the FIB work is done. For example, if working with higher beam currents, the ion beam will exhibit more spread in the ion trajectory and the rectangular

trench walls would end up more sloped, corresponding to a lower value for S in the modeling. An example of the micro-trench modeling in using the hyperbolic tangent function is shown below in Figure 5.9.

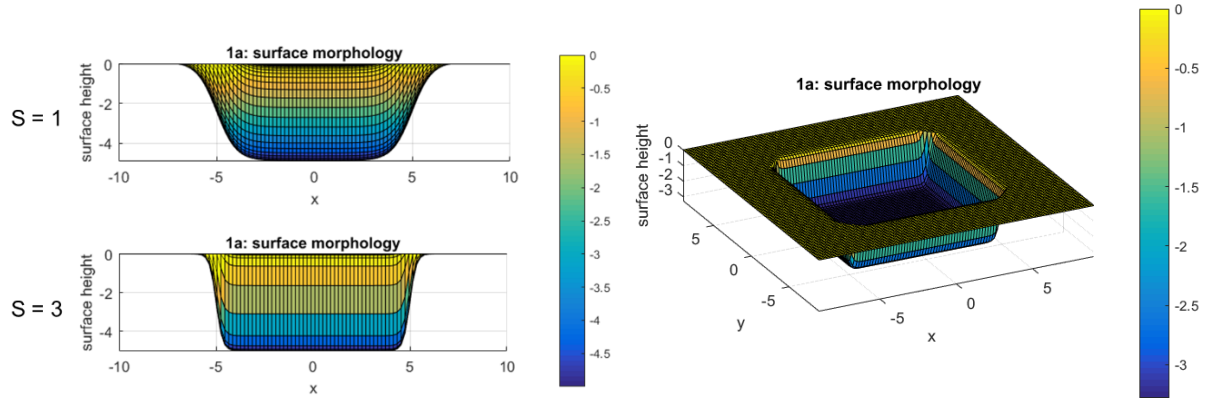


**Figure 5.9** – Example micro-trench geometries in MPR-Trench. Left, side views of a 10 x 4 x 5 μm are shown, with two different values for the sloping parameter S. Right, an angled view of a 10 x 10 x 4 μm trench with S = 3.

The next step is to use realistic ion angle distributions that occur within a divertor environment. Two literature sources were found which gave probability distribution functions for ion impact as a function of the impact angle [11,12]. These distributions were implemented into MPR-Trench and are shown in Figure 5.10. Datasets taken from these two studies were for highly inclined magnetic field angles, ~1-5° with respect to the surface parallel, which are typical on the divertor surface. Both sources defined their B-field angle with respect to the surface normal, so ~85-89° distribution data was used.

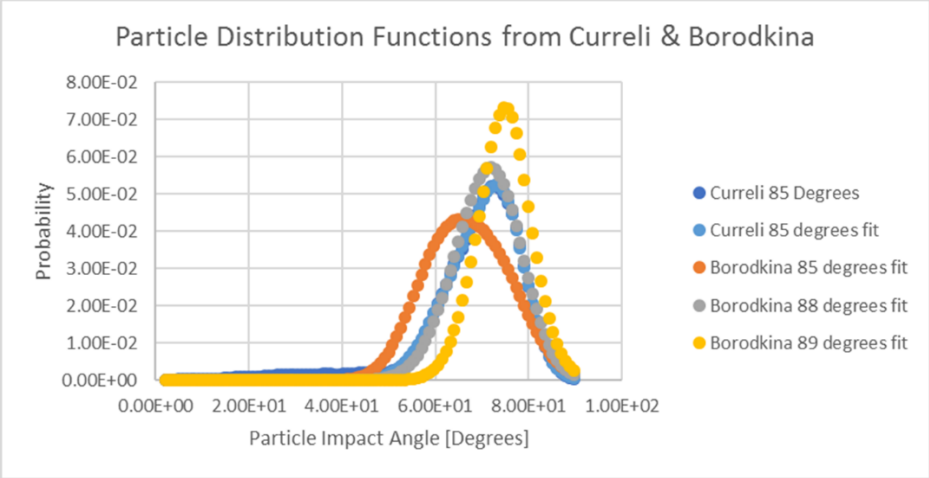


**Figure 5.10** – Ion impact angle distribution functions from Ref. [11] and [12], implemented in MPR-Trench MATLAB code.

Finally, sputter yield calculations used expressions and coefficients detailed in Eckstein and Berisch, *Sputtering and Particle Bombardment*, including the corrected fit equations from Ref. [13]. Corresponding reflection data published in the 17/12 IPP report was also used [14]. The energy-dependent and angle-dependent sputter yield equations were not modified for MPR-Trench, just the material-dependent coefficients used in those equations.

With the modified MPR-trench scripts developed, an optimization study was carried out to determine the FIB micro-trench sizes and orientations for the DIII-D experiment. Two trench geometries needed to be designed: 1) trench geometries which had their floors completely shadowed from initial particle impact, and 2) trench geometries that exhibited partial shadowing and partial erosion of their floor. The micro-trenches with a completely shadowed floor would allow for both methods of thickness loss described in Section 5.1 since the unmodified floor could then serve as a depth reference point alongside any FIB fiducial markings. The micro-trenches designed for intentional, partial erosion on the trench floor were designed specifically for ion impact angle studies. The optimization studies accounted for physical experiment limitations of making and analyzing the micro-trenches, with total dimensions limited to a square of 10 x 10 μm with 4μm depth.

The final, optimized micro-trench geometries were as follows: 10 x 4 μm rectangular trenches and 10 x 10 square trenches, each ~4 μm deep. The rectangular trenches were designed such that their floor should be completely shadowed from plasma. Sputtering and redeposition

patterns indicated that wider trenches led to less redeposition on the 'shadowed wall', the wall which would incorporate FIB fiducial markings as described in Section 5.1. Additionally, the trench depth directly determined the maximum possible length of the shadowed region. Both of these variables, width and depth, were maximized. There were competing factors in the trench length; considering the practical needs of both AFM data collection and angled SEM image requirements, a 1:1 ratio between depth and length was decided, resulting in 10 x 4 μm trenches of 4 μm depth. The elongated square trenches were simply designed with all maximum possible dimensions in order to exhibit a partially shadowed and partially eroded floor. From simulation results, ~40-60% of the square micro-trench floor was shadowed from particle impact, varying depending on the chosen distribution function. As a secondary experiment goal, erosion patterns on the square micro-trench floors would hopefully allow for some measurement of the true average ion impact angle. Successful angle measurements would shed light on the complex modification of ion trajectory through the plasma sheath and would verify the accuracy of distribution functions used in the modeling.

#### 5.2.2.3 – Preliminary DiMES Experiment on DIII-D

A test exposure of the micro-trench technique was successfully conducted at DIII-D on 7/07/2017. Polished, monocrystalline silicon samples provided by Sandia National Laboratories were prepared at Oak Ridge National Laboratory using their FEI Quanta FIB. The exposures were performed in the lower divertor of DIII-D, where DiMES is located, in ELM H-mode discharges during the plasma startup. Samples were located outboard of the outer strike point between $\Psi_N$ = 1.02 and 1.04, far from the separatrix. This was a non-ideal configuration, but since the exposure took place as a 'piggyback' experiment during startup, no control over the plasma conditions was granted. Each DiMES sample was exposed to 13 total discharges, with $T_e$ and $n_e$ at the target surface ranging from 1 – 60 eV and 0.1 – 2.4 $*10^{19}$ $m^{-3}$, respectively. The two micro-trenched Si samples were co-located on a 7-button DiMES holder with other experimenter's samples, with their locations and orientations displayed in Figure 5.11 below.

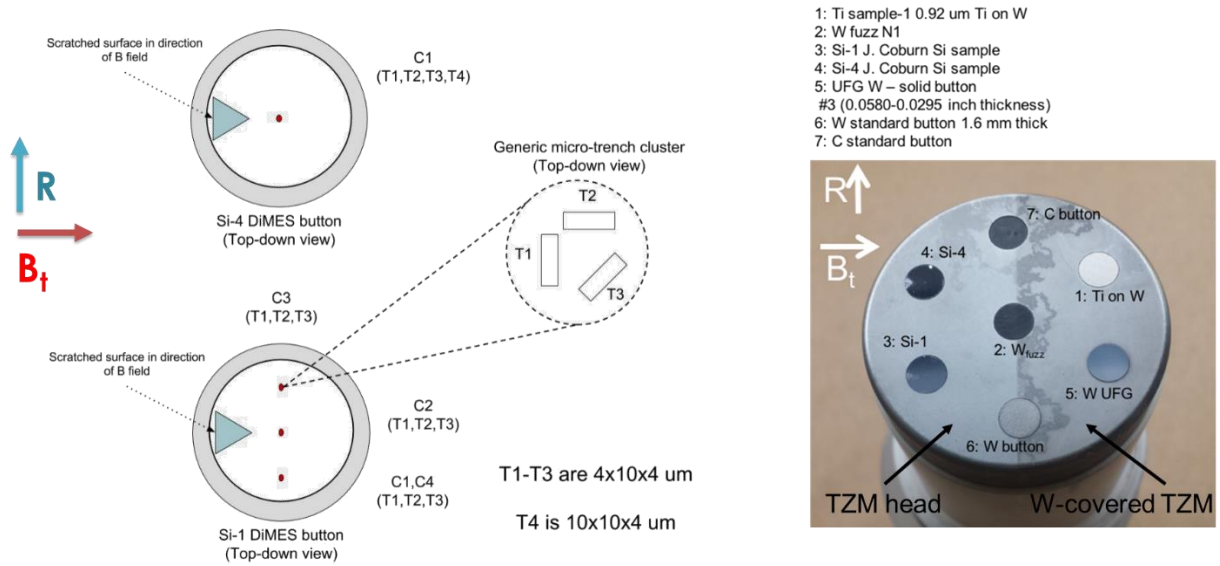


**Figure 5.11** – Map of silicon samples and clusters for the preliminary DiMES experiment on DIII-D. (Left) Micro-trench locations and orientations for the two Si samples, named Si-1 and Si-4. (Right) 7-button DiMES head, pre-exposure, with Si-1 and Si-4 located in the left-most button holders, upstream of plasma direction.

The test used the optimized micro-trench geometries based on the aforementioned MPR-Trench simulations: 10 x 4 μm rectangular trenches 4 μm deep with different orientations, along with one 10 x 10 x 10 μm square trench. One important observation from the literature was that the combination of ion gyro motion, sheath acceleration, and the corresponding ExB drift effects change the ion impact direction in the X-Y plane, i.e. the parallel sample surface [11]. Although the gyro-center ion motion generally follows the B-field, the individual ions are predicted to impact the material surface at a phase angle away from the tangential B-field (projected in the X-Y plane). For the 85° B-Field distribution, reference [11] predicted phase angles between 30° – 50°. Not knowing what the actual drift effects would be in the DIII-D divertor, clusters of 10 x 4 μm trenches were oriented at 0°, 45°, and 90° with respect to the magnetic field in order to see which orientation worked best for the FIB measurements.

This preliminary exposure experiment provided a good proof-of-concept, with samples demonstrating shadowing of the trench floor and edges as predicted by simulations, along with clear preferential sputtering on trench surfaces with respect to the trench orientation relative to the magnetic field. Figure 5.12a shows an example micro-trench cluster that was prepared but

unexposed, to give an idea of what the micro-trenches looked like pre-exposure. Figure 5.12b then shows micro-trench cluster ‘C1’ from sample Si-4 post exposure.

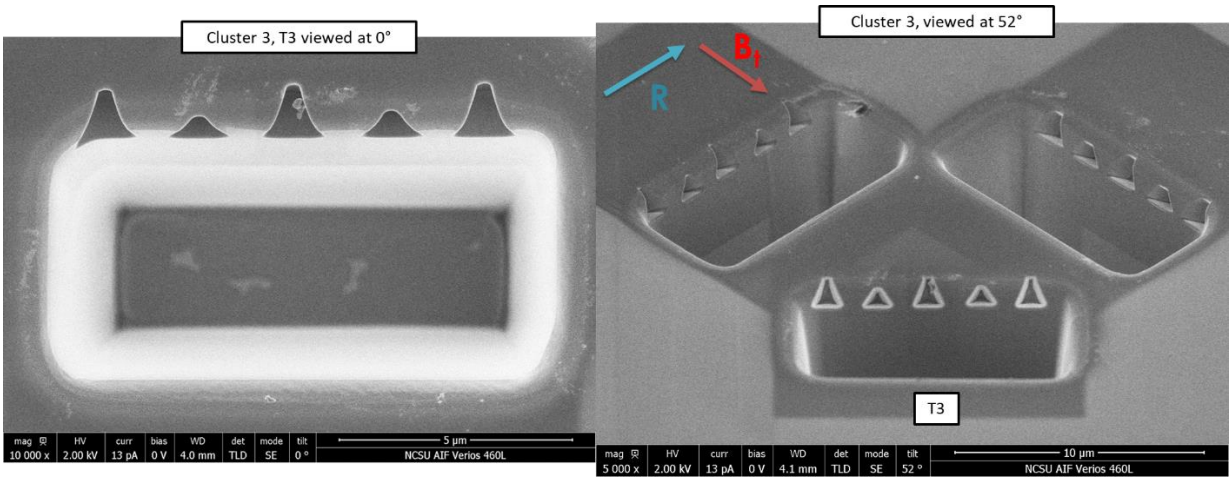


**Figure 5.12a** – An example micro-trench cluster in silicon sample Si-2, prepared but unexposed during the DIII-D preliminary experiment

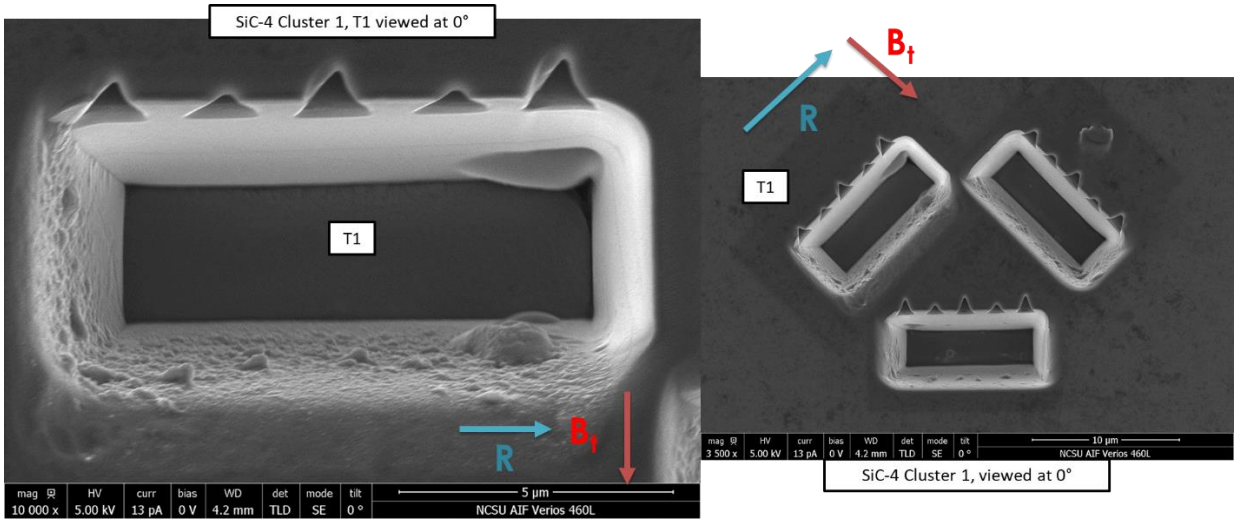


**Figure 5.12b** – Micro-trench cluster C1 from exposed silicon sample Si-4. (Left) Zoomed in image of micro-trench T1, which is oriented with DIII-D parameters R and $B_t$. (Right) All three 10 x 4 x 4 µm trenches of cluster C1. Erosion is seen to occur on the FIB triangle edges as well as the un-shadowed, downstream micro-trench walls.

The tips and certain sides of the triangular FIB markings have been eroded in Figure 5.12b. Additionally, the micro-trench walls downstream of $B_t$ (the plasma flow direction), which would

be un-shadowed from the divertor ion fluxes, show a clear erosion/deposition pattern. There is a directionality to these patterns, supporting the findings of reference [11] and indicating that the orientation of the 45° angled micro-trench was the most well-aligned with the ion flux. Simple measurements of the triangular fiducial markings indicated erosion depths approaching 0.2 μm were achieved. Shadowed erosion patterns in the one 10 x 10 x 10 μm square trench also confirmed this conclusion, as shown in Figure 5.13. The well-defined pattern of erosion on the trench floor matched general predictions from the MPR-Trench MATLAB modeling and gave preliminary results for the average ion impact angle, estimated to be 53º with respect to the magnetic field and -55º with respect to the surface normal. These results highlight the importance of sheath acceleration, ExB drift, and gyromotion effects on the ion impact angle, and therefore the orientation used for the micro-trenches. SEM images confirmed that the floors and desired walls for the optimized trench geometries are being properly shadowed from particle flux. Finally, they also confirmed which SEM microscopes at NC State and ORNL will have good enough resolution to properly photograph and analyze the FIB wall markings. The pre-exposure images for this experiment, for example, were of poor resolution and severely hindered any accurate erosion measurements.

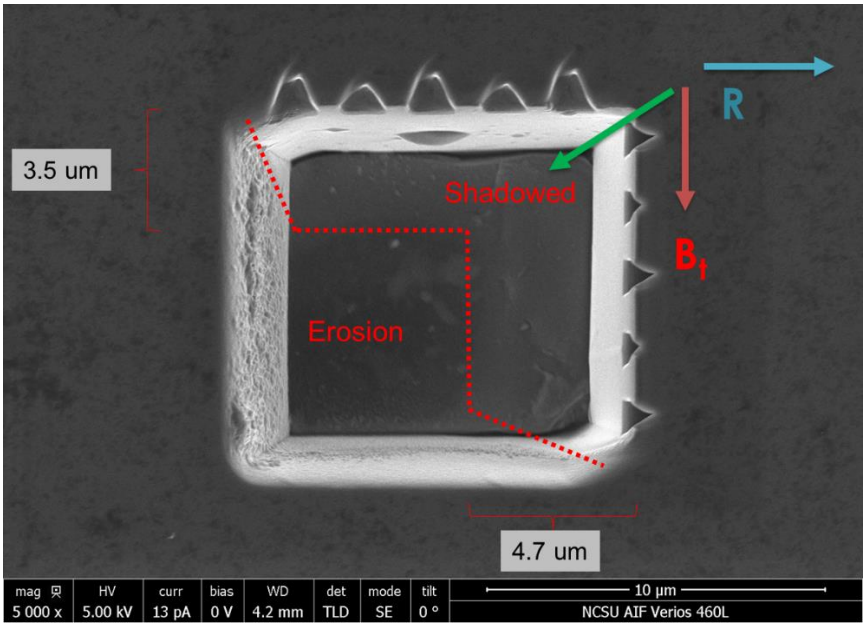


**Figure 5.13** – Square micro-trench on silicon sample Si-4 post DIII-D exposure. The micro-trench floor was partially shadowed from plasma exposure, and exhibited a clear erosion pattern which allowed for calculation of an average ion impact angle. The green arrow indicates the approximate ion impact angle wrt R and $B_t$.

## 5.3 – Electrothermal Plasma Sources

### 5.3.1 – Background on Electrothermal Plasmas

An electrothermal (ET) plasma source is a pulsed plasma discharge that operates in the confined ablative arc regime. The source consists of an electrode, an ablating liner, and a ground housing with source insulation. Charge is stored on a capacitor and then discharged through a spark gap switch, after which the arcing current through the source induces Joule heating and ablation of the liner material due to high radiant heat flux. This ablated material is then ionized, forming a low temperature, high density plasma which is discharged through the open ET barrel. The resulting plasma jet typically has temperatures on the order of 1-5 eV and an electron density on the order of $10^{22}$ – $10^{28}$ /m$^3$, depending on the magnitude of the discharge current. Most importantly, ET sources are capable of producing ~GW/m$^2$ heat fluxes, both on the liner material via radiation heat flux and at the barrel exit via the resulting plasma jet [15-17]. Such a capability

makes ET sources suitable for simulating ELM and disruption impacts for reactor-relevant PMI studies. A general ET plasma source schematic is shown in Figure 5.14.

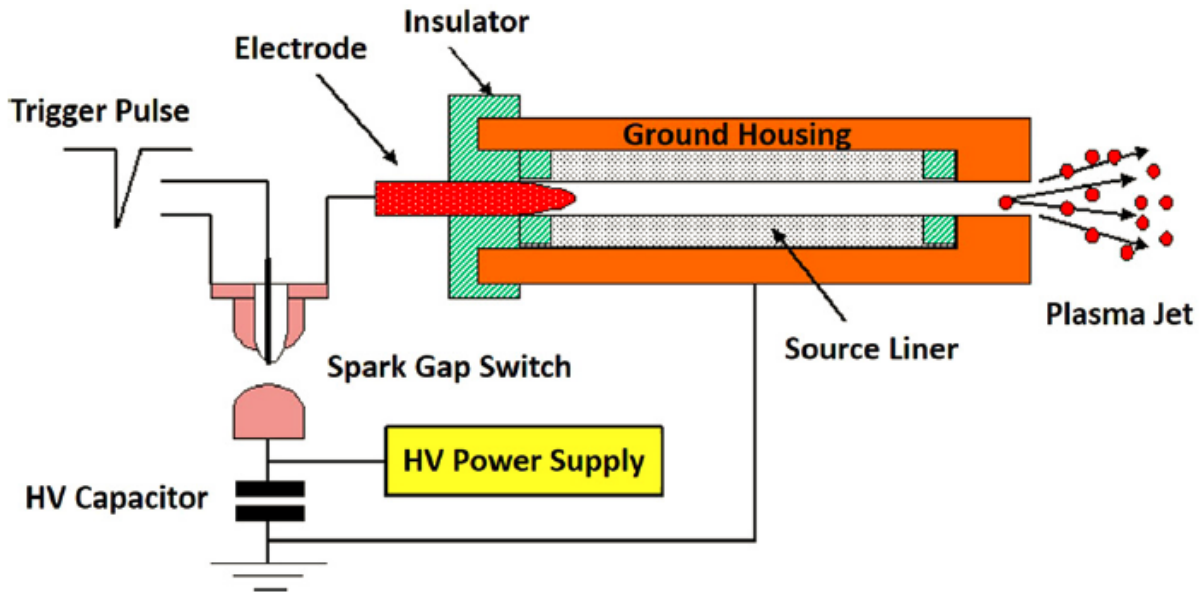


**Figure 5.14** – Layout of a typical electrothermal capillary discharge system [15]

The ablating capillary liner is on the order of centimeters in length and millimeters in diameter. It can be made of any material that will ablate due to radiant heat flux from joule heating via a direct driven current in the discharge volume. The chosen liner material determines the majority of the plasma composition, alongside backfill gas and impurities from the electrode. The base of the electrode is the same diameter as the capillary at the base, so it fits snugly in the bore of the capillary. The electrode is made of a highly conductive material and screws into a copper feedthrough, which is directly connected to the discharge end of the spark gap. An insulating liner isolates the capillary sleeve so that current only passes through the hollow capillary center. The ground housing is made out of an electrical conductor such as brass, copper, or tungsten, and acts as the current's path to ground. It houses the insulator sleeve and is the main contact point for the source to the chamber. For example, Figure 5.15 below shows an assembled and an expanded image of the source operated at Oak Ridge National Laboratory. The expanded image includes labels for each visual component.

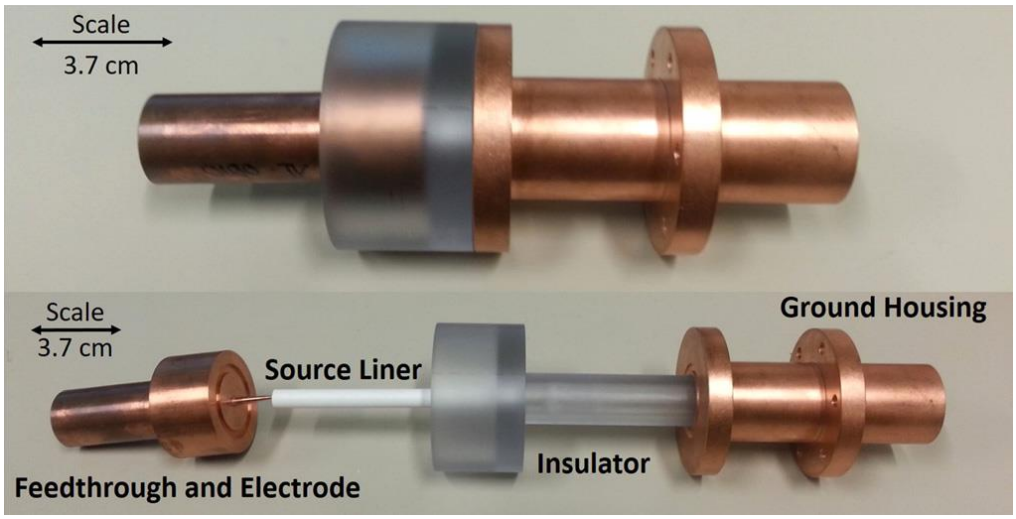


**Figure 5.15** – (Top) Assembled ET source. (Bottom) The same ET source expanded so that the individual components are seen and labeled [15]

Electrothermal plasmas have been a useful tool for numerous research projects, including nuclear fusion, small spacecraft thrusters, material deposition, propulsion, and hyper velocity launch devices. This section will provide a brief history of ET plasma source research within the context of fusion applications.

Electrothermal plasma technology originated from work studying arcs traveling through nozzles and capillary tubes. Initially, these experiments utilized two electrodes on either side of the capillary. In the early 1970's, Ogurtsova et al. [18] and Rozanov [19] were the first to recognize that these types of electrical arcs are controlled by the axial flow of ablated material in the direction of the discharge. Niemeyer [20] next showed that the arc is separated from the ablating liner by a layer of non-conducting vapor. They concluded that the black body properties of the plasma allow the input power to increase drastically while temperature increases only slightly. They also concluded that the increasing current density increases the ablation rate which leads to a positive current-voltage relationship, i.e. electric field increases as current density increases. W. Herman et al. conducted experiments and provided theory on stationary arcs with rectangular pulses through a supersonic nozzle [21]. In the experimental part of this work, various diagnostics were installed throughout the nozzle. The bore of the nozzle was fitted with pressure sensors and quarts windows to allow for axial pressure and optical/spectroscopic measurements. Herman et al. found that the pressures and temperatures were higher where the diameter of the nozzle is at a minimum. In 1980, E.Z. Ibrahim developed a 1-D model to predict ablation, pressures, and temperatures

throughout the bore of a uniform diameter capillary tube of polymethylmethacrylate with various lengths [22]. In the same paper, Ibrahim also conducted experiments where axial pressure measurements were taken in the capillary. It was found that the pressure was highest in middle of the capillary over the course of the discharge. A paper by Ruchti and Niemeyer in 1986 further solidified the mechanics of the ablative process and the theory of vapor shielding [23]. The study compared their model of the ablative liner to experimental results. The conclusions made in this work were that the arc itself was cylindrical and isothermal; that the pressure and electric field established by the arc are directly scalable in terms of current, tube geometry and material, and pressure at the exit of the capillary; and that photo-ablation is the dominant erosion mechanism which creates the vapor shielding effect. Other attempts have been made at modeling the ablation in an ET source. Keidar et al. attempted to implement a jump boundary condition at the Knudsen layer but it failed to account for any energy return to the system from the ablated material [24]. Sources of inaccuracies provided by this method of modeling were outlined and discussed in a paper by Zaghloul [25].

Starting in the early 1980's, the ET plasma source was further developed for various technological applications. The two-electrode system previously described was changed so that the grounded electrode became the end of the capillary itself, leaving the hollow capillary open on one end and shown in Figure 5.14. NASA conducted studies on ET technology for spacecraft and satellite thruster applications. One example study compared ET technology to multiple thruster types for primary positioning devices for orbit transfer missions. The study compared arc-jet plasmas, pulsed ET plasmas, ion acceleration, and conventional chemical systems as primary propulsion devices for small spacecraft [26]. They loosely concluded that an ET or arc-jet thruster system would allow for a much larger payloads than the conventional chemical propulsion system with a much longer transit time. Burton et al. with GT Devices wrote a full comprehensive report on the theory, experiment, and feasibility of using an ET source as a thruster for mid-range thrust [27,28]. The main conclusion made in [28] is that high recombination rates at the source exit permits recovery of ionization energies. This produces thrust efficiencies higher than other existing systems in the 1500-3000 second specific impulse ranges.

Interest also arose in using ET plasma sources in futuristic weapons. Specifically, electromagnetic rail launchers (railguns) and electrothermal chemical (ETC) weapons. Most of the ET work conducted in the 1990's centered on ETC guns. In an ETC gun, the ET plasma source is

used as an ignition device for a solid energetic chemical propellant. The idea was that the plasma would induce a more efficient burn than in a conventional ammunition round, and that the muzzle energy of the projectile could be adaptively controlled by changing the amount of electrical energy supplied to the ET source. The Army Ballistics Research Laboratory (BRL) was interested in understanding what went on inside of the actual ET source. They contracted GT Devices and North Carolina State University (NCSU) researchers to conduct experimental and theoretical research on the details of the ET sources, along with conducting work of their own at Aberdeen Proving Ground in Maryland. The army published two lengthy reports on their work [29-31]. The first of the two were published by Powell and Zielinski [29,30]. These papers walk through step-by-step derivations of the governing equations for an ablation driven ET source for a one-dimensional, time dependent model. The other paper was published by Bunte et al. and discussed measurements of an ET plasma using atomic emission spectroscopy [31].

North Carolina State University (NCSU) conducted many ET system experiments using the two ET systems available there: the plasma-propellant interaction experiment (PIPE) and SIRENS. Bourham et al. used the SIRENS device to develop the energy transmission factor associated with the vapor shielding effect [16]. A Lexan sleeve was used in a series of ET pulses at various shot energies. They found that an energy transmission through the vapor layer was best modeled at approximately 10%. This value was simulated in a code called ZEUS. This paper also presents measurements on liner erosion for various shot energies. It was shown that for increased shot energy, more material is ablated, resulting in larger erosion depths. Another experimental study on SIRENS measured the effects of an external magnetic field and how it impacts ablation [32]. The findings show that the when a magnetic field is applied around an ET source, the amount of surface ablation is decreased by 25-35% at lower energy inputs with Lexan source material. Adding a magnetic field also increases the plasma velocity, about 30% for a 3 T field. Hankins et al. at NCSU preformed spectroscopic measurements of pulses ranging from 1 -3 kJ through a Lexan liner [33]. The resulting temperature was found to be 1.2 to 1.9 eV over the range of input energies. To further fully understand the ET plasma source and its applications, Edwards et al. at NCSU conducted an experiment using PIPE that compared pressures between a pure ET source and an ET-chemical reaction.

There were many computational codes written to model the ET capillary discharge. A one-dimensional, time-dependent fluid dynamics code (ODIN) was published by Hurley et al. ODIN

computed plasma parameters and compared them to previous experimental results. It was found that the calculated parameters were in agreement of the experimentally measured values of source mass loss, pressure at source exit, and plasma resistivity [34]. Another code was developed and published in a study by Winfrey et al. The code is called ETFLOW and it is also a 1-D time-dependent model. Winfrey implemented ideal and non-ideal conductivity models into ETFLOW and compared them to experimental measurements of conductivity. It was found that at low discharge currents, the conductivities strongly agree with ideal conductivity models and as the current increases, trends tend toward the non-ideal model [17]. ETFLOW has since evolved to incorporate 2-D models, melt layer dynamics, multi-material liner materials, and other interesting capabilities [35,36].

NCSU was the first institution to apply the characteristics of an ET plasma to events that occur in tokamak fusion plasmas. Gilligan and Bourham conducted experiments using an ET source to simulate edge localized modes (ELMs) and plasma disruptions. As discussed in Chapter 4, both events result in a very high heat and particle flux impinging on the first wall materials. Gilligan and Bourham presented results from a series of shots which measured erosion thicknesses of various materials at similar energies with and without a magnetic field [37]. It was found that polycarbonates tend to ablate much more than typical fusion materials. Another researcher at NCSU, Sharpe, measured the size and number of particulates resulting from the ET discharge. Utilizing segmented source liners, they were able to expose both metals and polycarbonate materials to generate a mixed plasma species. They found that the liner with a Lexan-metal mix produced larger particulate sizes than the shots with only carbon-based materials. One intent of this work was to simulate the material produced in a tokamak disruption event. Echols et al. later published papers similar to the works of Sharpe et al, except without using polycarbonate materials [38-39]. Echols used Winfrey's ETFLOW code to simulate fusion related materials in an ablative liner. Tungsten, beryllium, molybdenum, and lithium were all run in the simulation under various heat fluxes, which is derived from the discharge energy. It was found that in the source of an ET capillary, pure, low-Z materials tend to ablate much less than pure, high-Z materials. Outside of PMI studies, other interesting fusion ET applications include pellet injection studies [39,40], material deposition experiments [35,41], and accelerators for magneto-inertial fusion devices [42].

5.3.2 – ET Experiment at Oak Ridge National Laboratory

Electrothermal plasma experiments represent the other significant portion of this dissertation, studying select PFM candidates under ELM- and disruption-relevant heat and particle fluxes. A material exposure experiment was proposed using the ET plasma source operated at Oak Ridge National Laboratory. The proposal was coordinated and conducted through the Fusion and Materials for Nuclear Systems Division (FMNSD) at ORNL, specifically the Experimental Plasma Physics group of FMNSD. Being a relatively small and available device, the proposal to work on the ET source was more informal than the DIII-D experiment. This setup allowed for coordination of multiple preliminary experiments leading up to the final exposure experiment with the desired PFMs. What follows is a brief description of the ORNL ET source and the experiment setup.

The ET plasma source at ORNL, referenced from here onwards as 'the ET source', follows the general description of Figure 5.14. The ET capillary is capped at one end by a cathode, and open at the other end so that the generated capillary plasma launches out as a plasma jet. Figure 5.15 is this specific ET source. The ground housing and feedthrough are solid copper, the electrode tip is a W-Cu tip, and the insulator is made of a Lexan brand polycarbonate "$C_{16}H_{14}O_3$" [15]. The source liner is variable for the ET source; Figure 5.15 displays a liner made of boron nitride. These experiments chose to use Lexan source liners since they are well tested in ET discharges. Post-experiment surface depositions from the Lexan were also relatively easy to clean without damaging the exposed samples. The ET source uses a DC capacitive discharge to drive a current axially down the hollow center of the Lexan liner, which then ablates, dissociates, ionizes, and forms the plasma. The liner is 105mm long and 4mm in diameter, with the inner diameter growing as the liner ablates with each current pulse [15]. A trigger module synchronizes all other diagnostic triggers to match the capacitor discharge. The ET source operates under vacuum, with the interior pumped to below 1mTorr before each discharge. The source is backfilled with helium gas to 40-60 Torr right before each trigger. This backfill allows adequate electrical breakdown for current arc to form within the source. The current pulse itself can be controlled by installing a pulse-forming network in the ET electrical system. Without the pulse-forming network, the natural current discharge lasts < 200 μs and is somewhat inconsistent in its discharge characteristics. Two pulse-forming networks are available for the ET source, designed to produce current pulse lengths

of 1ms and 2ms [15]. The 1ms network is comprised of a 0.1 mH inductor and a 1 Ω resistor, which is highlighted in the electrical system schematic in Figure 5.16.

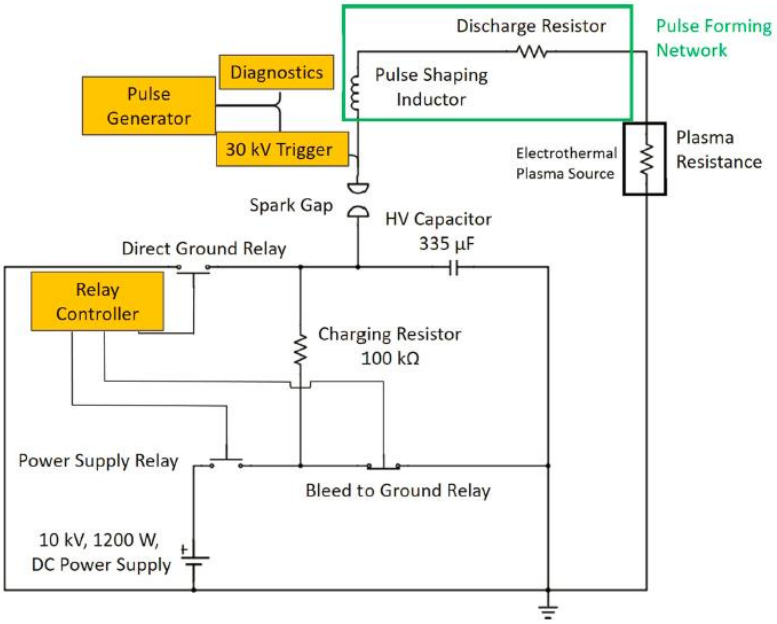


**Figure 5.16** – Schematic of the electrical system for the ORNL ET source [15]

Just as in the DIII-D experiment proposal, the main objective of the ET experiment is to measure each PFM's erosion rate as a function of the impinging heat flux. The same post-experiment microscopy method described in Section 5.1 gives the total net erosion thickness loss. This value can then be converted into an average erosion rate over the time duration of the plasma discharge. Although the impinging heat fluxes will be three orders of magnitude larger than that of the DIII-D experiment, the same microscopy method should work so long as melting and sublimation occurs uniformly across the sample surface. To measure the corresponding heat flux, the ET source housing can accommodate an infrared (IR) camera viewing port. The plasma generated by the current pulse impacts a target plate that is angled 45° with respect to the plasma jet. The target plate holds the prepared PFM samples at the center of the jet impact area. The target plate is angled in this way to accommodate the IR camera viewing angle. Coincidentally, a ~45° ion impact angle is more realistic than a normal incidence for a divertor environment, as highlighted in Section 5.2.2.2. A diagram of the ET source orientation with the target plate and IR camera is displayed in Figure 5.17. Additionally, an image of the entire ET source setup, within

the safety shielding box housing, is shown in Figure 5.18. It should be noted that many ET material erosion studies in the literature, such as references [17,37,43], analyze the heat flux on and mass loss of the liner material. The radiant heat flux in this case is comprised of photons from the Joule heating effect. Again, this dissertation experiment focuses on material samples placed at the end of the ET source barrel, such that the heat flux and erosion is due to impact of the ions, electrons, and hot neutrals from the plasma jet.

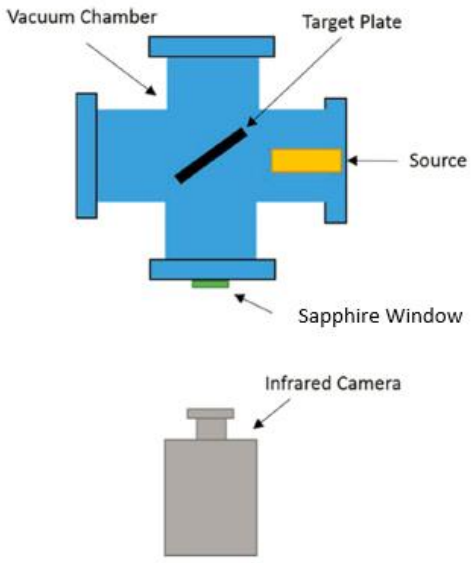


**Figure 5.17** – A top-down diagram of the ORNL ET source setup, including the source, target plate, and IR camera.

**Figure 5.18** – The Electrothermal plasma source at ORNL

5.3.3 – ETFLOW Simulations

The study of alternative PFMs for this dissertation work first began with electrothermal plasma simulation studies, and then evolved to focus on the experimental components at DIII-D and ORNL. ET plasma simulations set the groundwork for this research narrative and play an important role in evaluating PFM erosion characteristics in the sublimation-dominated erosion regime. Thus, a brief description of the specific ET simulation tool used, ETFLOW, is included. The 1-D, time dependent code ETFLOW models plasma formation and flow in a capillary and self-consistently solves the set of governing plasma equations [17]. It calculates numerous plasma parameters such as plasma temperature and density (electrons, first and second ionization, and neutral particles), kinetic pressure, plasma velocity, heat flux, total ablated mass, and plasma conductivity. The code is written in FORTRAN and runs in a VBA environment, with several modules and a library for various materials of interest. The basic equations are conservation of mass, momentum, and energy with the appropriate plasma models and essential plasma equations such as equation of state, ionization, Saha equation, viscosity and electrical conductivity [34]. Details of the governing equations for ETFLOW as well as its history can be found in the literature [25, 30, 40, 44]. While the code has both the ideal Spitzer model [45] and a non-ideal model, only the ideal model was used.

Important to this study are the particular equations for material ablation and the models used to evaluate the vapor shielding effect within the capillary. The continuity equation is written as in Equation 4, where $\dot{n}_{ablation}$ is the time rate of change of material density due to ablation of the inner liner material. The ablation rate is calculated via Equation 5, where $q''_{rad}$ is the radiant heat flux, R is the surface inner radius, and $H_{sub}$ is the total sublimation/vaporization energy required to dissociate the wall molecules into plasma atoms of average mass $A_p$. The radiant heat flux follows the Stefan-Boltzmann equation for radiation heat transfer, Equation 6, where $T_p$ is the plasma core temperature, $T_v$ is the wall surface temperature, and $f$ is a factor that accounts for vapor shielding mechanism.

$$Eq\ 4. \quad \frac{\partial n}{\partial t} = \dot{n}_{ablation} - \frac{\partial (nv)}{\partial z}$$

$$Eq\ 5. \quad \dot{n}_{ablation} = \frac{2q''_{rad}}{RH_{sub}A_p}$$

$$Eq\ 6. \quad q''_{rad} = f\sigma_b(T_p^4 - T_v^4)$$

Previous work analyzing vapor shielding effect with ETFLOW employed two models, both of which are used in this study [43]. In the first model, the transmission factor $f$ equates to the plasma emissivity coefficient for a plasma emitting radiation as a gray-body rather than a full black body. The emissivity coefficient ε is related to the plasma optical thickness $\tau_\omega$ by Equation 7. The optical thickness determines how radiation intensity is attenuated as it travels through the vapor shield towards the in-tact PFC surface, and has been found to vary with the radiant heat flux and vapor cloud density. Rosseland's averaging approximation is used for the calculation of the mean plasma opacity. The second model defines $f$ as the ratio of the energy reaching the capillary wall to the total energy emitted by the plasma core. Along with the sublimation energy, $f$ depends on the total energy of the plasma species, the density $\rho$ of the evaporated material, and the kinetic pressure *P* of the plasma, as described by Equation 8.

$$Eq\ 7. \quad \varepsilon = 1 - \exp(-\tau_\omega)$$

$$Eq\ 8. \quad f = \frac{\rho H_{sub}}{P + \rho H_{sub} + \rho U + \frac{1}{2}\rho v^2}$$

This 1-D version of ETFLOW is only capable of evaluating total material erosion for the liner material. Although this does not directly correspond to the total erosion of a material target at the end of the ET plasma jet, the erosion rate calculations are still useful for evaluating PFMs in a sublimation-dominated erosion regime. As described in Section 2.3, once the material surface reaches melting/sublimation temperatures, the avenue for heat flux deposition (photons versus ions) should become irrelevant. Of course, vapor shielding effects will be different for photon transport and ion transport through a vapor cloud, changing the final heat flux that ultimately impacts the sample surface. This assumption of heat flux medium also does not account for 3-D melt layer splashing effects, which could differ between photon and ion fluxes. Either way, it should be noted that ETFLOW calculates material erosion and vapor shielding effects for the liner material, not any target materials.

## REFERENCES


[1] "MFP-3D Origin+ AFM," *Oxford Instruments*, https://afm.oxinst.com/products/mfp-3d-afm-systems/mfp-3d-origin-plus-afm Accessed 19 July 2018

[2] "SPM Modi and Measurement Methods," *Semilab*, https://www.dme-spm.com/spmmodi.html Accessed 2 July 2018

[3] "AFM Probes, Tips, and Cantilevers," *Bruker AFM Probes*, https://www.brukerafmprobes.com/ Accessed 2 July 2018

[4] "User Facilities: DIII-D National Fusion Facility (DIII-D)," *DOE Fusion Energy Sciences*, https://science.energy.gov/fes/facilities/user-facilities/diii-d/ Accessed 2 July 2018

[5] J.L. Luxon, "A Design Retrospective of the DIII-D Tokamak," Nuclear Fusion, 42 (2002) 614-633

[6] R.J. Buttery et al., "DIII-D Research to Address Key Challenges for ITER and Fusion Energy," Nuclear Fusion, 55, 104017 (2015)

[7] R.D. Kolasinski et al. "High-flux plasma exposure of ultra-fine grain tungsten." *Int. Journal of Refractory Metals and Hard Materials*, vol. 60, 2016, pp. 28-36

[8] C.P. Wong et al. "Divertor materials evaluation system at DIII-D," *Journal of Nuclear Materials*, 196–198 (1992)

[9] A. Lasa et al., "A Hybrid Analytical – Computational Approach to Controlling Erosion, Reflection and Migration with Sculpted Surfaces," APS-DPP 2016, San Jose, CA

[10] A. Lasa and J. Coburn, "MPR" source code, https://github.com/ORNL-Fusion/MPR

[11] R. Khaziev and D. Curreli, "Ion energy-angle distribution functions at the plasma-material interface in oblique magnetic fields", Physics of Plasmas, 22, 043503 (2015)

[12] Borodkina, An Analytical Expression for the Electric Field and Particle Tracing in Modelling of Be Erosion Experiments at the JET ITER-likeWall", Contrib. Plasma Phys. 56, No. 6-8, 640 – 645 (2016)

[13] R. Behrisch & W. Eckstein, Sputtering by Particle Bombardment, Springer, Topics in Applied Physics, 2007

[14] W. Eckstein, "Reflection", IPP 17/12 (2009)

[15] T.E. Gebhart et al. "Material impacts and heat flux characterization of an electrothermal plasma source with an applied magnetic field," *Journal of Applied Physics*, **122**, 063302 (2017)

[16] M. A. Bourham, O. E. Hankins, O. Auciello, J. M. Stock, B. W. Wehring, R. B. Mohanti, J. G. Gilligan, "Vapor Shielding and Erosion of Surfaces Exposed to a High Heat Load in an Electrothermal Accelerator," *IEEE Transactions on Plasma Science*, Vol. 17, No. 3, June 1989.

[17] A. L. Winfrey et al. "A Study of Plasma Parameters in a Capillary Discharge with Calculations Using Ideal and Nonideal Plasma Models for Comparison With Experiment," *IEEE Transactions on Plasma Science*, 40, 843 (2012)

[18] N.N. Ogurtsova, I.V. Podmoshenskii, and P.N. Rogovtsev, "Calculation of the parameters of an optically dense plasma obtained by a discharge with an evaporating wall," High Temp., Vol. 9, Pg. 430-435, 1971.

[19] V.B. Rozanov, "Gas dynamic model of a capillary discharge with evaporating walls," High Temp., Vol. 9, Pg. 895-900, 1971.

[20] L. Niemeyer, "Evaporation dominated high current arcs in narrow channels," *IEEE Trans. On Power App. Syst.*, Vol. PAS-97, Pg. 950-958, 1978.

[21] W. Hermann, U. Kogelschatz, L. Neimeyer, "Experimental and theoretical study of a stationary high-current arc in a supersonic nozzle flow," *J. Phys. D: Applied Physics*, Vol. 7, 1974.

[22] E.Z. Ibrahim, "The ablation dominated polymethylmethacrylate arc," *J. Phys. D: Applied Physics*, Vol. 13, Pg. 2045-2065, 1980

[23] C.B. Ruchti, L. Neimeyer, "Ablation controlled arcs," *IEEE Transactions on Plasma Science*, Vol. PS-14, August 1986.

[24] M. Keidar, I.D. Boyd, "Ablation study in the capillary discharge of an electrothermal gun," *Journal of Applied Physics*, Vol. 99, 2006

[25] M. R. Zaghloul, "On the vaporization and heated compound-materials in ablation-controlled arcs," *Journal of Applied Physics*, Vol. 95, 3339, 2004

[26] S.Y. Wang, P.J. Staiger, "Primary Propulsion of Electrothermal, Ion, and Chemical Systems for Space-Based Radar Orbit Transfer," NASA technical memorandum 87043, NAS 1.15:87043, 1985.

[27] R. L. Burton, S. A. Goldstein, G. K. Hilko, D. A Tidman, N. K. Winsor, "Investigation of a Pulsed Electrothermal Thruster," GT Devices, prepared for NASA, October 1983.

[28] R.L. Burton, S.A. Goldstein, D.A. Tidman, N.K. Windsor, "Theory of the pulsed electrothermal thruster," 16th AIAA International Electric Propulsion Conference, Nov 17-19, 1982, New Orleans, LA

[29] J. D. Powell and A. E. Zielinski, "Theory and Experimentation for an Ablating-Capillary Discharge and Application to Electrothermal-Chemical Guns," Technical Report (BRL-TR-3355) for U.S. Army Laboratory Command, June 1992.

[30] J. D. Powell and A. E. Zielinski, "Capillary Discharge in the Electrothermal Gun," *IEEE Transactions on Magnetics*, 29, 591 (1993)

[31] S.W. Bunte, R.A. Beyer, A.E. Zielinski, "Temperature measurements of ET plasmas using atomic emission spectroscopy," Technical Report (BRL-TR-3196) for U.S. Army Laboratory Command, February 1991.

[32] J. G. Gilligan, M. A. Bourham, O. E. Hankins, W. H. Eddy, "Magnetic Vapor Shielding Mechanism in Electromagnetic and Electrothermal Launchers," *IEEE Transactions on Magnetics*, Vol. 29, No. 1, January 1993.

[33] O.E. Hankins, M.A. Bourham, J. Earnhart, J.G. Gilligan, "Visible light emissions measurements from a dense electrothermal launcher plasma," *IEEE Transactions on Magnetics*, Vol. 29, No. 1, January 1993.

[34] J. Hurley et al. "Numerical Simulation and Experiment of Plasma Flow in the Electrothermal Launcher SIRENS," IEEE Transactions on Magnetics, 31, 616 (1995)

[35] J. R. Echols, A. L. Winfrey, J. M. Nowak, M. A. Bourham, "Evaluation of Materials Deposited by a Novel Electrothermal Plasma Technique," IEEE Pulsed Power Conference, San Francisco, CA, June 2013.

[36] N. M. Almousa, J. G. Gilligan and M. Bourham, "Surface Ablation and Melting of Fusion Materials Simulated by Transient High Heat Flux Generated in an Electrothermal Plasma Source," *IEEE Transactions on Plasma Science*, vol. 44, no. 9, pp. 1642-1648, Sept. 2016.

[37] J.G. Gilligan and M.A. Bourham, "The use of an Electrothermal Plasma Gun to Simulate the Extremely High Heat Flux Conditions of a Tokamak Disruption," *Journal of Fusion Energy*, Vol. 12, pp. 311-316, September 1993.

[38] R. W. Kincaid and M. A. Bourham, "Electrothermal plasma gun as a pellet injector," Conference Proceedings: Topical on Fusion Energy, New Orleans, Louisiana, June 19-23, 1994.

[39] R. W. Kincaid, M. A. Bourham, and J. G. Gilligan, "Plasma gun pellet acceleration modeling and experiment," *Fusion Technology*, Vol. 30, Pg. 834-839, November 1996.

[40] A. L. Winfrey, M. A. Abd Al-Halim, A. V. Saveliev, J. G. Gilligan, M. A. Bourham, "Enhanced Performance of Electrothermal Plasma Sources as Fusion Pellet Injection Drivers and Space Based mini-Thrusters via Extension of a Flattop Discharge Current," *Journal of Fusion Energy*, Vol. 32, Issue 3, pp. 371-377, June 2013.

[41] Mohamed Abdel-Kader, Mohamed Abd Al-Halim and Mohamed Bourham, "Generation of Noble and Refractory Metals Plasma Jets by Electrothermal Discharge for Surface Deposition Applications", *IEEE Trans. Plasma Science*, Vol. 46(6), pp. 2099-2107, June 2018.

[42] F.D. Witherspoon, A. Case, S.J. Messer, "A contoured gap coaxial plasma gun with injected plasma armature," Review of Scientific Instruments, Vol. 80, 2009

[43] N. Almousa and M. Bourham, "Vapor Shield Models in Electrothermal Capillary Discharges and Comparison with Experiments," presented at IEEE ICOPS-Beams 2014, Washington DC, May 25–29, 2014.

[44] J. G. Gilligan and R. B. Mohanti, "Time-dependent Numerical Simulation of Ablation Controlled Arcs," *IEEE Transactions on Plasma Science*, 18, 190 (1990)

[45] L. Spitzer and R. Harm, "Transport Phenomena in a Completely Ionized Gas," *Phys. Rev.*, 89, 5, 971 (1953)

# CHAPTER 6 – RESULTS OF PFM EROSION STUDIES

## 6.1 - DIII-D Experiment

### 6.1.1 - Experiment Details

The material exposure experiment took place over the course of one half-day on DIII-D. Seven material samples were prepared and loaded on a single DiMES head depicted in Figure 6.1 (Left), which holds samples flush to the lower divertor of DIII-D [1]. Exposures were performed with the outer strike point placed at R = 1.47 m. Sample locations varied between R = 1.475 and R = 1.495, just outboard of the programmed strike point location. In order to increase the effective heat flux experienced by each material, angled samples were prepared with a 15° incline into the flux direction, as seen in Figure 6.1 (Right). For a typical DIII-D discharge with grazing magnetic field incidence angles of ~1.5° (from the surface parallel), it was predicted that the 15° angled faces should experience a ~10x increased heat flux magnitude. This increase would allow for heat flux exposures in the desired reactor-relevant range of 5-10 MW/m$^2$. The angled DiMES sample illustration in Figure 6.1 also includes the approximate locations for the micro-trench clusters. At the top of the angled samples is a flat portion meant to avoid any extreme leading-edge melting or fracture at the sample tip. This area was also utilized to obtain erosion data for a perpendicular heat flux angle. Accurate micro-trench location information can then give erosion rate information as a function of height and radial location within the divertor. Of the seven samples, two angled samples were polycrystalline β-3C SiC and two angled samples were $Ti_3SiC_2$. Two 'flush' samples were the same SiC and $Ti_3SiC_2$. Due to time limitations, the flush $Ti_3SiC_2$ sample did not have prepared micro-trenches.

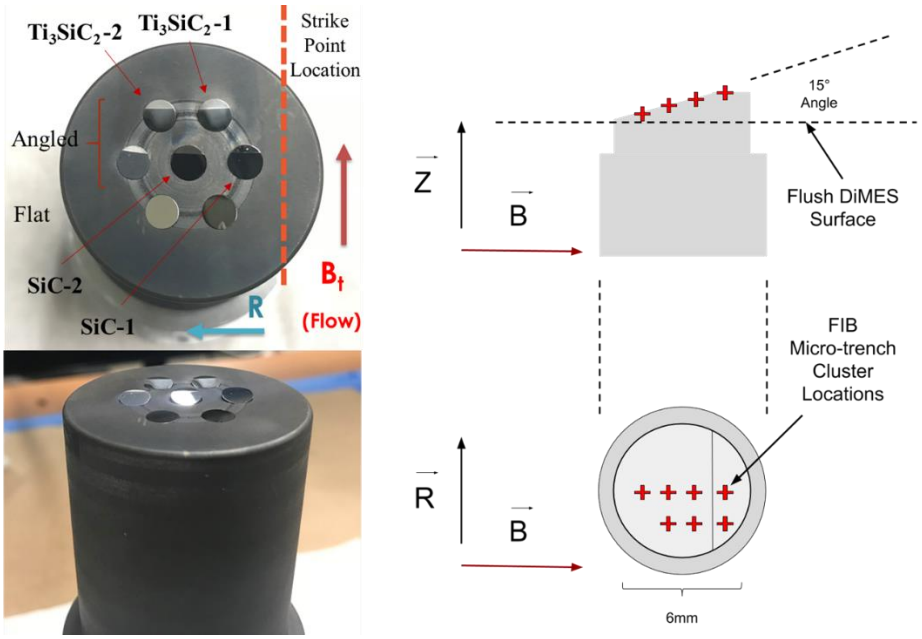


**Figure 6.1** – (Left) DiMES head containing Ti3SiC2 and SiC samples, post-experiment. (Right) Schematic of typical angled DiMES sample, where each red cross represents a FIB micro-trench location. The general plasma flow follows the toroidal magnetic field $B_t$.

Based on the MPR simulation results detailed in Section 5.2.2.2 of Chapter 5, 10 x 4 μm rectangular trenches and 10 x 10 μm square trenches were used in this experiment, each ~4 μm deep. The rectangular trenches were designed such that their floor should be completely shadowed from plasma. Clusters of 10 x 4 μm trenches were oriented at 0°, 50°, and 90° with respect to the toroidal magnetic field vector, along with clusters of one square and one rectangular trench. The micro-trenches angled at 50° were meant to be more closely aligned with the average ion impact angle based on the previous exposure experiment. Figure 6.2 shows an example 4 x 10 μm trench, approximately 4 μm deep, before and after plasma exposure. The combination of measurements from the top-down images (Left) and angled images (Middle) allow for more accurate erosion depth calculations, as described in Section 5.1.

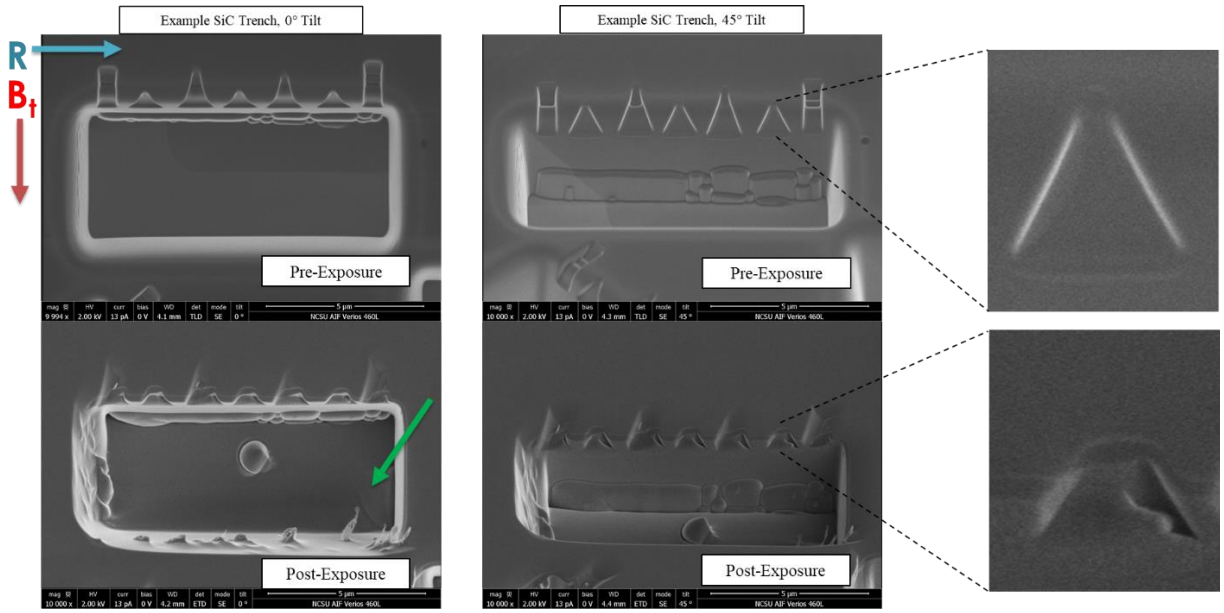


**Figure 6.2** – Example of a 4 x 10 μm trench, approximately 4 μm deep, before and after plasma exposures on DIII-D. Dimensions of the triangle fiducial markings from these SEM images are measured in order to calculate total erosion thickness loss. The green arrow represents the approximate direction of the ion impact.

The 10 x 10 μm square trenches were designed to exhibit a partially shadowed and partially eroded floor. A secondary experiment goal was to attempt to measure the true average ion impact angle, based on erosion patterns on the square micro-trench floors. Figure 6.3 shows an example of SEM micro-trench images before and after exposure, along with the corresponding AFM height retrace data used to interpret the SEM imaging. It was expected that two of the micro-trench walls would provide partial shadowing of the micro-trench floor. Past those areas would be a band of erosion, where some but not all of the ions manage to impact the trench floor since ions have a range of impact trajectories affected by their gyromotion, sheath acceleration, ExB drift effects, etc. Finally, past that band would be a region where ions of all trajectories within the distribution impact the trench floor, leading to uniform erosion that matches the normal surface erosion. It was also suggested by modeling that erosion of the 'downstream' micro-trench walls could lead to deposition of material within the trench, but it was unknown whether this would significantly manifest during the experiment.

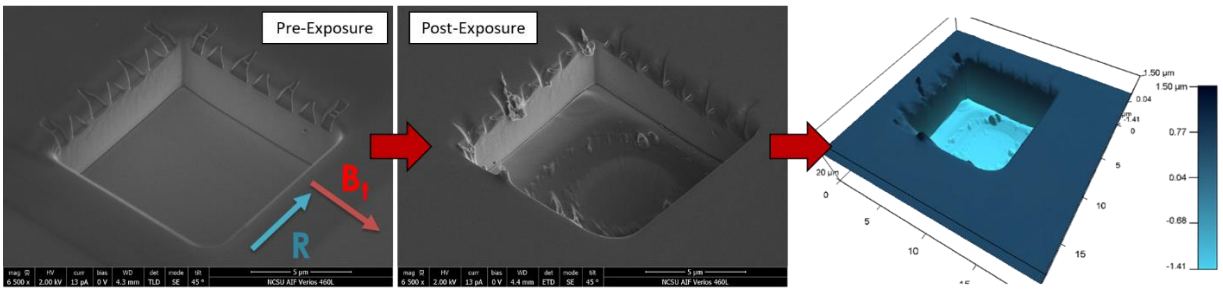


**Figure 6.3** - Example of a 10 x 10 μm square trench in SiC, approximately 4 μm deep, before and after plasma exposures on DIII-D. The floors of these square trenches are only partially shadowed from ion impacts, resulting in a distinct impact pattern. SEM images (Left) combined with 3D AFM data (Right) were used to estimate average ion impact angle based on this pattern.

Two methods were used to determine the heat flux on these sample surfaces during the experiment. The first used the 60° IRTV on DIII-D to measure temperature on graphite tiles. This time-dependent IR data was then used in the 2D code THEODOR [2] to estimate the heat flux on DiMES, assuming toroidal symmetry. The second method used the DiMES IRTV, which directly viewed the angled buttons to determine their surface temperature during plasma exposure. The corresponding heat flux on each individual button was then calculated based on the sample surface temperature rise. DiMES IRTV was calibrated for each material prior to the experiment by manually heating DiMES and fitting a function to the corresponding IR intensity, up to a temperature of 500 °C. Those fits are available in Appendix A.

To calculate the heat flux from the DiMES IRTV temperatures, the 1-D heat equation Eq 1 is solved for a 1-D slab geometry. The initial condition of a cold sample is specified in Eq 2, and the two boundary conditions for a finite slab of thickness x = d, where x = 0 represents the heated sample surface, are specified by Equations 3 and 4. As depicted in Figure 5.7 of Chapter 5, each DiMES sample rests on a ceramic insulator cap. There is lateral heat flow where the samples are pressed against the graphite DiMES cap, but for the 1-D approximation, insulated boundary conditions at x = d are acceptable.

$$Eq\ 1. \quad \frac{\partial T}{\partial t} = \frac{k}{C_p}\left(\frac{\partial^2 T}{\partial x^2}\right)$$

$$IC:\ Eq\ 2. \quad T = 0, at\ time\ t = 0, \quad for\ all\ x$$

$$BC:\ Eq\ 3. \quad -k\left(\frac{\partial T}{\partial x}\right) = F, at\ x = 0$$

$$BC:\ Eq\ 4.\quad -k\left(\frac{\partial T}{\partial x}\right)=0, at\ x=d$$

The solution for surface temperature T(x,t) is given in Equation 5.

$$Eq\ 5.\quad T(x,t)=\frac{Q''}{k}\sqrt{4\alpha t}\sum_{n=0}^{\infty}\left[-ierfc\left(\frac{2d(n+1)-x}{\sqrt{4\alpha t}}\right)-ierfc\left(\frac{2d(n)+x}{\sqrt{4\alpha t}}\right)\right]$$

Where $Q''=Heat\ Flux, k=thermal\ conductivity, C_p=specific\ heat\ capacity$, t = the time duration of the strike point heat load on the x = 0 surface, $\rho=density$, $\alpha=\frac{k}{\rho C_p}$, and the integral error function is defined as $ierfc(z)=z*\mathrm{erfc}(z)-\frac{e^{-z^2}}{\sqrt{\pi}}$, where $\mathrm{erfc}(z)=\int_z^{\infty}e^{-y^2}dy$. Evaluating the surface temperature at x = 0 using this model results in Eq 6.

$$Eq\ 6.\quad T(0,t)=\Delta T=\frac{Q''}{k}\sqrt{4\alpha t}\sum_{n=0}^{\infty}\left[-ierfc\left(\frac{2d(n+1)}{\sqrt{4\alpha t}}\right)-ierfc\left(\frac{2d(n)}{\sqrt{4\alpha t}}\right)\right]$$

By rearranging Eq. 6 to solve for heat flux Q'', the constant heat flux impinging on the DiMES sample surfaces can now be estimated using the IRTV temperature data. Average values of the temperature-dependent thermal properties $k$ and $C_p$ were used, based on material data and fits specified in Appendix A.

$$Eq\ 7.\quad Q''=\Delta Tk(4\alpha t)^{-\frac{1}{2}}\left(\sum_{n=0}^{\infty}\left[-ierfc\left(\frac{2d(n+1)}{\sqrt{4\alpha t}}\right)-ierfc\left(\frac{2d(n)}{\sqrt{4\alpha t}}\right)\right]\right)^{-1}$$

The plasma exposures were a combination of L-mode and H-mode plasma discharges due to difficulties maintaining L-mode during forward $B_t$ conditions. Samples were exposed to 7 discharges, summing to ~16 seconds of total plasma exposure. Average values of electron density $n_e$ and electron temperature $T_e$ were 1-2e$^{19}$ m$^{-3}$ and 20 – 40 eV, respectively, measured by Langmuir probes toroidally downstream at the same radial location as DiMES. ELMs were present during the H-mode discharges, which did affect the accuracy/error bars of the calculated average heat flux values for each shot. All DiMES samples were thermally insulated during plasma exposure but equilibrated with the DiMES holder in between plasma shots. The 60° IRTV gave an average heat flux measurement of ~0.5 MW/m$^2$ for flush sample surfaces, which would correspond to ~5.5 MW/m2 on the angled DiMES samples. Heat flux values measured on each individual sample by the DiMES IRTV are the heat fluxes reported in Section 3. These are localized measurements taken on 1mm$^2$ sections where each micro-trench is located. Example temperature

data from the DiMES IRTV, which is used to calculate the corresponding heat flux, is shown in Figure 6.4 for SiC. It highlights the differences in temperature rise between the L-mode exposures without ELMs and the H-mode exposures with ELMs.

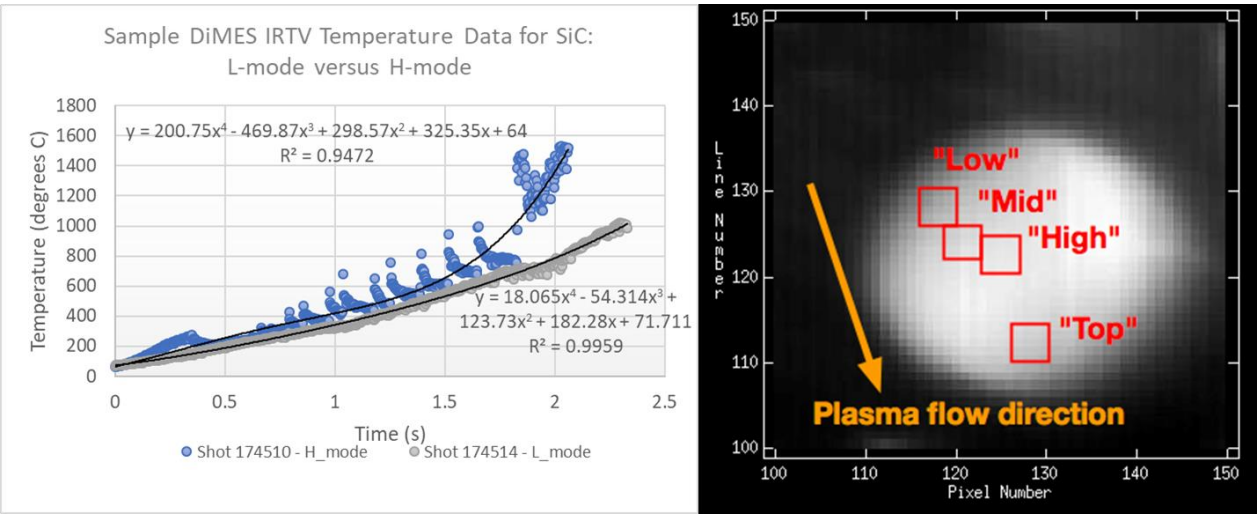


**Figure 6.4** – (Left) Example temperature data from the DiMES IRTV for sample SiC-1. The plot includes two shots, one L-mode and one H-mode, and corresponding polynomial fits used to calculate the heat flux. The data for both shots is taken at the same micro-trench location on SiC-1. (Right) Example intensity plot from the DiMES IRTV, zoomed in on one DiMES sample. The red squares indicate ~1mm$^2$ sampling areas that correspond to some of the micro-trench locations.

### 6.1.2 – Micro-trench Erosion Rates

Erosion rate results for the β-3C SiC and $Ti_3SiC_2$ are summarized in Figure 6.5. The FIB micro-trench technique worked well for the SiC samples, which survived average heat fluxes of 5 – 10 MW/m$^2$ over 16 seconds of plasma discharges. Maximum surface temperatures approached ~1600 °C. Total, net erosion thickness losses for the various micro-trench locations ranged from 0.42 – 1.16 μm, translating to average erosion rates of 27 – 73 nm/s. An increasing, possibly linear trend was expected for the relationship between net erosion rate and heat flux in Figure 6.5, since a higher heat flux inherently represents an increase in particle flux for the same average particle energy. An increasing, but split dataset is observed that is difficult to interpret and requires thorough discussion.

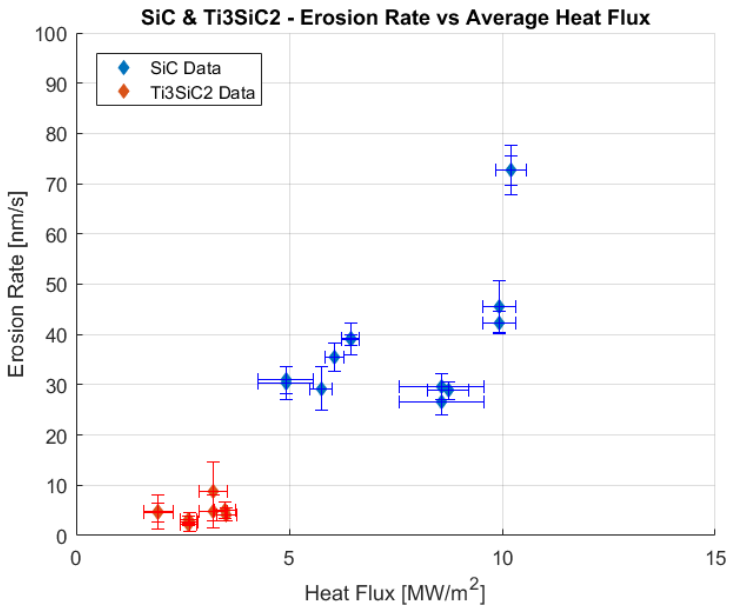


**Figure 6.5** – Average erosion rate versus average heat flux for angled SiC samples and angled $Ti_3SiC_2$ samples, from FIB micro-trench measurements and IR camera data. The SiC data exhibits a distinct increasing but split trend, while the $Ti_3SiC_2$ data shows no statistically significant trend for the heat flux range measured.

$Ti_3SiC_2$ samples survived average heat fluxes of 2 – 3.5 MW/m$^2$ over 16 seconds of plasma discharges. Maximum surface temperatures approached ~800 °C. Due to their location on DiMES, such a reduced heat flux could be attributed to shadowing of these samples by the angled SiC samples, which was observed in the IR data. Consequently, total net erosion thickness loss measurements ranged from 0 –140 nm, most of which were the same order of magnitude of the standard deviation of the dataset, ~30-50 nm. Corresponding erosion rates were 0 – 9 nm/s. Due to the low magnitudes of erosion thickness loss, the FIB micro-trench technique was not as successful; a statistically significant linear trend or split of linear trends cannot be discerned from the dataset. In Figure 6.5, the MAX phase erosion rates do somewhat follow the SiC data when linearly extrapolated to a lower heat flux. Thus, it could be implied that $Ti_3SiC_2$ would erode at roughly the same rate as the SiC, but it is difficult to conclude given the spread in the $Ti_3SiC_2$ data.

For the SiC samples, it was expected that the multiple micro-trenches along the angled sample surfaces would experience roughly the same heat flux. What is instead observed in the IR data is a gradual increase in heat flux as the micro-trenches increase in height (as depicted in the upper right image of Figure 6.1). This trend is highlighted in Figure 6.6. It was also expected that

the heat fluxes along the raised but flat portion of the angled samples would match the heat fluxes of other, completely flush sample surfaces. Instead, these locations also experienced a ~10x increased heat flux, although the magnitudes were lower than the angled sample results. It is possible that this phenomenon is due to a changing plasma sheath along the sample surface. The micro-trenches are only ~4 μm deep, smaller than typical Debye sheaths and orders of magnitude smaller than ~mm magnetic pre-sheaths. However, the entire sample surface does protrude 1.2 mm up into the plasma. The heat flux values reported in Figure 6.5 are the average value across the 7 mixed L-mode and H-mode exposures, with variations due to the mixed modes and ELMs accounted for by the horizontal error bars. Taking the precision of the heat flux calculations into account, the increase in heat flux along the angled sample surfaces does appear statistically significant. Although unexpected, this observation was beneficial in that it allowed for more data points at varying heat fluxes than originally expected for the experiment.

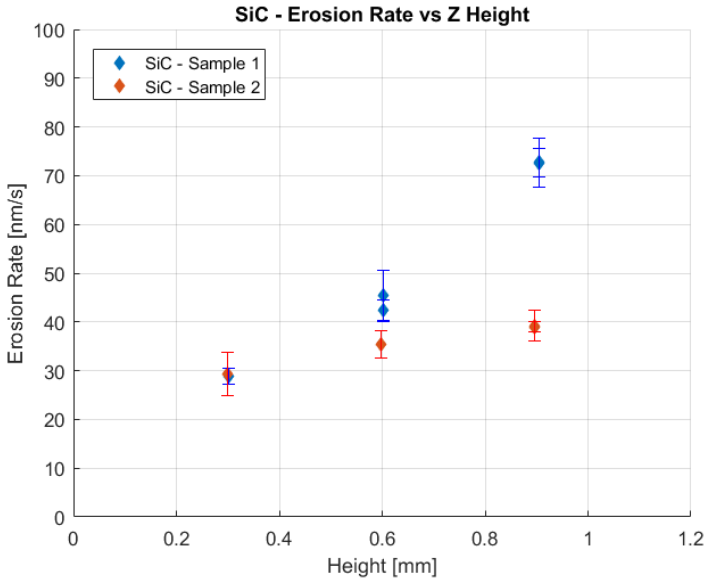


**Figure 6.6** – Average erosion rate of a SiC micro-trench versus the average height location, in mm, of each micro-trench.

Secondly, the apparent split in the SiC data is unexpected. The dataset is comprised of micro-trench results from two separate SiC DiMES samples, as highlighted in Figure 6.5 and 6.6. SiC sample 1 (SiC-1) was closer to the average strike point location, at R-$R_{sep}$ = 0.5 cm, while sample 2 (SiC-2) was farther away at R-$R_{sep}$ = 1.5 cm. With the samples being the same material,

the cause may lie in the heat flux variable. There are errors present in the heat flux analysis, specifically due to the averaging of mixed exposure types and calibration limitations. Accounting for these errors, along with error bars for the FIB micro-trench technique, the measurements are still precise enough to assert that the split trend is real. As for how to quantify the split, increasing trends, it is not clear what model is most appropriate. Figure 6.7 displays the SiC data from Figure 6.5, distinguishing which samples each micro-trench was located on, and includes two methods of interpretation. The left image shows plausible linear trends that can be calculated irrespective of the sample locations, with the following fits: $y = 8.44x - 14.3$ ($R^2 = 0.977$) and $y = 11.8x - 73.2$ ($R^2 = 0.963$). The right image shows plausible increasing trends if fits are based solely on the sample location, i.e. SiC-1 vs SiC-2: $y = 5.91x$ ($R^2 = 0.70$) for SiC-2 and $y = 0.961*\exp(0.4*x)$ ($R^2 = 0.986$) for SiC-1.

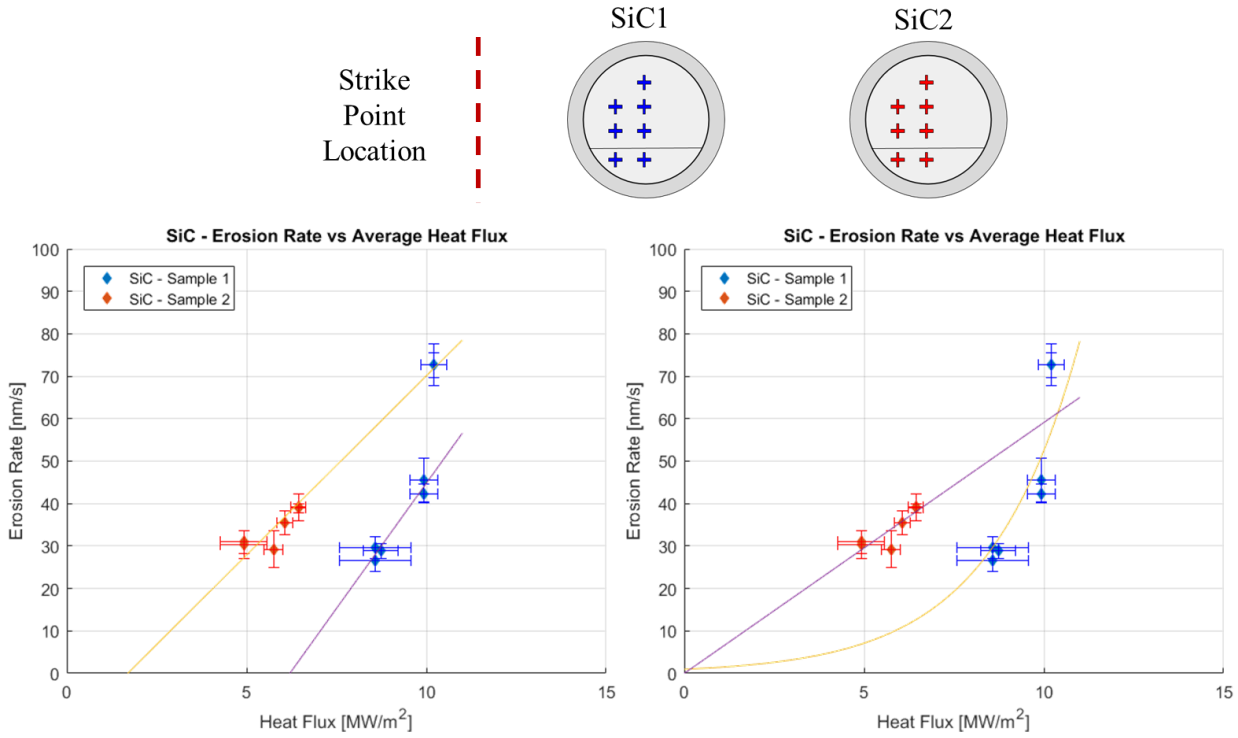


**Figure 6.7** - Average erosion rate versus average heat flux for angled SiC samples from FIB micro-trench measurements and IR camera data, distinguished by DiMES sample. (Left) SiC data with split linear trendlines irrespective of sample. (Right) The same SiC data, but with a combination of linear and exponential trendlines for each particular SiC sample. (Top) Designation of micro-trench and sample locations wrt the plasma strike point.

The effective plasma heat flux takes into account the energy and density of the plasma, which is comprised of varying masses and charge states. Individual ion properties such as energy and density are arguably more important to consider in a sputtering-dominated erosion regime. A difference in these ion parameters in the strike point/scrape-off-layer could cause the observed split in erosion rates at localized locations across the two SiC samples. For example, there could be a substantially higher percentage of impurities in the scrape-off-layer farther away from the strike point, which would increase sputter yields due to impact from more massive ions. Radial variations in impurity concentration have been observed on DIII-D both experimentally and computationally [3]. That explanation could account for lower erosion rates for sample 1, which was closer to the strike point, despite a higher overall heat flux. It could also explain the different heat flux thresholds implied by the two linear trends. Either way, results imply that there are radial and axial variations in erosion physics that have been captured by the angled, micro-trenched SiC samples.

### 6.1.3 – Average Ion Impact Angles

Clear ion impact patterns were visible within the four square micro-trenches of the SiC samples. Micro-trenches in the $Ti_3SiC_2$ samples exhibited uneven milling during the FIB manufacturing process, resulting in rough floors unsuitable for viewing impact patterns. SEM images of the impact patterns combined with AFM analysis, both before and after plasma exposure, allowed for calculations of the average ion impact angle as a function of radial and vertical location.

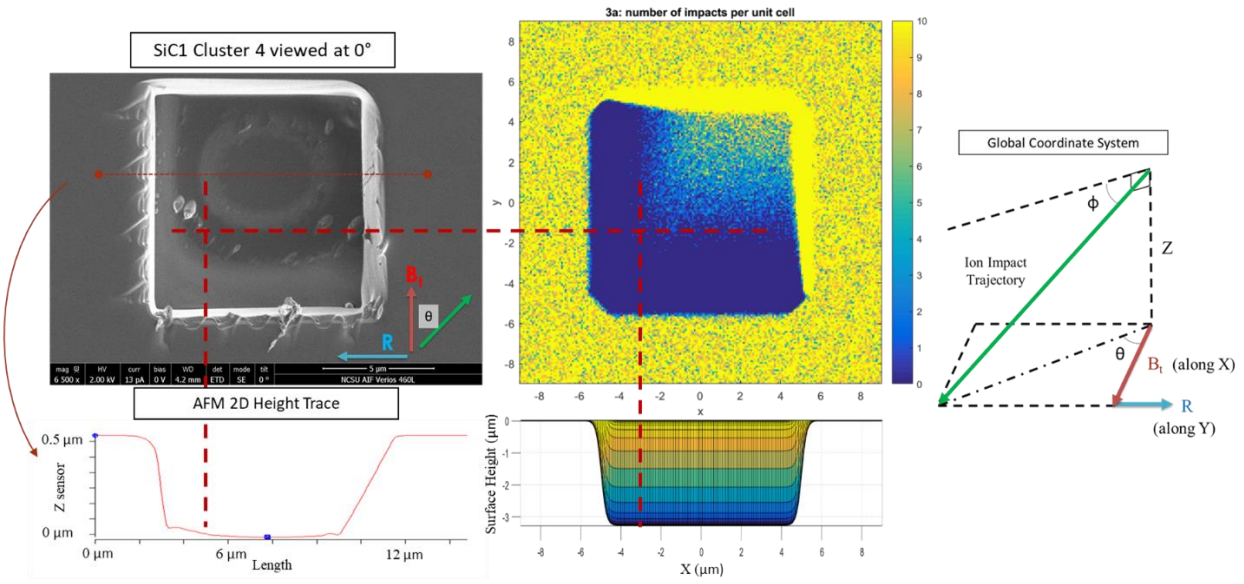


**Figure 6.8** – Ion impact patterns. (Left) Top-down view of a 10 x 10 µm square trench, aligned with 2D AFM height data. (Middle) Example results of Monte-Carlo simulations used to predict impact pattern within a 10 x 10 µm square trench. Represents the number of impacts per unit cell. (Right) Coordinate system for particle impact angle. Green arrow indicates ion impact vector.

3D AFM maps (Figure 6.3) and 2D AFM line traces (Figure 6.8) confirmed the interpretation of SEM imaging and allowed for calculations of the average ion impact patterns. The impact patterns matched the simulation predictions that accounted for divertor ion impact angle distribution data. The results are summarized in Table 6.1. Measurements indicated ion impact angles from $\theta = 24^o - 34^o$ with respect to $B_t$ and $\phi = 51.5^o - 55^o$ below the surface normal. The measurements are for the global coordinate system and are corrected for both the flat and angled trench surfaces. Each micro-trench exhibited a white band around a flat, eroded area on the trench floor. The middle of this white band is used to calculate the values for $\theta$ and $\phi$. The band width is designated as the +/- values in Table 6.1, representing a spread in the ion trajectories that just make it over the shadowed trench wall and impact the floor at slightly different locations. It was also observed that significant deposition of eroded material did accumulate in the shadowed floor areas 'upstream' of this white band, as seen in the 2D AFM height retrace in Figure 6.8.

Table 6.1 – Average Ion Impact Angle Estimations

| Sample Name | $R - R_{sep}$ (mm) | Height (mm) | θ | ϕ |
|---|---|---|---|---|
| SiC1 C2 | 5 | 0.6 | 34° ± 2° | 55° ± 3° |
| SiC1 C4 | 5 | 1.2 | 32.5° ± 2.5° | 54° ± 3° |
| SiC2 C5 | 14 | 0.6 | 24° ± 2° | 51.5° ± 4° |
| SiC2 C4 | 15 | 1.2 | 27.5° ± 2.5° | 52.5° ± 2.5° |

The results in Table 6.1 imply that θ and ϕ are dependent on the height and distance from the plasma strike point, supporting the observations in Section 3.1. For example, trenches closer to the strike point (on sample SiC-1) showed higher values for ϕ and higher values for θ. These variations in impact angles could explain the differences in heat flux observed on the angled faces. If the sheath is in fact altered by the ~1mm height increase along the angled surfaces, it would affect the density and energy of particles impacting the surface. A corresponding difference in average impact angle as a function of location would be expected. Post-experiment Monte-Carlo simulations were performed to find the best match to experimentally observed data (Figure 6.8). It was determined that ion angle distribution functions for an 88° B-field angle from Borodkina [4] (using the source's terminology for B) best match the experimental observations. This result is most closely matched in Khaziev [5] by their 85° B-field distribution. The 88° Borodkina distribution match agrees well with the average measured B-field at the samples during the 7 DIII-D exposures, which was 88.4° – 88.7° from perpendicular (1.3° – 1.6° from parallel).

### 6.1.4 – Summary

MAX Phase ceramic $Ti_3SiC_2$ was exposed for the first time to a tokamak plasma alongside high-purity β-3C SiC. Samples survived average heat fluxes of 2 – 10 MW/m$^2$ over 16 seconds of plasma discharges with no visible macroscopic damage. SiC samples experienced 5 – 10 MW/m$^2$, resulting in average erosion rates of 27 – 73 nm/s. A linear, but split, trend was observed for the erosion rate of SiC versus heat flux. The FIB micro-trench technique was successful in measuring the magnitudes of total erosion thickness loss. $Ti_3SiC_2$ samples saw lower than expected heat fluxes of 2 – 3.5 MW/m$^2$, potentially due to shadowing by upstream SiC angled samples.

Consequently, erosion rates ranged from 0 – 9 nm/s, with magnitudes on the same order of the dataset's standard deviations. A statistically significant linear trend could not be discerned from the data. Due to the low magnitudes of total erosion thickness loss, the FIB micro-trench technique was not as successful for the MAX phase samples. Measuring the average ion impact angle was achieved using both SEM imaging and AFM height retrace data. Erosion patterns matched those expected from simulations and are consistent with angle distributions reported in the literature, in particular reference [4]. Measurements ranged from $\theta = 24^{o}$ - $34^{o}$ with respect to $B_t$ and $\phi = 51.5^{o}$ - $55^{o}$ below the surface normal. These results imply that $\theta$ and $\phi$ are dependent on the height and distance from the plasma strike point, correlating with the explanations for observed local changes in heat flux across individual angled samples.

The FIB micro-trench technique's effectiveness was successfully demonstrated. This technique offers researchers another tool to utilize in future plasma-material interaction experiments, with room to refine and customize for other specialized studies. For example, more complex micro-trench geometries could be beneficial in dedicated ion impact angle studies on divertor or mid-plane targets. Both SiC and $Ti_3SiC_2$ survived the multiple DIII-D exposures with no discernable macroscopic damage, i.e. cracks or fracture, demonstrating their robustness as possible PFMs with manageable erosion from physical sputtering. Promising results from the complimentary electrothermal plasma experiment will further highlight the importance of exploring alternative PFM candidates such as SiC and MAX phase ceramics for use in future large-scale fusion reactors.

## 6.2 Electrothermal Plasma Source Experiment

### 6.2.1 Experiment Details

The final material exposure experiment on the ET source was conducted over the course of two days, with the source prepared and fired as described in Section 5.3.2. A helium backfill gas was used at 40-60 Torr before each discharge and a Lexan liner was used for all shots. The 1.0 ms pulse-forming network was implemented for every shot in order to produce consistent, ELM-relevant pulse lengths and energy magnitudes.

The objective was to expose various PFM samples to the ET source plasma jet in order to measure each PFM's erosion rate as a function of the impinging heat flux. The independent variables controlled in the experiment were: 1) the plasma-facing material sample, and 2) the ΔV across the capacitor, which determined the current magnitude of each plasma discharge and by consequence the impacting heat flux. The measured dependent variables were: 1) The current and voltage data from each ET discharge, 2) IR temperature data on the sample and sample holder, and 3) the total erosion of each FIB micro-trench, measured post-mortem.

All three PFMs of interest, $Ti_3SiC_2$, $Ti_2AlC$, and SiC, were exposed along with samples of silicon and W that were also available. Samples were manufactured at the same time as those for the DIII-D experiment, from the exact same material sources. They all have a cylindrical geometry with a flat, 6 mm diameter surface exposed to the ET plasma. Some were thin, 1.6 mm thick samples while others were of the larger 6 mm thick geometry. This dimensional difference was solely the consequence of using remaining samples not exposed in the DIII-D experiment. A custom carbon steel holder was manufactured to hold the samples within the ET source vacuum chamber, exposing only the circular 6mm diameter surface to incoming plasma flux. A schematic of the sample dimensions is shown in Figure 6.9 alongside photos of the actual samples.

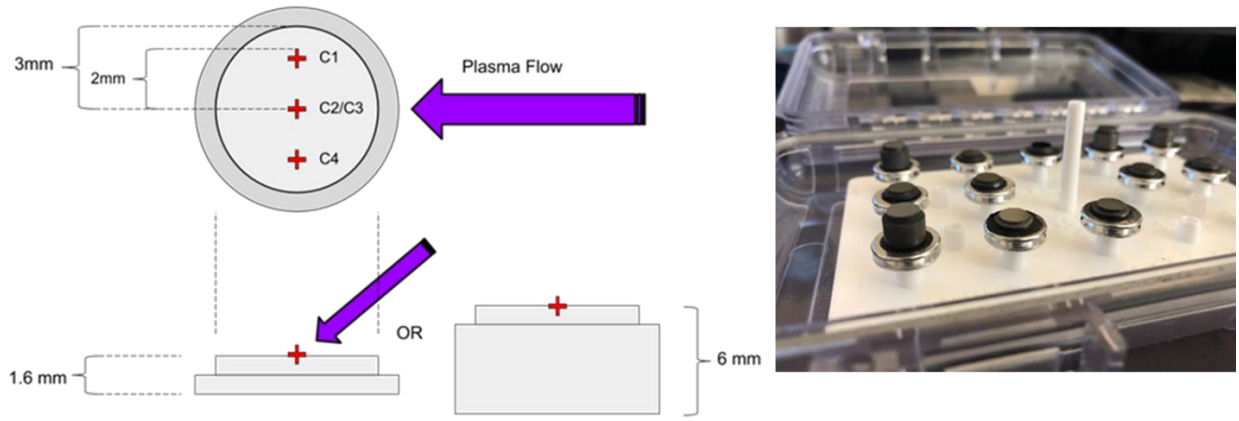


**Figure 6.9** – (Left) ET sample dimensions. The red crosshairs indicate the locations of specific micro-trench clusters, labeled C1 – C4. (Right) Photograph of material samples, resting on top of microscope stubs within a plastic container box.

The $Ti_3SiC_2$, $Ti_2AlC$, and SiC samples were polished at ORNL using colloidal silica (1-5 nm particle size) to a mirror finish. The silicon and W samples were sent to Sandia Livermore to be prepared and polished to a mirror finish "but with an unknown polishing method". After being manufactured and polished, each sample was cleaned via an ultrasonic cleaner with acetone, ethanol, and methanol (~2 minutes per solution), after which they were plasma cleaned via an Ar-O plasma for 5-10 minutes. Only after this cleaning process were the samples loaded into a FIB for micro-trench manufacturing and characterization.

The FIB micro-trench design for the ET samples is slightly different than that used in Section 6.1. Multiple preliminary exposures were performed to help discern the appropriate micro-trench geometries and cleaning methods. The final geometry iteration is depicted in Figure 6.10, a 10 μm wide x 12 μm long trench, at least 10 μm deep. Under ~GW/$m^2$ heat fluxes, it was expected that microns of material may be eroded from some sample surfaces, especially for multi-shot exposures. Test exposures on aluminum and stainless-steel samples at lower heat flux values confirmed this expectation, with erosion and melt layers on the order of microns. Therefore, a micro-trench geometry was chosen to view at least 10 μm deep into the sample surfaces. The micro-trench length required to take suitable 52° angled images was then set to 12 μm. For the width of the micro-trench wall with fiducial depth markings, a longer wall allows more area for multiple erosion/depth measurements. The limiting factor is then the increased time to manufacture larger trenches. For the purposes of manufacturing time, the width was then set to 10 μm. Micro-trenches were placed in three distinct locations 2mm apart from one another, as seen in the left side of Figure 6.9. It was thought that the micro-trenches located radially outward would experience a lower heat flux than those directly at the center, where the plasma jet would presumably have the hardest impact. If so, this choice would provide another method of gaining erosion values at varying heat flux magnitudes, better highlighting the relationship between erosion rate and heat flux.

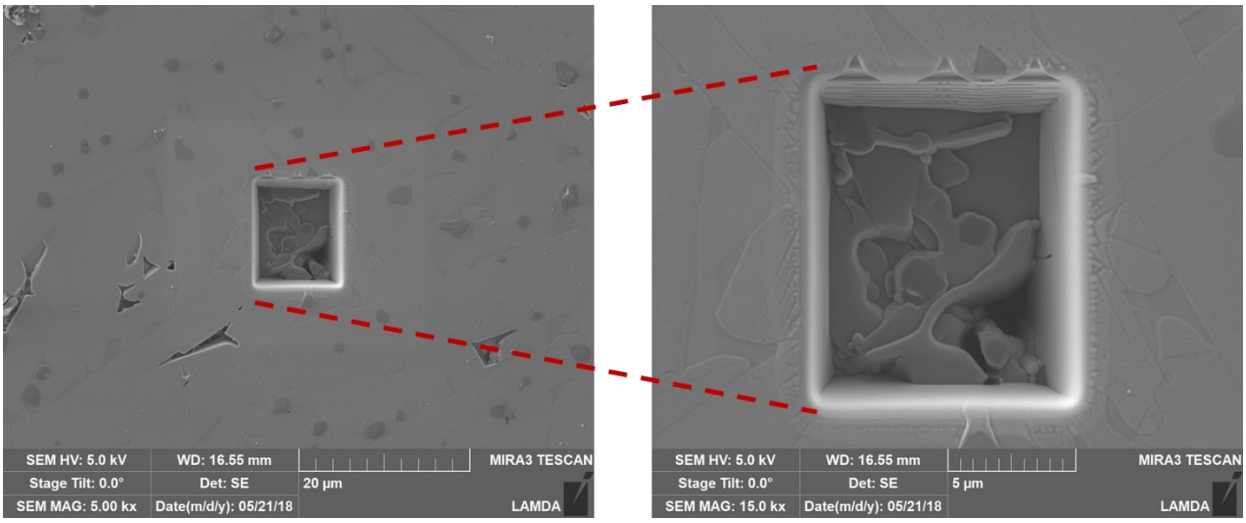


**Figure 6.10** – An example 10 µm x 12 µm FIB micro-trench, approximately 10 µm deep, in a sample of $Ti_2AlC$. Both images are 0°, top-down SEM images of the same micro-trench, TAC5 C4.

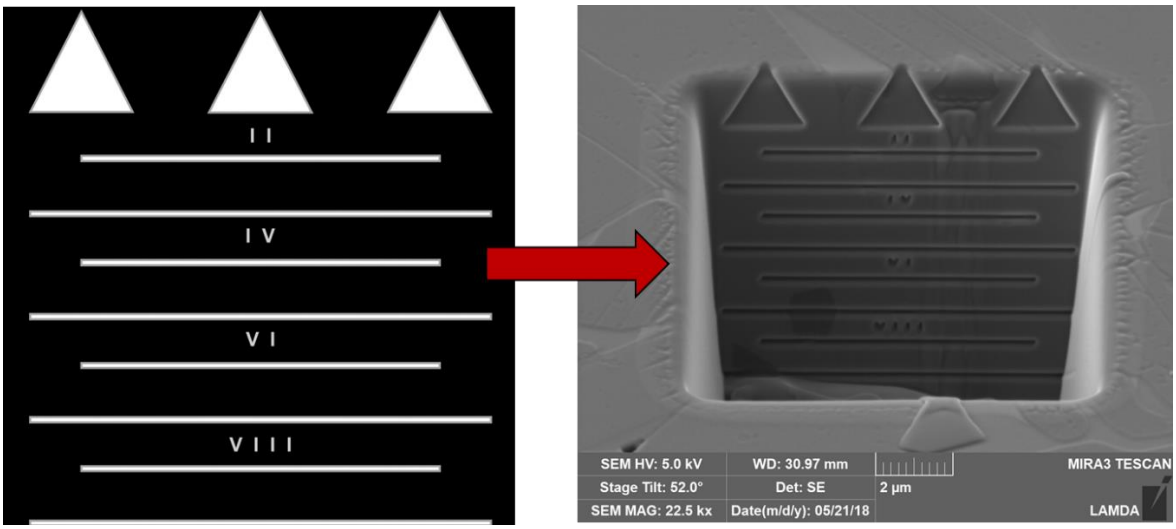


**Figure 6.11** – (Left) The FIB bitmap image used to mark the depth within the micro-trench, up to 10 µm. The triangles are 2 µm long, and each line is spaced 1 µm apart. (Right) A 52° angle SEM image of the same micro-trench in Figure 6.8, displaying the bitmap depth markings etched into the shadowed micro-trench wall.

To increase the accuracy of the depth measurement technique described in Section 5.1, a bitmap image was created to FIB into the shadowed micro-trench wall. The finalized bitmap image is displayed in Figure 6.11 along with an example of its implementation into a micro-trench wall.

Triangular shapes were again utilized to account for rounding effects on the trench edges. Lines were then added to extend the measurement capabilities up to 10 μm deep. Based on preliminary experiments where severe erosion took place, Roman numeral markings were included as well, for cases where some markings at the top and/or bottom become indiscernible and it's necessary to locally identify each line. During FIB manufacturing, the bitmap is scaled such that each triangle is a programmed 2 μm in depth, while each line is spaced 1 μm apart, totaling to a marked depth of 10 μm. The scaling accounts for the 38° FIB milling angle and represents a 10 μm deep image milled onto a perfectly vertical wall. As discussed in Section 5.1, the micro-trench walls are imperfectly milled, with noticeable rounding of the top edges and slight sloping of the walls. This characteristic causes the depth markings to be milled at slightly more shallow depths than desired. Thus, the two-image measurement technique described in 5.1 must be utilized for accurate depth calculations, rather than relying solely on the fiducial markings.

Preliminary experiment also provided insight into proper cleaning methods for experiments post-exposure. Using a Lexan liner for the ET shots results in a large amount of hydrocarbon ash being deposited throughout the ET vacuum chamber, especially on the sample surfaces. After the current pulse ends, a wave of cold hydrocarbons impacts and deposits on the eroded material surface, filling the micro-trenches and covering any viewable erosion patterns. However, despite the nature of these exposures, the hydrocarbon ash is relatively easy to clean without damaging the sample surface. Post-exposure, each sample was again placed in an ultrasonic cleaner filled with acetone, then ethanol, then methanol for ~2 minutes each, ending with ~5 minutes in an Ar-O plasma cleaner. Deep micro-trenches allowed for more efficient cleaning of the hydrocarbon backfill, also motivating the final, deep geometry.

A total of 15 material samples were prepared for the ET experiment. A shot plan was developed to expose each material to 2-3 different heat flux values. In order to generate the highest possible heat fluxes for the given ET setup (using the 1 ms pulse-forming network), the stored $\Delta V$ was varied between 6 and 7 kV. For the 3 PFMs of interest, at least one sample was also exposed to multiple shots. From preliminary experiments it was seen that multiple shots generated more uniform erosion on sample surfaces. The implemented shot plan is displayed in Table 6.2. Most shots were acquired successfully, with only one sample experiencing too many misfires to be usable.

Table 6.2 – Final ET Experiment Shot Plan

| Sample Name | Stored ΔV | # of Shots | Successful? |
|---|---|---|---|
| SiC8 | 6 kV | 5 | No |
| SiC9 | 6 kV | 1 | Yes |
| SiC10 | 6 kV | 5 | 1 shot @ 5 kV |
| SiC11 | 7 kV | 1 | Misfire, then 7 kV |
| TSC5 | 6 kV | 5 | Yes |
| TSC6 | 7 kV | 1 | Yes |
| TSC7 | 6 kV | 1 | Yes |
| TAC4 | 6 kV | 1 | Yes |
| TAC5 | 6 kV | 5 | Yes |
| TAC6 | 6.5 kV | 1 | Yes |
| TAC7 | 7 kV | 1 | Misfire @ 5.5 kV, then 7 kV |
| W1 | 6 kV | 1 | Yes |
| W2 | 6 kV | 5 | Yes |
| Si3 | 6 kV | 1 | Yes |
| Si5 | 6 kV | 5 | Yes |

### 6.2.2 Heat Flux Analysis

A FLIR IR camera was used to collect temperature data of the sample surface during exposures. As depicted in Figure 5.17 of Section 5.3.2, the IR camera viewed the sample holder through a small sapphire window, with the sample oriented at about a 45° angle. The camera was operated at the highest possible frame rate of 1337 Hz, allowing for the capture of 2-3 frames where the plasma jet visibly strikes the target. One important limitation on the IR camera was the available filter for the lens, which limits the temperature range the camera can calculate based on the viewed intensity. The highest-rated filter available at ORNL allowed for a 650 – 1500 °C temperature range. This limitation was much lower than desired, as surface temperatures over 3000 °C were needed for materials such as SiC and W. The FLIR analysis software accounts for the filter limitations, and for a given surface emissivity will consider the calculated temperature data "saturated" if it exceeds 1500 °C. However, by artificially manipulating the programmed emissivity used by the software, non-saturated temperature data could be obtained by the IR camera. Then, the temperature data could be re-calculated using the correct emissivity value. This unsaturated data is then used to directly calculate the heat flux values in a given 2-D thermal image.

The IR camera directly produces a 2-D matrix of temperature data as one thermal image frame, where multiple frames are used to then construct a video of the plasma exposure at 1337 Hz. The procedure used for converting the 2-D thermal data for each image into a heat flux map is as follows. Firstly, the FLIR software uses the Stefan-Boltzmann Law to calculate the surface temperature, T, for a programmed emissivity value, $\varepsilon_p$, and recorded IR light intensity, I, as in Equation 8.

$$Eq.8 \quad I = \varepsilon_p \sigma T^4$$

where σ is the Stefan-Boltzmann constant, $5.67 * 10^{-8}\ Wm^{-2}K^{-4}$. The acquired thermal data often had to be taken at an inflated emissivity value to avoid saturation by the FLIR software. Correcting this temperature data required the measurement of each PFM material's emissivity, which was performed using the IR camera (with no filter), a hot plate, and a thermocouple directly attached to the hot plate surface. Samples were simultaneously heated on the hot plate to ~280 °C, during which the emissivity programmed into the IR data was actively manipulated until the calculated temperature matched the sample's surface temperature. The results are summarized in Table 6.3.

Table 6.3 – Summary of Measured Sample Emissivities

| MATERIAL | EMISSIVITY (FRACTION) |
|---|---|
| **SIC** | 0.34 |
| **$Ti_3SiC_2$** | 0.17 |
| **$Ti_2ALC$** | 0.19 |
| **SI** | 0.27 |
| **W** | 0.15 |

These emissivity values are lower than those typically reported in the literature for the given materials [6]. This discrepancy is due to the fine polish of each sample surface, which drastically increases the surface reflectivity and hence decreases the emissivity. Two important assumptions should be noted regarding the use of these emissivity values. 1) Emissivity is assumed to not vary significantly with temperature, and 2) emissivity is assumed to not vary during the plasma exposure. In general, a material's emissivity is dependent on surface temperature, the specific infrared wavelength being measured, and the surface geometry (roughness, curvature,

etc.). The dynamic erosion, surface roughening, and hydrocarbon deposition during the actual plasma exposure, not to mention the sharp temperature increases, affect the surface emissivity in a complex fashion that was impossible to quantify during the experiment. Time and equipment were not available to generate the required material-specific emissivity vs. temperature curves, so a static emissivity value during the first 1-2 frames of IR data was assumed. The diagram in Figure 6.12 highlights the optical physics that are considered for the emissivity/temperature correction.

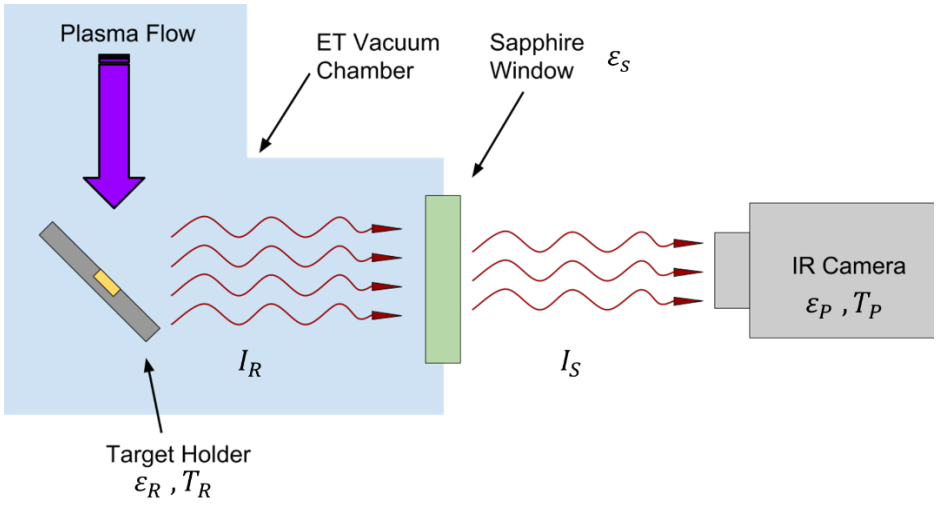


**Figure 6.12** – Diagram of ET sample target depicting the transport of emitted IR radiation to the IR camera

The IR camera sees an IR intensity $I_S$ that is affected by both the sample emissivity $\varepsilon_R$ and the transmission efficiency $\varepsilon_S$. It then calculates a surface temperature $T_P$ based off of $I_S$ and the programmed emissivity $\varepsilon_P$. The real surface temperature $T_R$ is calculated by defining the Stefan-Boltzmann law for the target (Eq 9) and for the calculated IR data (Eq 10), and by relating $I_S$ to $I_R$ via the window transmission efficiency (Eq 11).

$$Eq\ 9. \quad I_R = \varepsilon_R \sigma T_R^4$$

$$Eq\ 10. \quad I_S = \varepsilon_P \sigma T_P^4$$

$$Eq\ 11. \quad I_S = I_R \varepsilon_S$$

Solving this system of equations for $T_R$ yields Equation 12, which is applied to the IR temperature data to give the correct 2-D surface temperature map.

$$Eq\ 12. \quad T_R = \left(\frac{\varepsilon_P}{\varepsilon_R \varepsilon_S}\right)^{\frac{1}{4}} T_P$$

After the emissivity correction, one more correction is applied to the temperature data before calculating the heat flux. Although the IR temperature data became saturated during peak heat flux using the correct emissivity ($\varepsilon_P = \varepsilon_R$), later data frames taken as the sample cools sometimes yielded unsaturated data. Equation 5 was tested in these cases by comparing $T_R$ calculations using both the correct emissivity and the $\varepsilon_P$ required for the peak heat flux frames. What is observed is a 5-20% difference between the calculated $T_R$ values. Upon further analysis, it was clear that as the difference between $\varepsilon_P$ and $\varepsilon_R$ increased, the error between calculated $T_R$ values linearly increased according to Equation 13.

$$Eq\ 13. \quad F = 0.3669\,\Delta\varepsilon + 1.0332$$

Where $\Delta\varepsilon = \varepsilon_P - \varepsilon_R$ and F is the ratio of $T_R$ calculated when $\varepsilon_P = \varepsilon_R$ to the $T_R$ calculated with the inflated $\varepsilon_P$. This 5-20% difference in values is inherent to the FLIR IR software calculations and may represent some unknown physics calculations not considered in Equation 12. In order to account for this error for the high heat flux datasets (when an inflated $\varepsilon_P$ is necessary to use), this emissivity correction factor F is calculated from Equation 13 and applied to Equation 12, resulting in Equation 14. The 2-D heat flux data can now be generated using the $T_R$ data from Equation 14.

$$Eq\ 14. \quad T_R = F\left(\frac{\varepsilon_P}{\varepsilon_R \varepsilon_S}\right)^{\frac{1}{4}} T_P$$

To calculate the heat flux, the 1-D heat equation Eq 1 is again solved for a 1-D slab geometry. The initial condition of a cold sample is specified in Eq 2, and the two boundary conditions for a semi-infinite slab, where x = 0 represents the heated sample surface, are specified by Eqs 15 and 16. Due to the short time span of the ET pulse, the penetration depth of the heat load into the sample surface should be smaller than the sample thickness, so the semi-infinite boundary condition approximation is appropriate and leads to a simpler solution for the ET experiment.

$$Eq\ 1. \quad \frac{\partial T}{\partial t} = \frac{k}{C_p}\left(\frac{\partial^2 T}{\partial x^2}\right)$$

$$IC{:}\ Eq\ 2. \quad T = 0\,,\ at\ time\ t = 0,\ for\ all\ x$$

$$BC{:}\ Eq\ 15. \quad -k\left(\frac{\partial T}{\partial x}\right) = F\,, at\ x = 0$$

$$BC:\ Eq\ 16.\quad -k\left(\frac{\partial T}{\partial x}\right) = 0, at\ x = \infty$$

The solution for surface temperature T(x,t) is given in Equation 17.

$$Eq\ 17.\quad T(x,t) = \frac{Q''}{k}\sqrt{4\alpha t}\left[-ierfc\left(\frac{x}{\sqrt{4\alpha t}}\right)\right]$$

Where $Q'' = Heat\ Flux, k = thermal\ conductivity, C_p = specific\ heat\ capacity$, t = the time duration of the ET heat load on the x = 0 surface, $\rho = density$, $\alpha = \frac{k}{\rho C_p}$, and the integral error function is defined as $ierfc(z) = z * \mathrm{erfc}(z) - \frac{e^{-z^2}}{\sqrt{\pi}}$, where $\mathrm{erfc}(z) = \int_z^\infty e^{-y^2}dy$. Evaluating the surface temperature at x = 0 using this model results in Eq 18.

$$Eq\ 18.\quad T(0,t) = T_R = \frac{Q''}{k}\sqrt{\frac{4\alpha t}{\pi}}$$

Rearranging Eq 18 to solve for heat flux Q'', the constant heat flux impinging on the ET samples can be estimated using the IR temperature data as shown in Eq.19.

$$Eq\ 19.\quad Q'' = T_R k\left(\frac{4\alpha t}{\pi}\right)^{-\frac{1}{2}}$$

Figure 6.13 shows an example photo of a material sample housed in the target holder after plasma exposure. The polished, circular PFM sample surface is flush with the carbon-steel holder's surface. The four holes surrounding the sample are screw holes for a back plate which holds the PFM sample in place. The impact and flow of the plasma jet onto the holder can be inferred from the deposition pattern of hydrocarbon ash. Multiple test shots were performed to ensure the impact center aligned as close as possible with the center of the PFM samples.

**Figure 6.13** – Post-exposure image of the ET target holder with a SiC sample, uncleaned. The ET plasma jet impacted this holder at about 45° from right to left, which generated the deposition pattern around the sample and the surrounding empty holes.

Since the PFM sample possesses different emissivity values and thermal properties than the carbon steel holder, the sample was usually discernable in the IR thermal data. The 4 screw holes were also usually visible, allowing for further certainty in determining the PFM sample location in the 2-D thermal maps. Figure 6.14 shows an example frame of IR thermal data ($T_R$) for a SiC sample exposure and the corresponding heat flux map (Q’’). Figure 6.15 shows a series of raw frames from the IR camera that depict the evolution of the plasma jet impact. As the plasma jet exits the ET source barrel on the right and travels left, it hits the target and sample at a 45° angle, heating the sample surface as the plasma jet spreads outwards due to the impact.

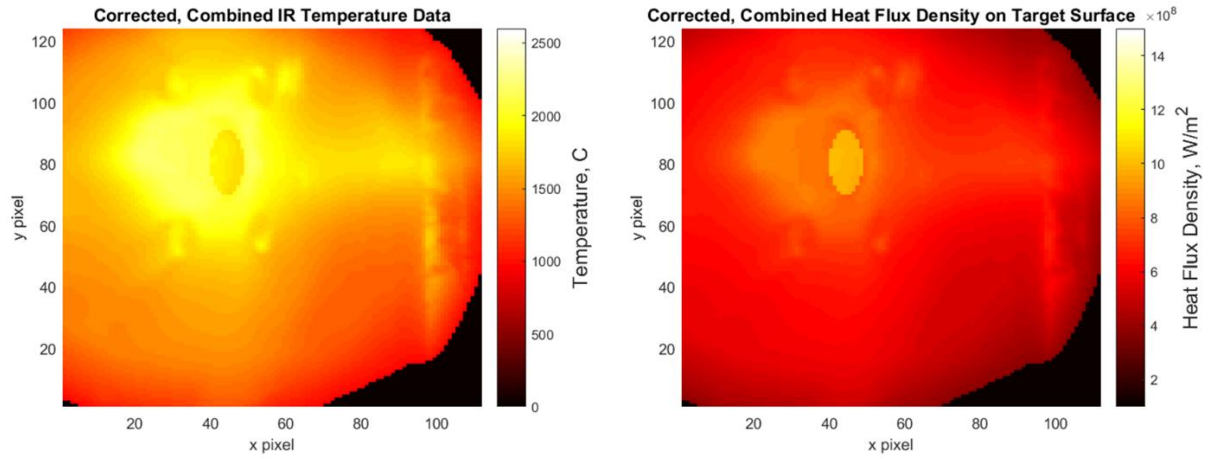


**Figure 6.14** – (Left). Temperature map from IR camera data for shot 58 on a SiC sample. This temperature map displays the emissivity-corrected temperatures ($T_R$), calculated separately for both the PFM sample and the carbon steel holder. (Right) Heat flux density calculated from the $T_R$ temperature map, calculated separately for the PFM sample and the carbon steel holder. The central temperature is ~1850 °C for the SiC sample, resulting in a corresponding heat flux calculation of ~1 GW/m$^2$.

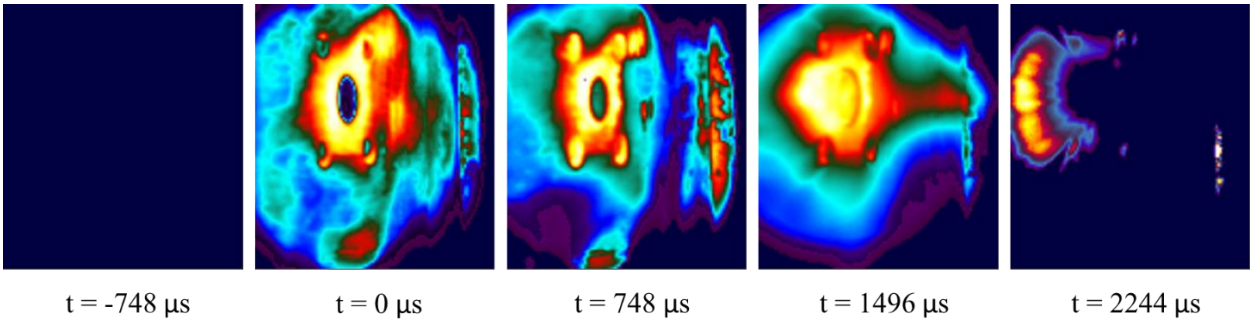


**Figure 6.15** – A time-lapse of raw IR temperature data frames for Shot 58 on a SiC sample. The plasma jet is shot from the ET source barrel on the right of each frame, travelling from right to left until impact is made on the angled target holder. A programmed emissivity $\varepsilon_P$ of 0.55 is used for these frames.

Ideally, IR camera data would have been available for each shot of the ET experiment, providing individual heat flux data for each exposure of each PFM sample. At the start of the experiment, hydrocarbon ash generated by the Lexan liner began to cover the inside of the sapphire window. This coating significantly reduced the IR signal measured by the IR camera, resulting in

smeared or blank temperature datasets that were deemed unusable. Over 2/3 of the PFM samples had already been exposed by the time this problem was treated. Therefore, in order to best estimate the heat flux on samples for which there was no direct IR temperature data, it was necessary to evaluate the measured heat flux values as a function of the ET discharge parameters, which were successfully collected for all shots.

With the use of the pulse-forming network, the ET source demonstrated consistent discharges at the specified ΔV values, which implies a consistent heat flux onto the samples. Figure 6.16 displays example current and power profiles for a series of shots where the ΔV was varied from 5.5 kV to 7 kV, specifically to collect suitable IR data at each value. A total of 9 shots were collected which provided clean IR temperature data and thereby good heat flux calculations. More would have been collected if not for operating time limitations on the ET source.

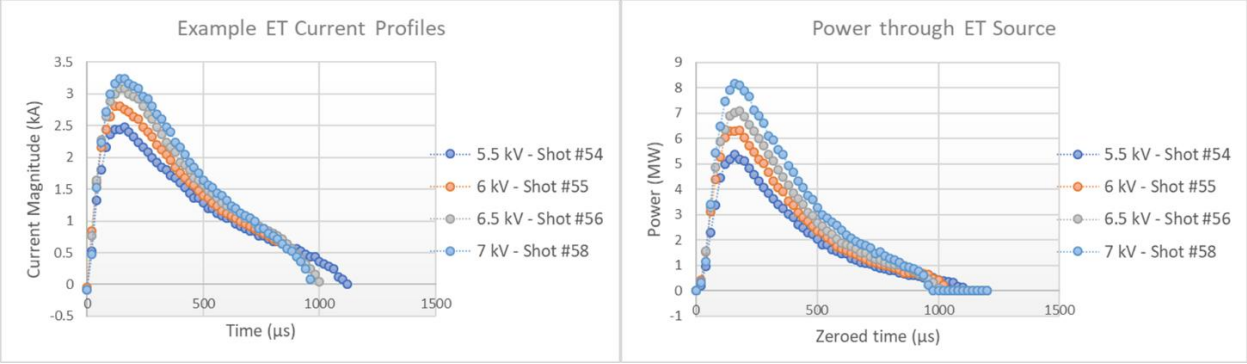


**Figure 6.16** – Example profiles of current (Left) and the calculated power (Right) generated in the ET source as a function of time.

In general, the calculated heat flux values exhibited large deviations. This characteristic is to be expected due to the relatively low precision of the IR camera compared to the ET discharge time. At the maximum frame rate of 1337 Hz, or 1 frame every 748 µs, the IR camera could only capture 2-3 images of the plasma jet impact. The discharge time was designed to be 1000 µs. Depending on when the IR camera triggers relative to the ET discharge, the first frame to capture IR data could "miss" the peak heat flux value by a couple 100 µs. The variation in calculated heat flux therefore likely comes from the significant difference in sampling times relative to the time of peak heat flux.

For each shot dataset, the frame of IR data with the highest corrected temperature value was used to calculate heat flux via Eq. 19. For the time duration t, the timespan of the ET power profile was used; going frame-by-frame through the IR images for the 9 shots, the plasma impact visibly lasted between 750 – 1500 μs, so this seems a reasonable assumption. Average values of the temperature-dependent thermal properties $k$ and $C_p$ were used, based on material data and fits specified in Appendix A. It was found that scaling Q'' to the maximum power of the ET discharge (rather than total or average energy) gave the most accurate linear fit. To easily discern the desired relationship, and to generate some statistical information from the 9 available data points, heat flux values for a specific ΔV discharge were averaged together. The results are displayed in Fig. 6.17.

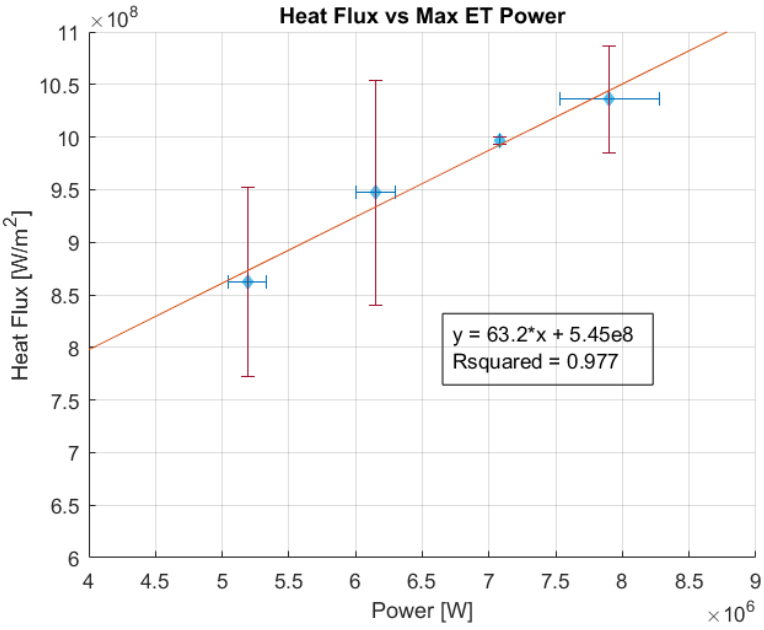


**Figure 6.17** – Calculated heat flux as a function of maximum ET source power

The linear fit of Fig. 6.17 provides the relationship used to estimate heat flux values for the PFM exposures with available current/voltage data without IR data. The maximum power generated during each shot is calculated and then input into Eq. 20 to determine the estimated, average heat flux Q'' in W/m$^2$. This heat flux value is related to the total amount of material erosion experienced by each sample.

$$Eq\ 20. \quad Q'' = 63.2\ (P_{max}) + 5.45 * 10^8$$

It should be noted that each heat flux data point used in Fig. 6.17 and Eq. 20 uses heat flux measurements at each micro-trench location (C1-C4) averaged together. The heat fluxes at each individual micro-trench location were evaluated separately per the original experiment plan, with the assumption that a significant difference in heat flux would occur across the 2 mm gap between micro-trench locations. Fairly uniform heat fluxes across the micro-trench locations were observed, as seen in the right side of Fig. 6.14. The standard deviation of the averaged heat fluxes used to determine Eq. 20 are on the order of 5 – 10%, which is due to the IR camera's low frame rate. Since the differences in heat flux across micro-trench locations for the same sample are small (< 5%), and would be washed out by the error in Eq. 20, it is not statistically significant to distinguish between micro-trench locations. Consequently, the corresponding FIB erosion data will also be averaged across all micro-trenches on a single sample.

### 6.2.3 – Microscopy Analysis – Silicon

Two silicon samples were exposed during the ET experiment, labeled Si3 and Si5. Sample Si3 was exposed to one plasma shot at a programmed 6 kV, while sample Si5 was exposed to a series of 5 plasma shots all at 6kV. The material is monocrystalline silicon that was left over from the preliminary DIII-D experiment mentioned in Chapter 5 Section 5.2.2.3. Silicon exhibits much lower melting and boiling points than the PFMs of interest, 1412 °C and 2900 °C, respectively [7]. Additionally, silicon is known to be quite brittle at room temperature. With such poor thermal and mechanical properties, silicon serves as a worse-case example in this experiment with which the PFMs of interest can be compared.

As expected, extreme melting, boiling, and fracturing was observed on the surfaces of both silicon samples. Figure 6.18 depicts pre- and post-experiment SEM images of example silicon surfaces, at lower magnification to highlight this extreme degradation of the material surface.

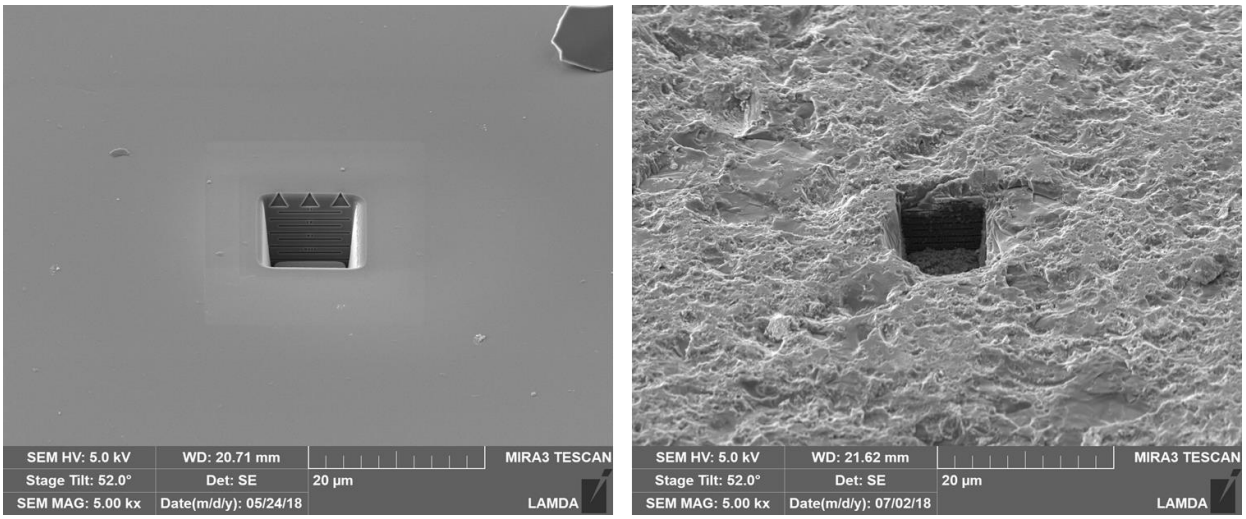


**Figure 6.18** –Micro-trench cluster C1 in silicon sample Si3, before (Left) and after (Right) 1 ET plasma exposure, showing evidence of surface melting.

Erosion of the sample surface is non-uniform, with boiling and fractured pits on the same size scale as the micro-trenches. This roughness made measuring the actual surface depth along the micro-trench walls difficult. In addition to the severe erosion of the surface, deeper fractures were observed along the micro-trench walls, sometimes on the shadowed walls with the FIB fiducial depth markings. These fractures sometimes led to ejection of pieces of the micro-trench wall. These wall fractures may indicate the depths of fractures within the bulk material, or they may be an artifact of just the micro-trench geometry. For this reason, depth measurements were made for both the non-uniform material surface and the bulk fracture depths within the micro-trench. Figures 6.19 and 6.20 highlight the most extreme micro-trench erosion example for the 1 shot silicon sample. For the silicon sample exposed to 5 consecutive plasma shots, the erosion was so extreme that no micro-trenches could be found/identified. This result implies that for the 5 shot case, at least ~8.5 µm of erosion occurred on the sample surface, which is included in the final dataset strictly for comparison with the other PFMs.

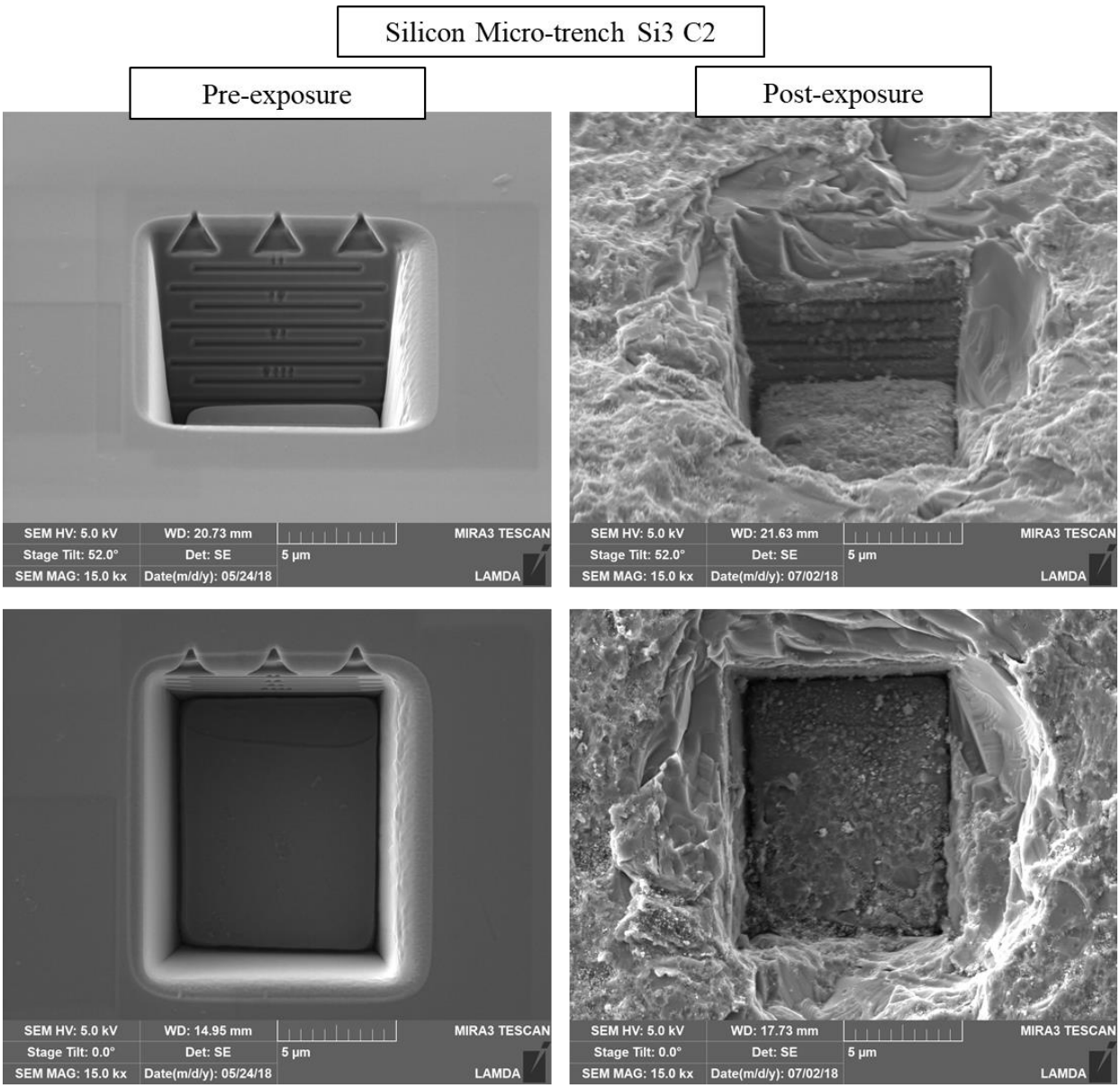


**Figure 6.19** – Pre-exposure (Left) and post-exposure (Right) images of an example micro-trench in silicon exposed to one, 6 kV ET plasma discharge, at both a 52° tilt (top images) and a top-down 0° tilt (bottom images).

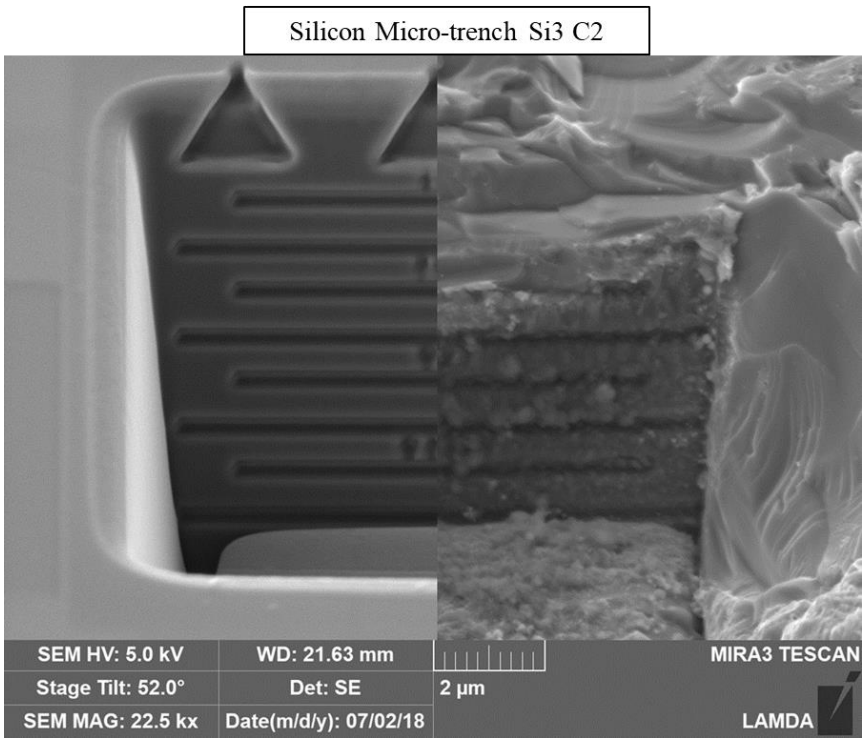


**Figure 6.20** – Overlaid images of a silicon micro-trench for pre-exposure (Left) and post-exposure (Right), highlighting fracturing of the micro-trench wall down to the 6 µm depth marker.

6.2.4 – Microscopy Analysis – Tungsten

Two tungsten samples were exposed during the experiment, labeled W1 and W2. Sample W1 was exposed to one plasma shot at a programmed 6 kV, while sample W2 was exposed to a series of 5 plasma shots all at 6kV. Although there is no specific ITER-grade of tungsten, these tungsten samples were labeled as "ITER-grade" when provided for the experiment. They serve as an example for what will be used in the final divertor design for the ITER tokamak. Thus, the tungsten results represent the standard by which the alternative materials should be compared to, at least in regards to their use as divertor PFMs. With such high melting and boiling points (3422 and 5930 °C, respectively), it was unknown whether the ET pulse would be sufficient to reach a sublimation-dominated erosion regime for W.

Significant melting and melt-layer motion was observed on the surfaces for both the 1 shot and 5 shot cases, consistent with expectations from [8] and [9]. Figure 6.21 depicts pre- and post-

experiment SEM images of the two W surfaces, at lower magnification to highlight this extreme degradation of the material surface.

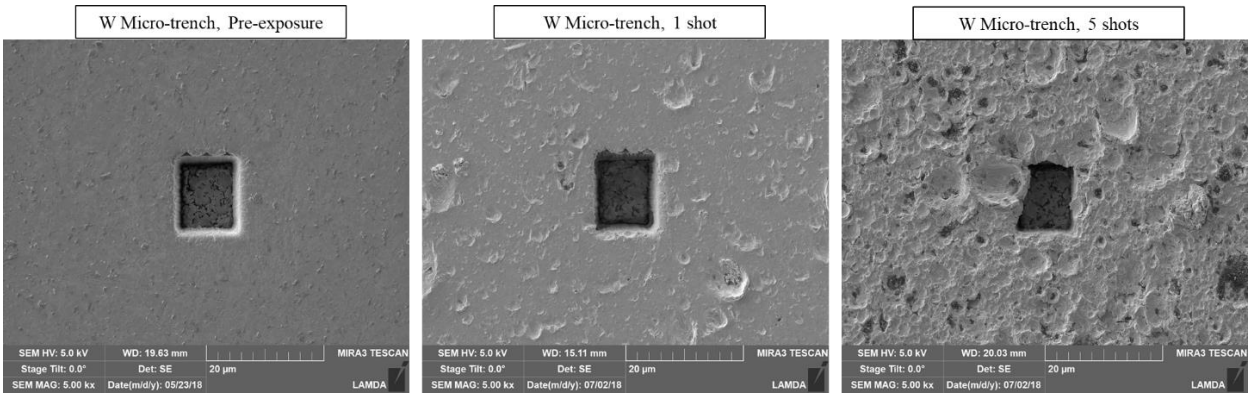


**Figure 6.21** – (Left) Example W micro-trench, pre-exposure, at a 0° top-down view. (Middle) W micro-trench after being exposed to one ET plasma shot at a programmed 6 kV. (Right) W micro-trench after being exposed to 5 consecutive shots at 6 kV. The Left and Right images are of the same micro-trench pre- and post-exposure, while the Middle image depicts a micro-trench at the same C4 location.

In the case of one ET plasma exposure, the molten pits are uniformly dispersed over the sample surface and vary in size from about 2 – 5 μm in diameter. They do not however constitute the entire surface, meaning that any material loss on the surface is localized. Multiple melting pits did occur on the micro-trench edge with fiducial markings, providing some information on their depth, about 1-2 μm deep on average. An example is shown in Fig. 6.22. Based on deformation of some of the micro-trench fiducial markings, the melt layer penetrated ~2 μm into the surface, but there was no significant melt-layer motion or deformation of the micro-trench geometry. The individual molten pits do exhibit melt motion and re-solidification in the plasma flow direction.

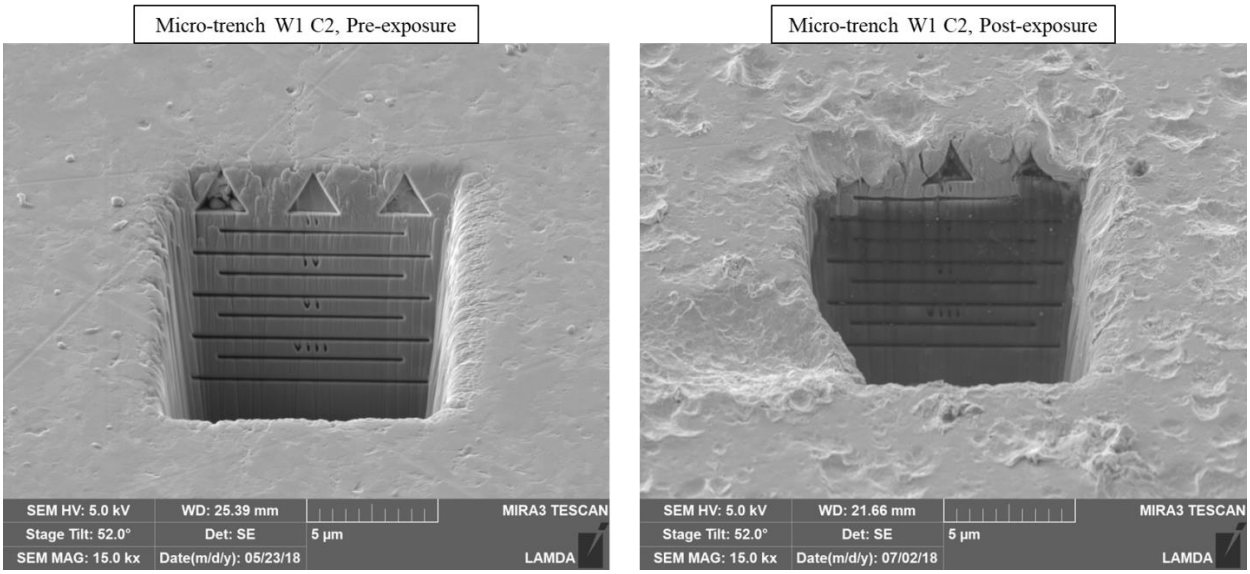


**Figure 6.22** – (Left) Pre-exposure image of a W micro-trench at location C2, exposed to one ET plasma shot at 6 kV. (Right) Post-exposure image of the same micro-trench, exhibiting molten material motion and loss at the micro-trench edge.

In the case of the 5-shot ET plasma exposure, the surface melt layer that formed was much more extreme and uniform than the 1-shot case. The molten pits are larger in size, up to 10 µm in diameter, and all blend together to comprise a fully deformed surface. Repeated plasma exposures appear to have grown the molten pits with each successive shot, as well as induced significant melt-layer motion of the entire surface. Of the three micro-trenches available to observe on the 5 shot sample, only one survived enough to obtain suitable measurements (for location C4) and is displayed in Fig. 6.23. Significant deformation of the micro-trench structure and the corresponding fiducial markings is observed, with only the middle triangle marking being suitable for direct height comparisons. One micro-trench exhibited a cascade of the melt-layer into the micro-trench, displayed in Fig. 6.24, which extended so far as to prevent surface height data due to the inability to obtain top-down image measurements. These two samples did provide insight into the melt layer depth, at least in terms of how deep the FIB micro-trench geometry was deformed. The third micro-trench was backfilled with a mass of molten W that obscured the fiducial markings and prevented any measurements.

Figure 6.25 shows pre- and post-exposure images of the FIB label carved into tungsten sample W2, further highlighting the extreme melting and deformation that occurred due to 5 consecutive ET plasma exposures. This is the same label featured in Fig. 5.5 of Chapter 5.

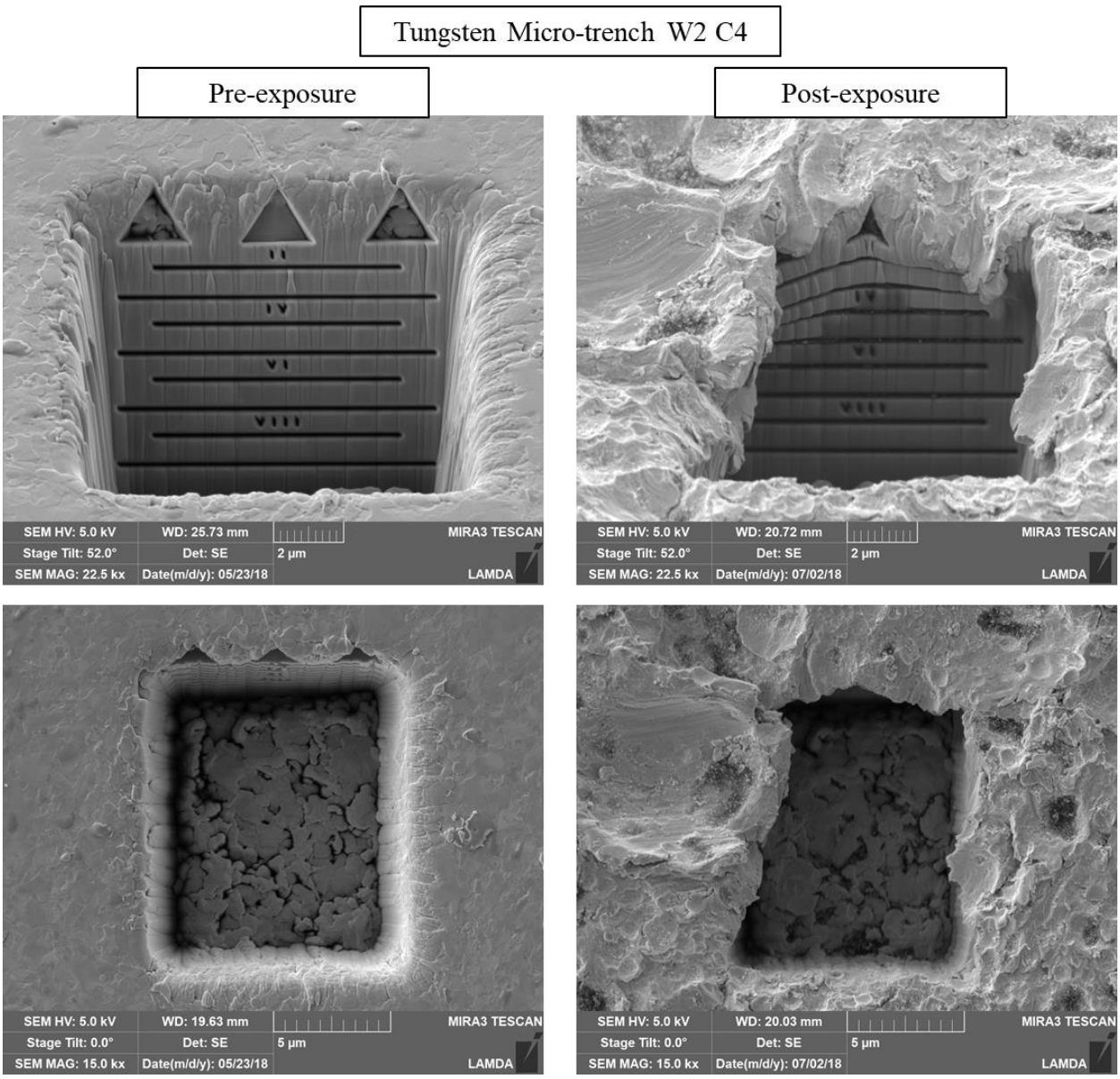


**Figure 6.23** - Pre-exposure (Left) and post-exposure (Right) images of an example micro-trench in W exposed to 5 consecutive, 6 kV ET plasma discharges, at both a 52° tilt (top images) and a top-down 0° tilt (bottom images).

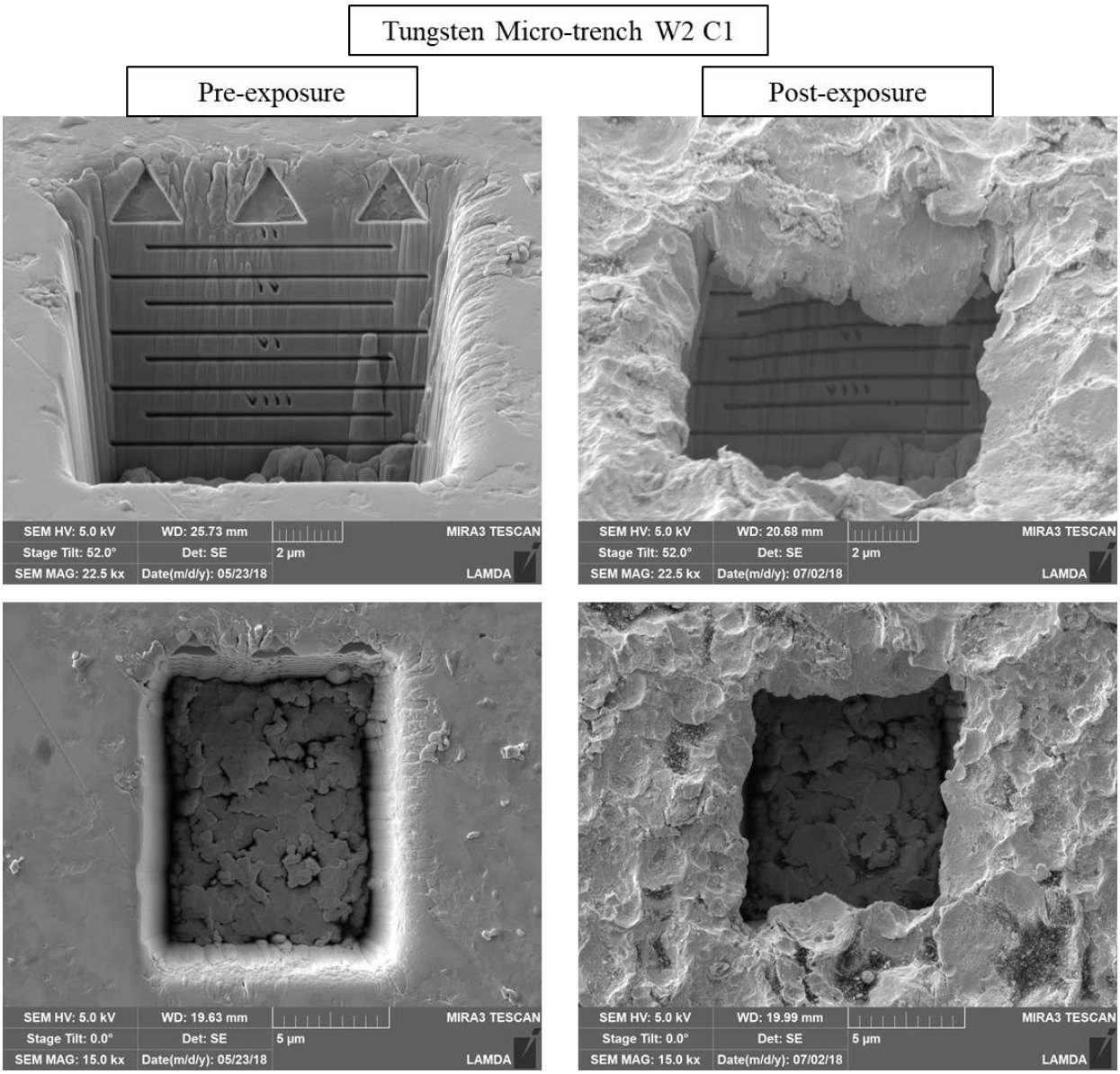


**Figure 6.24** - Pre-exposure (Left) and post-exposure (Right) images of an example micro-trench in W exposed to 5 consecutive, 6 kV ET plasma discharges, at both a 52° tilt (top images) and a top-down 0° tilt (bottom images).

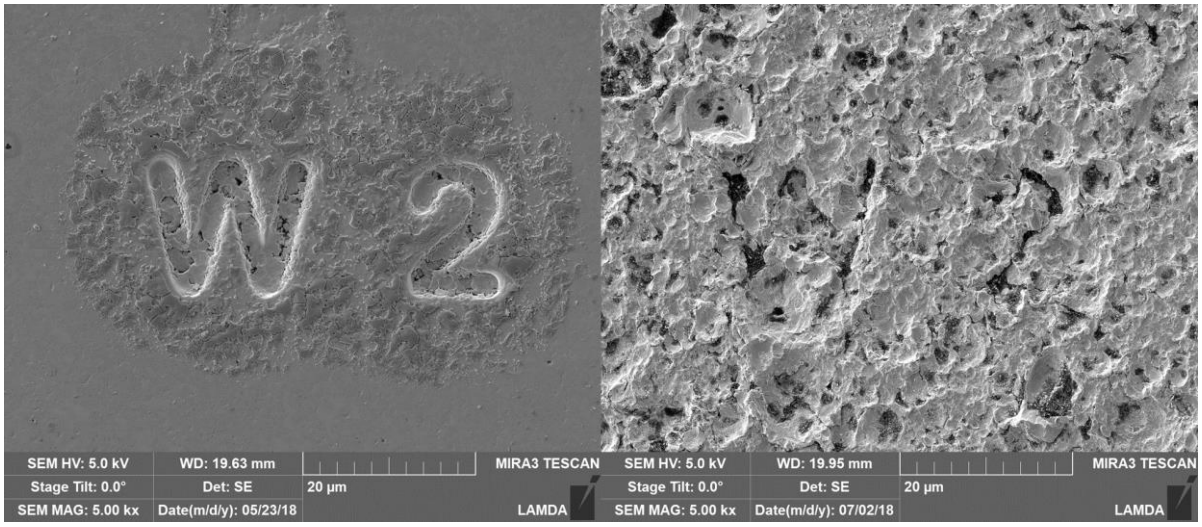


**Figure 6.25** – Pre-exposure (Left) and post-exposure (Right) images of the FIB label used to uniquely identify tungsten sample W2. The label is carved approximately 1.5 µm into the sample surface.

### 6.2.5 – Microscopy Analysis – $Ti_3SiC_2$

Three $Ti_3SiC_2$ samples were exposed during the experiment, labeled TSC5, TSC6, and TSC7. Sample TSC5 was exposed to a series of 5 plasma shots at 6 kV, while samples TSC6 and TSC7 were exposed to a single plasma shot, at a programmed 7 kV and 6 kV, respectively. The expectations for $Ti_3SiC_2$ were somewhat unknown for the ET exposures. The MAX phase ceramics were chosen for this study due to their reportedly high thermal-shock resistance and damage tolerance at high operating temperatures. However, the high heat flux ET exposures were designed to test the Max phases far past the operating temperature limits discussed in Chapter 4 (1700 °C for $Ti_3SiC_2$). Additionally, rather than melting or sublimating, the MAX phases are expected to dissociate past this temperature limit. It was uncertain how the combined physics of dissociation and melting/sublimation would affect the morphology and erosion of the surface layer, let alone the calculations for net erosion depth.

The post-exposure $Ti_3SiC_2$ samples exhibited a combination of melting, boiling, and fracturing on the surface. Small, scattered molten pits were observed for the 1 shot cases, at least where the surface was not terribly damaged from fracturing. These pits were smaller than those observed for the tungsten samples, ranging from about 0.1 – 1.5 µm in diameter, as highlighted in

Fig. 6.26. There did not appear to be an increase in average size with an increase in heat flux magnitude. A more significant erosion mechanism is the deep fracturing of the $Ti_3SiC_2$ material, which resulted in the formation of jagged, sharp holes and crevices as fractured material was ejected from the surface. The depth and magnitude of this material loss due to fracture does appears to increase with an increase in heat flux. EDX analysis was performed on the samples to attempt to measure any dissociation that may have occurred, mainly a lack of the A-group element Si. The Ti, Si, and C were uniformly seen across the surface, implying that the molten/deformed material is bulk $Ti_3SiC_2$. However, it is possible that the $e^-$ beam voltage of 10 kV penetrated too deep into the surface and was measuring Si signals far below the deformed layer of interest.

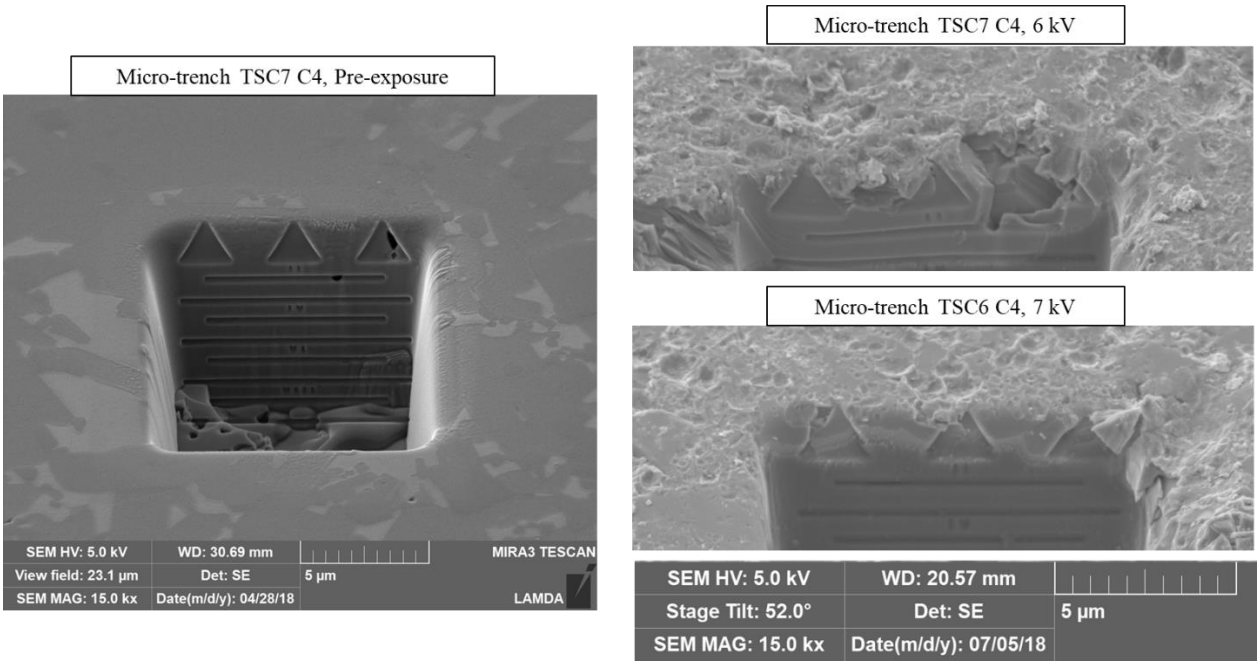


**Figure 6.26** – (Left) Pre-exposure image of an example $Ti_3SiC_2$ micro-trench. (Right) zoomed-in images of $Ti_3SiC_2$ micro-trench edges after exposure to one ET discharge at a programmed 6 kV (Top Right) and 7 kV (Bottom Right). In both cases, small molten pits of various sizes are visible along the surface. All images are for the same micro-trench location (C4).

In the case of one ET plasma exposure, there was a wide mix of erosion phenomena observed on the micro-trench edges. In cases where significant fracturing was not present along the edge, erosion depth measurements for the flat material surface were easily obtained. Some deformation of the edge geometry was observed, i.e. bending and elongation, however a clear layer

of melt motion was not visible. In other cases, bulk fracturing of the material surface did occur along the trench edges with the fiducial markings, often making it difficult to make depth measurements for the actual, average material surface. There were many extreme cases of material fracturing that could be observed within the micro-trenches. In some instances, the triangular depth markings would be completely destroyed along the edge, requiring the use of the deeper line markings. In other cases, entire portions of the micro-trench wall were observed to have fractured and collapsed within the micro-trench, in the direction of plasma impact. Figure 6.27 highlights an example where material loss due to surface melting and from fracturing are both observed along the micro-trench edge. Figures 6.28 and 6.29 feature a few of the multiple examples of extreme fracture that were observed amongst the one-shot samples. Qualitatively, fracture effects from the 7kV exposure appeared more severe than in the 6kV case.

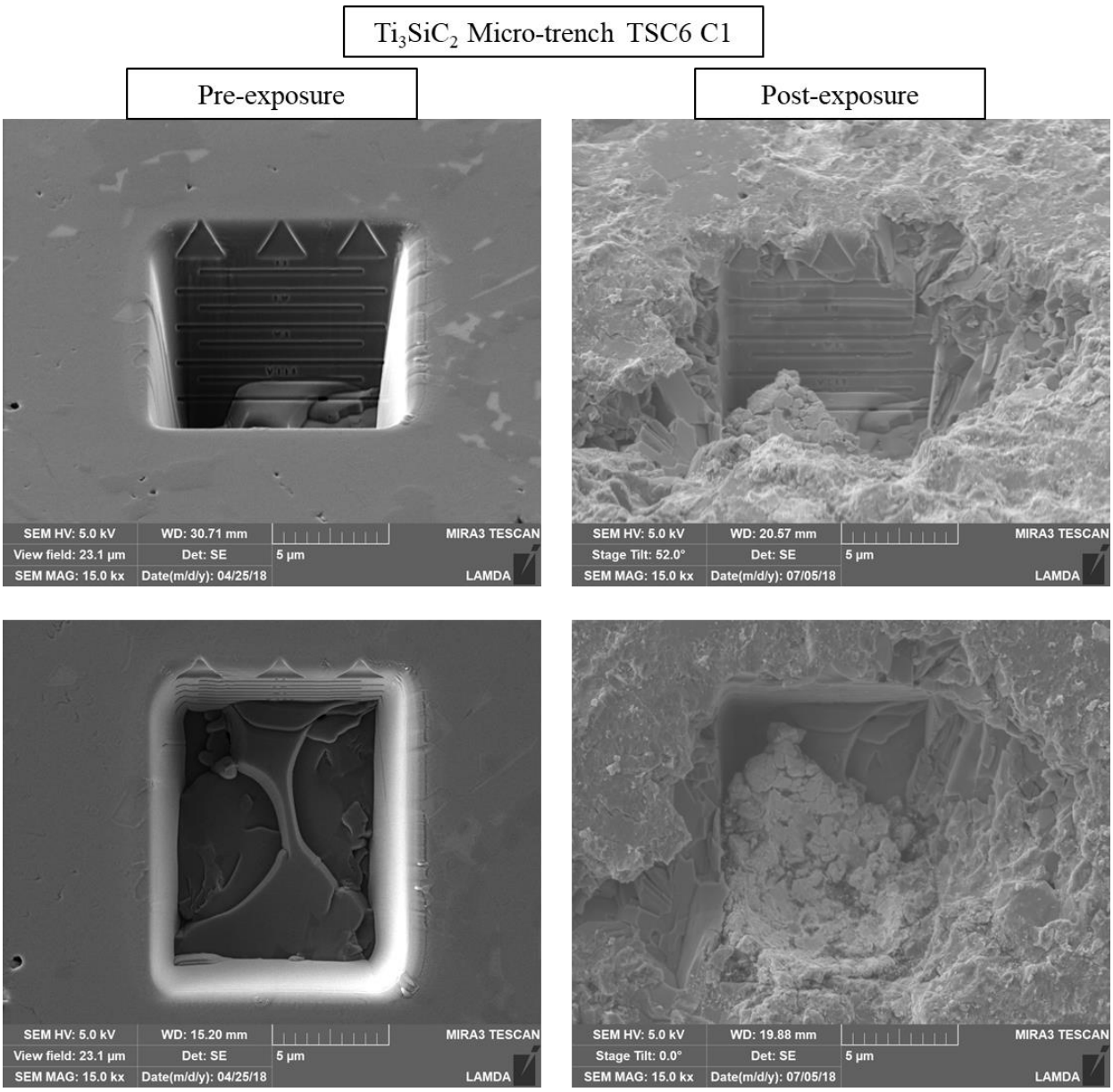


**Figure 6.27** – Pre-exposure (Left) and post-exposure (Right) images of an example micro-trench in $Ti_3SiC_2$ exposed to one 7kV ET plasma discharge, at both a 52° tilt (top images) and a top-down 0° tilt (bottom images).

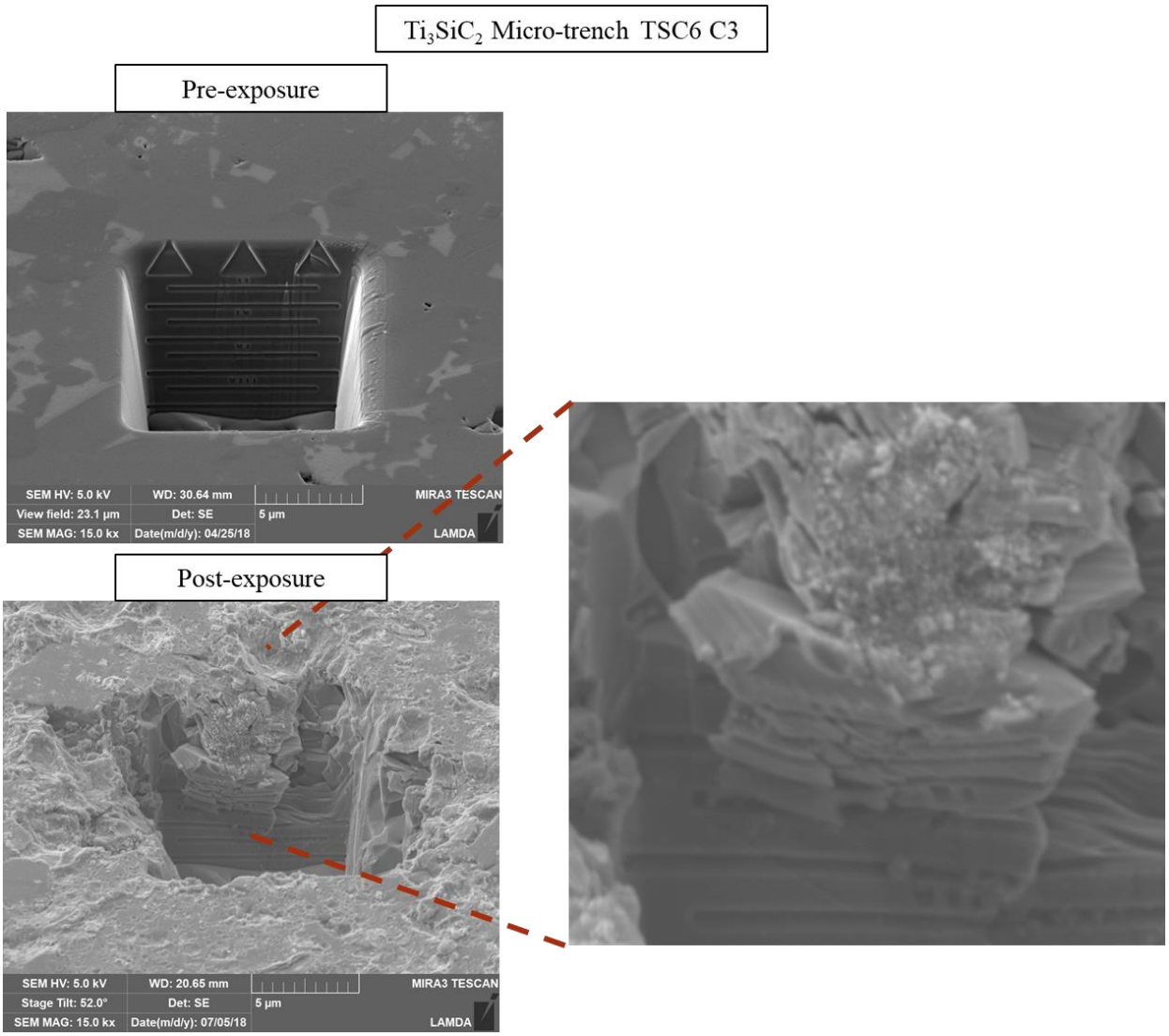


**Figure 6.28** - Pre-exposure (Top Left) and post-exposure (Top Right) images of an example micro-trench in $Ti_3SiC_2$ exposed to one 7kV ET plasma discharge. A collapse of the depth-marked micro-trench wall is observed, highlighted with a zoomed-in image on the Right.

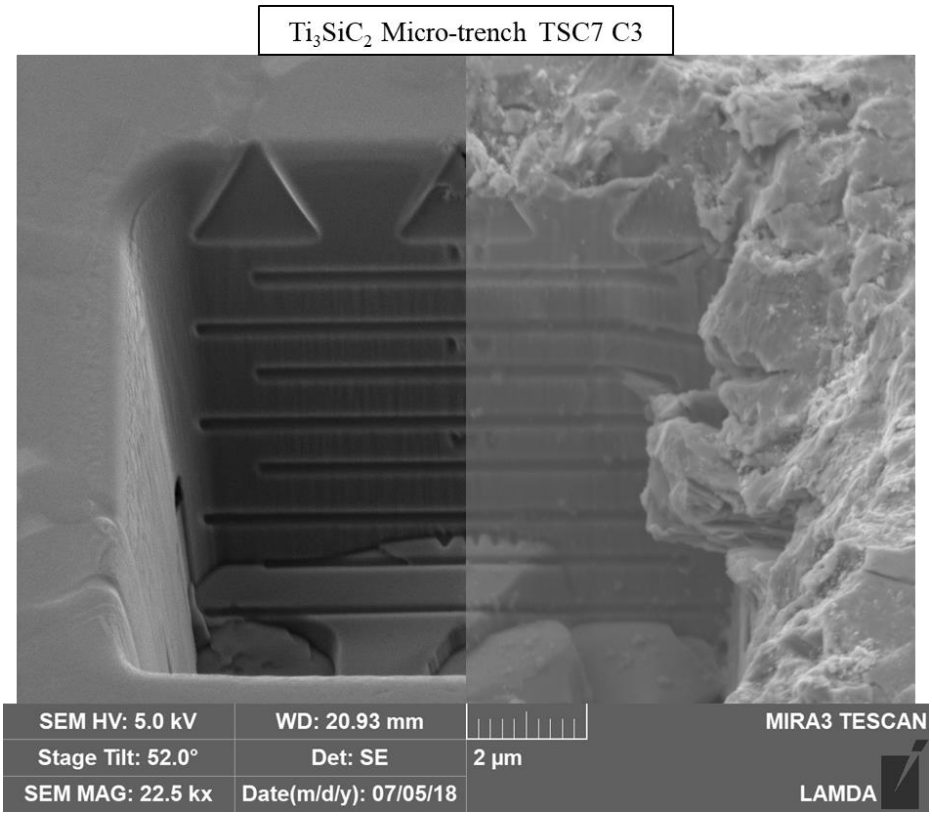


**Figure 6.29** - Overlaid images of a $Ti_3SiC_2$ micro-trench for pre-exposure (Left) and post-exposure (Right), highlighting fracturing of the micro-trench wall down to the 6 µm depth marker.

In the case of the consecutive 5-shot ET exposure, uniform fracturing and erosion loss was observed on the sample surface and along each micro-trench wall. Figure 6.30 provides a surface comparison between the 1 shot and 5 shot cases, displaying images at a 52° to highlight the difference in surface roughness. As the fracture sites are generated during successive plasma shots, they propagate from one another, resulting in a uniformly jagged and eroded material surface. Consequently, the amount of fracturing and material loss on the micro-trench walls was more severe than in the 1-shot case. In one instance, material loss from fracture spanned past the maximum 10 µm FIB depth markings. Just like in the silicon analysis, it was important to take depth measurements for both the average surface height and for the fracture depth within the micro-trench wall. These wall fractures may be artifacts from just the micro-trench geometry, although many instances of bulk material ejection at similar depths and sizes of the micro-trenches themselves were observed on the surface. Figure 6.31 is another overlaid image meant to highlight the extreme depth of fracturing observed in the 5-shot sample.

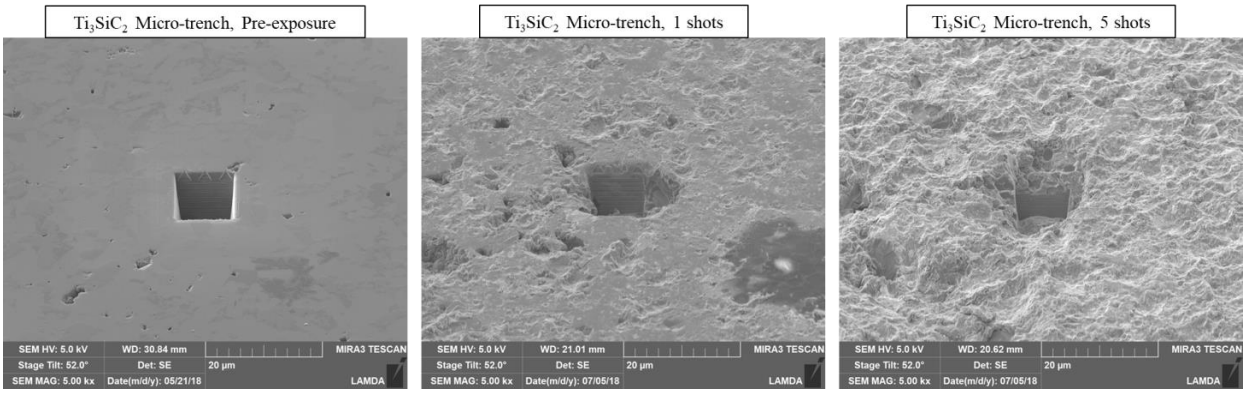


**Figure 6.30** - (Left) Example $Ti_3SiC_2$ micro-trench, pre-exposure, at a 52° angled view. (Middle) $Ti_3SiC_2$ micro-trench after being exposed to one ET plasma shot at a programmed 6 kV. (Right) $Ti_3SiC_2$ micro-trench after being exposed to 5 consecutive shots at 6 kV. The Left and Right images are of the same micro-trench pre- and post-exposure, while the Middle image depicts a micro-trench at the same C1 location.

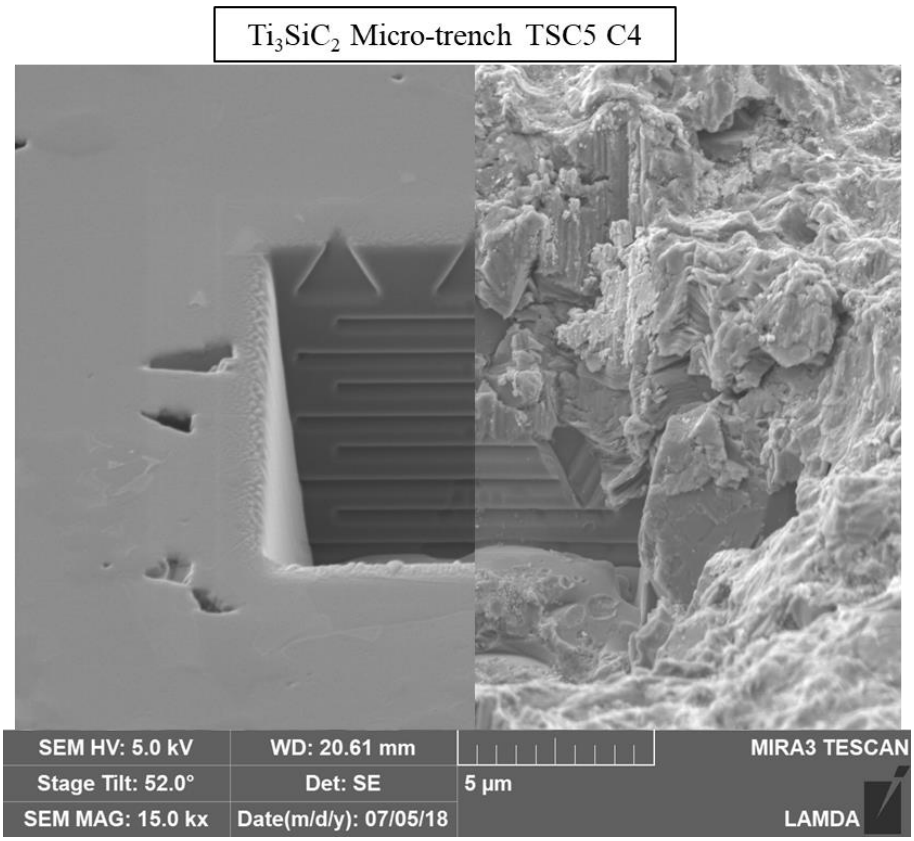


**Figure 6.31** - Overlaid images of a $Ti_3SiC_2$ micro-trench for pre-exposure (Left) and post-exposure (Right), highlighting fracturing of the micro-trench wall down to the 9 µm depth marker.

6.2.6 – Microscopy Analysis – $Ti_2AlC$

Four $Ti_2AlC$ samples were exposed during the experimental campaign, labeled TAC4, TAC5, TAC6, and TAC7. Samples TAC4, TAC6, and TAC7 were exposed to a single plasma shot at a programmed $\Delta V$ of 6 kV, 6.5 kV, and 7 kV, respectively. Sample TAC5 was exposed to 5 consecutive plasma shots at 6 kV. As with $Ti_3SiC_2$, the expectations for $Ti_2AlC$ were somewhat unknown for the ET exposures. The high heat flux ET exposures were designed to test the MAX phases far past their operating temperature limits (1600 °C for $Ti_2AlC$). Additionally, rather than melting or sublimating, the Max phases are expected to dissociate past this temperature limit. It was uncertain how the combined physics of dissociation and melting/sublimation would affect the morphology and erosion of the surface layer, let alone the calculations for net erosion depth. Compared to $Ti_3SiC_2$, $Ti_2AlC$ does possess slightly higher thermal conductivity and specific heat values, so there was a slight expectation for it to better handle the high heat loads.

The post-exposure $Ti_2AlC$ samples exhibited a combination of melting, boiling, and fracturing on the surface. Small, scattered molten pits were observed for the 1-shot and 5-shot cases. These pits were of the same scale as those observed on the $Ti_3SiC_2$ samples, ranging from about 0.1 – 1 μm in diameter. There did not appear to be an increase in average size with an increase in heat flux magnitude. Figure 6.32 depicts pre- and post-experiment SEM images of the $Ti_2AlC$ for the 1-shot and 5-shot, 6kV cases, at lower magnification to highlight the increased degradation of the material surface.

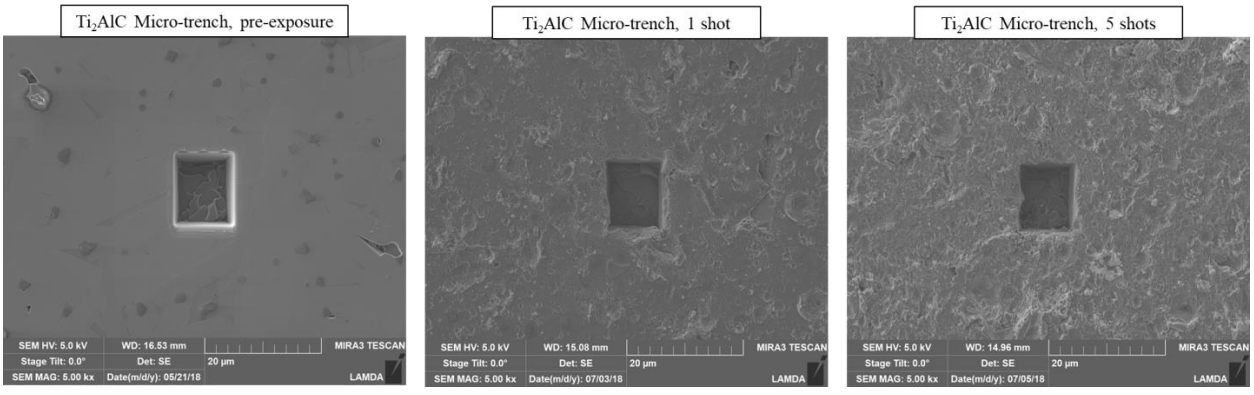


**Figure 6.32** – (Left) Example $Ti_2AlC$ micro-trench, pre-exposure, at a 0° top-down view. (Middle) $Ti_2AlC$ micro-trench after being exposed to one ET plasma shot at a programmed 6 kV. (Right) $Ti_2AlC$ micro-trench after being exposed to 5 consecutive shots at 6 kV. The Left and Right images

are of the same micro-trench pre- and post-exposure, while the Middle image depicts a micro-trench at the same C2 location.

In the case of one ET plasma exposure, relatively uniform erosion from the melting/boiling pits was observed on the micro-trench edges. A distinct, shallow melt layer was observed along the edges, often less than 1 μm deep. Compared to the $Ti_3SiC_2$ samples, erosion depth measurements for the flat material surface were easily obtained. Fracturing and material ejection were observed in some $Ti_2AlC$ samples, to a much less severe extent than in the $Ti_3SiC_2$ samples. Most were shallow fractures less than 4 μm in depth. Due to the number of available samples, it was possible to gradually increase the heat flux exposure amongst the three 1 shot samples. Qualitatively, fracture effects did appear slightly more severe with increasing heat flux, especially the depth of visible cracks that did not necessarily result in material ejection. There was no observable increase in melting pit size or areal density with the increase in heat flux. Figure 6.33 highlights an example where material loss due to surface melting and from fracturing are both observed along the micro-trench edge for the 6.5 kV shot. Figure 6.34 is an overlaid image that provides a good example of uniform melt layer formation and surface erosion for the 6kV shot.

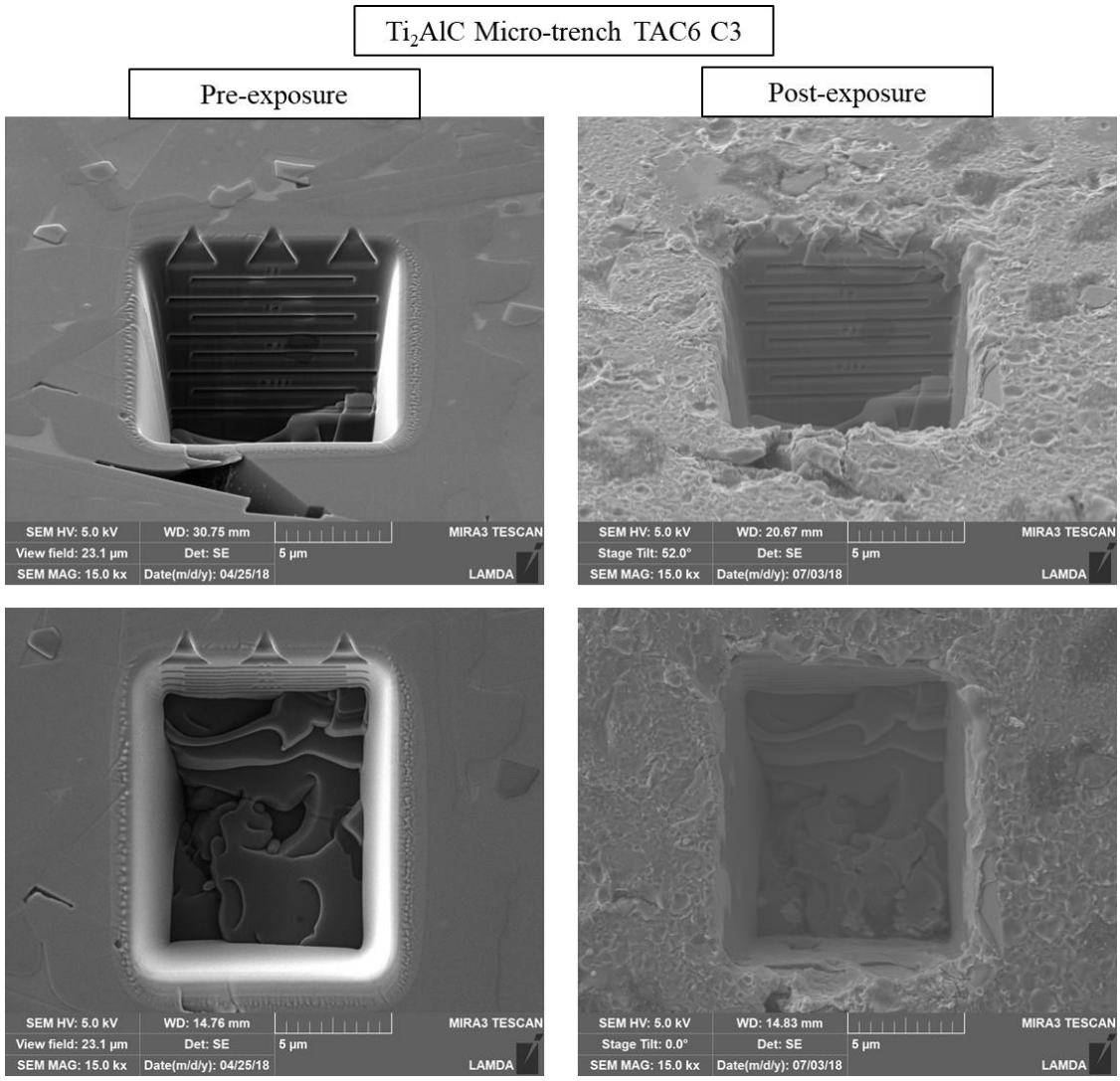


**Figure 6.33** - Pre-exposure (Left) and post-exposure (Right) images of an example micro-trench in $Ti_2AlC$ exposed to one 6.5kV ET plasma discharge, at both a 52° tilt (top images) and a top-down 0° tilt (bottom images).

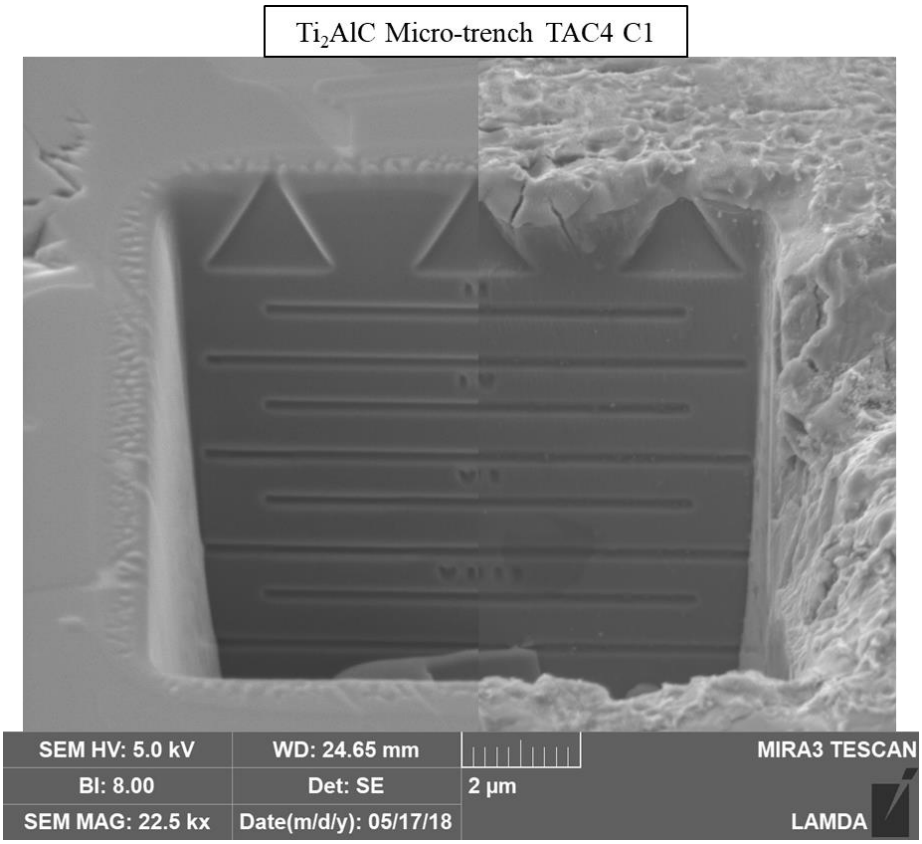


**Figure 6.34** - Overlaid images of a $Ti_2AlC$ micro-trench for pre-exposure (Left) and post-exposure (Right), highlighting the melting and boiling along the micro-trench edge.

In the case of 5 consecutive ET plasma exposures, uniform fracturing and erosion loss was observed on the sample surfaces and along the micro-trench walls. Figure 6.35 provides a surface comparison between the 1 shot and 5 shot cases, displaying images at a 52° to highlight the difference in surface roughness. In many instances, deep fractures were observed to form along the micro-trench walls without resulting in mass material ejection. The material loss that did occur was usually contained to above the 4 µm depth marker. As with the $Ti_3SiC_2$ analysis, it was important to take depth measurements for both the average surface height and for the fracture depth within the micro-trench wall. Figure 6.36 shows pre- and post-exposure images of the FIB label carved into the TAC5 sample, further highlighting the melting, boiling, and fracturing caused by the 5 consecutive ET plasma exposures.

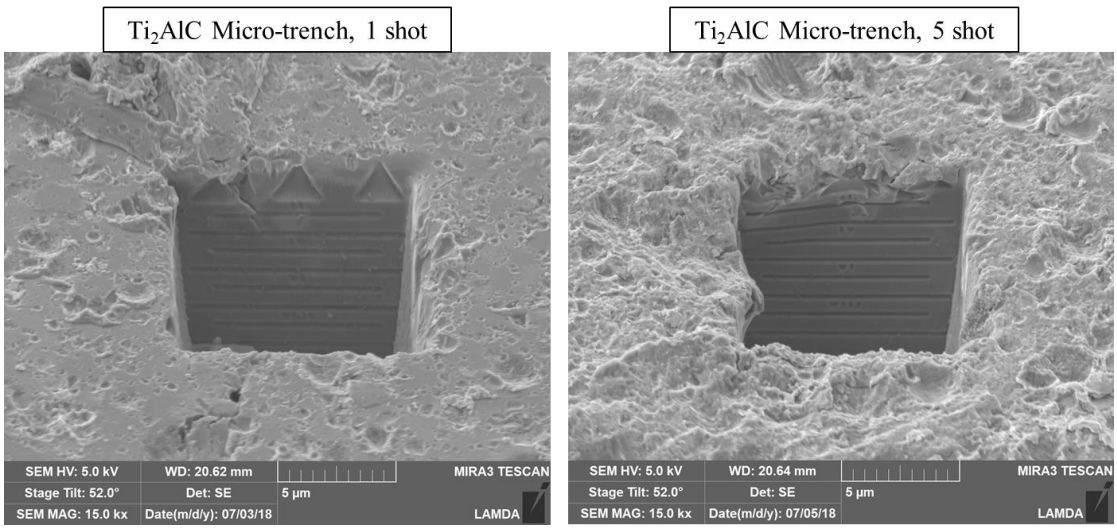


**Figure 6.35** - (Left) $Ti_2AlC$ micro-trench after being exposed to one ET plasma shot at a programmed 6 kV. (Right) $Ti_2AlC$ micro-trench after being exposed to 5 consecutive shots at 6 kV. The Left and Right images are of micro-trenches at the same C2/C3 location, and are displayed at a 52° angle to highlight the difference in surface roughness.

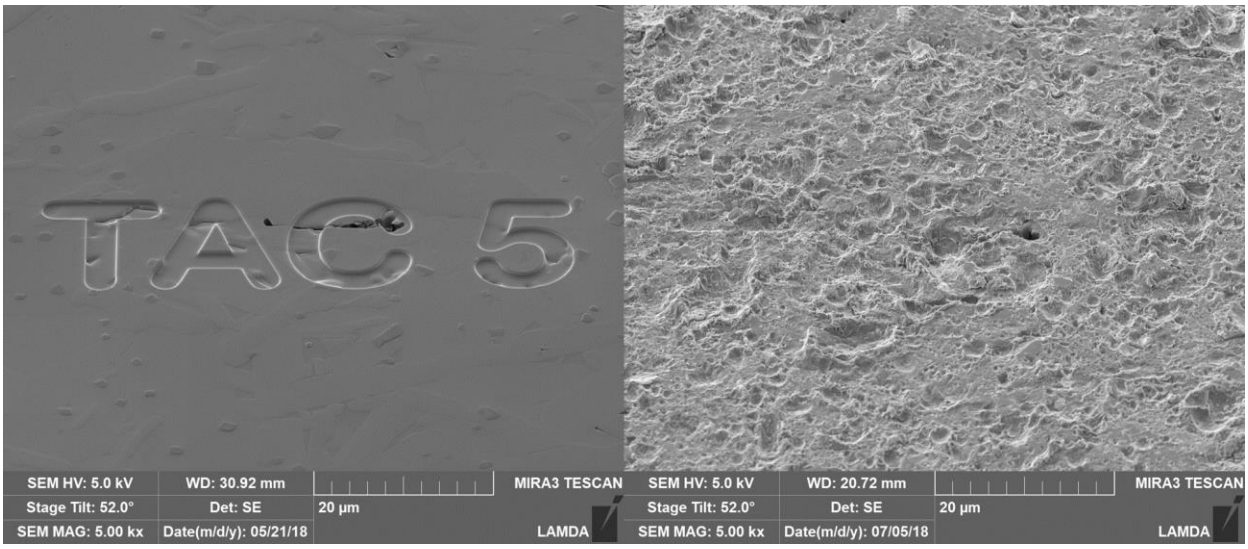


**Figure 6.36** - Pre-exposure (Left) and post-exposure (Right) images of the FIB label used to uniquely identify tungsten sample TAC5. The label is carved approximately 0.5 µm into the sample surface.

6.2.7 – Microscopy Analysis – Silicon Carbide

Four SiC samples were exposed during the experiment, labeled SiC8, SiC9, SiC10, and SiC11. An additional, un-micro-trenched SiC sample was also available for IR heat flux calibrations. Samples SiC9 and SiC11 were exposed to a single plasma shot at a programmed $\Delta V$ of 6 kV and 7 kV, respectively. Samples SiC8 and SiC9 were planned for 5 consecutive plasma shots at 6 kV. However, SiC8 experienced too many misfires to be easily interpreted, and was scrapped and used as another calibration sample. This left only three SiC samples for erosion analysis. As discussed in Chapter 4, silicon carbide has excellent thermal properties, strong covalent bonds, and sublimates rather than melting. It was expected that this combination of properties would lead to a uniform, low erosion rate across the sample surfaces.

The post-exposure SiC samples proved much more robust than expected. Sample surfaces showed a small increase in surface roughness, in some instances exhibiting small pits on the order of 0.2 μm in diameter as displayed in Fig. 6.37. Despite the surface roughening, the FIB fiducial depth markings looked the same to the naked eye, causing worry that not enough sublimation occurred to obtain measurable gross erosion values. Only during the SEM image analysis, at high magnification, was a small amount of surface erosion confirmed. Although SiC is a ceramic, no surface fracturing was observed on the flat sample surfaces.

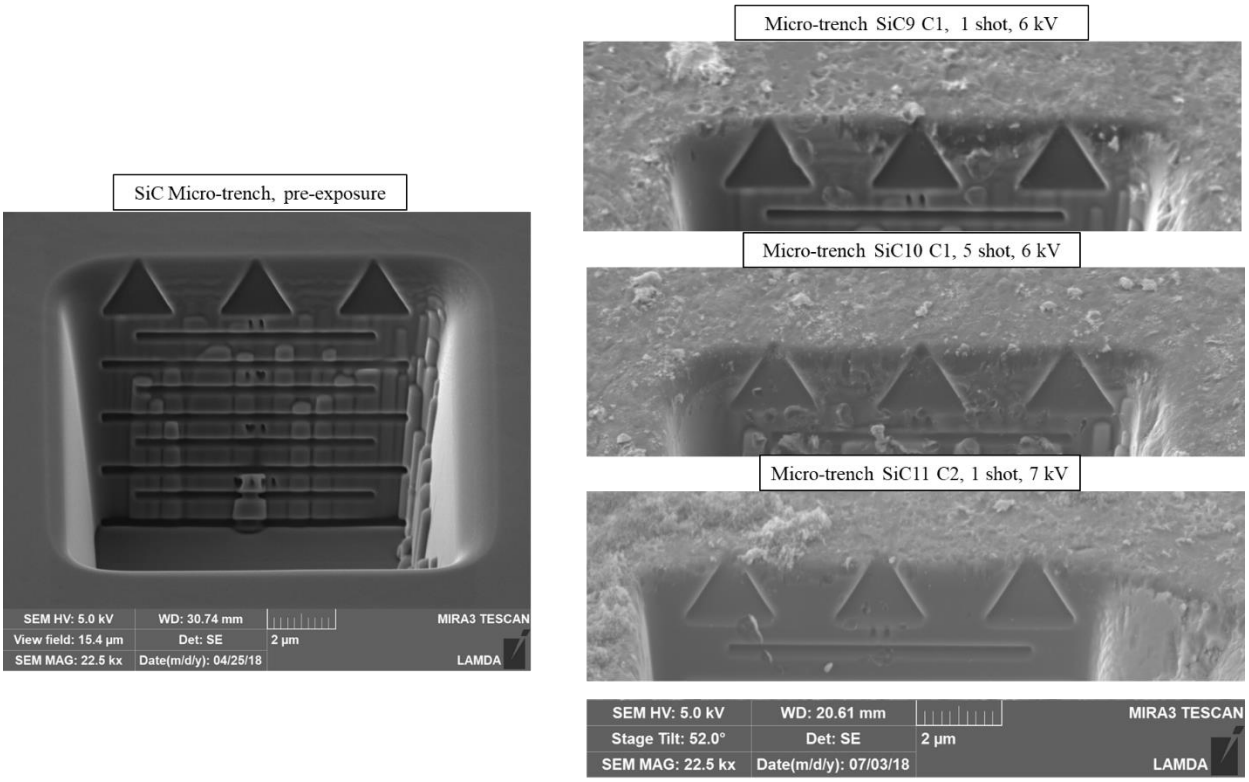


**Figure 6.37** - (Left) Pre-exposure image of an example SiC micro-trench. (Right) Zoomed-in images of SiC micro-trench edges after exposure to one ET discharge at a programmed 6 kV (Top Right), to 5 shots at 6 kV (Middle Right), and one shot at 7 kV (Bottom Right). Small pits are only observed in the 1-shot, 6 kV case, while the other post-experiment images display a small amount of uniform surface roughening with no distinct pits.

The two samples that withstood one ET plasma discharge looked similar to one another in that negligible erosion was visible on the FIB fiducial markings. The one notable difference was the presence of the small, 0.2 μm pits in the lower heat flux shot, again highlighted in the top right of Fig. 6.37. For the case of 5 ET exposures at 6kV, a similar roughened surface was seen, implying that any small erosion pits that formed were uniformly blended together after successive heat fluxes. Figure 6.38 shows an example micro-trench before and after the 5-shot exposure. The sample surface is dirty from hydrocarbon debris but otherwise exhibits negligible damage, showing just how robust the SiC samples were to the incoming heat flux and plasma ions. It was noted in the lab book that the SiC sample surfaces maintained their mirror finish after the experiment.

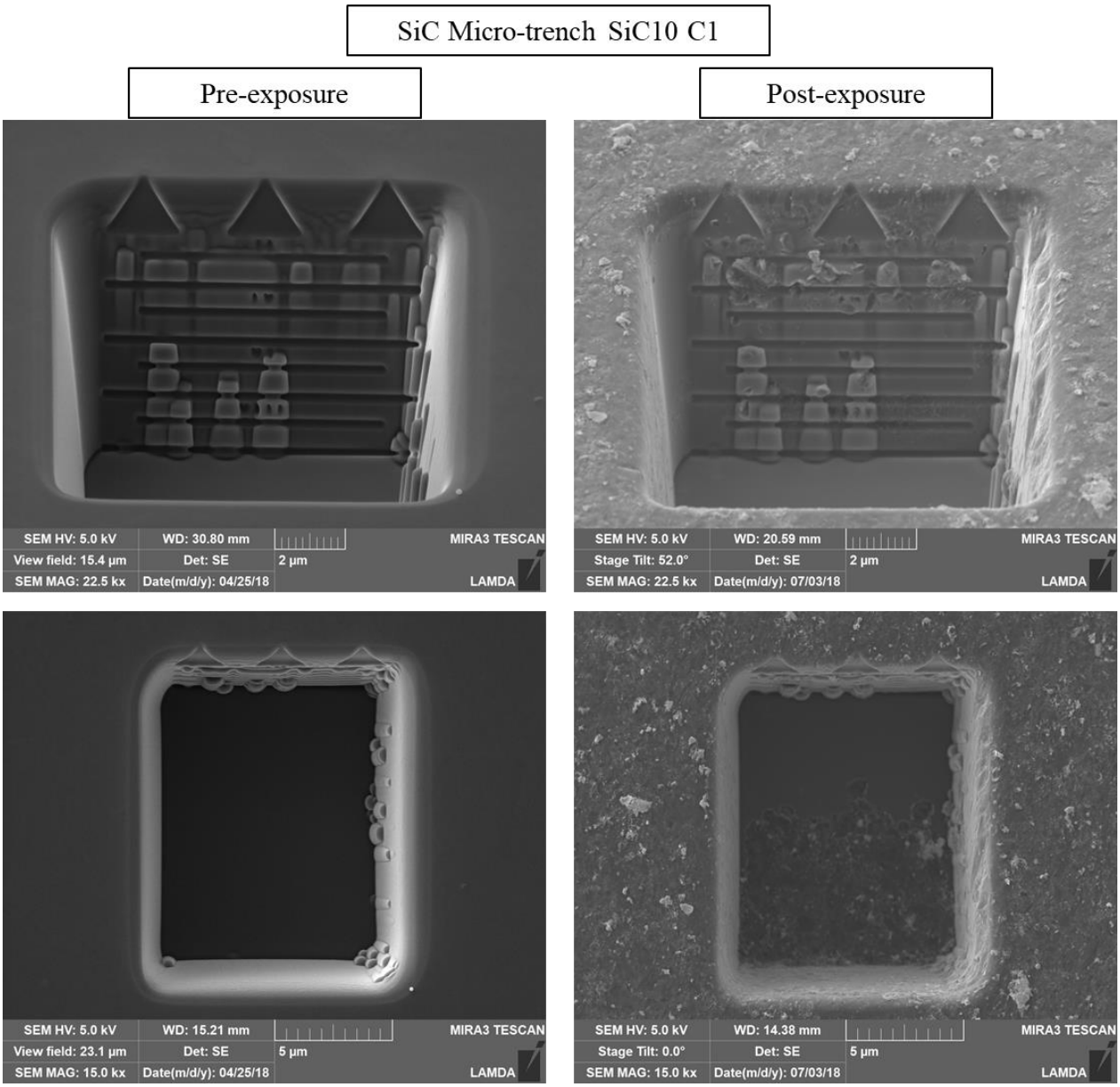


**Figure 6.38** – Pre-exposure (Left) and post-exposure (Right) images of an example micro-trench in SiC exposed to five ET plasma discharges at 6 kV, at both a 52° tilt (top images) and a top-down 0° tilt (bottom images).

After the samples were cleaned and imaged post-experiment, there was skepticism that the material erosion would be too negligible to make any depth measurements. The decision was made to re-expose two of the SiC samples, SiC 9 and SiC 10, for repeated plasma exposures. This was in addition to the shot plan in Table 6.2. SiC 9 was exposed to an additional four ET discharges at a programmed 7 kV, while SiC 10 was exposed to an additional 10 6 kV shots. Even after these

added exposures, negligible surface damage was observed in the SEM images. More pronounced, uniform surface roughening was seen but still not to the extent of the other PFMs. New hydrocarbon deposition patterns on the micro-trench floors confirmed that the samples were impacted by the ET plasma flux. The patterns indicated that the heat flux came at a slightly more normal angle (~40° compared to 45°) which even implies a slightly greater heat flux to the surface normal. A micro-trench example from sample SiC10, which experienced the most plasma exposures at a total of 15, is shown in the overlaid image in Fig. 6.39. These results solidify silicon carbide's superior performance to the other PFMs tested during the ET experiment.

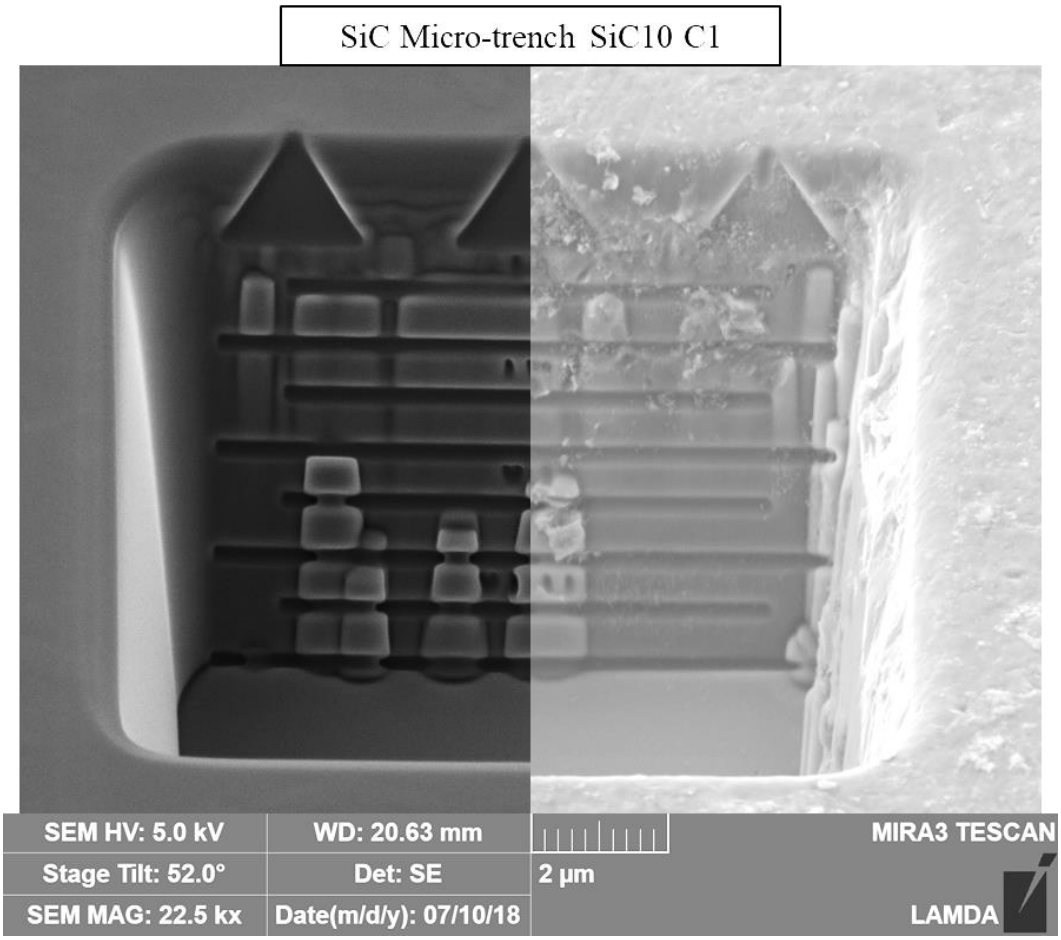


**Figure 6.39** - Overlaid images of a SiC micro-trench for pre-exposure (Left) and post-exposure (Right), highlighting the robustness of SiC after experiencing a total of 15 ET plasma discharges at 6 kV.

6.2.8 Combined Erosion Results and Discussion

The total gross erosion for each material was calculated using the methods described in Chapter 5 Section 5.1, combining one 0° top-down and one 52° angled image for each height measurement of interest ($\Psi = 52°$ for Eqs 1 and 2). SEM image length measurements were scaled by the scale bar provided in each image.

The additional erosion mechanism of material ejection due to surface fracture complicated the microscopy analysis method. The materials $Ti_3SiC_2$, $Ti_2AlC$, and Si all exhibited fracturing into the micro-trench wall itself, which may correspond to the depths of fracturing seen on the polished surface or may just be related to the micro-trench geometry. This complication necessitated two different erosion depth measurements: the average erosion depth experienced by the total surface, $\Delta t_s$, and the average erosion depth of cracks into the micro-trench $\Delta t_c$, which is measured with respect to the new eroded surface height. For the original goals of the dissertation, $\Delta t_s$ is the quantity of interest. Figure 6.40 highlights the relationship between $\Delta t_s$ and $\Delta t_c$ in a sample of silicon where there is clear material loss from the average surface in addition to cracks propagating into the micro-trench geometry.

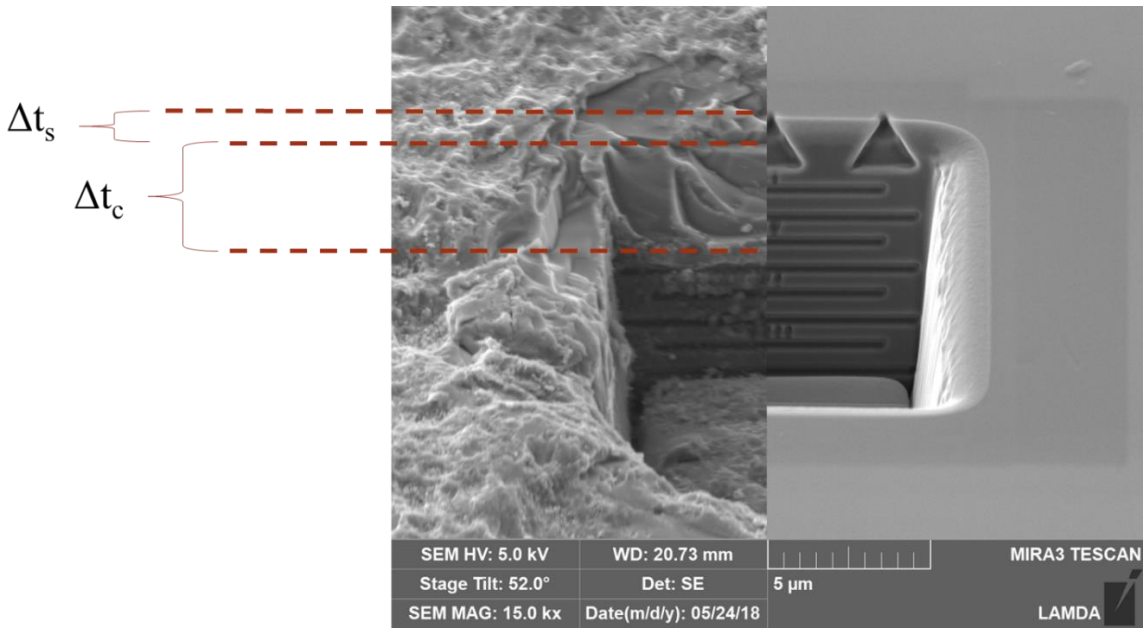


**Figure 6.40** - Overlaid images of a SiC micro-trench for post-exposure (Left) and pre-exposure (Right), highlighting the relatively uniform loss of material from the surface ($\Delta t_s$) along with material loss due to fracture within the micro-trench ($\Delta t_c$).

Values for $\Delta t_s$ were measured for all possible micro-trenches of each ET sample. Values for $\Delta t_c$ were measured for any micro-trench that possessed a fracture into the trench wall which resulted in loss of material. $\Delta t_c$ represents the maximum depth of this fracture. As discussed in Section 6.2.2, the small spread in heat flux magnitudes across the different micro-trench locations C1-C4, relative to the error associated with Eq. 20, motivated the averaging of depth measurements together for one exposed sample. The associated errors for this method turned out to be quite high, ranging from 25 – 90%. Upon further investigation, it was seen that the measurements for individual micro-trench locations (2 – 3 points per micro-trench) were in general more precise. This realization implies non-uniformity of erosion on the surface, which is further enhanced by melting and fracturing of the sample surface which can change local surface heights. For the purpose of material comparison, it was therefore decided to instead analyze the maximum average erosion rate calculated at an individual micro-trench on each sample surface. Doing so emphasizes the worst-case scenario for each material exposure while allowing for more interpretable comparisons from the uncertain dataset.

The results are split into three main graphs of average erosion rate vs average heat flux. It was observed that multi-shot ET exposures often exhibited erosion rates less than the corresponding 1-shot cases. It was presumed that sublimation-dominated erosion should occur at the same rate across a uniform sample surface. However, as the surfaces roughen after each successive plasma shot, this assumption does not remain true. In the case of the MAX phases and Si, the ~μm scale surface fractures that were observed across some samples would build on one another and greatly increase the average erosion rate. In the case of SiC, the small sublimation pits would roughen and blend together, resulting in an overall reduced average erosion rate. Thus, the 1-shot and multi-shot data are split into two datasets to be evaluated separately. Figure 6.41 displays the final surface erosion rate results for all 1-shot cases, calculated from the total surface erosion $\Delta t_s$. The error bars represent +/- 1 standard deviation for the data across an individual sample.

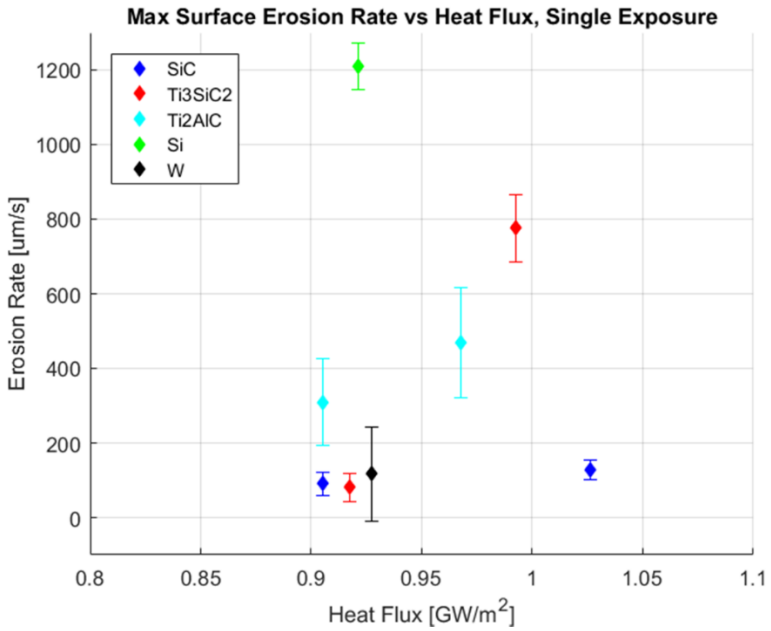


**Figure 6.41** – Average erosion rate of sample surfaces as a function of the average impinging heat flux. Error bars represent +/- 1 standard deviation for all erosion rate measurements across each individual material sample.

For W, the erosion depth and its corresponding erosion rate can be considered to be 0 μm/s. The error is due to the melt-layer motion observed in the SEM images; the measurement for the new surface height changes depending on how the molten pits and melt layers re-solidify after moving across the surfaces. SiC was the only material to exhibit relatively uniform surface erosion across all micro-trench locations, leading to relatively consistent measurements. The microscopy analysis did measure relevant surface erosion, ranging from 90 – 128 μm/s. Erosion rates for both MAX phase materials were inconsistent across the different micro-trench locations, leading to more variation in the averaged results. $Ti_2AlC$ appears to possess a lower erosion rate than $Ti_3SiC_2$ at the lower heat flux value, while the reverse is true closer to 1 GW/m$^2$. On average, both exhibit higher surface erosion rates than SiC. The one Si erosion rate value is the highest among all samples at 1209 μm/s.

Figure 6.42 displays the final surface erosion rate results for all multi-shot cases, again calculated from the total surface erosion $\Delta t_s$. Of the 4 materials evaluated, the $Ti_3SiC_2$ sample exhibited the greatest surface erosion due to the combination of surface erosion and surface fracturing. $Ti_2AlC$, although exhibiting some surface fracturing, also exhibited a deformed melt

layer which likely hindered some of the crack propagation. The results indicate that W experienced significant melting but little material loss, while SiC experienced much lower, uniform surface erosion compared to the MAX phase material. Averaging over multiple plasma exposures, the resulting erosion rates for all materials are lower than those reported in Fig. 6.41 for a single exposure, particularly for the SiC samples which eroded as little as 23 μm/s.

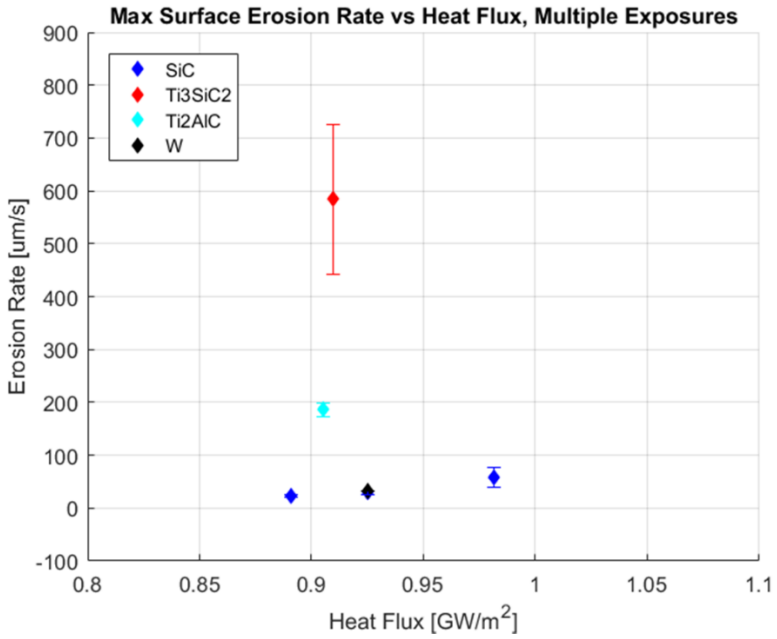


**Figure 6.42** - Average erosion rate of sample surfaces as a function of the average impinging heat flux. Error bars represent +/- 1 standard deviation for all erosion rate measurements across each individual material sample.

The average surface erosion rate calculated from $\Delta t_s$ is important from an erosion physics perspective. From an engineering perspective, the total depth of erosion damage, $\Delta t_s + \Delta t_c$, is arguably more important. The last comparison of erosion rates takes into consideration the total rate of erosion damage into the sample surface, displayed in Fig. 6.43. Since SiC exhibited no surface fracturing or significant melt-layer ejection, their reported values are the same as in Fig. 6.41 and 6.42, much lower than the erosion damage values for the MAX phase materials and Si. The W values for $\Delta t_s + \Delta t_c$ are calculated based on the melt-layer depth along the micro-trench walls. In this graph, a statistically significant increase in the erosion damage rate can be discerned as a function if impinging heat flux. Error bars are calculated from the standard deviation for the

$\Delta t_s$ erosion rate measurements, since there is only one data point for $\Delta t_c$ across each individual micro-trench.

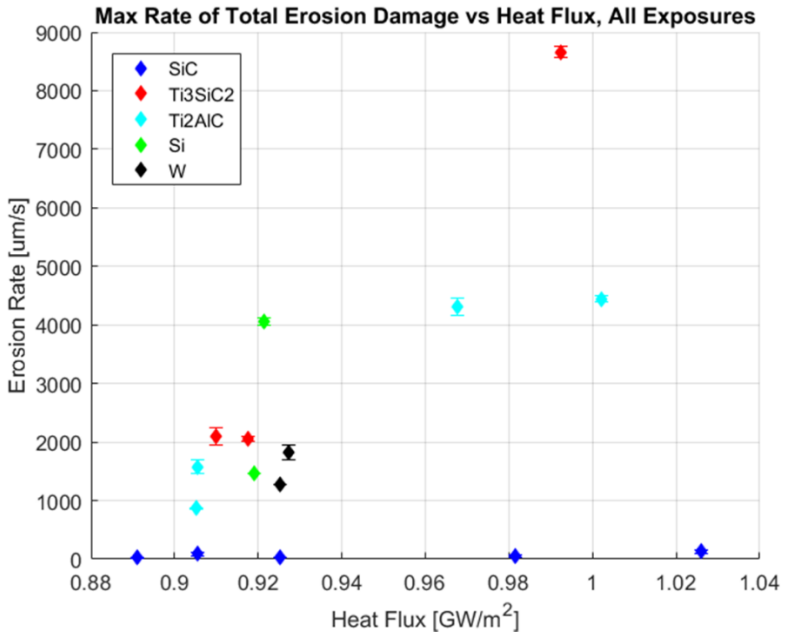


**Figure 6.43** - Average erosion damage rate as a function of the average impinging heat flux. Error bars represent +/- 1 standard deviation for the $\Delta t_s$ erosion rate measurements.

Evaluating the SEM erosion data alongside the qualitative damage mechanisms viewed in each sample, the following conclusions can be made. In terms of surface erosion, tungsten exhibited the best performance with practically zero material erosion loss. However, extreme melt-layer formation and motion was observed across the entire surface, with melt-layer deformation observed to penetrate 1 – 7 μm deep. This melting led to significant morphology changes that would impact further erosion rates. Silicon carbide proved more robust than expected, in one case surviving 15 consecutive ET plasma exposures of about 0.9 GW/m$^2$ heat flux with an average erosion rate of about 26 μm/s. The MAX phase materials displayed surface erosion rates on par with one another across the explored heat flux range, within their standard deviations. However, $Ti_3SiC_2$ was significantly more prone to deep surface fractures and material ejections than $Ti_2AlC$, especially in the higher heat flux range as seen in Fig. 6.43. As expected, silicon performed the worst of all the tested materials, although the MAX phases did not perform much better once surface fracturing was considered. Evaluating both the erosion data and the observed material

deformation mechanisms, silicon carbide demonstrated the best performance under the high heat flux ET discharges.

### 6.3 – ETFLOW Simulations

Simulation results were obtained for SiC, $Ti_3SiC_2$, $Ti_2AlC$, and other ITER-relevant PFMs. Total erosion was obtained from the ETFLOW code using current pulses of temporal and spatial magnitudes relevant to uncontrolled ELMs, VDEs and unmitigated disruptions in ITER-size machines. The same normalized pulse shape was used for each simulation, varying the temporal length and current magnitude to generate a suitable dataset. Simulations were run for vacuum conditions, so the plasma species is determined solely by ablation of the liner material. The version of ETFLOW used for this study allowed for simulation with and without the aforementioned vapor shielding effects, highlighting the contribution of different erosion mechanisms. Results are divided into two sections, simulations for those without a vapor shield mechanism, and simulations using both types of vapor shielding models. The heat fluxes from ELMs and disruptions are due to particle and radiative heat fluxes impacting PFMs, while the vapor shield effects seen in ET plasmas are solely based on radiative photon transport in the current research [10,11], while other models have included melting and splattering [12]. Thus, these results, which only consider photon transport through a vapor cloud, do not directly correlate with vapor shield effects expected from ELMs/disruptions with particle impact. Vapor shielding still occurs and plays a key role in reducing heat loads on PFCs in tokamaks, so the results give an analog for what could be expected from particle-based heat fluxes.

#### 6.3.1 – Ablation Simulations without Vapor Shielding

Ablation results without vapor shielding were obtained for SiC, $Ti_3SiC_2$, and $Ti_2AlC$, as well as ITER relevant materials W, Be, C, and Fe for comparison. Simulations were performed for 60-200 kA current pulses spanning 0.2-1 ms, resulting in average heat fluxes of ~30-150 GW/m$^2$ and total energy depositions of ~3-200 MJ/m$^2$. Plasma-material interactions (PMI) and erosion are both a surface area dependent phenomenon, and the amount of material lost per unit surface area

was found to be linear with respect to the energy deposition profile for all simulations and takes the form of Equation 21:

$$Eq\ 21. \quad M_{abl} = K \int_0^T Q"(t)dt$$

where $M_{abl}$ is the total ablated mass per $m^2$, Q"(t) is the time dependent heat flux in $W/m^2$ impacting the liner material surface over T seconds, and K is a linear constant hereafter referred to as the ablation constant. The ablation constant is a useful number as it is unique for each PFM and can be used to directly compare erosion characteristics irrespective of ELM/disruption conditions. K is most strongly determined by a material's overall heat of sublimation, with an inverse relationship $K \propto \frac{1}{H_{sub}}$. When considering material lifetime, comparing the volume or thickness loss is of importance. Dividing Equation 21 by density gives

$$Eq\ 22. \quad t_{abl} = \frac{K}{\rho} \int_0^T Q"(t)dt$$

where $t_{abl}$ is the thickness lost from a given ELM/disruption and ρ is the PFC material density. K/ρ is also unique for a given material, and can be used to directly compare erosion characteristics in terms of erosion depth. The resulting values for K and K/ρ for all simulations are given in Table 6.4. For visual comparison, graphs of the mass loss and erosion thickness as a function of time are shown in Figure 6.44 for the same shot conditions of 150 kA, 0.5 μs.

Table 6.4 – Ablation constant values from simulations with no vapor shielding

| *Material* | *Density [g/cm^3]* | *H_sub [kJ/mol]* | *Avg. K Value [kg/GJ]* | *Stdev [%]* | *K/ρ [cm^3/MJ]* |
|---|---|---|---|---|---|
| *6H SiC* | 3.2 | 802.005 | 27.01 | 1.65% | 8.44 |
| *3C SiC* | 3.2 | 803.105 | 26.99 | 1.62% | 8.43 |
| *$Ti_3SiC_2$* | 4.46 | 3244.6 | 32.63 | 0.83% | 7.32 |
| *$Ti_2AlC$* | 4.1 | 1870.15 | 38.33 | 1.34% | 9.35 |
| *Be* | 1.85 | 291 | 16.76 | 0.56% | 9.05 |
| *C* | 2.25 | 711.28 | 9.56 | 1.08% | 4.25 |
| *Fe* | 7.86 | 415.5 | 71.58 | 1.33% | 9.11 |
| *W* | 19.4 | 851 | 116.02 | 1.25% | 5.98 |

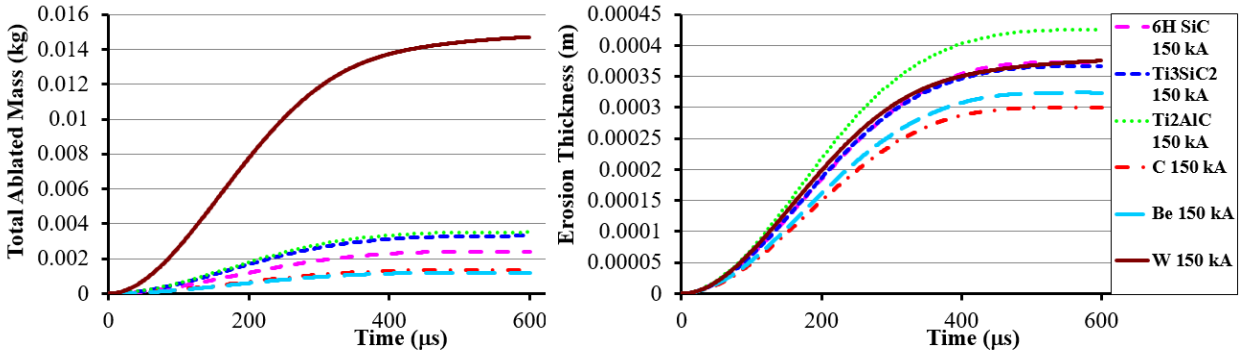


**Figure 6.44** - ETFLOW results of total eroded mass (Left) and eroded thickness (Right) for 150 kA discharge current, 500 μs pulse lengths for various tested materials.

The multiple SiC polytypes tested all gave nearly identical results due to little difference in sublimation energy, so only the 6H and 3C polytypes are given in Table 6.4. Differences in other important material properties between polytypes, namely thermal conductivity, should be taken into account for more in-depth PFM evaluations. Based on the K/ρ values, W and C still possess the best erosion resistance as far as thickness lost, since a lower K/ρ implies less erosion per unit energy flux. $Ti_3SiC_2$ is the next best value, followed by SiC. $Ti_2AlC$ performed the worst out of all materials.

6.3.2 – Ablation Simulations with Vapor Shielding

Simulations using both models of vapor shielding were performed for 6H SiC, Ti3SiC2, and Ti2AlC. Simulations were performed for 60-200 kA current pulses spanning 0.2-1 ms, the same discharge profiles from Section 6.3.1. The two different vapor shield models, the opacity and the fractional models, evolve the vapor shield quite differently with respect to time, which naturally results in stark differences in shielding efficiency. Using the same discharge current, the two models can be compared using the ratio of the total erosion with the vapor shield model to the total erosion in the equivalent ablation only simulation. One can then observe if and how this efficiency ratio changes in regards to disruption time and magnitude. These efficiency ratios, although related, should not be confused with the calculated transmission factor *f*. For the opacity model, the efficiency ratio will be denoted as $M_{abl\ O}/M_{abl.}$, and for the fractional model the ratio will be denoted as $M_{abl\ F}/M_{Abl}$.

Results from the fractional vapor shield model were relatively straightforward: each PFM candidate produced nearly identical efficiency ratios independent of the pulse profile. The transmission factor for this model follows the current/heat flux profile as it develops, with *f* decreasing as the impinging heat flux rises and relaxing back to unity as the heat flux extinguished. The efficiency ratios are given in Table 6.5. Results from the opacity model, on the other hand, show a strong variation with both heat flux magnitude and time span. General relationships between the efficiency of the vapor shield and a given disruption time and magnitude can be discerned from Figure 6.45, which shows results for $Ti_3SiC_2$. An efficiency ratio of 1.0 implies little to no effect of the vapor shield on material erosion, while a lower efficiency ratio implies a more effective vapor shield attenuating the heat flux and reducing material erosion. Two key relationships were observed for all materials: 1) For the same time profile, as the magnitude of the heat flux/energy deposition increases, the efficiency ratio increases, implying decreased vapor shielding. 2) For similar total energy fluxes over shorter time spans, i.e. increased heat fluxes across different time profiles, the efficiency ratio increases, again implying decreased vapor shielding. The range of opacity model efficiency ratios are tabulated in Table 6.5 based on disruption time.

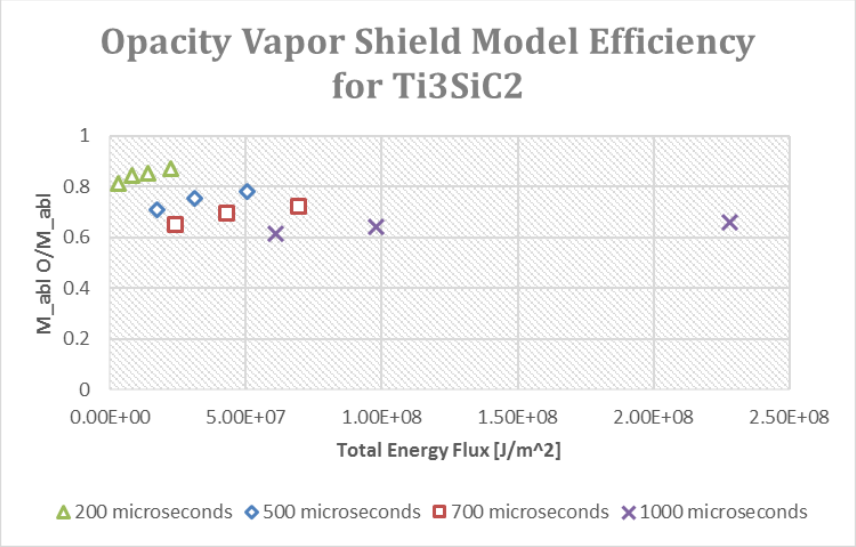


**Figure 6.45** – Efficiency ratios for $Ti_3SiC_2$ as a function of total energy flux

Table 6.5 – Efficiency ratio results for vapor shielding simulations

| Material | Time [μs] | Energy Deposition [MJ/m^2] | $M_{abl\ O}/M_{abl}$ | $M_{abl\ F}/M_{Abl}$ |
|---|---|---|---|---|
| SiC | 200 | 3-19 | 0.83-0.85 | 0.83 |
| | 500 | 16-45 | 0.67-0.74 | |
| | 700 | 22-62 | 0.59-0.67 | |
| | 1000 | 31-196 | 0.50-0.64 | |
| Ti3SiC2 | 200 | 3.0-22 | 0.81-0.87 | 0.87-0.89 |
| | 500 | 17-50 | 0.71-0.78 | |
| | 700 | 24-70 | 0.65-0.72 | |
| | 1000 | 61-230 | 0.62-0.66 | |
| Ti2AlC | 200 | 3-20 | 0.82-0.88 | 0.88 |
| | 500 | 16-46 | 0.72-0.79 | |
| | 700 | 22-63 | 0.66-0.73 | |
| | 1000 | 31-205 | 0.58-0.66 | |

In comparing the three alternative PFM candidates, SiC shows a slightly stronger effect of vapor shielding than the MAX Phases across similar ranges. $Ti_3SiC_2$ and $Ti_2AlC$ both show similar vapor shielding.

Based on simulations without vapor shielding, $Ti_3SiC_2$ is the superior alternative PFM candidate with SiC a close second. However, SiC shows superior vapor shielding efficiency. To properly discern which material exhibits the best erosion resistance, one must look at data points for total eroded thickness for similar pulse lengths as a function of total energy deposition, accounting for vapor shielding effects. Figure 6.46 shows that for similar disruption conditions, SiC exhibits the lowest alternative PFC thickness loss while $Ti_3SiC_2$ exhibits comparable erosion resistance, superior to the other MAX Phase $Ti_2AlC$.

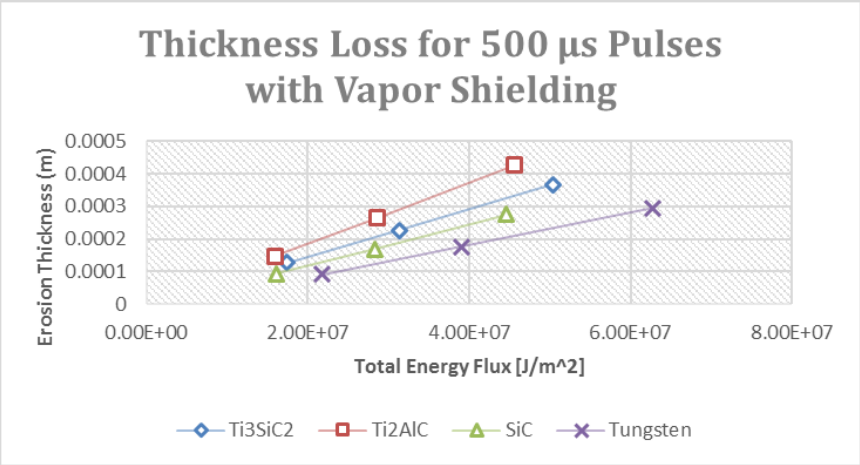


**Figure 6.46** – Thickness losses for alternative PFM candidates for 500 µs disruptions using the opacity vapor shielding model.

## REFERENCES


[1] C.P. Wong et al. "Divertor materials evaluation system at DIII-D." *Journal of Nuclear Materials*, vol. 196–198, 1992

[2] A. Herrmann et al. "Energy flux to the ASDEX-Upgrade diverter plates determined by thermography and calorimetry." *Plasma Phys. Control. Fusion*, vol. 37, 1995

[3] T. Abrams et al. "The inter-ELM tungsten erosion profile in DIII-D H-mode discharges and benchmarking with ERO+OEDGE modeling." Nuclear Fusion, vol. 57, no. 056034, 2017

[4] I. Borodkina et al. "An Analytical Expression for the Electric Field and Particle Tracing in Modelling of Be Erosion Experiments at the JET ITER-like Wall." *Contrib. Plasma Phys.*, vol. 56, no. 6-8, 2016, pp. 640 – 645

[5] R. Khaziev and D. Curreli, "Ion energy-angle distribution functions at the plasma-material interface in oblique magnetic fields." *Physics of Plasmas*, vol. 22, no. 043503, 2015

[6] "Emissivity Values," *Optotherm Thermal Imaging*, https://www.optotherm.com/emiss-table.htm Accessed 15 Aug. 2018

[7] "Si - Thermal Properties," IOFFE materials database, http://www.ioffe.ru/SVA/NSM/Semicond/Si/thermal.html Accessed 18 Aug. 2018

[8] G. Miloshevsky and A. Hassanein, "Stability and Erosion of Melt Layers Developed on Plasma Facing Components of Tokamaks." *Nuclear Fusion*, vol. 54, no. 043016, 2014

[9] R.A. Pitts et al. "A Full Tungsten Divertor for ITER: Physics Issues and Design Status," *Journal of Nuclear Materials*, vol. 438, 2013, S48-S56

[10] A. L. Winfrey et al. "A Study of Plasma Parameters in a Capillary Discharge with Calculations Using Ideal and Nonideal Plasma Models for Comparison With Experiment," *IEEE Transactions on Plasma Science*, 40, 843 (2012)

[11] N. Almousa and M. Bourham, "Vapor Shield Models in Electrothermal Capillary Discharges and Comparison with Experiments," presented at IEEE ICOPS-Beams 2014, Washington DC, May 25–29, 2014.

[12] N. Almousa, J. Gilligan and M. Bourham, "Surface Ablation and Melting of Fusion Materials Simulated by Transient High Heat Flux Generated in an Electrothermal Plasma Source." *IEEE Trans Plasma Sc.*, vol. 44, 2016

# CHAPTER 7 – DISCUSSION AND CONCLUSION

## 7.1 – DIII-D Experiment (Physical Sputtering Regime)

Only two of the desired alternative plasma-facing materials were exposed in the DIII-D tokamak using the FIB micro-trench technique. Of the 10 cut, polished, and micro-trenched samples of SiC, $Ti_3SiC_2$, and $Ti_2AlC$ prepared for the experiment, only 6 were allowed exposure time on DIII-D. These consisted of the two angled SiC samples and the two angled $Ti_3SiC_2$ samples analyzed in Chapter 6 Section 6.1, along with two flush SiC samples which yielded no quantifiable results. This material constraint was due to run-time limitations on DIII-D. The original DIII-D experiment proposal called for multiple DiMES sample holders to expose alternating SiC, $Ti_3SiC_2$, $Ti_2AlC$, and W under separate L-mode and H-mode exposures. For the two samples that did receive exposure time, the DIII-D experiment was overall successful. Both SiC and $Ti_3SiC_2$ survived the multiple DIII-D exposures with no discernable macroscopic damage, demonstrating their robustness as possible PFMs with manageable net erosion from physical sputtering. The desired heat flux range of 5 – 10 MW/m$^2$ was achieved on the SiC samples, while the $Ti_3SiC_2$ samples only experienced 2 – 3.5 MW/m$^2$ according to the DiMES IRTV analysis. Although lower than desired, this heat flux is still relevant to the lower-end of large-scale reactor operations and is a decent first dataset for the MAX phase material.

There were multiple complications with the DIII-D experiment that were discussed in Chapter 6 in an isolated context. They are further addressed and considered here in the context of the overall dissertation goals. First, there are multiple sources of error associated with the heat flux analysis. The greatest source of uncertainty comes from the mixed L-mode and H-mode plasma exposures. The micro-trench erosion technique is an integral method for this experiment; samples experienced consecutive heat and particle fluxes across the 7 plasma discharges, with the erosion rates of Fig. 6.5 – 6.7 corresponding to the total amount of observed erosion divided by the total integrated exposure time. Thus, the erosion rate of each material due to ELM impacts is incorporated with the erosion rates due to steady-state plasma impact. For physical sputtering, the increase in particle energies and densities will lead to different rates of erosion compared to the steady-state plasma flux. The presence of ELMs in half of the plasma discharges led to increased variation in the average temperature rise, as in Fig. 6.4, which was used to calculate the average heat flux across the 7 discharges. Importantly, the error introduced by this averaging is small

compared to the trend seen for SiC, asserting that the increase of erosion rate with increased heat flux is real. Looking at the temperature profiles for the samples, only ~10 ELMs per shot were observed in the IR data for the four H-mode exposures. At about 0.001 s per ELM, the total erosion due to ELMs would only account for a conservative 0.04 s of the total 16 s of plasma exposure time. Thus, what is reported for the results can be considered a good representation of the average erosion rate for the reported average heat flux values, meeting the dissertation goals.

There are two sources of error associated with the micro-trench analysis. The first comes from the resolution of the SEM images. The highest-magnification images (10,000x) possessed resolutions of about 8 nm/pixel for both the top-down images and angled images. Since each length measurement was done by eye, one can estimate a precision of 5-6 pixels per measurement (2-3 for each end of the length measurement), resulting in a precision error of at-most +/- 45 nm. The second, more prevalent source of error represents the standard deviation in the erosion depth magnitudes across micro-trench samples. These errors manifest from differences in the three triangular fiducial markings measured for each micro-trench, and represent the deviation in erosion uniformity. Propagating the error from image resolution into this error measurement, the resulting total error is about 1 – 5 nm/s for most samples. This precision was appropriate for drawing conclusions for the SiC dataset, equating to a 5-10% error. Unfortunately, erosion magnitudes for the $Ti_3SiC_2$ data were on the same order of the dataset's standard deviations, so a statistically significant linear trend could not be discerned. In this regard, adequate conclusions for this dissertation can be drawn for the SiC, but only a general statement of 0-9 nm/s at heat fluxes of 2 – 3.5 MW/m$^2$ can be confidently claimed for $Ti_3SiC_2$.

Attempting to correlate material erosion rates as a function of impinging heat flux did make it difficult to compare with results from the literature. Physical sputtering studies usually correlate total gross erosion rates to the average ion impact energy, with the goal of generating sputter yield curves as in Fig. 2.1. The average heat flux in those experiments is often excluded in the corresponding manuscripts. It was expected that, in general, the higher Z materials would exhibit lower gross erosion rates due to sputtering. Keeping in mind that other microscopic properties should also affect the average sputtering rate, it was assumed that the high purity and high covalent bonding of SiC, along with an average high-Z in the MAX phases, would lead to low sputtering yields when compared to W, Be, and C.

Similar exposures of W samples on DIII-D report erosion rates of about 0.5 – 1.5 nm/s under L-mode exposures (~0.5 - 1 $MW/m^2$) [1,2], and 0.5 - 1 nm/s under H-mode exposures with ELMs (~1 $MW/m^2$ steady state, a few $MW/m^2$ during ELMs) [3,4]. Assuming a linear relationship with heat flux, these experimental values conservatively translate to about 5 – 10 nm/s net erosion rates under 5 – 10 $MW/m^2$ heat flux conditions. For Be exposures, DIII-D has performed DiMES experiments using Al as a proxy to Be, which reported net erosion rates of 2 – 6 nm/s under L-mode conditions [5]. A conservative translation to the 5 – 10 $MW/m^2$ conditions leads to an estimated 20 – 60 nm/s. Translating and comparing these results at the same heat flux magnitudes, the SiC erosion rates are less than an order of magnitude greater than W erosion under similar exposure conditions. The $Ti_3SiC_2$ results, although less certain, are in general the same as SiC and thereby compare similarly with W. These results are somewhat expected, with W having a much higher $Z_{eff}$ (74) than SiC (10) and $Ti_3SiC_2$ (15.3).

Evaluating the quantitative and qualitative performance of SiC and $Ti_3SiC_2$ in the DIII-D experiment, and comparing it to similar W erosion experiments from the literature, the relative performance rankings for each material in a sputtering-dominated erosion regime are as displayed in Table 7.1. Tungsten is estimated to exhibit the lowest net erosion rate under reactor-relevant steady state heat fluxes by almost an order of magnitude compared to the other materials. The imprecise erosion data for $Ti_3SiC_2$ lies in-between the split dataset for SiC when extrapolated. The safest argument in this case is that $Ti_3SiC_2$ erodes at a similar rate to SiC. However, if considering the worst-case scenario, $Ti_3SiC_2$ does appear to exhibit about 50% lower erosion rates than the highest SiC erosion rate case (for a linear model). This conclusion is of course not a strong one due to the error associated with the $Ti_3SiC_2$ dataset.

Table 7.1 – Ranking of material performance during DIII-D experiment

| PFM Performance Comparison – Physical Sputtering Regime | | | | |
|---|---|---|---|---|
| Material | Relative Erosion Rate | Macroscopic Damage | Microscopic Surface Damage | **Overall PFM Ranking** |
| Tungsten | Great | Great | Ok | 1st |
| $Ti_3SiC_2$ | Ok | Great | Great | 2nd |
| SiC | Ok | Great | Great | 3rd |
| $Ti_2AlC$ | N/A | N/A | N/A | N/A |

At the end of the analysis, the DIII-D experiment did not give a straightforward erosion rate comparison. The micro-trench technique was a success for SiC, providing a dataset with confident trends and error values. It is unfortunate that a straightforward comparison with the $Ti_3SiC_2$ data cannot be discerned due to 1) the low net erosion of $Ti_3SiC_2$ due to heat flux shadowing of the DiMES samples and 2) the double trend observed in the SiC data. The local precision of the micro-trench technique highlighted the variations in ion trajectories and erosion physics with analysis location. However, the overall study is a testament to why analyzing erosion in a physical-sputtering dominated regime as a function of impinging heat flux is not sufficient. Analyzing the impinging particle energy and particle flux separately, and then considering their combined effects on the net average surface erosion, is more meaningful. With the spectroscopy results being unusable for this experiment, many physics questions relating to specific sputtering events are left unanswered. For any future erosion experiments focused on heat flux in DIII-D, it is recommended to prioritize the traditional variables of ion species, density, and temperature, and then calculate the effective heat flux from those variables.

### 7.2 – ET Experiment (Melting/Sublimation Regime)

All of the selected alternative plasma-facing materials were tested by ET exposures using the FIB micro-trench technique. Of the 15 cut, polished, and micro-trenched samples, 13 yielded quantifiable erosion results. The desired heat flux range was 1 – 10 GW/m$^2$. The attained heat flux range, 0.9 – 1 GW/m$^2$, is at the threshold for disruption- and ELM-relevant heat fluxes expected

in large-scale fusion devices. An ELM-relevant timescale of 1000 – 1200 μs was achieved for all ET discharges.

There were multiple complications with the ET experiment that were discussed in Chapter 6 in an isolated context. They are further addressed and considered here in the context of the overall dissertation goals. First, the error associated with the calculated heat flux values are larger than expected. Two experiment variables were introduced to obtain a range of heat fluxes: different charges across the capacitor bank (changing the current discharge through the source) and micro-trenches set at the center and 2 mm away from the center. The limited IR dataset indicates a negligible (< 5 %) difference across the three micro-trench locations for individual shots. In addition, there are a multitude of error sources associated with estimating the heat flux data via Eq. 15 of Chapter 6, including: 1) limited clean shot data, resulting in only 2 – 3 data points available for averaging at a given ΔV, 2) lack of precision in capturing the peak temperature in IR data due to a slow frame rate, and 3) emissivity correction issues associated with the IR data. These issues combine into a propagated standard deviation of 5 – 10 % associated with the data in Figs. 6.41 – 6.43. These error bars were not displayed because their overlap significantly crowded the figures. In reality, one standard deviation encompasses the majority of the 0.9 – 1 GW/m$^2$ heat flux range.

This error could have been partially improved if more calibration shot data had been available, or if the hydrocarbon ash had not been an issue. Using a boron-nitride source liner as in reference [6] would have yielded both a cleaner window and an increased heat flux range. The use of Lexan was driven by its availability, its consistent performance in ET sources, and the established cleaning method for the time-intensive micro-trench samples. The available IR camera was operated at the fastest possible frame rate. Further error reduction due to frame precision would have required a relatively new and improved camera. Finally, the error introduced by emissivity requirements is largely unquantifiable. Emissivity values are known to be temperature dependent. Further, the emissivity value of each sample surface likely changes during the plasma exposure. As surfaces erode, roughen, and are covered with ash, emissivity likely increases over the course of the plasma discharge. The option to re-evaluate the sample emissivity post-exposure was discussed. There was a concern with heating the ash-covered samples and modifying any erosion features within the micro-trenches, so this option was not implemented. A static emissivity value had to be assumed across the discharge, at least up to the first analyzed frame of IR data.

Great effort was taken to reduce errors in the heat flux analysis. Even so, limited shot data and diagnostic capabilities lead to a small heat flux range with substantial error. As such, the trends of erosion rate as a function of increasing heat flux cannot be reliably discerned with this dataset.

Errors amongst the microscopy erosion dataset should also be reviewed. The IR data implies a uniform heat flux across an individual sample surface, as in Fig. 6.14 of Chapter 6. For this reason, the erosion rate data (from $\Delta t_S$ and $\Delta t_{S+C}$) were initially averaged across all micro-trench locations. Contrary to the heat flux data, the microscopy results imply non-uniform erosion across the samples, with standard deviations ranging from 25 – 90% for the fully averaged datasets. Local measurements taken at the individual micro-trench locations were on average more precise. Unexpected, complex surface erosion mechanisms further inflated the local nature of the micro-trench method. For these reasons, it was decided (as mentioned in Chapter 6) to focus solely on the individual micro-trench with the highest magnitude erosion measurements. This decision allows for more interpretable material comparisons for the uncertain dataset. Choosing to only focus on the worst-case scenario for each sample at a given heat flux value is reasonable given the spread in heat flux data alone. A general comparison between materials can be made in confidence.

The original intention of the ETFLOW code simulations in Section 6.3 of Chapter 6 were to directly complement the ET source experiments at ORNL. This comparison relied on the ET material exposures quickly reaching a fully sublimation-dominated erosion regime. From both the microscopy images and the IR data, it is clear that the W surface temperature exceeded the 3420 °C melting point but stayed below the 5930 °C boiling point. IR data implied that SiC stayed at lower temperatures than W, barely exceeded the required sublimation temperature of 2800 °C. Such behavior would explain the low erosion rates measured for SiC. Until the material surface is brought up to the proper sublimation temperature, energy from the ET heat and particle flux will go into physical sputtering and raising the bulk temperature. The ETFLOW simulations are designed and validated for modeling erosion of the liner material under 10's of GW/m$^2$ of radiant heat flux within the ET source. Without any temperature control, the ET targets located outside the source exit inherently traverse all possible erosion regimes, evolving from physical sputtering to melting to sublimation throughout the course of the short ET discharge. Comparing the two datasets is therefore uninformative due to such stark differences in erosion mechanisms and heat flux magnitudes.

Evaluating the quantitative and qualitative performance of all PFMs in the ET experiment, and comparing the results to those expected from ideal ETFLOW simulations, the relative performance rankings for each material under ELM and disruption conditions is displayed in Table 7.2.

Table 7.2 – Ranking of material performance during ET experiment

| **PFM Performance Comparison – Melting/Sublimation Regime** | | | | |
|---|---|---|---|---|
| Material | Relative Erosion Rate | Macroscopic Damage | Microscopic Surface Damage | **Overall PFM Ranking** |
| SiC | Great | Great | Great | 1st |
| Tungsten | Great | Ok | Ok | 2nd |
| $Ti_2AlC$ | Poor | Great | Ok | 3rd |
| $Ti_3SiC_2$ | Poor | Ok | Poor | 4th |

Both MAX phase ceramics demonstrated poor performance in their first high heat flux plasma exposures. In terms of the surface erosion parameter $\Delta t_S$, the maximum erosion rates of both materials were a few factors higher than SiC and W, as in Figs. 6.41 and 6.42 of Chapter 6. However, the greatest impact on performance is the surface fracture erosion mechanic seen in both MAX phase ceramics. The MAX phases were originally selected for their reported thermal shock resistance at elevated temperatures. These microscopy results definitively conclude that the materials cannot survive such intense thermal shocks, at least when starting at room temperature conditions. The magnitudes of erosion damage recorded in Fig. 6.43 will be unacceptable for any reactor environment with unexpected ELMs or disruptions. $Ti_3SiC_2$ was more prone to deep surface fractures and material ejection than $Ti_2AlC$. This observation is likely due to the slightly better thermal properties of $Ti_2AlC$ compared to $Ti_3SiC_2$. The thin melt-layer formation and bulk deformation observed in $Ti_2AlC$ probably dampened any bulk fracturing as well. For this reason, $Ti_2AlC$ is ranked the superior MAX phase ceramic under the ET plasma conditions. Tungsten did exhibit the best performance in terms of $\Delta t_S$ with practically zero material erosion. However, extreme melt-layer formation and motion was observed across the entire surface, with melt-layer deformation observed to penetrate 1 – 7 μm deep. It is the melt-layer depth that is accounted for in Fig. 6.43 for tungsten. Consecutive exposures were seen to notably increase molten pit

formation and melt-layer motion, confirming long-term material performance concerns in studies for ITER [7]. Silicon carbide exhibited stellar performance by comparison, surviving up to 15 consecutive ET plasma exposures of about 0.9 GW/m$^2$ heat flux with an average erosion rate of about 20 μm/s. Evaluating both the erosion data and the observed material deformation mechanisms, silicon carbide demonstrated the best performance under the high heat flux ET discharges.

With all of the aforementioned errors associated with this ET experiment campaign, it is important to recognize that the rankings in Table 7.2 are more qualitative in nature. Additionally, the erosion results represent the full, time-dependent materials response to ELMs/disruptions rather than erosion in an ideal 'sublimation-dominated' regime. A few suggestions are presented for any future experiments using the ORNL ET source. An additional method of heat flux measurement to complement any IR camera analysis is highly recommended, such as thermocouples attached to a specially engineered sample plus holder combination. A high-speed IR camera is still necessary for time resolution, as the feedback from thermocouples would be time-limited by sample thermal diffusivity. An IR camera with greater frame rate capabilities is highly recommended. Substantial reduction in heat flux uncertainty can be gained from taking temperature data closer to the peak of plasma flux impacting the sample surface. The last suggestion for any erosion rate experiments on the ET source is to incorporate heated samples if possible. The MAX phases, for example, might have avoided severe cracking if brought closer to their engineered operating temperatures. In a large-scale fusion reactor, the divertor and first wall will be operated at elevated temperatures but with active cooling systems. The time-dependent thermal response from ELM and disruption impacts will differ in this scenario from the ET exposures with no temperature control. The introduction of heating systems was briefly discussed for this experiment but eventually set aside due to time and safety constraints. The value of performing material exposure experiments at realistic operating temperatures is hereby emphasized.

### 7.3 – Overall PFM Performance

As described in Chapter 1, the alternative PFMs of interest are to be evaluated under reactor-relevant conditions expected in large-scale tokamaks. Practical materials must present a

sufficient lifetime under steady-state operating conditions with contingency room to handle erosion from undesired ELMs and disruptions. ITER will push material limitations into uncharted territory while striving to achieve a burning plasma and surpassing energy breakeven. At present, the ITER design represents the best estimate for conditions PFMs must handle in next-generation reactors. Predicted survival of these alternative PFMs in ITER is a good first step to their consideration in future devices.

The steady state heat flux conditions in ITER are well established at 5 – 10 MW/m$^2$, with the capability to handle up to 20 MW/m$^2$ during planned, "slow" transient events [7,8,9]. The expectations of allowable ELMs and disruptions is more uncertain. For ELMs, the best-case scenario is total suppression via the RMP field coils. If those prove ineffective when scaled to ITER-size plasmas, the contingency plan is to operate the three pellet injector systems for ELM mitigation. Expected injection frequencies are currently set to be 45 – 60 Hz, with the goal of reducing ELM energies impacting the divertor to below 0.5 MJ/m$^2$ [10]. The R&D efforts to determine the maximum acceptable disruption rate on ITER are ongoing. The disruption information found in references [7,9,11] can provide an estimate for this study. In these literature sources, the first W divertor is expected to last through the entirety of the first D-T fueled campaign, which will consist of about 12,000 pulses that equate to about 8*10$^6$ s of plasma exposure. These exposures will extend up to the maximum operating requirements, from Q = 2 up to Q = 10. They must also involve radiative divertor operations, providing up to a 90% reduction in radiated power. For disruptions, a conservative disruption fraction of 5% can be considered for these high current operations, with high expectations for disruption mitigation system efficiency of 95%. These rough estimates predict a total of 30 unmitigated, high-power disruptions during the D-T campaign, depositing heat fluxes as high as 2 – 75 GW/m$^2$ [7].

Based on the erosion rate data from Section 7.1, tungsten would exhibit the lowest total erosion under steady state 10 MW/m$^2$ conditions at ~8 mm. This rough calculation using DIII-D data ignores factors such as prompt redeposition that will likely be enhanced in the higher pressure, higher B ITER divertor region, further lowering the erosion rate. The current ITER W divertor utilizes a 6 mm thick W armor [12]. SiC and $Ti_3SiC_2$ erosion data from the DIII-D experiment then implies an order of magnitude increase to about 50 – 60 mm thick armor, which may or may not be practical for a reactor-scale tokamak. The analysis changes when considering possible ELM-ing and disruption conditions. Assuming an ELM-ing H-mode regime with 45 Hz ELM mitigation

for half of the D-T ITER operations, an estimated $1.8*10^8$ ELMs would be generated. However, not all of those ELMs impact the same surface area; a factor of 10-20 decrease is often appropriate to estimate the actual impact rate at DIII-D. Considering this for a 250 μs, 0.5 MJ/m$^2$ series of ELMs alongside a series of conservative 2 GW/m$^2$ disruption condition, an overall additional thickness of about 45 mm is estimated for W, without addressing melt-limits. For SiC, this translates to an equivalent 49 mm or so. Figure 6.43 implies an increased dimensional requirement on the order of meters for $Ti_3SiC_2$ or $Ti_2AlC$, which is entirely unrealistic. For W, melting is predicted for Q = 10 operations, even including ELM broadening effects [7]. Modeling of erosion due to melt-layer motion and splashing is rapidly evolving [12] but was considered outside the scope of this dissertation work, so material loss is assumed but the exact amount is uncertain.

For the final performance evaluation, an operating scenario is envisioned where high energy ELMs are mitigated, rather than suppressed, and disruptions go unmitigated every 1/400 exposures. Considering both the quantitative and qualitative performance of the alternative PFMs across all dissertation experiments, the relative ranking for each material is displayed in Table 7.3. A visual comparison of each PFM's performance (from the ET experiment) is also displayed in Figure 7.1 to further highlight the PFM rankings.

Table 7.3 – Overall ranking of material performance across all experiments

| **Overall PFM Performance Comparison** | | | | |
|---|---|---|---|---|
| Material | Relative Erosion Rate | Macroscopic Damage | Microscopic Surface Damage | **Overall PFM Ranking** |
| SiC | Ok | Great | Great | 1st |
| Tungsten | Great | Ok | Ok | 2nd |
| $Ti_2AlC$ | Poor | Great | Ok | 3rd |
| $Ti_3SiC_2$ | Poor | Ok | Poor | 4th |

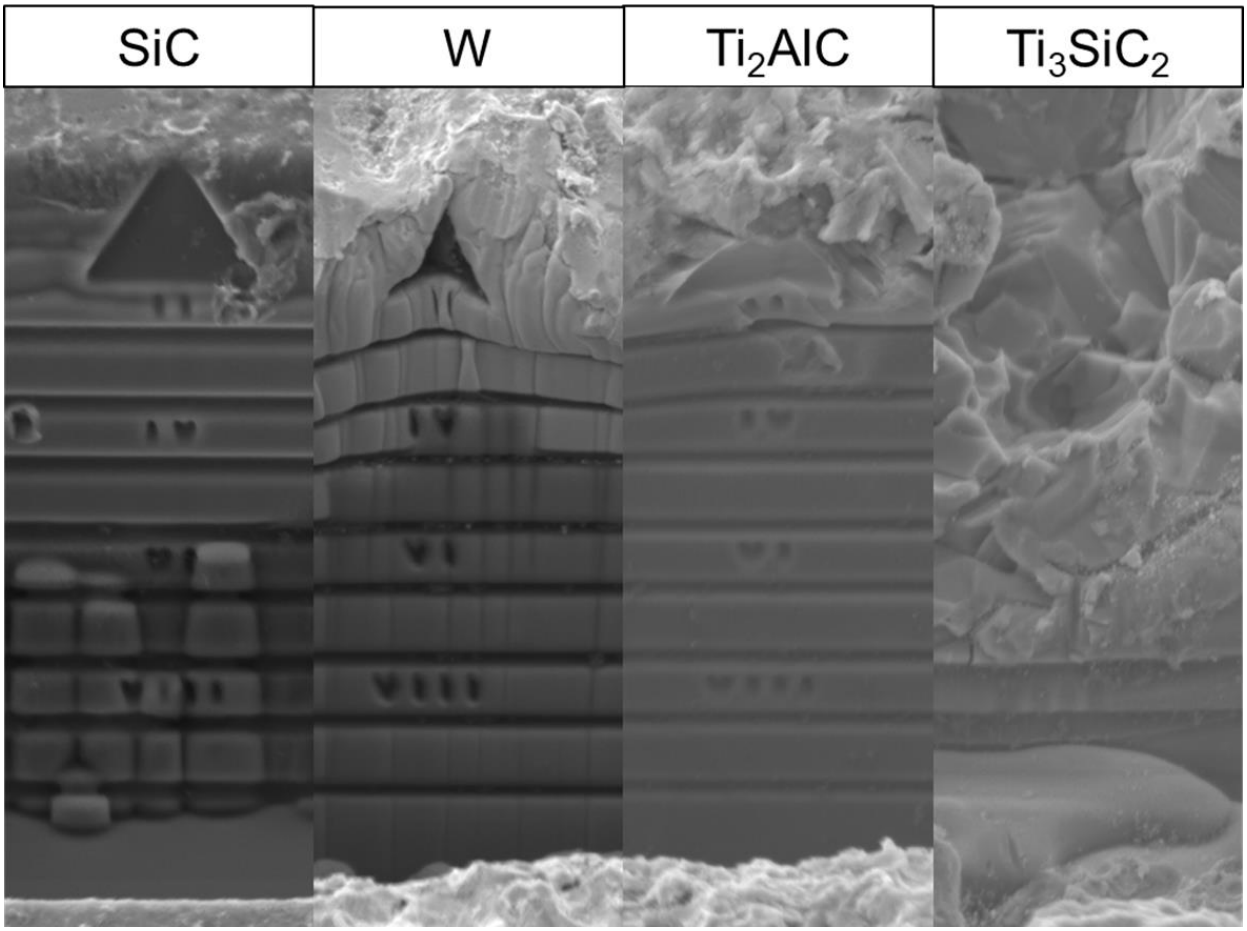


**Figure 7.1** – Visual comparison of PFM performance from similar ET exposures, highlighting the overall PFM rankings for the dissertation. The materials are arranged in order of best to worst performance, with SiC showing the best erosion resistance and $Ti_3SiC_2$ the worst erosion resistance.

Strictly from a physical sputtering erosion standpoint, W is the superior material, requiring almost 10x less material to build divertor armor tiles. However, the risk of macroscopic damage due to melt-layer motion is severe. ELM-ing regimes are enough to warrant melting concerns in ITER [7,9], let alone the risk due to unscheduled disruptions. The two major benefits to SiC in this regard are that it sublimates rather than melting while offering comparable thermal properties at elevated operating temperatures [Appendix A]. Other tangential benefits to using SiC rather than W include improved neutronics, low-Z ions for better plasma compatibility, and low tritium retention. If high-purity β-3C SiC can withstand ITER-grade ELMs and disruptions in the same manner as in the ET experiments, with little to no discernable surface damage, it is the clear

material choice for risky operational regimes. These benefits combined seem well worth the engineering cost of thicker PFM armor dimensions to compensate for higher sputtering yields. In an ideal reactor environment with no ELMs or disruptions, the MAX phase ceramics could serve as viable PFMs. However, considering the extreme erosion due to surface fracturing observed in Chapter 6, both $Ti_3SiC_2$ and $Ti_2AlC$ are likely unfit to serve as PFMs in either the divertor or first wall region. Another experiment with heated samples is the only foreseen avenue through which these two particular MAX phases should be again explored.

### 7.4 – Final Remarks and Future Work Suggestions

The final results plot envisioned in Fig. 1.4 of Chapter 1 was able to be constructed at the end of the dissertation study as Figure 7.2. The plot is not ideal, requiring linear extrapolations for some materials' datasets as well as some tungsten data from the literature [1-4]. Points in Fig. 7.2 with error bars are from this dissertation's experiments while points without error are either extrapolated or from literature sources. Although it is not a complete picture, the log-log plot does provide a means of comparison between the alternative PFMs of interest across a wide range of heat flux values. In retrospect the type of erosion rate study is too complex to relate solely to the impinging heat flux. A material's transition to a melting or sublimation dominated erosion regime is driven by both the average impinging heat flux magnitude and the average time duration of that heat flux. In this regard, the results displayed in Figs. 6.5 – 6.7 and Figs 6.41 – 6.43 are sufficient.

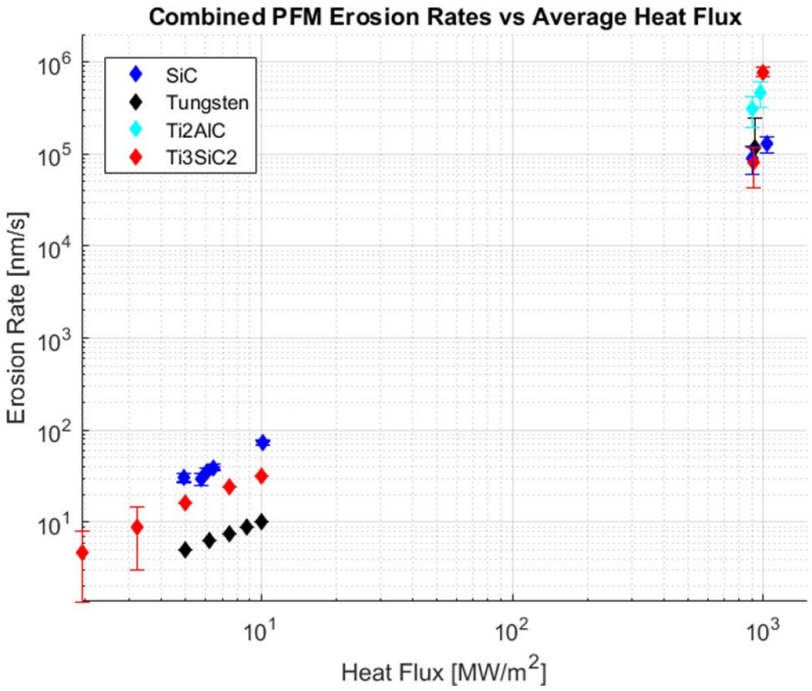


**Figure 7.2** – PFM erosion rate comparison as a function of impinging heat flux, the final goal of this research work

The FIB micro-trench technique was well-worth developing for this comprehensive erosion study. The advanced microscopy tools and techniques available at ORNL and NC State were utilized as best as possible, allowing for the successful development of a non-destructive post-mortem analysis technique. The precise localization of erosion results allowed for unique conclusions to be drawn with respect to micro-trench location, particularly in the DIII-D experiment. The combination of the micro-trench technique alongside AFM mapping proved especially intriguing for collaborators at DIII-D. Interest in ET source capabilities has also been piqued at ORNL, largely driven by the observed melting of tungsten samples.

Although erosion results for the alternative plasma-facing materials of interest were not ideal, qualitative conclusions have been confidently made and broad estimations of PFM performance on an ITER-like tokamak have been performed. This dissertation highlights the importance of continued exploration into alternative PFMs, and has played the role of evaluating new materials while developing advanced analysis methods. For future work inspired by this dissertation, it is recommended to continue exploring well-engineered SiC materials and other ceramics that sublimate rather than melting. If further tokamak exposures are designed, such as on

DIII-D, a dedicated L-mode vs H-mode experiment with ideal exposure conditions would be valuable. This type of study would be well-complemented by plasma exposures on linear devices, such as Proto-MPEX/MPEX at ORNL, so long as the exposure conditions are made to match plasma impacts within a tokamak. For SiC in particular, a simultaneous test of the high-purity β-3C CVD with SiC/SiC composites would be valuable as that material was not acquired for this study. Another recommendation is to further develop the micro-trench technique for dedicated ion impact angle studies, combining SEM imaging and AFM mapping capabilities with micro-trenches specifically designed for a dedicated tokamak experiment. There might be possibilities for redeposition and material migration studies as well. As for the MAX phase ceramics, if they are again tested, it is recommended to test the MAX phases under heated conditions. This recommendation is particularly important for any further ELM or disruption studies. Different MAX phase ceramics should also be explored. Selecting MAX phases with better thermal and mechanical properties, irrespective of irradiation properties and commercial availability, could lead to vastly different erosion performance under extreme conditions.

## REFERENCES


[1] J.N. Brooks et al. "Analysis of a tungsten sputtering experiment in DIII-D and code/data validation of high redeposition/reduced erosion." *Fusion Engineering and Design*, vol. 94, 2015

[2] D.L. Rudakov et al. "Net versus gross erosion of high-Z materials in the divertor of DIII-D." *Physica Scripta*, vol. T159, 2014

[3] T. Abrams et al. "The inter-ELM tungsten erosion profile in DIII-D H-mode discharges and benchmarking with ERO+OEDGE modeling." *Nuclear Fusion*, vol. 57, 2017

[4] J.L. Barton et al. "Comparison of heat flux measurement techniques during the DIII-D metal ring campaign." *Physica Scripta*, vol. T170, no. 014007, 2017

[5] C. Chrobak et al. "Measurements of gross erosion of Al in the DIII-D divertor." *Journal of Nuclear Materials*, 2014

[6] T.E. Gebhart et al. "Material impacts and heat flux characterization of an electrothermal plasma source with an applied magnetic field," *Journal of Applied Physics*, vol. 122, no. 063302, 2017

[7] R.A. Pitts et al. "A Full Tungsten Divertor for ITER: Physics Issues and Design Status," *Journal of Nuclear Materials*, vol. 438, 2013, S48-S56

[8] M. Merola et al. "ITER Plasma-facing Components." *Fusion Engineering and Design*, vol. 85, 2010, pp. 10-12

[9] R.A. Pitts et al. "Physics Basis and Design of the ITER Plasma-Facing Components," *Journal of Nuclear Materials*, vol. 415, 2011

[10] A. Loarte, "ITER and Pedestal Physics." Presentation, 2015 ITER International School, USTC, Hefei, China 2015

[11] P.C. de Vries et al. "Survey of Disruption Causes at JET", Nuclear Fusion, vol. 51, no. 053018, 2011

[12] R.A. Pitts et al. "Physics basis for the ITER tungsten divertor," Presentation, 23rd International Conference on Plasma Surface Interactions, Princeton, USA 2018

# APPENDIX

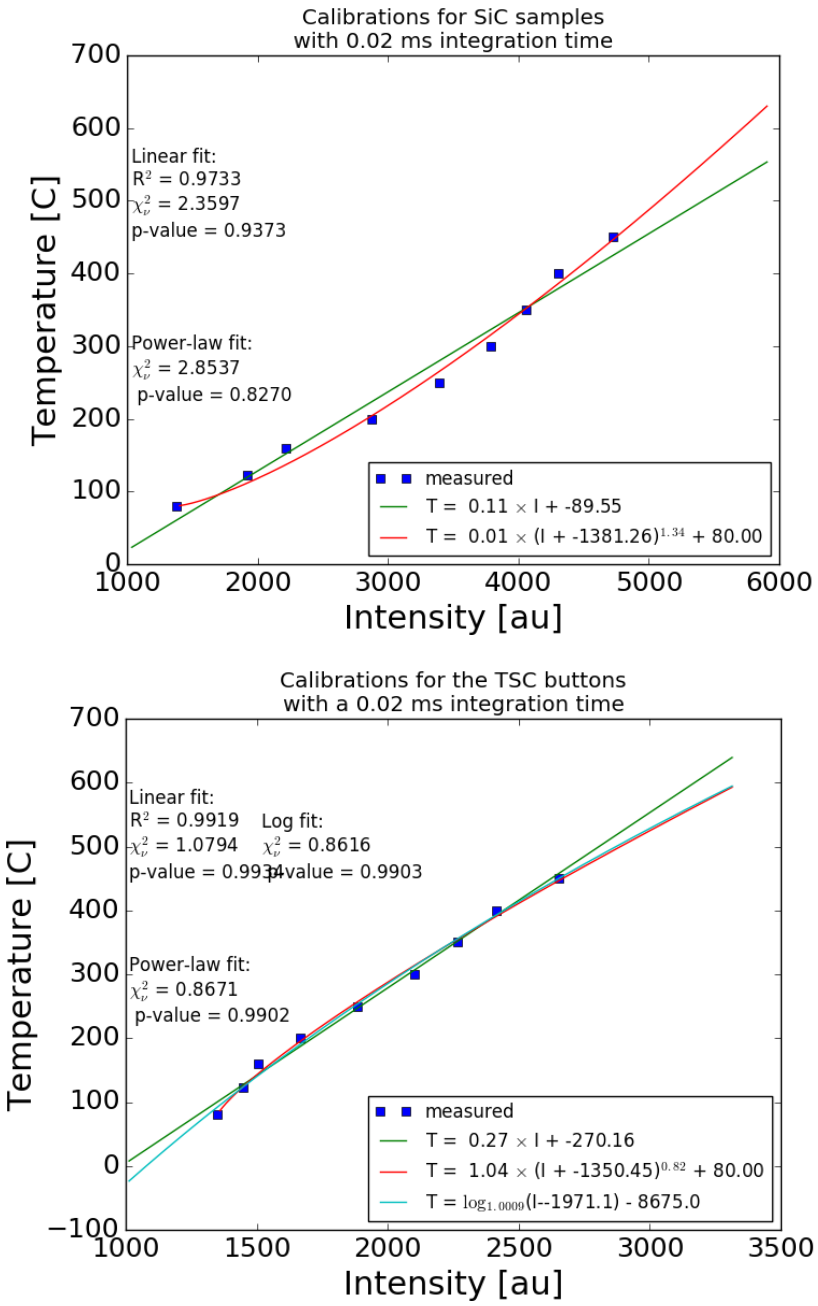


**Figure A.1** – DiMES IRTV Fits for Temperature vs. Intensity

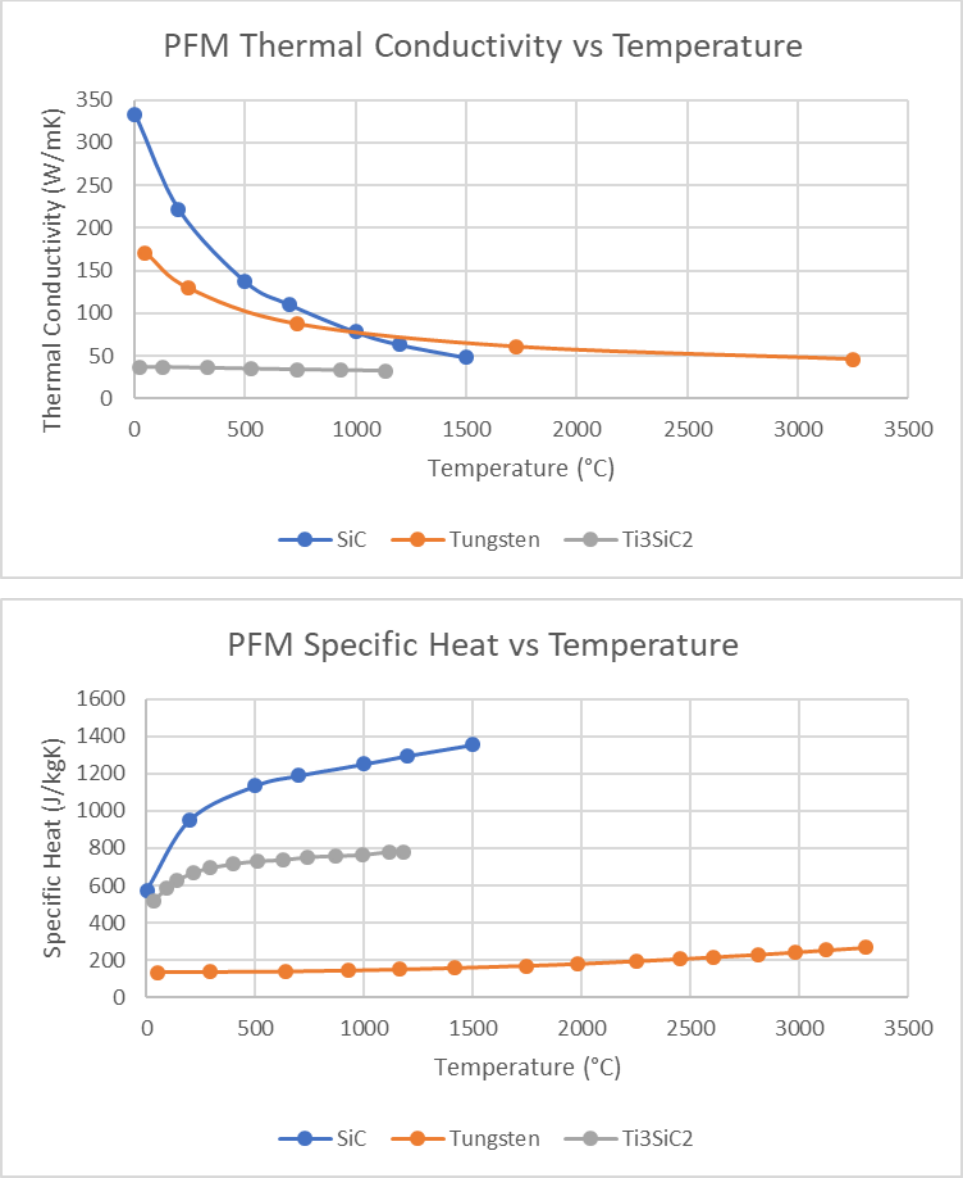


**Figure A.2** – PFM Thermal Properties

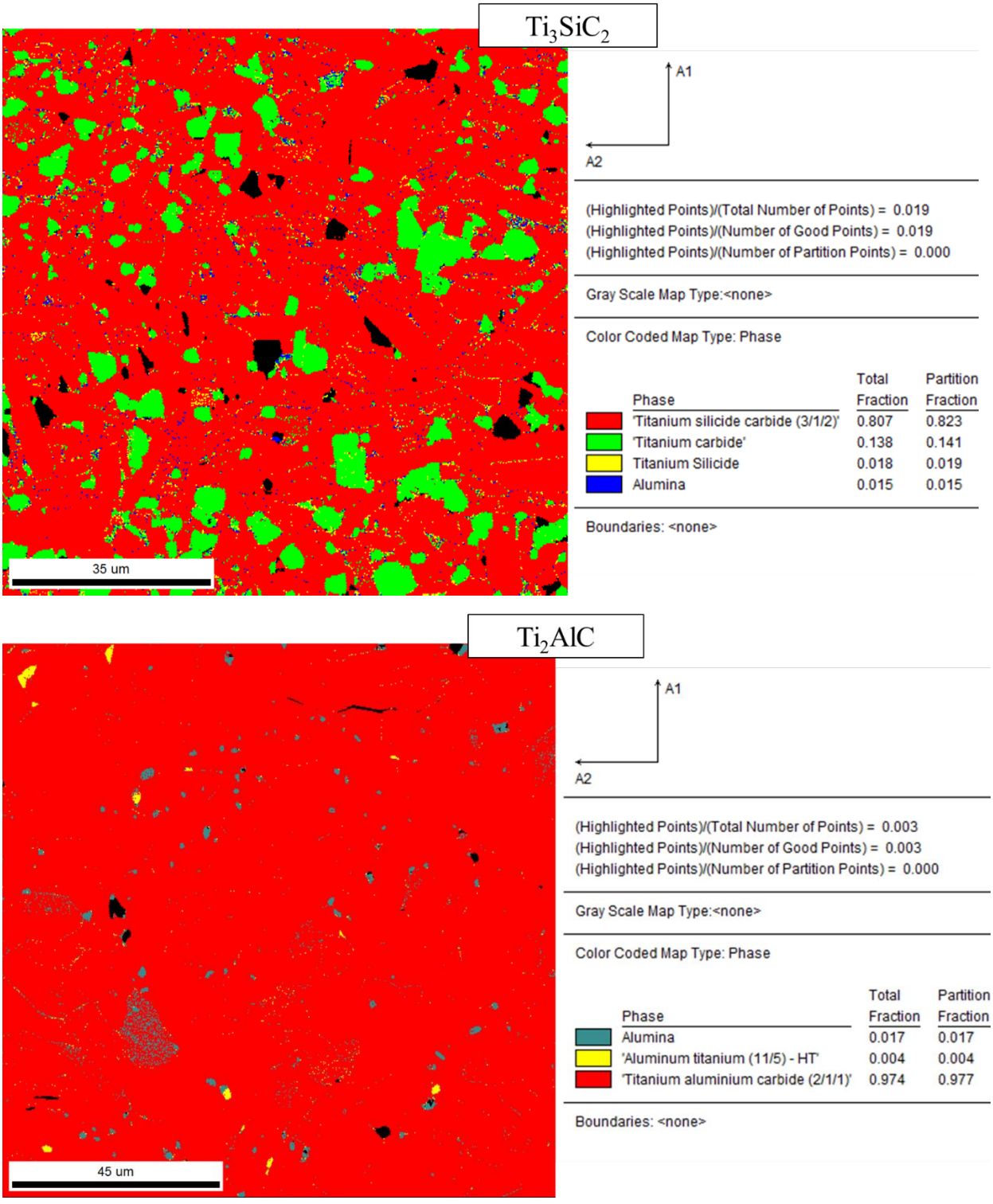


**Figure A.3** – MAX Phase Ceramic Compositional Analysis